

First measurements of radiative B decays in LHCb

Memòria per a optar al títol de doctor en Física

per

Albert Puig Navarro

Febrer de 2012
Dir. Ricardo Graciani Díaz

Programa de Doctorat de Física de l'EEES



Contents

Resum	v
Summary	xvii
Introduction	1
1. Radiative decays of B mesons	3
1.1. The Standard Model	3
1.2. Radiative B Decays in the Standard Model	14
1.3. Current theoretical and experimental status	20
2. CERN and the LHC	23
2.1. The European Organization for Nuclear Research (CERN)	23
2.2. The Large Hadron Collider	26
2.3. The experiments at the LHC	29
2.4. Computing resources for the LHC	31
3. The LHCb experiment	33
3.1. LHCb 2011 running conditions	35
3.2. Detector layout	36
3.3. The Tracking System	40
3.4. The Particle Identification System	50
3.5. The Trigger System	64
3.6. The Online System	68
3.7. Computing and resources	69
4. Trigger strategies for radiative B decays at LHCb	75
4.1. Data samples	75
4.2. Methods for determining trigger efficiencies	76
4.3. L0 channels	78
4.4. HLT1 lines	79
4.5. HLT2 lines	81
4.6. Exclusive strategy	92
4.7. Inclusive strategy	94
4.8. Performance in 2011	95
4.9. Prospects for 2012	100

5. Measurement of the ratio $\mathcal{B}(B^0 \rightarrow K^{*0}\gamma)/\mathcal{B}(B_s^0 \rightarrow \phi\gamma)$	107
5.1. Data samples and software versions	108
5.2. Event selection	110
5.3. Signal shape	115
5.4. Background composition	121
5.5. Fit	134
5.6. Extraction of the ratio of branching fractions	141
5.7. Result	155
6. Conclusions	159
A. Helicity formalism and angular distributions	161
A.1. The helicity formalism	161
A.2. Angular distributions in two-body decays	164
B. Isospin-conserving decay of the K^{*0} vector meson	169

Resum

El Model Estàndard (ME) és la descripció més fonamental de la matèria i les seves interaccions, i la seva consistència ha estat validada per un gran nombre d'experiments. Malgrat el seu èxit, el ME no incorpora elements com la gravetat, l'energia fosca, la matèria fosca o les (ja observades) oscil·lacions de neutrins.

Els hadrons B constitueixen un excel·lent banc de proves per a mesurar paràmetres del ME tals com els elements de la matriu CKM or la violació de simetria CP . A més, els corrents neutres amb canvi de sabor (CNCS), que no són possibles a nivell arbre i, per tant, són molt sensibles a noves partícules massives, poden ser utilitzats com a proves per a la recerca de física més enllà del Model Estàndard. Les desintegracions radiatives d'hadrons B són un bon exemple d'aquest tipus de corrent. L'experiment LHCb, un dels sis experiments del Gran Col·lidor d'Hadrons, està dedicat a l'estudi de la violació de CP i de les desintegracions rares dels hadrons B .

Per tal d'estudiar desintegracions radiatives d'hadrons B a LHCb, és necessari distingir-les i salvar-les d'entre la gran quantitat d'esdeveniments de fons produïts a l'LHC, la majoria del quals són rebutjats pel sistema de *trigger* de l'experiment instants després que s'hagin produït. Aquest document descriu el procés de redisseny i optimització dels algoritmes de *trigger* ja existents per a aquest tipus de desintegracions, i la introducció de nous per tal d'ampliar el programa de desintegracions radiatives d'LHCb a canals no previstos inicialment.

A més, aquest document descriu la mesura de la raó entre les fraccions d'embrancament \mathcal{B} de $B^0 \rightarrow K^{*0}\gamma$ i $B_s^0 \rightarrow \phi\gamma$ a partir d' 1.0 fb^{-1} de dades recollides el 2011. El resultat obtingut és compatible amb la predicció teòrica i amb les mesures anteriors, i s'ha fet servir, juntament amb la mitjana mundial de $\mathcal{B}(B^0 \rightarrow K^{*0}\gamma)$, per a obtenir la mesura més precisa de $\mathcal{B}(B_s^0 \rightarrow \phi\gamma)$.

Desintegracions radiatives de mesons B

En el Model Estàndard, els CNCS del tipus $b \rightarrow s\gamma$ són únicament possibles a través de transicions electromagnètiques a un *loop*, dominades per un quark top virtual que s'aparella amb un bosó W . Extensions del ME preduïen partícules addicionals que, circulant en el *loop*, poden introduir efectes mesurables a la dinàmica de la transició.

Els processos a nivell de quarks tals com $b \rightarrow s\gamma$ no es poden observar directament perquè la interacció forta fa que es formin hadrons a partir dels quarks. Aquest procés d'hadronització es majoritàriament no perturbatiu, i per tant provoca incerteses significants en el càlcul de les fraccions d'embrancament exclusives.

Les prediccions teòriques es realitzen separant les parts perturbativa i no perturbativa dels elements de matriu hadrònics mitjançant SCET (*Soft Collinear Effective Theory*).

Les contribucions perturbatives són conegeudes parcialment fins a NNLO (*Next-to-Next-Leading Order*), i el càlcul de les contribucions no perturbatives s'efectua mitjançant regles de suma de QCD (*Quantum Chromodynamics*) sobre el con de llum. La prediccó per a les \mathcal{B} de $B^0 \rightarrow K^{*0}\gamma$ i $B_s^0 \rightarrow \phi\gamma$ és $(4.3 \pm 1.4) \times 10^{-5}$, i el càlcul de la seva raó dona 1.0 ± 0.2 a causa de la cancel·lació d'algunes incerteses.

Les desintegracions radiatives del mesó B^0 van ser observades per primer cop per la col·laboració CLEO, l'any 1993, a través del mode $B^0 \rightarrow K^{*0}\gamma$. El 2007, la col·laboració Belle va anunciar la primera observació de la desintegració anàloga del mesó B_s^0 , $B_s^0 \rightarrow \phi\gamma$. Els valors mesurats per a $\mathcal{B}(B^0 \rightarrow K^{*0}\gamma)$ i $\mathcal{B}(B_s^0 \rightarrow \phi\gamma)$ són $(4.33 \pm 0.15) \times 10^{-5}$ i $(5.7_{-1.8}^{+2.1}) \times 10^{-5}$, respectivament. Aquest valors són compatibles amb les prediccions teòriques obtingudes de càlculs a NNLO. El valor experimental de la raó de $\mathcal{B}(B^0 \rightarrow K^{*0}\gamma)$ entre $\mathcal{B}(B_s^0 \rightarrow \phi\gamma)$ és 0.7 ± 0.3 , també compatible amb la prediccó del ME.

El CERN i l'LHC

L'Organització Europea per a la Recerca Nuclear, coneguda com a CERN, és el laboratori de física de partícules més gran del món, i està situat a la frontera franco-suïssa, prop de Ginebra. Actualment compta amb 20 Estats Membres, però molts països no Europeus es troben involucrats de maneres diverses. En total, uns 10,000 científics de 608 instituts i universitats de 113 països, la meitat dels físics de partícules del món, utilitzen les seves instal·lacions.

Al CERN s'hi han fet un gran nombre de descobriments, com per exemple els bosons W^\pm i Z . Al llarg de la seva història, diversos científics que treballaven allà han estat guardonats amb premis Nobel de física. A més, el laboratori ha estat la seu de diversos col·lidors de partícules, incloent el primer col·lidor protó-protó, el primer col·lidor protó-antiproto i, actualment, el col·lidor més potent del món, el Gran Col·lidor d'Hadrons (*Large Hadron Collider*, LHC).

L'LHC és un col·lidor protó-protó dissenyat per a funcionar amb una energia al centre de masses de 14 TeV i està instal·lat al túnel circular de 27 km de perímetre que antigament havia contingut l'accelerador LEP.

Al voltant de quatre punts d'interacció de l'anell de l'LHC es troben situats quatre grans detectors i dos petits experiments, que són:

- ALICE, dedicat a l'estudi de la física derivada de la col·lisió de nuclis pesants (Pb-Pb).
- ATLAS, un experiment de propòsit general construït amb l'objectiu de posar a prova el ME a l'escala del TeV i de buscar el bosó de Higgs i física més enllà del Model Estàndard.
- CMS, un altre experiment de propòsit general destinat a l'estudi del mecanisme de la ruptura de simetria electrofèble, de la qual es considera responsable el mecanisme de Higgs, i a l'estudi del ME a energies per sobre d'1 TeV.
- LHCb, dedicat a l'estudi de la violació de CP i de les desintegracions rares de partícules amb contingut de quark b .
- LHCf, un petit experiment dissenyat per a mesurar la secció eficaç de pions neutres i neutrons a angles molt petits.

- TOTEM, que intenta mesurar la secció eficaç pp amb un mètode independent de la lluminositat, basat en el Teorema Òptic.

L'experiment LHCb

L'experiment LHCb està dedicat a l'estudi de la física dels quarks massius a l'LHC. El seu principal objectiu és la mesura de la violació de CP i de les desintegracions rares d'hadrons b i \bar{b} . Està situat al Punt d'Interacció 8 de l'LHC, antigament utilitzat per l'experiment DELPHI de LEP.

Disseny del detector

Tal i com es mostra a la Fig. 1, LHCb és un espectròmetre que cobreix un angle d'aproximadament 15 – 300 mrad en el pla horitzontal i de 15 – 250 mrad en el vertical. L'elecció d'aquesta geometria ve motivada pel fet que, a l'LHC, les parelles $b\bar{b}$ són produïdes majoritàriament en la mateixa direcció, ja sigui cap endavant o cap endarrera.

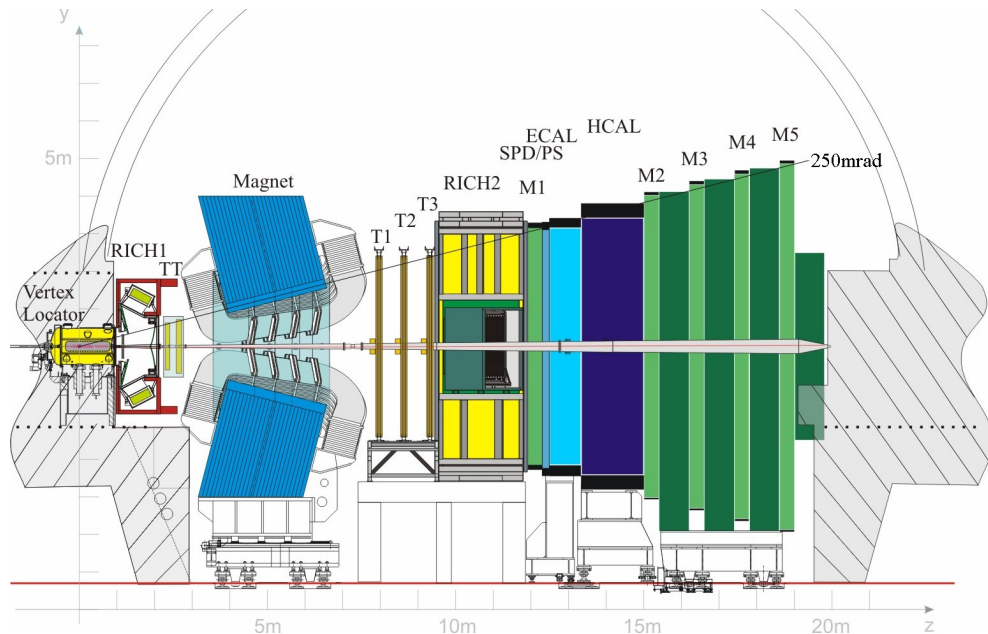


Figure 1. Vista lateral del detector LHCb.

Començant pel punt d'interacció, situat a l'esquerra de la Fig. 1, el sistema de traces d'LHCb està format per tres subdetectors:

- El *Vertex Locator* (VELO), format per tires de silici que permeten mesurar amb precisió la posició dels vèrtexs de producció i desintegració de les partícules, envolta la zona d'interacció protó-protó (pp).
- El *TT*, que consta d'una gran superfície de tires de silici i està situat davant d'un imant amb una capacitat de curvatura d'aproximadament 4 Tm.

-
- Les estacions de mesura de trajectòries (*Inner Tracker* (IT) i *Outer Tracker* (OT)), són una combinació de detectors de tires de silici i de tubs de deriva situats al darrera de l'imant.

El sistema de traces complet té una resolució en moments $\delta p/p$ que va del 0.3% al 0.5% en el rang de moments $5 - 100 \text{ GeV}/c$.

Dos detectors d'anells Cherenkov, *Ring Imaging Cherenkov* (RICH), equipats amb diversos tipus de materials radiadors, són responsables de la identificació d'hadrons carregats en el rang de moments $2 - 100 \text{ GeV}/c$.

El sistema de calorimetria és l'encarregat de la detecció de partícules neutres i de la identificació d'electrons i fotons. Està format per un calorímetre electromagnètic, l'ECAL, i un d'hadrònic, l'HCAL. A més, dos plans de material centellejador, separats per un absorbent de plom i situats abans de l'ECAL, són utilitzats per a millorar la identificació de partícules, especialment al primer nivell de *trigger*. El primer d'aquests plans està destinat a la separació fotons i electrons, mentre que el segon s'utilitza per a la identificació de cascades electromagnètiques. La correcta calibració de l'ECAL és un requisit clau per a la mesura de desintegracions radiatives, ja que la seva característica distintiva a nivell experimental és un fotó d'alta energia.

Finalment, els muons són identificats i mesurats a les cambres de muons, formades per cinc capes de cambres proporcionals multifils separades per absorbent de ferro.

Sistema de *trigger*

El sistema de *trigger* d'LHCb redueix el ritme d'esdeveniments dels 10 MHz produïts per les col·lisions de l'LHC fins als 3 kHz permesos per els recursos d'emmagatzematge. Està dividit en dues fases: la primera fase, el L0, està implementada mitjançant plaques electròniques dissenyades especialment per a aquesta tasca, i redueix el ritme d'esdeveniments fins a 1 MHz fent servir la informació proporcionada pels sistemes de calorimetria i de muons; la segona fase, el *High Level Trigger* (HLT), consisteix en un conjunt d'algoritmes que s'executen en una gran granja d'ordinadors i que efectuen de manera selectiva la reconstrucció completa dels esdeveniments.

Sistema Online

El sistema *Online* és l'encarregat d'assegurar que la transferència de dades des de l'electrònica del detector fins als sistemes d'emmagatzematge s'efectua d'una manera consistent i controlada. Està dividit en tres sub-sistemes:

- El sistema d'adquisició de dades (DAQ) transporta les dades acceptades pel L0 fins al sistema d'emmagatzematge.
- El sistema de *Timing and Fast Control* (TFC) controla el flux de dades entre el detector i la granja d'ordinadors.
- El sistema de control de l'experiment (ECS) permet controlar i monitoritzar el detector i els sistemes de *trigger*, DAQ i TFC.

Aplicacions informàtiques

El programari d'LHCb està basat en l'arquitectura GAUDI, que proporciona un marc comú per a totes les aplicacions usades a l'experiment i que té la flexibilitat per a

permetre executar el flux de dades d'LHCb per a simulacions Monte Carlo (MC) i per a dades reals fent servir les mateixes eines. Les dades es guarden en disc en un format basat en ROOT, un conjunt de paquets de programari dissenyat per a manejar i analitzar grans volums de dades.

La simulació de col·lisions pp i la interacció dels seus productes amb el detector és realitzada per l'aplicació GAUSS; llavors, l'aplicació BOOLE simula la digitalització de les deposicions energètiques en el detector i en el L0. Arribats a aquest punt, les dades, reals o simulades, passen a través de l'aplicació MOORE, que executa l'HLT i decideix si els esdeveniments són acceptats o descartats; en el cas de les dades reals, els esdeveniments acceptats són transferits al sistema d'emmagatzematge per a ser processades i arxivades posteriorment. Aquestes dades (reals o simulades), encara pends de processar, s'analitzen amb l'aplicació BRUNEL, que s'encarrega de reconstruir les partícules. A continuació, l'aplicació DAVINCI classifica filtra aquestes partícules en un procés anomenat *Stripping*, i acaba produint al final un arxiu en format ROOT, anomenat *Summary Data Tape* (DST). Aquests arxius DST poden ser analitzats més tard mitjançant DAVINCI per tal de produir NTuples de ROOT, adequades per a la realització d'anàlisi.

Les dades reals són reprocessades diversos cops a l'any per tal d'afegir millors en les aplicacions, algoritmes i constants de calibració de la reconstrucció, l'aliniament i l'*Stripping*.

Condicions de presa de dades de 2010 i 2011

El 2010, l'LHC va proporcionar a LHCb 37 pb^{-1} de dades i va aconseguir arribar al 80% de la lluminositat de disseny. Malgrat això, aquesta lluminositat es va assolir mitjançant l'ús de paràmetres de l'accelerador diferents dels previstos, i com a conseqüència es va produir un augment del nombre d'interaccions visibles, μ . L'augment de μ implica un nombre major d'interaccions (i, per tant, de vèrtex) per xoc, un augment en les taxes de lectura del detector i un augment en de la mida dels esdeveniments i del temps necessari per a processar-los. Tot i el gran efecte que una μ alta té sobre les condicions de treball del *trigger*, el sistema de *trigger* d'LHCb ha sigut capaç d'adaptar-se perfectament.

El 2011, l'LHC ha proporcionat a LHCb $\sim 1.2 \text{ fb}^{-1}$ de dades, les quals han estat desades amb una eficiència del 91%. El nombre mitjà de col·lisions pp inelàstiques ha estat també per sobre del valor de disseny, però ha estat considerablement inferior al de 2010.

Estratègies de *trigger* per desintegracions radiatives d'hadrons B a LHCb

Un *trigger* eficient és essencial per a l'estudi de desintegracions radiatives d'hadrons B , ja que la seva raó d'embrancament és petita, de l'ordre de 10^{-5} o inferior, i per tant la seva producció es troba limitada a un màxim d'uns pocs milions per fb^{-1} , que a més es troben diluïts entre un gran nombre d'esdeveniments de fons.

Estratègies de *trigger*

En el L0, els canals **L0Electron** i **L0Photon** seleccionen aquells esdeveniments que tenen una deposició energètica a l'ECAL amb una energia transversa respecte a la direcció dels feixos de protons, E_T , superior a un cert llindar, col·locat a 2.5 GeV durant el 2011. A més, un subgrup dels esdeveniments que són acceptats per aquests canals també passen els canals **L0ElectronHi** i **L0PhotonHi**, de característiques similars però amb un llindar superior, 4.2 GeV. El requisit per a desintegracions radiatives és que el fotó de senyal hagi estat la causa de disparar el L0, això és, que o **L0Electron** o **L0Photon** siguin TOS (*Trigger On Signal*).

En l'HLT1, les línies rellevants per a desintegracions radiatives són les línies d'una traça, **Hlt1TrackAllL0** and **Hlt1TrackPhoton**, que seleccionen els esdeveniments basant-se en el moment transvers, p_T , i el paràmetre d'impacte, IP, d'una de les traces de l'esdeveniment. Per un costat, **Hlt1TrackAllL0** accepta esdeveniments amb photons de baixa E_T mitjançant un tall més dur en el p_T de la traça. Per l'altre costat, **Hlt1TrackPhotonL0** permet relaxar el tall en p_T de les traces requerint una E_T més alta al fotó. Per a desintegracions radiatives, el requisit aplicat en l'HLT1 és que o **Hlt1TrackAllL0** o **Hlt1TrackPhotonL0** siguin TOS.

En l'HLT2, s'han estudiat dues estratègies, inclusiva i exclusiva. Les línies exclusives per a desintegracions radiatives, **Hlt2Bd2KstGamma** i **Hlt2Bs2PhiGamma**, són versions relaxades de les seleccions utilitzades a les analisis. Per a 2011, s'han modificat per tal que únicament s'executin en esdeveniments que passen els canals **L0Electron** o **L0Photon** al L0; a més, s'han optimitzat els talls emprats en la selecció d'esdeveniments. La seva eficiència està per sobre del 85% per a $B^0 \rightarrow K^{*0} \gamma$ i $B_s^0 \rightarrow \phi \gamma$, tal i com es mostra a la Taula 1, però no ofereixen un bon resultat per a altres canals, com $B^+ \rightarrow \phi K^+ \gamma$ i $B^+ \rightarrow K^{*0} \pi^+ \gamma$, per als quals no van ser dissenyades.

	Hlt2Bd2KstGamma (%)	Hlt2Bs2PhiGamma (%)
$B^0 \rightarrow K^{*0} \gamma$	85.6 ± 0.3	0.002 ± 0.004
$B_s^0 \rightarrow \phi \gamma$	35.4 ± 0.4	89.4 ± 0.2
$B^+ \rightarrow \phi K^+ \gamma$	17.5 ± 0.8	18.0 ± 0.8
$B^+ \rightarrow K^{*0} \pi^+ \gamma$	42.2 ± 1.8	0.5 ± 0.2

Table 1. Eficiència TOS de les línies exclusives de l'HLT2, calculada sobre esdeveniments simulats, amb els requisits **L0Photon** o **L0Electron** TOS i **Hlt1TrackAllL0** o **Hlt1TrackPhoton** TOS.

El rendiment de les línies topològiques de l'HLT2, basades en un mètode multivariat anomenat BBBDT i àmpliament utilitzades a LHCb, es mostra a la primera columna de la Taula 2. S'ha conclòs que, tot i que clarament milloren l'eficiència de selecció dels canals $B^+ \rightarrow \phi K^+ \gamma$ i $B^+ \rightarrow K^{*0} \pi^+ \gamma$, el seu impacte negatiu en les eficiències de $B^0 \rightarrow K^{*0} \gamma$ i $B_s^0 \rightarrow \phi \gamma$ és massa alt.

Per aquesta raó s'ha desenvolupat i introduït un nou conjunt de línies topològiques radiatives per a l'HLT2. Tot i estar basades en les mateixes idees que el *trigger* topològic, les línies topològiques radiatives s'aprofiten de la presència del fotó per tal de relaxar alguns dels criteris de selecció aplicats sobre la resta dels productes de la desintegració. Per a aquestes línies, s'han estudiat dos enfocys diferents, un basat

	Topo basat en BBDT (%)	Radiatiu basat en talls (%)	Radiatiu basat en BBDT (%)	ϕ inclusiu (%)
$B^0 \rightarrow K^{*0}\gamma$	33.1 ± 0.4	75.6 ± 0.4	80.5 ± 0.4	—
$B_s^0 \rightarrow \phi\gamma$	47.1 ± 0.4	77.3 ± 0.3	84.4 ± 0.3	95.51 ± 0.15
$B^+ \rightarrow \phi K^+\gamma$	50.1 ± 1.1	90.0 ± 0.6	91.4 ± 0.6	81.4 ± 0.8
$B^+ \rightarrow K^{*0}\pi^+\gamma$	48.8 ± 1.8	89.3 ± 1.1	91.5 ± 1.0	—

Table 2. Eficiència TOS de les línies inclusives de l'HLT2, calculada sobre esdeveniments simulats, amb els requisits LOPhoton o LOElectron TOS i Hlt1TrackAllL0 o Hlt1TrackPhoton TOS.

únicament en talls i l'altre basat en el mètode BBDT. La segona i tercera columnes de la Taula 2 mostren les diferències en el rendiment d'aquestes dues línies sobre dades MC. Es recuperen bones eficiències per a $B^0 \rightarrow K^{*0}\gamma$ i $B_s^0 \rightarrow \phi\gamma$, aproximadament un 5% inferiors a les proporcionades per les línies exclusives, i a la vegada l'eficiència per a $B^+ \rightarrow \phi K^+\gamma$ i $B^+ \rightarrow K^{*0}\pi^+\gamma$ es veu augmentada fins al 90%. Per tant, mitjançant l'ús d'aquestes línies es pot obtenir una eficiència en l'HLT2 superior al 80% per a totes les desintegracions estudiades.

Finalment, per tal d'augmentar l'eficiència en un canal clau com és $B_s^0 \rightarrow \phi\gamma$, la línia inclusiva per al mesó ϕ ha estat redissenyada i inclosa en el trigger per a 2011. Aquesta línia funciona amb la idea de buscar traces de càrrega oposada, identificar-les com a kaons mitjançant un tall suau en les variables d'identificació proporcionades pel RICH, i combinar-les per a formar un mesó ϕ . Aquesta línia proporciona un enfoc transversal per al trigger de desintegracions que contenen una ϕ i, tal i com es mostra en la última columna de la Taula 2, proporciona un rendiment excel·lent per a $B_s^0 \rightarrow \phi\gamma$.

Resumint, la comparació entre les Taules 1 i 2 mostra que, en tres dels quatre canals estudiats, el rendiment de l'estrategia inclusiva és superior al de l'exclusiva. L'eficiència de les línies és exclusives és únicament més alt en el cas de $B^0 \rightarrow K^{*0}\gamma$.

Reconstrucció del calorímetre a l'HLT2

La introducció de les línies radiatives topològiques a l'HLT2 provoca un augment de nombre d'esdeveniments pels quals és necessari reconstruir un fotó. Aquest fet provoquaria un augment inacceptables del temps d'execució de l'HLT2, ja que la reconstrucció del calorímetre en el trigger no ha estat optimitzada per a ser executada amb limitacions de temps.

Això ha obligat al desenvolupar un nou procediment de reconstrucció del calorímetre per a l'HLT2, basat en restringir el procés d'agrupació de deposicions energètiques a zones situades al voltant d'objectes calorimètrics del L0. Aquest mètode, introduït al trigger el juny de 2011, proporciona una disminució d'un factor tres en el temps d'execució amb el cost d'una petita pèrdua d'eficiència.

Rendiment al 2011

En general, la determinació de les eficiències absolutes de les diverses línies de trigger mitjançant les dades preses el 2011 no ha estat possible a causa de la falta de dades. El mètode TISTOS només ha pogut ser utilitzat en el cas de la línia exclusiva per a

$B^0 \rightarrow K^{*0}\gamma$, i s'ha trobat una eficiència de $(84 \pm 3)\%$, en acord amb el valor determinat amb el MC, $(85.6 \pm 0.3)\%$

Tot i així, ha estat possible realitzar una comparativa quantitativa del rendiment de les diverses línies de *trigger*, basada en l'estudi de les distribucions de massa invariant de $B^0 \rightarrow K^{*0}\gamma$ i $B_s^0 \rightarrow \phi\gamma$. S'ha conclòs que, tot i que les línies exclusives proporcionen una quantitat més alta d'esdeveniments, les línies inclusives tenen més capacitat per a rebutjar esdeveniments de fons, i per tant proporcionen una millor raó S/B amb el cost d'una petita disminució d'eficiència. A més, el *trigger* inclusiu de mesons ϕ ha tingut un rendiment extraordinari per a $B_s^0 \rightarrow \phi\gamma$, tant en termes de nombre d'esdeveniments de senyal com en termes de rebuig d'esdeveniments de fons.

Plans per a 2012

El gran rendiment de les línies radiatives topològiques de l'HLT2 a finals de 2011 permet afirmar que, el 2012, l'estratègia de *trigger* per a desintegracions radiatives serà inclusiva.

Aquest canvi serà molt beneficiós, tant per a diverses anàlisis ja iniciades, com l'estudi de la asimetria CP en $B^+ \rightarrow \phi K^+\gamma$ i $B^+ \rightarrow K^{*0}\pi^+\gamma$ o l'estudi de les desintegracions radiatives dels barions Λ_b , com per a obrir camí a noves anàlisis com l'estudi de la asimetria d'isospin de $B^0 \rightarrow K^{*0}\gamma$ o la asimetria CP de les transicions $b \rightarrow d\gamma$, representades per $B \rightarrow \rho\gamma$.

Les línies exclusives es mantindran com a control de les línies inclusives, però han estat modificades per tal de disminuir el màxim possible el seu impacte en el nombre d'esdeveniments acceptats per l'HLT2. Aquesta reducció s'ha aconseguit mitjançant l'aplicació de talls molt més durs, convertint-les de manera efectiva en quasi-seleccions offline.

Mesura de la raó $\mathcal{B}(B^0 \rightarrow K^{*0}\gamma)/\mathcal{B}(B_s^0 \rightarrow \phi\gamma)$

El principal objectiu d'aquesta anàlisi és l'extracció de la raó de les fraccions d'embrancament de $B^0 \rightarrow K^{*0}\gamma$, amb $K^{*0} \rightarrow K^\pm\pi^\mp$, i $B_s^0 \rightarrow \phi\gamma$, amb $\phi \rightarrow K^+K^-$, i els seus complexos conjugats. A partir d'aquesta mesura, el valor de $\mathcal{B}(B^0 \rightarrow K^{*0}\gamma)$ pot ser utilitzat per a obtenir $\mathcal{B}(B_s^0 \rightarrow \phi\gamma)$.

Selecció d'esdeveniments

La selecció de les dues desintegracions B s'ha dissenyat per tal d'obtenir la màxima cancel·lació d'incerteses sistemàtiques al calcular la raó de les seves eficiències. En aquest sentit, tant el procés de reconstrucció dels candidates com els requisits que s'hi apliquen es mantenen el més similars possible: els mesons B^0 (B_s^0) són reconstruïts a partir de la combinació d'un fotó i un mesó vector K^{*0} (ϕ), construït a partir de parelles kaó-pió (pió-kaó) de càrrega oposada.

Les dues traces carregades amb les quals es construeix el mesó vector (V) han de tenir $p_T > 500 \text{ MeV}/c$ i no poden apuntar cap a un vèrtex d'interacció pp , condició garantida pel requisit $\text{IP } \chi^2 > 25$. La identificació de les traces com a kaó o pió es realitza mitjançant l'aplicació de talls en la identificació de partícules (PID) proporcionada pel RICH. El PID està basat en la comparació entre dues hipòtesis d'identificació de partícula, i es representa amb la diferència entre els logaritmes de les funcions de

versemblança (DLL) entre les dues hipòtesis. Els kaons han de tenir $DLL_{K\pi} > 5$ i $DLL_{Kp} > 2$, mentre que els pions han de complir $DLL_{\pi K} > 0$. Amb aquests talls, els kaons (pions) que formen part dels canals estudiats són identificats correctament amb una eficiència del ~ 70 (83) %, amb un ~ 3 (2) % de contaminació de pions (kaons).

Les combinacions de dues traces són acceptades com a candidats a K^{*0} (ϕ) si formen un vèrtex amb $\chi^2 < 9$, si el p_T d'una de les dues traces està per sobre de $1.2 \text{ GeV}/c$, i si la seva massa invariant es troba dins d'una finestra de massa de 50 (10) MeV/c^2 al voltant de la massa nominal del K^{*0} (ϕ).

El candidat a V resultant és combinat amb un fotó amb $E_T > 2.6 \text{ GeV}$. Els *clusters* electromagnètics a l'ECAL són separats entre neutres i carregats basant-se en la seva compatibilitat amb traces extrapolades al calorímetre, mentre que els dipòsits neutre de fotons i π^0 són identificats en base a la forma de les cascades electromagnètiques a l'ECAL.

Els candidats a B han de tenir la massa invariant dins d'una finestra de masses d' $1 \text{ GeV}/c^2$ al voltant de la massa nominal del mesó corresponent, $p_T > 3 \text{ GeV}/c$, han d'haver volat des del punt d'interacció un mínim de 100 unitats en χ^2 , i han d'apuntar a un vèrtex d'interacció pp , $\text{IP } \chi^2 < 9$. L'angle d'helicitat θ_H , definit com l'angle entre el moment de qualsevol de les filles de V i el moment del candidat a B en el sistema de referència en què V està en repòs, es distribueix com $\sin^2 \theta_H$ per $B \rightarrow V\gamma$ i com a $\cos^2 \theta_H$ per els fons de tipus $B \rightarrow V\pi^0$. Per tant, l'estructura d'helicitat imposta per la senyal pot ser explotada per a eliminar fons del tipus $B \rightarrow V\pi^0$, en els quals el pió neutre s'ha identificat incorrectament com un fotó, requerint que $|\cos \theta_H| < 0.8$. El fons provinent de desintegracions parcialment reconstruïdes d'hadrons B es rebutja mitjançant un tall en l'aïllament del vèrtex: el χ^2 del vèrtex del candidat ha d'augmentar en més de dues unitats quan se liafegeix qualsevol altra traça de l'esdeveniment.

Extracció de la raó de fraccions d'embrancament

La raó de fraccions d'embrancament es calcula a partir del nombre de candidates de senyal en els canals $B^0 \rightarrow K^{*0}\gamma$ i $B_s^0 \rightarrow \phi\gamma$,

$$\frac{\mathcal{B}(B^0 \rightarrow K^{*0}\gamma)}{\mathcal{B}(B_s^0 \rightarrow \phi\gamma)} = \frac{\mathcal{N}_{B^0 \rightarrow K^{*0}\gamma}}{\mathcal{N}_{B_s^0 \rightarrow \phi\gamma}} \frac{\mathcal{B}(\phi \rightarrow K^+K^-)}{\mathcal{B}(K^* \rightarrow K^+\pi^-)} \frac{f_s}{f_d} \frac{\epsilon_{B_s^0 \rightarrow \phi\gamma}}{\epsilon_{B^0 \rightarrow K^{*0}\gamma}}, \quad (1)$$

on \mathcal{N} correspon al nombre de candidats de senyal observats, $\mathcal{B}(\phi \rightarrow K^+K^-)$ i $\mathcal{B}(K^* \rightarrow K^+\pi^-)$ són les fraccions d'embrancament visible del mesons vector, f_s/f_d és la raó de les fraccions d'hadronització dels mesons B^0 i B_s^0 en col·lisions pp a $\sqrt{s} = 7 \text{ TeV}$ i $\epsilon_{B_s^0 \rightarrow \phi\gamma}/\epsilon_{B^0 \rightarrow K^{*0}\gamma}$ és la raó de les eficiències dels dos canals. Aquest últim terme es pot dividir en les contribucions provinents de l'acceptància (r_{Acc}), la la reconstrucció i selecció ($r_{\text{Reco}\&\text{SelNoPID}}$), els requisits de PID (r_{SelPID}), i la selecció de *trigger* (r_{Trigger}) :

$$\frac{\epsilon_{B_s^0 \rightarrow \phi\gamma}}{\epsilon_{B^0 \rightarrow K^{*0}\gamma}} = r_{\text{Trigger}} \times r_{\text{Acc}} \times r_{\text{Reco}\&\text{SelNoPID}} \times r_{\text{SelPID}}. \quad (2)$$

La raó d'eficiències de PID, $r_{\text{PID}} = 0.839 \pm 0.005$ (stat), s'ha calculat a partir de les dades mitjançant un procediment de calibració realitzat sobre mostres pures de kaons i pions procedents de desintegracions $D^{*\pm} \rightarrow D^0(K^+\pi^-)\pi^\pm$, seleccionades únicament amb criteris cinemàtics. La resta de raons d'eficiència s'han extret a partir d'esdeveniments simulats. La raó d'eficiències d'acceptància i reconstrucció, $r_{\text{Acc}} = 1.099 \pm 0.004$ (stat), és més gran que la unitat a causa de la correlació en

l'acceptància dels kaons provocada per les limitacions en l'espai de fases en la desintegració $\phi \rightarrow K^+ K^-$. Aquests limitacions en l'espai de fases també provoquen una pitjor resolució espacial del vèrtex de la ϕ , i afecten l'eficiència de selecció de $B_s^0 \rightarrow \phi\gamma$ a través dels talls en IP χ^2 , distància de vol i aïllament del vèrtex. Per contra, els talls en el p_T de les traces són menys eficients a l'actuar sobre el pió del K^{*0} , amb un espectre molt més suau. La raó d'eficiències de reconstrucció i selecció val $r_{\text{Reco\&SelNoPID}} = 0.881 \pm 0.005$ (stat) i s'observa la cancel·lació majoritària de les incerteses sistemàtiques gràcies a que les seleccions cinemàtiques són quasi iguals pels dos canals. La raó d'eficiències de *trigger*, $r_{\text{Trigger}} = 1.080 \pm 0.009$ (stat), s'ha calculat tenint en compte les contribucions de les diverses configuracions del *trigger* durant el període de presa de dades.

El nombre d'esdeveniments de senyal s'ha extret d'un ajust simultani de màxima versemblança de les distribucions de la massa invariant de les dades recollides el 2011. Cadascuna de les senyals s'ha descrit mitjançant la combinació de dues funcions Crystal Ball, amb els paràmetres de cua fixats a partir de dades simulades, i amb la diferència de masses entre el mesó B^0 i el mesó B_s^0 limitada al valor extret del PDG mitjançant una distribució Gaussiana amb mitjana $87.0 \text{ MeV}/c^2$ i amplada $0.6 \text{ MeV}/c^2$. L'amplada dels pics de senyal s'ha deixat lliure en l'ajust.

El fons combinatori s'ha parametritzat amb una funció exponencial, amb diferent constant de desintegració per cada canal. La contribució de $B \rightarrow hh\pi^0$, de $B_s^0 \rightarrow K^{*0}\gamma$, de $B^+ \rightarrow K^{*0}\pi^+\gamma$, de $B^+ \rightarrow \phi K^+\gamma$ i de desintegracions bariòniques radiatives a la senyal s'ha avaluat a partir de dades MC. La forma d'aquestes contaminacions s'ha fixat a partir de la simulació, i les seves amplituds s'han fixat, excepte en el cas dels canals parcialment reconstruïts $B_s^0 \rightarrow K^{*0}\gamma$ i $B^+ \rightarrow K^{*0}\pi^+\gamma$. Altres fons parcialment reconstruïts, que podrien contaminar la finestra de massa d'una manera considerable en el cas de $B^0 \rightarrow K^{*0}\gamma$, han estat modelats mitjançant una funció Argus extreta del MC, i la seva contaminació a la finestra de massa s'ha deixat com a paràmetre lliure de l'ajust. S'ha determinat que les contribucions de la contaminació entre els dos canals i dels múltiples candidats a B per esdeveniments són negligibles.

Finalment, s'ha introduït una funció d'acceptància per tal de modelar els efectes de la incorrecta calibració del calorímetre en el *trigger*, ja que les constants de calibració aplicades a posteriori, en la reconstrucció, no estaven aplicades a aquest nivell. Els seus efectes són perceptibles fins a $200 \text{ MeV}/c^2$ de distància dels límits de la finestra de massa.

Els resultats de l'ajust, que inclou tant la senyal com el fons, es mostren en la Fig. 2. Per un costat, s'observen 5280 ± 89 esdeveniments del canal $B^0 \rightarrow K^{*0}\gamma$, amb una raó S/B de 5.4 ± 0.4 a la finestra de masses de 2σ . Per altre costat, s'observen 694 ± 42 esdeveniments corresponents a $B_s^0 \rightarrow \phi\gamma$, amb una raó S/B de 7.3 ± 0.7 a la finestra de massa de 2σ . L'ajust ha retornat un valor de $X^2/\text{dof} = 101.23/100 \sim 1.0123$, que correspon a una probabilitat del 45%.

Incerteses sistemàtiques

El nombre limitat d'esdeveniments MC emprats en el càcul de r_{Acc} , $r_{\text{Reco\&SelNoPID}}$ i r_{Trigger} induceixen una incertesa sistemàtica en la raó de fraccions d'embrancament. A més, r_{Acc} és afectat per les incerteses en l'eficiència de reconstrucció d'hadrons que sorgeixen de les diferències entre la interacció de pions i kaons amb el detector i de les incerteses en la descripció de la quantitat de material en el detector. Les diferències

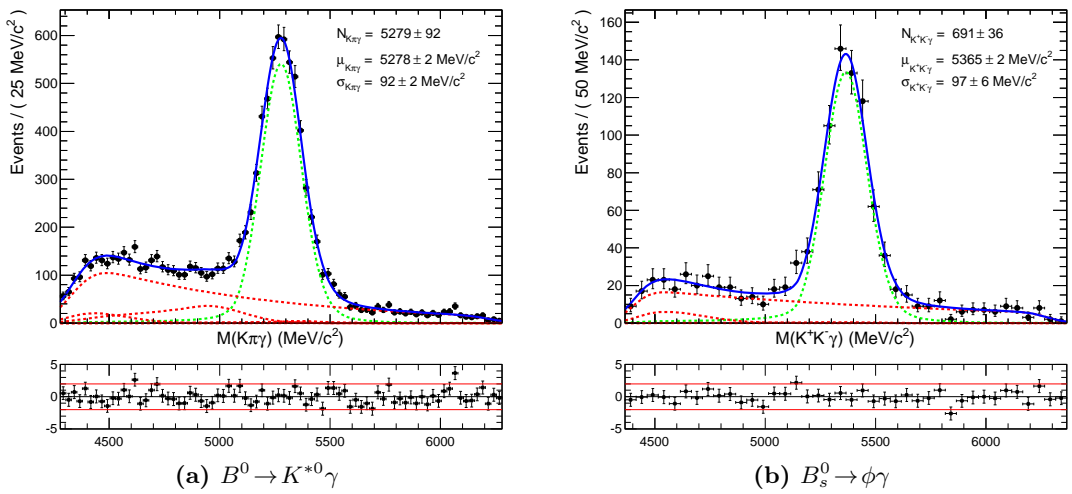


Figure 2. Distribució de massa invariant dels esdeveniments de $B^0 \rightarrow K^{*0}\gamma$ i $B_s^0 \rightarrow \phi\gamma$ data samples. El model ajustat està dibuixat amb una línia contínua blava, amb la senyal i els fons representats amb línia discontinua verda i vermella, respectivament.

en la mida de la finestra de masses dels mesons V , combinada amb petites diferències entre dades i MC en la posició dels pics de massa dels mesons K^{*0}/ϕ , produeixen una incertesa sistemàtica en $r_{SelNoPID}$ que s'ha avaluat movent el centre de la finestra de masses a la posició dels pics de massa determinats de les dades.

La poca fiabilitat de la simulació per a descriure l'IP χ^2 de les traces i l'aïllament del vèrtex de la B s'ha propagat com a incertesa de $r_{SelNoPID}$: la mostra de MC s'ha repesat per a reproduir la corresponent distribució de les dades, obtinguda mitjançant l'aplicació de la tècnica sPlot per a separar la senyal del fons a partir de l'ajust de la distribució de la massa invariant. No s'assignen més incerteses sistemàtiques a l'ús de simulació MC, ja que és ben conegut que les propietats cinemàtiques de les desintegracions estan ben descrites. Les incerteses sistemàtiques associades amb el fotó són negligibles, ja que la seva reconstrucció en ambdós canals és idèntica.

La incertesa sistemàtica associada al mètode de calibració del PID ha estat calculada fent ús de la simulació MC. L'error estadístic provocat per la mida de les mostres de pions i kaons emprades per a la calibració també ha estat propagada a r_{SelPID} .

L'efecte sistemàtic de la finestra de massa escollida s'ha avaluat repetint el procediment d'ajust en una finestra de massa de $\pm 700 \text{ MeV}/c^2$.

Els efectes de fixar la forma i l'amplitud de les contaminacions del fons a partir del MC també s'han tingut en compte. L'ajust s'ha repetit 10,000 vegades, variant aleatoriament els valors dels paràmetres fixos dins de la seva incertesa, i l'efecte sobre la raó entre el nombre d'esdeveniments s'ha calculat mitjançant el mètode d'intervals centrals.

Mitjançant els resultats resumits a la Taula 3, s'ha obtingut un valor per a la raó de fraccions d'embrancament de

$$\frac{\mathcal{B}(B^0 \rightarrow K^{*0}\gamma)}{\mathcal{B}(B_s^0 \rightarrow \phi\gamma)} = 1.31 \pm 0.08 \text{ (estad)} \pm 0.04 \text{ (sist)} \pm 0.10 \text{ } (f_s/f_d), \quad (3)$$

$r_{\mathcal{N}}$	$7.63 \pm 0.38^{+0.17}_{-0.16}$
$r_{\mathcal{B}}$ del mesó vector	0.735 ± 0.008
f_s/f_d	$0.267^{+0.021}_{-0.020}$
r_{ϵ}	0.877 ± 0.017

Table 3. Resum dels resultats intermitjos, amb les corresponents incerteses sistemàtiques, necessaris per a calcular la raó de fraccions d'embrancament segons l'Eq. 1.

compatible amb la predicció teòrica, 1.0 ± 0.2 . El valor d'aquesta raó s'ha combinat amb el valor ben conegit de la fracció d'embrancament del $B^0 \rightarrow K^{*0}\gamma$ per tal d'extreure el valor mesurat més acurat de la fracció d'embrancament de la desintegració radiativa $B_s^0 \rightarrow \phi\gamma$,

$$\mathcal{B}(B_s^0 \rightarrow \phi\gamma) = (3.3 \pm 0.3) \times 10^{-5}, \quad (4)$$

que també és compatible amb la predicció teòrica, $(4.6 \pm 1.4) \times 10^{-5}$. La incertesa en $\mathcal{B}(B_s^0 \rightarrow \phi\gamma)$ es redueix des del 35% al 9%, i, per tant, el coneixement d'aquesta fracció d'embrancament ha millorat considerablement.

Summary

The Standard Model (SM) is currently the most fundamental description of elementary particles and their interactions, and its consistency has been validated by a large number of experiments. Despite its success, the SM fails to incorporate elements such as gravity, dark energy, dark matter, and the already observed neutrino oscillations.

B hadrons constitute an excellent benchmark for measuring SM parameters such as the CKM matrix elements or CP violation. Furthermore, flavor-changing neutral currents (FCNC), which are only possible through loop processes and thus are very sensitive to new heavy particles circulating in the loop, can be used as probes of physics beyond the Standard Model. Radiative B hadron decays constitute excellent examples of this type of currents. The LHCb experiment, one of the six experiments of the Large Hadron Collider (LHC), is dedicated to the study of CP violation and rare decays in the B sector.

In order to study radiative B decays at LHCb, it is necessary to distinguish and save such events from the copious amount of background produced at the LHC, most of which is rejected by the experiment trigger system. Existing trigger algorithms have been redesigned and optimized, and new ones have been introduced in order to increase the efficiency and extend the LHCb radiative decays program to channels which were not initially foreseen.

Using 1.0 fb^{-1} of data recorded by LHCb in 2011, the ratio between the branching fractions of the $B^0 \rightarrow K^{*0}\gamma$ and $B_s^0 \rightarrow \phi\gamma$ has been measured. The value obtained is compatible with the theoretical prediction and with previous measurements, and it has been used, together with the well-known value of $\mathcal{B}(B^0 \rightarrow K^{*0}\gamma)$, to obtain the world-best measurement of $\mathcal{B}(B_s^0 \rightarrow \phi\gamma)$.

Radiative decays of B mesons

In the Standard Model the FCNC $b \rightarrow s\gamma$ proceeds through one-loop electromagnetic penguin transitions, dominated by a virtual intermediate top quark coupling to a W boson. Extensions of the SM predict additional one-loop contributions that can introduce sizeable effects on the dynamics of the transition.

Quark-level FCNC processes such as $b \rightarrow s\gamma$ cannot be directly observed because the strong interaction forms hadrons from the underlying quarks. The hadronization process is largely non-perturbative, and therefore introduces significant uncertainties in the calculation of exclusive branching fractions. Theoretical predictions are made by separating the perturbative and non-perturbative parts of the hadronic matrix elements with the help of Soft Collinear Effective Theory (SCET). Perturbative contributions are partially known up to NNLO, while non-perturbative calculations are performed

by making use of light cone QCD sum rules. The current prediction for the branching fractions of both $B^0 \rightarrow K^{*0}\gamma$ and $B_s^0 \rightarrow \phi\gamma$ is $(4.3 \pm 1.4) \times 10^{-5}$, with their ratio being calculated to be 1.0 ± 0.2 due to the cancellation of some uncertainties.

Radiative decays of the B^0 meson were first observed by the CLEO collaboration in 1993 through the $B^0 \rightarrow K^{*0}\gamma$ mode. In 2007 the Belle collaboration reported the first observation of the analogous decay in the B_s^0 sector, $B_s^0 \rightarrow \phi\gamma$. The current world averages of the branching fractions of $B^0 \rightarrow K^{*0}\gamma$ and $B_s^0 \rightarrow \phi\gamma$ are $(4.33 \pm 0.15) \times 10^{-5}$ and $(5.7_{-1.8}^{+2.1}) \times 10^{-5}$, respectively. These results are in agreement with the theoretical predictions from NNLO calculations. The ratio of experimental branching fractions is measured to be 0.7 ± 0.3 , also in agreement with the SM prediction.

CERN and the LHC

The European Organization for Nuclear Research, known as CERN, is the world’s largest particle physics laboratory, and is situated on the Franco-Swiss border, near Geneva. It is currently run by 20 European Member States, but many non-European countries are also involved in different ways. Overall, a total of 10,000 visiting scientists from 608 institutes and universities from 113 countries around the world —half of the world’s particle physicists— use its facilities.

Many discoveries have been made at CERN, such as the W^\pm and Z bosons, and, during its history, several Novel Prizes have been awarded to scientists working there. In addition, the laboratory has hosted many particle colliders, including the first proton-proton collider, the first proton-antiproton collider, and, currently, the largest collider in the world, the Large Hadron Collider.

The LHC is a proton-proton collider installed in the 27 km tunnel built to host the LEP machine, designed to run at a center-of-mass energy of 14 TeV. Four big detectors and two smaller experiments are located around the four interaction points of the LHC ring. These experiments are:

- ALICE, dedicated to the study of the physics of strongly interacting matter and quark-gluon plasma in heavy nuclei (Pb-Pb) collisions.
- ATLAS, a general purpose experiment with the objective to test the SM at the TeVscale, and to search for the Higgs boson and physics beyond the Standard Model.
- CMS, another general purpose experiment with the aim of studying the mechanism of electroweak symmetry breaking, for which the Higgs mechanism is presumed to be responsible, and testing the SM at energies above 1 TeV.
- LHCb, dedicated to the study of CP violation and rare decays in the b quark sector.
- LHCf, a small experiment designed to measure the very forward production cross sections and energy spectra of neutral pions and neutrons.
- TOTEM, which intends to measure the total pp cross section with a luminosity-independent method based on the Optical Theorem.

The LHCb experiment

The LHCb experiment is dedicated to the study of heavy flavor physics at the LHC. Its main aim is to make precise measurements of CP violation and rare decays of beauty and charm hadrons. It is located at Interaction Point 8 of the LHC accelerator, previously used by the DELPHI experiment from LEP.

Detector layout

Shown in Fig. 3, LHCb is a forward spectrometer with a polar angle coverage of approximately 15 – 300 mrad in the horizontal bending plane and 15 – 250 mrad in the vertical non-bending plane. This geometry choice is motivated by the fact that $b\bar{b}$ pairs produced at the LHC are produced in a large proportion in the same direction, either forward or backward.

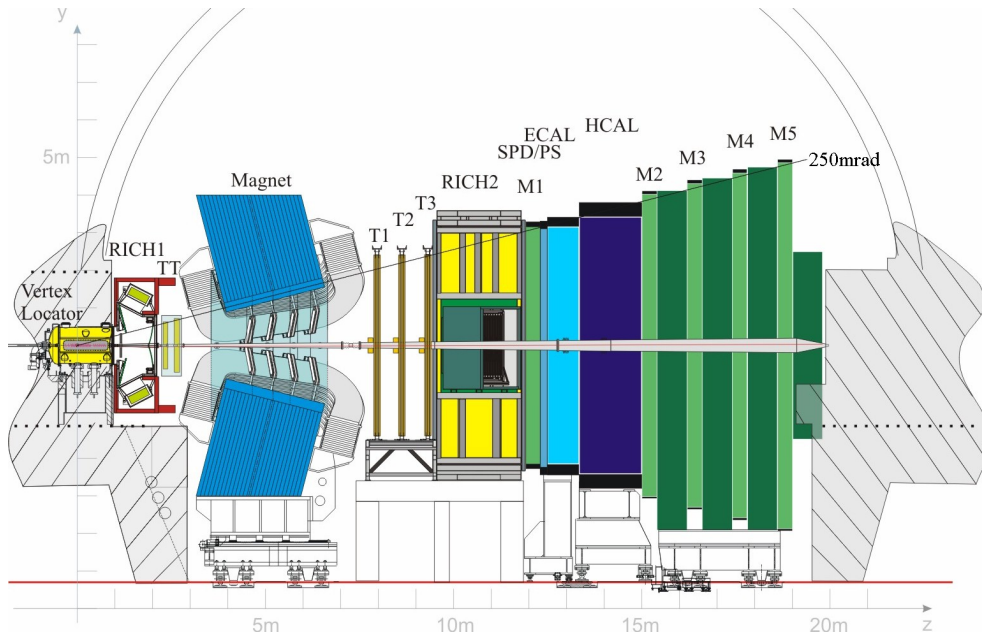


Figure 3. View of the LHCb detector.

Starting from the interaction point, at the left of Fig. 3, the LHCb tracking system consists of a silicon strip device surrounding the proton-proton (pp) interaction region (the Vertex Locator), a large area silicon strip detector (the TT) located upstream of a dipole magnet which has a bending power of about 4 Tm, and a combination of silicon strip detectors and straw drift-tubes placed downstream of the magnet (the IT and OT). The combined tracking system has a momentum resolution $\delta p/p$ that varies from 0.3% to 0.5% in the 5 – 100 GeV/ c range.

Charged hadron identification in the momentum range 2 – 100 GeV/ c is provided by two Ring Imaging Cherenkov (RICH) detectors with different radiators.

A calorimeter system is used for the detection of neutral particles and for the identification of electrons and photons. It consists of an electromagnetic (ECAL) and a hadronic (HCAL) sampling calorimeter. In addition, two scintillating planes separated by a lead absorber placed upstream of the ECAL are used to provide improved particle

identification, especially for the first level of trigger. The first of these planes provides separation between electrons and photons, while the second one is used for tagging electromagnetic showers. The correct calibration of the ECAL is a key requisite for the study of radiative decays, since their distinct experimental signature is a high energy photon.

Finally, muons are identified and measured by means of the muon chambers, which consist of five layers of multiwire proportional chambers separated by iron absorbers.

Trigger system

The LHCb trigger system reduces the event rate from the 10 MHz produced by the LHC collisions down to the 3 kHz allowed by the storage resources. It is divided in two stages: the first stage, the L0, is implemented using custom front-end electronics and reduces the event rate down to 1 MHz by making use of the information provided by the calorimeter and muon systems; the second stage, the High Level Trigger (HLT), consists in a set of software algorithms running on a large farm of commercial processors which applies a selective full event reconstruction.

Online system

The Online system is in charge of ensuring the transfer of data from the front-end electronics of the LHCb detector to permanent storage in a known and controlled fashion. It is divided in three subsystems: the Data Acquisition (DAQ) system, in charge of transporting the L0-accepted data from the front-end electronics to permanent storage, the Timing and Fast Control (TFC) system, in control of the data flow between the front-end electronics and the Event Filter Farm, and the Experiment Control System (ECS), which allows to control and monitor the LHCb detector, the trigger, DAQ and TFC systems.

Computing

The LHCb software is based on the GAUDI architecture, which provides a common framework for all the applications used within the experiment, and has the flexibility to allow running the LHCb data flow for Monte Carlo simulation and real data with the same tools. Data persistency is based on the ROOT software, a set of frameworks designed to handle and analyze large amounts of data.

In MC simulation, pp collisions and the interaction of their products with the detector are handled by the GAUSS application; then, the BOOLE application simulates the digitization of the energy depositions in the detector and in the L0 trigger. At this point, real and simulated data go through the MOORE application, which runs the HLT and decides whether an event is to be kept or not; in the case of real data, accepted events are transferred to permanent storage for further processing and archiving. These unprocessed data, real or simulated, are used by the BRUNEL application to reconstruct the physical particles, which are then further filtered using the DAVINCI application, in a process called *Stripping*, the final result of which is a Data Summary Tape (DST file); in the case of real data, only stripped data are available for physics analysis. DST files can be further analyzed with DAVINCI in order to produce ROOT-based NTuples suitable for analysis.

Real data are reprocessed several times a year to incorporate improvements in the reconstruction, alignment and stripping software, algorithms and calibration constants.

2010 and 2011 running conditions

In 2010, the LHC delivered 37 pb^{-1} to LHCb and managed to achieve 80% of the design luminosity. However, this luminosity was achieved with different accelerator parameters than the nominal ones, leading to an increase of the number of visible interactions, $\mu \sim 2.5$. An increase in μ means more interactions—and thus, vertices—per bunch crossing, an increase in the readout rate per bunch crossing, and an increase of the event size and processing time. Even though a high μ affects greatly the trigger working conditions, the LHCb trigger has managed to adapt perfectly.

In 2011, the LHC has delivered $\sim 1.2 \text{ fb}^{-1}$ to LHCb, which have been recorded with an efficiency of 91%. The average number of inelastic pp collisions, $\mu \sim 1.5$, has also been above the design value, but they have been substantially lower than in 2010.

Trigger strategies for radiative B decays at LHCb

An efficient trigger is an essential prerequisite for radiative B decays, since their branching ratio is small, of $\mathcal{O}(10^{-5})$ or lower, and therefore their production is limited at most to few millions per fb^{-1} , diluted in a large amount background events.

Trigger strategies

In L0, `L0Electron` and `L0Photon` select those events with an electromagnetic deposition in the ECAL with a transverse energy with respect to the beam direction, E_T , greater than a given threshold, placed at 2.5 GeV during 2011. Additionally, a subset of the events that pass these two lines also pass the `L0ElectronHi` and `L0PhotonHi` lines, which require a higher E_T value of 4.2 GeV. The L0 requirement for radiative B decays is that the signal photon has been responsible for firing the L0, *i.e.*, either the `L0Electron` or `L0Photon` is TOS (Trigger On Signal).

In the HLT1, the relevant lines for radiative B decays are `Hlt1TrackAllL0` and `Hlt1TrackPhoton` single track lines. They select events based on the transverse momentum (p_T) of the tracks with respect to the beam direction and their impact parameter (IP). On one side, `Hlt1TrackAllL0` selects low- E_T photons with a harder cut in the required track; on the other side, `Hlt1TrackPhotonL0` allows to lower the p_T requirement for the track at the cost of a harder E_T cut on the photon. For radiative decays it is required that `Hlt1TrackAllL0` or `Hlt1TrackPhotonL0` are TOS.

In HLT2, two strategies, exclusive and inclusive, have been studied. The exclusive radiative lines, `Hlt2Bd2KstGamma` and `Hlt2Bs2PhiGamma`, which are loose versions of the respective offline selections, have been redesigned to run on events that pass the `L0Electron` and `L0Photon` lines and their cuts have been optimized. Their efficiency is above 85% for $B^0 \rightarrow K^{*0}\gamma$ and $B_s^0 \rightarrow \phi\gamma$, as shown in Table 4, but they offer a poor performance for other channels, such as $B^+ \rightarrow \phi K^+\gamma$ and $B^+ \rightarrow K^{*0}\pi^+\gamma$, for which they were not designed.

The performance of the widely used multivariate BBDT-based HLT2 topological lines, shown in the first column of Table 5, has been assessed and it has been concluded

	Hlt2Bd2KstGamma (%)	Hlt2Bs2PhiGamma (%)
$B^0 \rightarrow K^{*0} \gamma$	85.6 ± 0.3	0.002 ± 0.004
$B_s^0 \rightarrow \phi \gamma$	35.4 ± 0.4	89.4 ± 0.2
$B^+ \rightarrow \phi K^+ \gamma$	17.5 ± 0.8	18.0 ± 0.8
$B^+ \rightarrow K^{*0} \pi^+ \gamma$	42.2 ± 1.8	0.5 ± 0.2

Table 4. TOS efficiency of the HLT2 exclusive lines over L0 and HLT1 TOS, defined as L0Photon TOS or L0Electron TOS and Hlt1TrackAllL0 TOS or Hlt1TrackPhoton TOS, respectively, in offline-selected simulated data.

	BBDT-based Topo (%)	Cut-based Radiative (%)	BBDT-based Radiative (%)	Inclusive ϕ (%)
$B^0 \rightarrow K^{*0} \gamma$	33.1 ± 0.4	75.6 ± 0.4	80.5 ± 0.4	–
$B_s^0 \rightarrow \phi \gamma$	47.1 ± 0.4	77.3 ± 0.3	84.4 ± 0.3	95.51 ± 0.15
$B^+ \rightarrow \phi K^+ \gamma$	50.1 ± 1.1	90.0 ± 0.6	91.4 ± 0.6	81.4 ± 0.8
$B^+ \rightarrow K^{*0} \pi^+ \gamma$	48.8 ± 1.8	89.3 ± 1.1	91.5 ± 1.0	–

Table 5. TOS efficiency of the HLT2 inclusive lines over L0 and HLT1 TOS, defined as L0Photon TOS or L0Electron TOS and Hlt1TrackAllL0 TOS or Hlt1TrackPhoton TOS, respectively, in offline-selected simulated data.

that, while they clearly improve the efficiency for selecting $B^+ \rightarrow \phi K^+ \gamma$ and $B^+ \rightarrow K^{*0} \pi^+ \gamma$, their negative impact on the $B^0 \rightarrow K^{*0} \gamma$ and $B_s^0 \rightarrow \phi \gamma$ efficiencies is too high.

For this reason a new set of radiative topological lines has been developed and introduced in mid-2011. Based on the same ideas as the regular topological lines, they take advantage of the presence of the photon to relax some of the selection criteria. Two different approaches have been used for these new lines: cut-based or BBDT-based. The second and third columns of Table 5 show the performance on MC data of the two radiative topological lines. Good efficiencies are recovered for the $B^0 \rightarrow K^{*0} \gamma$ and $B_s^0 \rightarrow \phi \gamma$ decays, around 5% less than when using the exclusive lines, while the efficiency for $B^+ \rightarrow \phi K^+ \gamma$ and $B^+ \rightarrow K^{*0} \pi^+ \gamma$ gets bumped to $\sim 90\%$. Therefore, by making use of the radiative topological lines, an HLT2 efficiency over 80% can be obtained for the studied radiative decays.

In order to increase the efficiency for the key channel $B_s^0 \rightarrow \phi \gamma$, the inclusive ϕ line has been redesigned and included in the 2011 trigger. This line works by looking for pairs of oppositely charged tracks identified as kaons by a soft requirement in their RICH PID. It provides a transversal approach to the trigger of decays containing a ϕ , and, as shown in the last column of Table 5, it provides an excellent efficiency for $B_s^0 \rightarrow \phi \gamma$.

Summing up, the comparison between Table 4 and Table 5 shows that in three out of the four studied channels, the inclusive strategy outperforms the exclusive one. Only in the case of $B^0 \rightarrow K^{*0} \gamma$ the exclusive lines show a slightly better performance.

Calorimeter reconstruction in HLT2

The introduction of the HLT2 radiative topological lines has the effect of increasing the number of events for which the photon reconstruction is needed. Given the fact that the HLT2 calorimeter reconstruction was not optimized for running with timing constraints, the addition of the inclusive lines implies an unacceptable increase of the HLT2 timing budget.

For this reason a new reconstruction procedure for the calorimeter in the trigger has been developed. Based on reducing the calorimeter clusterization to regions of interest around L0 calorimeter objects, it provides a three-fold decrease in the timing at the cost of a small efficiency loss. This new procedure was introduced in the trigger in June 2011.

Performance in 2011

The determination of the absolute efficiencies of the various radiative trigger lines during the 2011 data taking has not been possible due to the lack of statistics. Only in the case of the exclusive line for $B^0 \rightarrow K^{*0}\gamma$ it has been possible to use the TISTOS method, and the HLT2 efficiency has been found to be $(84 \pm 3)\%$, in good agreement with the value calculated from MC, $(85.6 \pm 0.3)\%$.

A quantitative performance comparison between the exclusive and inclusive triggers has been performed by studying the invariant mass distributions of the $B^0 \rightarrow K^{*0}\gamma$ and $B_s^0 \rightarrow \phi\gamma$. It has been concluded that, while the exclusive lines provide a higher yield than the individual inclusive lines, the latter offer an improved background rejection, resulting in an enhanced S/B ratio for a moderate loss in efficiency for $B^0 \rightarrow K^{*0}\gamma$. In addition, the inclusive ϕ trigger has shown an outstanding performance for $B_s^0 \rightarrow \phi\gamma$, both in terms of yield and S/B .

Prospects for 2012

Given the excellent performance provided by the HLT2 radiative topological trigger at the end of 2011, the radiative decays trigger strategy for 2012 will be inclusive.

Several new analyses, such as the CP -asymmetry studies for $B^+ \rightarrow \phi K^+\gamma$ and $B^+ \rightarrow K^{*0}\pi^+\gamma$, or the study of radiative decays of Λ_b baryons, which were not included in the exclusive lines, will benefit from this change. Further studies with other channels, such as the $B^0 \rightarrow K^{*0}\gamma$ isospin-asymmetry, or the CP asymmetry of $b \rightarrow d\gamma$ transitions such as $B \rightarrow \rho\gamma$, will also be possible in the future because these events will have already been triggered with significant efficiency.

The exclusive lines will also be kept for cross checks of the inclusive lines, but they have been modified in order to lower their rate to a negligible rate. This rate reduction has been achieved by tightening the cuts in the lines, effectively turning them into quasi-offline selections.

Measurement of the ratio $\mathcal{B}(B^0 \rightarrow K^{*0}\gamma)/\mathcal{B}(B_s^0 \rightarrow \phi\gamma)$

The main aim of this analysis is to extract the ratio of branching fractions of $B^0 \rightarrow K^{*0}\gamma$ with $K^{*0} \rightarrow K^\pm\pi^\mp$ and $B_s^0 \rightarrow \phi\gamma$ with $\phi \rightarrow K^+K^-$ (and complex conjugates). From

this measurement, and using the well-known value of $\mathcal{B}(B^0 \rightarrow K^{*0}\gamma)$, $\mathcal{B}(B_s^0 \rightarrow \phi\gamma)$ has been extracted.

Event selection

The selection of both B decays is tuned to maximize the cancellation of systematic uncertainties in the ratio of their efficiencies. The procedure and requirements are kept as similar as possible: the B^0 (B_s^0) mesons are reconstructed from a selected K^{*0} (ϕ), built from oppositely charged kaon-pion (kaon-kaon) pairs, combined with a photon.

The two charged tracks used to build the vector meson are both required to have $p_T > 500 \text{ MeV}/c$ and to point away from all pp interaction vertex by requiring IP $\chi^2 > 25$. The identification of the kaon and pion tracks is made by applying cuts to the particle identification (PID) provided by the RICH system. The PID is based on the comparison between two particle hypotheses, and it is represented by the difference in logarithms of the likelihoods (DLL) between the two hypotheses. Kaons are required to have $\text{DLL}_{K\pi} > 5$ and $\text{DLL}_{Kp} > 2$, while pions are required to have $\text{DLL}_{\pi K} > 0$. With these cuts, kaons (pions) coming from the studied channels are identified with a ~ 70 (83) % efficiency for a ~ 3 (2) % pion (kaon) contamination.

Two-track combinations are accepted as K^{*0} (ϕ) candidates if they form a vertex with $\chi^2 < 9$, the highest p_T of the two tracks is above $1.2 \text{ GeV}/c$, and their invariant mass lies within 50 (10) MeV/c^2 of the nominal K^{*0} (ϕ) mass. The resulting vector meson candidate is combined with a photon of $E_T > 2.6 \text{ GeV}$. Neutral and charged electromagnetic clusters in the ECAL are separated based on their compatibility with extrapolated tracks while photon and π^0 deposits are identified on the basis of the shapes of the electromagnetic shower in the ECAL.

B candidates are required to have an invariant mass within $1 \text{ GeV}/c^2$ of the corresponding B hadron mass, to have $p_T > 3 \text{ GeV}/c$, to have a flight distance χ^2 above 100 units, and to point to a pp interaction vertex by applying a cut at IP $\chi^2 < 9$. The distribution of the helicity angle θ_H , defined as the angle between the momentum of any of the daughters of the vector meson V and the momentum of the B candidate in the rest frame of the vector meson, is expected to follow a $\sin^2 \theta_H$ function for $B \rightarrow V\gamma$, and a $\cos^2 \theta_H$ for the $B \rightarrow V\pi^0$ background. Therefore, the helicity structure imposed by the signal decays is exploited to remove $B \rightarrow V\pi^0$ background, in which the neutral pion is misidentified as a photon, by requiring that $|\cos \theta_H| < 0.8$. Background coming from partially reconstructed b -hadron decays is rejected by requiring vertex isolation: the χ^2 of the B vertex must increase by more than 2 units when adding any other track in the event.

Extraction of the ratio of branching fractions

The ratio of the branching fractions is calculated from the number of signal candidates in the $B^0 \rightarrow K^{*0}\gamma$ and $B_s^0 \rightarrow \phi\gamma$ channels,

$$\frac{\mathcal{B}(B^0 \rightarrow K^{*0}\gamma)}{\mathcal{B}(B_s^0 \rightarrow \phi\gamma)} = \frac{\mathcal{N}_{B^0 \rightarrow K^{*0}\gamma}}{\mathcal{N}_{B_s^0 \rightarrow \phi\gamma}} \frac{\mathcal{B}(\phi \rightarrow K^+ K^-)}{\mathcal{B}(K^* \rightarrow K^+ \pi^-)} \frac{f_s}{f_d} \frac{\epsilon_{B_s^0 \rightarrow \phi\gamma}}{\epsilon_{B^0 \rightarrow K^{*0}\gamma}}, \quad (5)$$

where \mathcal{N} corresponds to the observed number of signal candidates (yield), $\mathcal{B}(\phi \rightarrow K^+ K^-)$ and $\mathcal{B}(K^{*0} \rightarrow K^+ \pi^-)$ are the visible branching fractions of the vector mesons, f_s/f_d is the ratio of the B^0 and B_s^0 hadronization fractions in pp collisions at $\sqrt{s} =$

7 TeV, and $\epsilon_{B_s^0 \rightarrow \phi\gamma} / \epsilon_{B^0 \rightarrow K^{*0}\gamma}$ is the ratio of efficiencies of the two decays. This latter ratio is split into contributions coming from the acceptance (r_{Acc}), the reconstruction and selection requirements ($r_{\text{Reco\&SelNoPID}}$), the PID requirements (r_{SelPID}), and the trigger requirements (r_{Trigger}) :

$$\frac{\epsilon_{B_s^0 \rightarrow \phi\gamma}}{\epsilon_{B^0 \rightarrow K^{*0}\gamma}} = r_{\text{Trigger}} \times r_{\text{Acc}} \times r_{\text{Reco\&SelNoPID}} \times r_{\text{SelPID}}. \quad (6)$$

The PID efficiency ratio is measured from data to be $r_{\text{PID}} = 0.839 \pm 0.005$ (stat), by means of a calibration procedure using pure samples of kaons and pions from $D^{*\pm} \rightarrow D^0(K^+\pi^-)\pi^\pm$ decays selected utilizing purely kinematic criteria. The other efficiency ratios have been extracted using simulated events. The acceptance efficiency ratio, $r_{\text{Acc}} = 1.099 \pm 0.004$ (stat), exceeds unity because of the correlated acceptance of the kaons due to the limited phase-space in the $\phi \rightarrow K^+K^-$ decay. These phase-space constraints also cause the ϕ vertex to have a worse spatial resolution than the K^{*0} vertex. This affects the $B_s^0 \rightarrow \phi\gamma$ selection efficiency through the IP χ^2 , FD χ^2 , and vertex isolation cuts. Conversely, the p_T track cuts are less efficient on the softer pion from the K^{*0} decay. Both effects almost compensate and the selection efficiency ratio is found to be $r_{\text{Reco\&SelNoPID}} = 0.881 \pm 0.005$ (stat), where the main systematic uncertainties in the numerator and denominator cancel out since the kinematical selections are mostly identical for both decays. The trigger efficiency ratio $r_{\text{Trigger}} = 1.080 \pm 0.009$ (stat) has been computed taking into account the contributions from the different trigger configurations during the data taking period.

The yields of the two channels are extracted from a simultaneous unbinned maximum likelihood fit to the invariant mass distributions of the data. Each of the signals is described using two Crystal Ball functions, with their tail parameters fixed to their value extracted from MC simulations and the mass difference between the B^0 and B_s^0 signals constrained to the PDG value with a Gaussian distribution with mean 87.0 MeV/ c^2 and width 0.6 MeV/ c^2 . The width of the signal peak is left as a free parameter.

Combinatorial background is parametrized by an exponential function with a different decay constant for each channel. The contribution of the $B \rightarrow hh\pi^0$, $B_s^0 \rightarrow K^{*0}\gamma$, $B^+ \rightarrow K^{*0}\pi^+\gamma$, $B^+ \rightarrow \phi K^+\gamma$, and baryonic radiative decays to the signal has been assessed from MC data. The shape of these contributions has been fixed from simulation, and their amplitudes have been fixed, except in the case of the partially reconstructed $B_s^0 \rightarrow K^{*0}\gamma$ and $B^+ \rightarrow K^{*0}\pi^+\gamma$. Other partially reconstructed backgrounds, which can have a potentially large contribution, specially in $B^0 \rightarrow K^{*0}\gamma$, have been parametrized with an Argus function from MC simulation, and their contamination in the mass window has been left free. The contribution from cross feed between signal channels and multiple candidates per event has been found to be negligible.

Finally, an acceptance function is introduced to model the effects of calorimeter miscalibration in the trigger, where the calibration coefficients applied at the reconstruction level were not applied. Its effects are noticeable up to 200 MeV/ c^2 from the border.

The results of the fit, including both the signal and the backgrounds, are shown in Fig. 4. On one side, $B^0 \rightarrow K^{*0}\gamma$ is observed with a yield of 5280 ± 89 events and a S/B ratio of 5.4 ± 0.4 in the 2σ mass window. On the other side, 694 ± 42 $B_s^0 \rightarrow \phi\gamma$ events have been observed with a S/B of 7.3 ± 0.7 in the 2σ mass window, constituting the

largest $B_s^0 \rightarrow \phi\gamma$ sample collected. A value of $X^2/\text{dof} = 101.23/100 \sim 1.0123$ has been determined for the fit, which corresponds to a p -value of 45%.

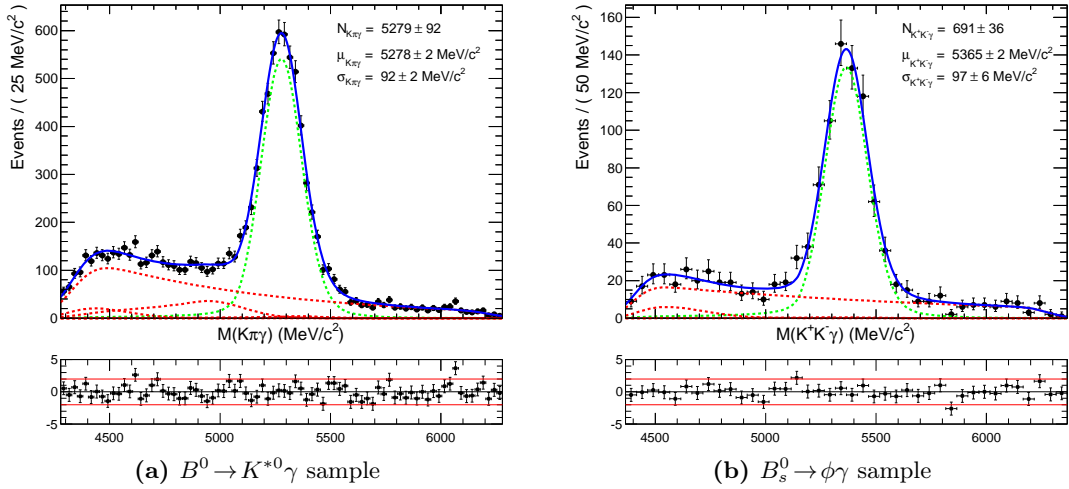


Figure 4. Mass distribution of the $B^0 \rightarrow K^{*0}\gamma$ and $B_s^0 \rightarrow \phi\gamma$ data samples. The fit model PDF is overlaid in a solid blue line, with the signal (dashed green) and background (dashed red) components.

Systematics

The limited MC statistics in the calculation of r_{Acc} , $r_{\text{Reco\&SelNoPID}}$, and r_{Trigger} induce a systematic uncertainty in the ratio of branching fractions. In addition, r_{Acc} is affected by uncertainties in the hadron reconstruction efficiency, arising from differences in the interaction of pions and kaons with the detector and the uncertainties in the description of the material of the detector. Differences in the mass window size of the vector mesons, combined with small differences in the position of the K^{*0}/ϕ mass peaks between data and MC, produce a systematic uncertainty in r_{SelNoPID} which has been evaluated by moving the center of the mass window to the value found in data.

The reliability of the simulation to describe the IP χ^2 of the tracks and the B vertex isolation have been propagated into an uncertainty for r_{SelNoPID} ; the MC sample has been reweighted to reproduce the background-subtracted distributions from data obtained by applying the $s\mathcal{P}$ lot technique to separate signal and background component on the basis of the B candidate invariant mass distribution. No further systematics are associated with the use of MC simulation, since kinematical properties of the decays are known to be well modeled. Systematic uncertainties associated with the photon are negligible due to the fact that the reconstruction in both decays is identical.

The systematic uncertainty associated with the PID calibration method has been evaluated using MC simulation. The statistical error due to the size of the kaon and pion calibration samples has also been propagated to r_{SelPID} .

The systematic effect of the chosen mass window is assessed by applying a narrower B mass window of $\pm 700 \text{ MeV}/c^2$ and repeating the fit procedure.

The systematical effects of fixing the shape and amplitude of the background contaminations from the simulation have also been taken into account. The fit has been

r_N	$7.63 \pm 0.38 {}^{+0.17}_{-0.16}$
$r_{\text{vector meson } B}$	0.735 ± 0.008
f_s/f_d	$0.267 {}^{+0.021}_{-0.020}$
r_ϵ	0.877 ± 0.017

Table 6. Summary of the intermediate results, with their corresponding systematic errors, needed for the calculation of the ratio of branching fractions, as defined in Eq. 5.

repeated 10,000 times, randomly varying the values of the fixed parameters within their uncertainties, and the effect on the ratio of yields has been determined using the central intervals method at 95% confidence level.

Results and conclusions

By making use of the intermediate results summarized in Table 6, the ratio of branching fractions has been measured as

$$\frac{\mathcal{B}(B^0 \rightarrow K^{*0}\gamma)}{\mathcal{B}(B_s^0 \rightarrow \phi\gamma)} = 1.31 \pm 0.08 \text{ (stat)} \pm 0.04 \text{ (syst)} \pm 0.10 (f_s/f_d), \quad (7)$$

and thus has been found to be compatible with the theory prediction of 1.0 ± 0.2 . The value of the ratio has been combined with the well-measured value of the $B^0 \rightarrow K^{*0}\gamma$ branching fraction to extract the world-best measurement of the branching fraction of the radiative $B_s^0 \rightarrow \phi\gamma$ decay,

$$\mathcal{B}(B_s^0 \rightarrow \phi\gamma) = (3.3 \pm 0.3) \times 10^{-5}, \quad (8)$$

which is also in agreement with the theoretical prediction of $(4.6 \pm 1.4) \times 10^{-5}$. The uncertainty in $\mathcal{B}(B_s^0 \rightarrow \phi\gamma)$ is reduced from 35% down to 9%, and thus the knowledge of this branching fraction is largely improved.

Introduction

The Standard Model of particle physics is a set of theories, developed during the second half of the 20th century, which aim to explain the electromagnetic, weak and strong interactions of subatomic particles. While its theoretical formulation was finalized in the 1970's, experimental confirmation of some of its predictions, like the *top* quark and the *tau* neutrino, had to wait until the end of the century. The last key piece of the Standard Model, the Higgs boson, still remains to be experimentally confirmed.

Despite its success, the Standard Model fails to incorporate gravity, as described by general relativity, dark energy, dark matter, as it doesn't contain any viable candidate for dark matter, and neutrino oscillations, already observed by several experiments. It also contains several unnatural features that give rise to the strong *CP* and hierarchy problems.

Particles containing a *beauty* quark, called *B hadrons*, constitute an excellent benchmark for measuring Standard Model aspects, such as the mixing between quark families and *CP* violation, controlled by the CKM matrix, and indirect effects caused by some of its extensions. The LHCb experiment, one of the experiments of the Large Hadron Collider, is dedicated to the study of *CP* violation and rare decays in the *B* sector.

One topic of interest is flavor-changing neutral currents, which are only possible through loop processes and thus are very sensitive to new heavy particles circulating in the loop. Radiative *B* hadron decays, *i.e.*, *B* hadron decays with a photon in the final state, constitute an excellent example of this type of decays.

With branching fractions of $\mathcal{O}(10^{-5})$ or lower, the production of rare *B* decays in LHCb, specially those in the B_s^0 sector, is small and found diluted in a large amount background events. Therefore, in order to avoid limiting the analysis potential of the experiment, it is critical to develop efficient trigger strategies to pick these events apart at the data taking stage. In the case of radiative *B* decays, the presence of a neutral particle, the photon, makes this selection even more challenging.

The first measurement of radiative *B* decays in the LHCb experiment, as well as the development of the trigger strategies that allow this and future measurements, are the subject of this work.

Chapter 1 describes the Standard Model and provides the key elements to understand how to formulate predictions for radiative *B* decays within its framework. While inclusive calculations have good predicting power for branching fractions, exclusive predictions, more accessible experimentally, suffer from big uncertainties. These uncertainties lead to a situation where the experimental results, also summarized in Chapter 1, are more precise than their theoretical counterparts.

Chapter 2 briefly introduces the European Organization for Nuclear Research, known as CERN, and its history. It also describes the world's largest particle accelerator, the

Large Hadron Collider, including its six experiments.

The LHCb experiment is described in Chapter 3. The running conditions during the data taking periods of 2010 and 2011 are analyzed, and the LHCb detector systems and subsystems are presented in detail.

Two trigger strategies for radiative B decays are studied in Chapter 4, an exclusive and an inclusive approach. New or redesigned trigger lines are described, and their efficiencies on simulated data are presented. The performance of the 2011 strategy is analyzed, and the strategy adopted for the 2012 data taking is outlined.

Chapter 5 presents the measure of the ratio of branching fractions of the $B^0 \rightarrow K^{*0}\gamma$ and $B_s^0 \rightarrow \phi\gamma$ decays on the full 2011 dataset. The procedure for extracting this ratio, including event selection, signal yield extraction and systematical uncertainties determination, is discussed. From the measured result, the value of $\mathcal{B}(B_s^0 \rightarrow \phi\gamma)$ is extracted.

The conclusions of this work, as well as its impact on future radiative measurements to be carried out in LHCb, are discussed in Chapter 6.

1

Radiative decays of B mesons

Radiative $b \rightarrow s\gamma$ decays are an example of effective *flavor-changing neutral current* interactions, which arise from the Standard Model through loop processes such as *penguin* or *box* diagrams. Such processes allow to probe physics at high energies through the virtual particles circulating in the loop. This feature makes them a good testing ground in searches for Physics beyond the Standard Model, which may introduce new heavy flavor-changing particles to which radiative decays could be sensitive to.

Theoretical predictions for exclusive radiative decays, more accessible experimentally than inclusive ones, are more difficult to calculate; quark-level processes cannot be accessed directly in the experiment, and thus predictions have to be made at the hadronic level, where there are sizeable non-perturbative—and thus hard to calculate—contributions. Predictions are based on QCD factorization theorems derived from effective field theories, but suffer from large uncertainties due to non-perturbative QCD contributions. Some observables, such as CP or isospin asymmetries, benefit from cancellations of some these uncertainties, making them better targets for experimental study.

1.1. The Standard Model

The *Standard Model* (SM) is the theory that describes our current knowledge of the elementary constituents of matter and their interactions. It was formulated in the 1960's and 1970's and it has been very successful so far. Many of its predictions have been confirmed experimentally with a high level of precision, except for the neutrino masses [1–4] and the yet unobserved Higgs boson [5–7].

The SM is built upon the foundation of *relativistic quantum field theory*, which embeds the dynamical framework of quantum field theory within the space-time structure of special relativity [8].

Symmetries are imposed to the theory through the principle of *local gauge invariance* [9–11], which postulates that the theory is invariant under transformations of the fields following the form

$$\psi(x_\mu) \rightarrow e^{i\alpha_a(x_\mu)T_a} \psi(x_\mu), \quad (1.1)$$

where T_a are the generators of a Lie group and $\alpha_a(x_\mu)$ are a set of arbitrary real

functions of the space-time coordinate x_μ , one for each generator. In order to preserve the invariance of the kinetic term of the lagrangian, it is necessary to replace the partial derivatives ∂_μ by *covariant derivatives* D_μ build with *gauge fields* A_μ^a :

$$\partial_\mu \Rightarrow D_\mu \equiv \partial_\mu + igT^a A_\mu^a, \quad (1.2)$$

where the gauge fields transform as:

$$A_\mu^a \rightarrow A_\mu^a - \frac{1}{g} \partial_\mu \alpha_a(x_\mu). \quad (1.3)$$

This construction allows the transformations of the gauge field to cancel terms arising from the derivative of the gauge-transformed field $\psi(x_\mu)$. Local gauge and Lorentz invariance dictate that the A_μ^a particles are spin-1 Lorentz vectors transforming under the adjoint representation of the Lie group. The coupling constant g is universal for a given gauge group, and determines the strength of the interaction.

The Standard Model is a collection of gauge theories in which the constituents of matter —the fermions— interact through the exchange of force carrier gauge bosons arising from the symmetry group

$$\text{SU}(3)_C \times \text{SU}(2)_L \times \text{U}(1)_Y. \quad (1.4)$$

The electroweak interaction corresponds to the $\text{SU}(2)_L \times \text{U}(1)_Y$ [12–14], and is mediated by the massless photon and the massive W^\pm and Z^0 bosons, while the strong interaction, described by Quantum ChromoDynamics (QCD), derives from $\text{SU}(3)_C$ [15] and is carried by the massless gluons.

The representation of the T_a generators within the covariant derivative for the fermions determines their group transformation and gauge interaction properties. The fermions couple with the gauge bosons through the covariant derivative if the T_a generators are a non-trivial representation of the group. Otherwise, they are singlets under the gauge group and are transparent to the considered interaction.

As a final step, the mechanism of *spontaneous symmetry breaking* [16–20] is required to give mass to the particles within the SM through the introduction of a new field, the *Higgs field*. Electroweak gauge bosons —and the Higgs boson itself— and fermions acquire mass through quadratic terms and Yukawa mass terms, respectively.

In summary, the Standard Model Lagrangian can be written as

$$\mathcal{L} = \mathcal{L}_{\text{QCD}} + \mathcal{L}_{\text{EW}} + \mathcal{L}_{\text{Higgs}} + \mathcal{L}_{\text{Yukawa}}. \quad (1.5)$$

In the SM, elementary particles are divided into *bosons* and *fermions* according to their spin. Each particle has a corresponding antiparticle which carries the opposite quantum numbers. In some cases, such as the photon or the Z^0 , the particle is its own antiparticle.

1.1.1. Elementary Particles

Fermions are the constituents of matter and are indivisible. They have spin 1/2 and obey Fermi-Dirac statistics. Taking into account the group representation of the SM symmetries, fermions are divided into two categories:

- Six *quarks*, which transform under the fundamental representation of $\text{SU}(3)_C$, and thus participate in QCD.

□ Six *leptons*, which are $SU(3)_C$ singlets, and therefore are not affected by QCD.

Both groups can be divided into three families or *generations*. The various types of quarks and leptons are collectively called *flavors*, and their main properties are summarized in Table 1.1.

	Q (e)	m (MeV/ c^2)	L	B	
Leptons	e^-	-1	$0.510998910 \pm 0.000000013$	+1	0
	ν_e	0	$< 2.2 \times 10^{-6}$	+1	0
	μ^-	-1	$105.6583668 \pm 0.0000038$	+1	0
	ν_μ	0	< 0.19	+1	0
	τ^-	-1	1776.82 ± 0.16	+1	0
	ν_τ	0	< 18.2	+1	0
Quarks	u	$+2/3$	2.34 ± 0.19	0	$+1/3$
	d	$-1/3$	4.78 ± 0.11	0	$+1/3$
	c	$+2/3$	1294 ± 4	0	$+1/3$
	s	$-1/3$	100.2 ± 2.4	0	$+1/3$
	t	$+2/3$	$(172.9 \pm 0.6 \pm 0.9) \times 10^3$	0	$+1/3$
	b	$-1/3$	$(4.670^{+0.018}_{-0.060}) \times 10^3$	0	$+1/3$

Table 1.1. The Standard Model fermions. The classification includes three families of leptons and quarks with electric charge Q , mass m , and their corresponding leptonic (L) and baryonic (B) numbers [21]. The corresponding anti-fermions are omitted for simplicity..

Leptons

Leptons interact through the electroweak interaction, but are unaffected by the strong interaction, as they are $SU(3)_C$ singlets. As shown in Table 1.1, there are six known leptons —plus their corresponding antiparticles—, which are distinguishable by their masses, electric charge and interaction modes.

The three charged leptons are the *electron*, e^- , the *muon*, μ^- , and the *tau*, τ^- . They all carry the same electric charge, $Q = e = -1.602 \times 10^{-19}$ C. The charged leptons are associated to three neutral leptons, the *neutrinos*, which are assumed to have zero mass in the Standard Model. However, the phenomenon of neutrino oscillations [24] between the three neutrino families requires that at least two of them have non-zero mass.

Leptons are divided horizontally into generations and vertically into an electroweak $SU(2)_L$ doublet consisting of a pair of left-handed neutrino and the corresponding charged lepton. The interaction projects out the left-handed component of the fermion field, resulting in parity violation (see §1.1.3).

$$\begin{pmatrix} \nu_e \\ e^- \end{pmatrix}, \begin{pmatrix} \nu_\mu \\ \mu^- \end{pmatrix}, \begin{pmatrix} \nu_\tau \\ \tau^- \end{pmatrix}. \quad (1.6)$$

The right-handed components are singlets of $SU(2)_L$, and thus each doublet $(l, \nu_l)_L$ has a corresponding singlet l_R which is not sensitive to the weak interaction.

Quarks

Quarks transform under the fundamental representation of chromodynamic $SU(3)_C$ and therefore carry an extra quantum number, the chromodynamic charge, called *color*. The six quarks are classified into *up*-type quarks, with electric charge $+2/3$, and *down*-type quarks, with electric charge $-1/3$, as shown in Table 1.1.

Similarly to the leptons, quarks are horizontally divided into generations and vertically grouped in pairs of up- and down-type left-handed quarks as $SU(2)_L$ doublets. The first family is composed by the lightest quarks, the *up* (u) and *down* (d), which are the most abundant in Nature as they constitute the basic components of the proton and the neutron; the second quark family is composed by the heavier *charm* (c) and *strange* (s) quarks; the heaviest quarks, the *top* (t) and the *bottom* or *beauty* (b) make up the third family.

$$\begin{pmatrix} u \\ d \end{pmatrix}, \begin{pmatrix} c \\ s \end{pmatrix}, \begin{pmatrix} t \\ b \end{pmatrix}. \quad (1.7)$$

Due to the *confinement* property of QCD (see §1.1.2), colored objects can only appear in colorless combinations; thus, quarks are always found grouped in colorless particles, called *hadrons*. There are two types of hadrons: *mesons*, composed by a quark-antiquark pair ($q\bar{q}$), and *baryons*, antisymmetric color triplets of different color (qqq , $\bar{q}\bar{q}\bar{q}$).

1.1.2. Fundamental Interactions

In the SM, particles interact through the exchange of the gauge bosons that arise from imposing local gauge invariance with respect to the symmetry groups in Eq. 1.4. Gravitation is not included in the Standard Model, so the three interactions to consider are:

Electromagnetic interaction. It affects all particles with electric charge. It is described by Quantum ElectroDynamics (QED) [22–29], a quantum field theory with the photon as the force mediator.

Strong interaction. Interaction which confines the quarks into hadrons. It is described by the theory of Quantum ChromoDynamics (QCD). The eight massless gauge bosons arising from the adjoint representation of $SU(3)_C$ are called *gluons*, and are said to carry the color charge. QCD has two distinct properties:

- *Confinement.* Unlike all other forces, the strength of the strong force does not diminish with increasing distance. This phenomenon is called *color confinement*, and it implies that only hadrons, and not individual free quarks or gluons, can be observed. In simple terms, the energy needed to pull two quarks apart is so high that a new pair of quark-antiquark, which will pair up with the original ones, can be produced. Although analytically unproven, confinement is believed to be true due to the consistent failure of free quark searches.
- *Asymptotic freedom.* At very high-energy reactions, quarks and gluons interact very weakly. This analytical prediction of QCD was discovered in the 1970's by Politzer, Wilczek and Gross [30, 31], which were awarded the Nobel Prize in Physics.

Weak interaction. Responsible for the β -decay, the weak interaction has an extremely short range, about 10^{-16} cm, implying very massive mediators. The three gauge bosons associated with it are the charged W^+ and W^- , and the neutral Z^0 , with masses of $\sim 80 \text{ GeV}/c^2$ for the first two and $\sim 90 \text{ GeV}/c^2$ for the latter. This interaction allows decays forbidden by the strong and electromagnetic interactions, such as flavor-changing decays and CP violation processes.

The main properties of the gauge bosons are summarized in Table 1.2.

	Electric charge (e)	Mass (GeV/c^2)
γ	0	0
Gluon	0	0
W^+/W^-	$+1/-1$	80.399 ± 0.023
Z^0	0	91.1876 ± 0.0021

Table 1.2. Electric charge and mass of the strong, electromagnetic and weak gauge bosons [21].

1.1.3. Discrete symmetries

The connection between symmetries and conservation laws, summarized in the Noether theorems [32], is a fundamental piece in building particle physics theories, since considerations on symmetries of the interactions determine the structure of the Lagrangian.

Some discrete transformations are particularly interesting in the Standard Model. Considering a particle of momentum \vec{p} and helicity $h = \vec{s} \cdot \vec{p}/|\vec{p}|$, where \vec{s} is its spin, represented by the quantum state $|\vec{p}, h\rangle$, we can define

Parity Spatial inversion, represented by the parity operator P ,

$$P|\vec{p}, h\rangle = \eta_P|-\vec{p}, -h\rangle, \quad (1.8)$$

where η_P is the parity of the particle.

Charge Conjugation Exchange between the particle and antiparticle, represented by the charge conjugation operator C :

$$C|\vec{p}, h\rangle = \eta_C|\vec{p}, h\rangle, \quad (1.9)$$

where η_C is a phase factor.

Time Inversion Reversion of the direction of time, represented by the operator T :

$$T|\vec{p}, h\rangle = \eta_T|-\vec{p}, h\rangle^*, \quad (1.10)$$

where η_T is a phase factor that depends on the spin.

These three symmetries C , P and T are preserved by the strong and electromagnetic interactions, but experimental evidence shows clear violations of charge conjugation and parity [33, 34].

Even though C and P are violated, it is possible that the combination between two, CP , remains unbroken. Violation of the CP symmetry in the kaon system was observed by Cronin and Fitch in 1964 [35], and in the B system by the B -factories at the turn of the 2000's [36, 37]. A first indication of CP violation in decays of neutral D mesons has been recently reported by the LHCb collaboration [38].

The combination of the three symmetries, CPT , is considered a fundamental symmetry of physical laws. The CPT theorem proves that any Lorentz invariant local quantum field theory with a Hermitian Hamiltonian must have CPT symmetry. It was implicitly used by Schwinger to prove the connection between spin and statistics in 1951, and explicitly derived by Lüders and Pauli in 1957 [39]. It has very important and general consequences, *e.g.*, the mass and the lifetime of an elementary particle and its antiparticle must be equal. Up to now, all experimental measurements are consistent with CPT conservation.

1.1.4. Standard Model Lagrangian

The Standard Model is the combination of QCD, the theory describing strong interactions, and the Electroweak Theory, the unification of the weak and electromagnetic interactions. Globally, it is based on the gauge symmetry $SU(3)_C \times SU(2)_L \times U(1)_Y$ with spontaneous symmetry breaking $SU(2)_L \times U(1)_Y \rightarrow U(1)_Q$.

The electroweak theory, proposed by Glashow, Salam and Weinberg [12–14] is a non-abelian theory based on $SU(2)_L \times U(1)_Y$ describing the electromagnetic and weak interaction between quarks and leptons. In addition of the $SU(2)$ generators, I_{\pm} and I_3 , the hypercharge $Y \equiv 2(Q - I_3)$, where Q is the electric charge, is introduced in order to accommodate the difference between the electric charges for the left-handed doublets. Thus, the four generators I_{\pm} , I_3 and Y are associated to four gauge fields, $\vec{W} = (W_{\mu}^1, W_{\mu}^2, W_{\mu}^3)$ and B_{μ} , respectively.

The strong interaction, based on the color symmetry group $SU(3)_C$, adds eight gauge fields G_{μ}^i to the SM, corresponding to the eight gluons.

Combining the gluons with the electroweak gauge bosons, the following lagrangian can be written:

$$\mathcal{L} = -\frac{1}{4}B_{\mu\nu}B^{\mu\nu} - \frac{1}{4}W_{\mu\nu}^iW^{i\mu\nu} - \frac{1}{4}G_{\mu\nu}^jG^{j\mu\nu} \quad (1.11)$$

with the tensor field strengths defined as

$$B_{\mu\nu} = \partial_{\mu}B_{\nu} - \partial_{\nu}B_{\mu}, \quad (1.12)$$

$$W_{\mu\nu}^i = \partial_{\mu}W_{\nu}^i - \partial_{\nu}W_{\mu}^i + g\epsilon^{jkl}W_{\mu}^kW_{\nu}^l, \quad j = 1, 2, 3, \quad (1.13)$$

$$G_i^{\mu\nu} = \partial_{\mu}G_{\nu}^i - \partial_{\nu}G_{\mu}^i - g_s f^{ijk}G_{\mu}^jG_{\nu}^c, \quad j = 1, \dots, 8, \quad (1.14)$$

where ϵ^{jkl} and f^{ijk} are the $SU(2)_L$ and $SU(3)$ structure constants, respectively, and g_2 and g_s is the coupling constant for corresponding the group. The non-abelian nature of the $SU(2)_L$ and $SU(3)_C$ groups is showcased by the presence of the structure constants, and it leads to the appearance of self-interactions of the gauge fields V_{μ} from Eq. 1.11¹:

$$\text{triple gauge boson coupling} = ig_i \text{Tr}(\partial_{\nu}V_{\mu} - \partial_{\mu}V_{\nu})[V_{\mu}, V_{\nu}], \quad (1.15)$$

$$\text{quadruple gauge boson coupling} = \frac{1}{2}g_i^2 \text{Tr}[V_{\mu}, V_{\nu}]. \quad (1.16)$$

¹ V_{μ} denotes either the W_{μ} or the G_{μ} gauge fields, with the corresponding g_i , g or g_s , implied whenever V_{μ} is used.

Following Eq. 1.2 we need to introduce the covariant derivatives to preserve the invariance of the kinetic terms of the lagrangian. A suitable representation of the generators T^a of the SM symmetry groups is chosen: the hypercharge generator Y_q for $U(1)_Y$; the 2×2 Pauli matrices τ_i , with $i = 1, 2, 3$ for $SU(2)_L$; and the 3×3 Gell-Mann matrices λ_i , with $i = 1, \dots, 8$, for $SU(3)_C$ [40]. Thus, the partial derivatives in the SM have to be replaced by the following covariant derivative:

$$D_\mu \psi = \left(\partial_\mu - i \underbrace{\frac{g_s}{2} \lambda_i G_\mu^i}_{\text{QCD}} - i \underbrace{\frac{g}{2} \tau_j W_\mu^j}_{\text{EWT}} - i \frac{g'}{2} Y_q B_\mu \right) \psi. \quad (1.17)$$

This covariant derivative leads to fermion-gauge boson couplings of the type $-g_i \bar{\psi} V_\mu \gamma^\mu \psi$. In addition, when coupling left- and right-handed fermion fields to a gauge field, ψ_L and ψ_R are assigned to different representations of the gauge group, and thus the covariant derivative affects them differently. Therefore,

- Left-handed fermions

$$E_{L_i} = \begin{pmatrix} \nu_e \\ e^- \end{pmatrix}_L \quad Q_{L_j} = \begin{pmatrix} u \\ d \end{pmatrix}_L, \quad (1.18)$$

where i runs through the 3 lepton families (e, μ, τ) and j through the three quark generations, are grouped in weak isodoublets with $I_3 = \pm 1/2$, and $Y = -1/2$ and $Y = +1/6$, respectively. Right-handed fermions, e_{R_i} , u_{R_j} and d_{R_j} form weak isosinglets with $I_3 = 0$, and therefore $Y = +2/3$ for u_R and $Y = -1$ for e_R .

- Leptons are not affected by the strong interaction and therefore are singlets in $SU(3)_C$.
- Mass terms of the form $-m_e(\bar{e}_L e_R + \bar{e}_R e_L)$ are forbidden because the fields e_L and e_R belong to different $SU(2)$ representations and have different $U(1)$ charges.

Ignoring fermion masses, the fermion kinetic energy terms can be written as

$$\mathcal{L} = \bar{E}_{L_i}(iD^\mu)E_{L_i} + \bar{e}_{R_i}(iD^\mu)e_{R_i} + \bar{Q}_{L_j}(iD^\mu)Q_{L_j} + \bar{u}_{R_j}(iD^\mu)u_{R_j} + \bar{d}_{R_j}(iD^\mu)d_{R_j}, \quad (1.19)$$

where the covariant derivative is given by Eq. 1.17; only the particular representation to which each of the fermion field belongs is considered, *i.e.*, leptons are $SU(3)_C$ singlets, and therefore the $\lambda_i G_\mu^i$ term gives zero coupling.

Spontaneous Symmetry Breaking

At this point of the discussion, the electroweak theory is formulated as a $SU(2)_L \times U(1)_Y$ gauge theory with massless bosons and fermions. Its explicit lagrangian can be written as

$$\begin{aligned} \mathcal{L}_{\text{EW}} = & -\frac{1}{4} B_{\mu\nu} B^{\mu\nu} - \frac{1}{4} W_{\mu\nu}^i W^{i\mu\nu} + \\ & + \bar{E}_{L_i} \gamma^\mu \left(\partial_\mu - i \frac{g}{2} \tau_i W_\mu^i - i \frac{g'}{2} Y_q B_\mu \right) E_{L_i} + \bar{e}_{R_i} \gamma^\mu \left(\partial_\mu - i \frac{g'}{2} Y_q B_\mu \right) e_{R_i} + \\ & + \bar{Q}_{L_j} \gamma^\mu \left(\partial_\mu - i \frac{g}{2} \tau_i W_\mu^i - i \frac{g'}{2} Y_q B_\mu \right) Q_{L_j} + \bar{u}_{R_j} \gamma^\mu \left(\partial_\mu - i \frac{g'}{2} Y_q B_\mu \right) u_{R_j} + \\ & + \bar{d}_{R_j} \gamma^\mu \left(\partial_\mu - i \frac{g'}{2} Y_q B_\mu \right) d_{R_j} \end{aligned} \quad (1.20)$$

The Higgs-Brout-Englert-Guralnik-Hagen-Kibble mechanism of *spontaneous symmetry breaking* [41–43], known as the *Higgs Mechanism*, allows the creation of massive gauge bosons without the violation of the gauge symmetry which would otherwise result if explicit mass terms for the W^\pm and Z^0 bosons were inserted into the SM lagrangian. It can also be used to generate mass for the leptons and quarks.

The fundamental idea is to introduce an extra scalar field, the Higgs field, which does not vanish into the vacuum (defined at the state in which all the fields have their lowest possible energy). This field is a complex $SU(2)_L$ doublet ϕ ,

$$\Phi = \begin{pmatrix} \phi^+ \\ \phi^0 \end{pmatrix} \quad Y_\Phi = +1, \quad (1.21)$$

which is assumed to carry no color.

In order to respect the gauge invariance, the kinetic term of the Higgs field must also enter the lagrangian via the gauge covariant derivative:

$$\mathcal{L}_{\text{Higgs}} = \left| \left(\partial_\mu - i \frac{g}{2} \tau_i W_\mu^i - i \frac{g'}{2} Y_q B_\mu \right) \Phi \right|^2 - V(\Phi), \quad (1.22)$$

where the Higgs potential $V(\phi)$ is such that its minima are at non-zero values of the Higgs field.

$$V(\Phi) = \mu^2 (\Phi^\dagger \Phi) + \lambda (\Phi^\dagger \Phi)^2, \quad (1.23)$$

with $\mu^2 < 0$. The Higgs field acquires then a non-zero vacuum expectation value (*vev*)

$$v = \sqrt{\frac{-\mu^2}{\lambda}}, \quad (1.24)$$

and the electroweak gauge fields acquire mass from terms quadratic in the Higgs field. Since QED must stay an exact symmetry in order to keep the photon massless, the *vev* cannot be in the charged direction:

$$\langle 0 | \Phi | 0 \rangle = \begin{pmatrix} \langle 0 | \phi^+ | 0 \rangle \\ \langle 0 | \phi^0 | 0 \rangle \end{pmatrix} = \begin{pmatrix} 0 \\ \frac{v}{\sqrt{2}} \end{pmatrix}. \quad (1.25)$$

Then, the Φ field can be parametrized by writing

$$\Phi = U(x) \frac{1}{\sqrt{2}} \begin{pmatrix} 0 \\ v + H(x) \end{pmatrix}, \quad (1.26)$$

where $U(x)$ is an arbitrary $SU(2)$ gauge transformation that allows to produce the most general complex-valued spinor field, and $H(x)$ is a fluctuating real field with $\langle H(x) \rangle = 0$. $U(x)$ can be eliminated from the lagrangian with a gauge transformation, and therefore the ϕ field is reduced to a field with one physical degree of freedom.

Expanding the covariant derivative of Eq. 1.22 in terms of the Higgs doublet, one can identify the new electroweak boson fields W_μ^\pm , Z_μ and A_μ , as the mass eigenstates:

$$W_\mu^\pm = \frac{1}{\sqrt{2}} (W_\mu^1 \mp W_\mu^2) \quad m_W = \frac{1}{2} v g, \quad (1.27)$$

$$Z_\mu = \frac{g W_\mu^3 - g' B_\mu}{\sqrt{g^2 + g'^2}} \quad m_Z = \frac{1}{2} v \sqrt{g^2 + g'^2}, \quad (1.28)$$

$$A_\mu = \frac{g W_\mu^3 + g' B_\mu}{\sqrt{g^2 + g'^2}} \quad m_A = 0. \quad (1.29)$$

The Higgs mechanism breaks the $SU(2)_L \times U(1)_Y$ symmetry and decouples the weak and electromagnetic interaction, giving rise to the massless photon, A_μ , and the three massive weak bosons, W^\pm and Z^0 .

The Higgs boson

The terms related to the Higgs potential in Eq. 1.23 give rise to

$$\mathcal{L}_V = -\lambda v^2 H^2 - \lambda v H^3 - \frac{1}{4} \lambda H^4, \quad (1.30)$$

and therefore the field $H(x)$ is a scalar particle with mass $m_H^2 = 2\lambda v^2 = -2\mu^2$. This particle is known as the *Higgs boson*, and remains the only undiscovered piece of the Standard Model.

Fermion masses

It is not possible to put ordinary mass terms for the fermions into the Lagrangian, because left- and right-handed components of the fermionic fields have different quantum numbers and so simple mass terms violate gauge invariance.

Fermions acquire their masses through the spontaneous symmetry breaking mechanism. Using the Higgs field it is possible to write a gauge-invariant coupling linking E_L , e_R and Φ :

$$\mathcal{L}_e = -\frac{1}{\sqrt{2}} \lambda_e \bar{E}_L \Phi e_R + \text{h.c.}, \quad (1.31)$$

where the $SU(2)$ indices of the doublets E_L and Φ are contracted, and λ_e is a new dimensionless coupling constant. Introducing the parametrization of Eq. 1.26 and choosing the unitary gauge, the previous equation becomes

$$\mathcal{L}_e = -\frac{1}{\sqrt{2}} \lambda_e v \bar{e}_L \Phi e_R + \text{h.c.} + \dots \quad (1.32)$$

This is a mass term for the electron, with

$$m_e = \frac{\lambda_e v}{\sqrt{2}}. \quad (1.33)$$

The Standard Model makes no predictions for the λ_e : it is an input parameter of the theory that has to be determined from experiment.

The mass terms for the quark fields can be written in the same way:

$$\mathcal{L}_q = -\frac{1}{\sqrt{2}} \lambda_d v \bar{d}_L d_R - \frac{1}{\sqrt{2}} \lambda_u v \bar{u}_L u_R + \text{h.c.} + \dots, \quad (1.34)$$

with

$$m_d = \frac{\lambda_d v}{\sqrt{2}}, \quad m_u = \frac{\lambda_u v}{\sqrt{2}}. \quad (1.35)$$

The CKM Matrix

When additional generations of quarks are introduced into the theory, there can appear further terms that mix generations. This can be avoided by diagonalizing the Higgs couplings through a base change for the quark fields. However, these mass eigenstates may not be the same as the flavor eigenstates that arise from the electroweak lagrangian (Eq. 1.20). Let

$$u_L^i = (u_L, c_L, t_L), \quad d_L^i = (d_L, s_L, b_L), \quad (1.36)$$

denote the up- and down-type quarks in the flavor basis, and u'^i_L and d'^i_L the corresponding quarks in the mass-diagonal —physical— basis. The two bases are related by unitary transformations:

$$u_L^i = U_u^{ij} u'^j_L, \quad d_L^i = U_d^{ij} d'^j_L. \quad (1.37)$$

In this new basis, the coupling of the W^+ bosons to the quarks take the form

$$\frac{1}{\sqrt{2}} \bar{u}_L^i \gamma^\mu d_L^i W_\mu^+ = \frac{1}{\sqrt{2}} \bar{u}'_L^i \gamma^\mu (U_u^{ik\dagger} U_d^{kj}) d'^j_L W_\mu^+ = \frac{1}{\sqrt{2}} \bar{u}'_L^i \gamma^\mu V_{ij} d'^j_L W_\mu^+, \quad (1.38)$$

where the V_{ij} is the unitary Cabibbo-Kobayashi-Maskawa (CKM) matrix [44, 45]. The off-diagonal terms of the CKM matrix allow transitions between quark generations, which are more clearly visualized when writing the previous expression explicitly:

$$\frac{1}{\sqrt{2}} (\bar{u}_L \quad \bar{c}_L \quad \bar{t}_L) \gamma^\mu \begin{pmatrix} V_{ud} & V_{us} & V_{ub} \\ V_{cd} & V_{cs} & V_{cb} \\ V_{td} & V_{ts} & V_{tb} \end{pmatrix} \begin{pmatrix} d_L \\ s_L \\ b_L \end{pmatrix} W_\mu^+. \quad (1.39)$$

This result is analogous for the W^- boson.

The complex CKM matrix contains 18 parameters. Its unitarity, $V_{\text{CKM}} V_{\text{CKM}}^\dagger = 1$, can be exploited to reduce the number of independent parameters to nine by applying the set of constraints

$$\sum_{k=1}^3 V_{ki}^* V_{kj} = \delta_{ij}. \quad (1.40)$$

Six of the remaining parameters correspond to relative phases between the quark fields; all but one —the overall common phase— can be absorbed in the quark fields. The resulting four free parameters are three rotation angles, the *quark mixing angles* θ_{ij} , and one complex phase δ , which is the only source of CP -violation in the SM:

$$V_{\text{CKM}} = \begin{pmatrix} c_{12} c_{23} & s_{12} c_{13} & s_{13} e^{-i\delta} \\ -s_{12} c_{23} - c_{12} s_{23} s_{13} e^{i\delta} & c_{12} c_{23} - s_{12} s_{23} s_{13} e^{i\delta} & s_{23} c_{13} \\ s_{12} s_{23} - c_{12} c_{23} s_{13} e^{i\delta} & -c_{12} s_{23} - s_{12} c_{23} s_{13} e^{i\delta} & c_{23} c_{13} \end{pmatrix}, \quad (1.41)$$

where $s_{ij} = \sin \theta_{ij}$ and $c_{ij} = \cos \theta_{ij}$.

While the weak interactions are characterized by a universal coupling constant resulting from the $SU(2)_L \times U(1)_Y$ symmetry, the interactions between quarks of different generations are scaled by the appropriate CKM matrix elements; this means that certain quark transitions are more favorable, while others are suppressed due to small CKM matrix elements. To clearly show this hierarchy, it is useful to use the Wolfenstein parametrization [46], which allows to write the CKM matrix as an expansion on s_{12} ,

$$\lambda = s_{12} = \frac{|V_{us}|}{\sqrt{|V_{ud}|^2 + |V_{us}|^2}}. \quad (1.42)$$

For CP violation studies it is necessary to expand the CKM matrix up to terms of $\mathcal{O}(\lambda^5)$ because $V_{td}V_{ts}$ is of this order:

$$V_{\text{CKM}} = \begin{pmatrix} 1 - \frac{\lambda^2}{2} & \lambda & A\lambda^3 \left(\rho - i\eta + i\eta \frac{\lambda^2}{2} \right) \\ -\lambda & 1 - \frac{\lambda^2}{2} - i\eta A^2 \lambda^4 & A\lambda^2 (1 + i\eta \lambda^2) \\ A\lambda^3 (1 - \rho - i\eta) & -A\lambda^2 & 1 \end{pmatrix} + \mathcal{O}(\lambda^5), \quad (1.43)$$

with the A , ρ and η defined as

$$s_{23} = A\lambda^2 = \lambda \frac{|V_{cb}|}{V_{us}}, \quad s_{13}e^{i\delta} = A\lambda^3(\rho + i\eta) = V_{ub}^*, \quad (1.44)$$

and with the following experimental values [21]:

$$\lambda = 0.2253 \pm 0.0007, \quad A = 0.808^{+0.022}_{-0.015}, \quad \rho = 0.132^{+0.022}_{-0.014}, \quad \eta = 0.341 \pm 0.013. \quad (1.45)$$

The SM makes no predictions for the V_{ij} matrix elements aside from unitarity, so they need to be determined from experiment. Interestingly, the individual elements of the CKM matrix can be measured independently without making use of the theoretical unitarity requirement; thus, unitarity can be used to over-constrain the CKM matrix and test the weak sector of the SM.

The unitarity of the CKM matrix can be conveniently summarized in *unitarity triangles* by picturing each of the unitarity relations in Eq. 1.40 as a triangle in a complex plane. For example, the first and third columns of the CKM matrix, *i.e.*, the b and d sectors, can be used to build an unitarity relation,

$$V_{ud}^* V_{ub} + V_{cd}^* V_{cb} + V_{td}^* V_{tb} = 0, \quad (1.46)$$

which can be represented as a triangle, as shown in Fig. 1.1, with its sides normalized and rotated by dividing by $V_{cd}^* V_{cb}$. The angles α , β and γ are defined as

$$\alpha = \arg \left(-\frac{V_{td}^* V_{tb}}{V_{cd}^* V_{cb}} \right), \quad \beta = \arg \left(-\frac{V_{cd}^* V_{cb}}{V_{td}^* V_{tb}} \right), \quad \gamma = \arg \left(-\frac{V_{ud}^* V_{ub}}{V_{cd}^* V_{cb}} \right), \quad (1.47)$$

with the $(\bar{\rho}, \bar{\eta})$ vertex given by

$$\bar{\rho} + i\bar{\eta} = -\frac{V_{ud}^* V_{ub}}{V_{cd}^* V_{cb}}. \quad (1.48)$$

The sides of the triangle, which correspond to magnitudes of CKM elements, can be measured by analyzing the decay rates of processes involving these elements, while the angles, which correspond to the relative phases between the elements, can be accessed experimentally through CP -violating asymmetries. The current experimental situation of this unitarity triangle is shown in Fig. 1.2 [47].

GIM Mechanism

Spontaneous symmetry breaking, which gives quarks different masses, is responsible for the GIM suppression —from Glashow, Iliopoulos and Maiani [48]— in loop processes by interfering with the balance imposed by the unitarity of the CKM matrix, which would otherwise forbid effective flavor-changing neutral current processes.

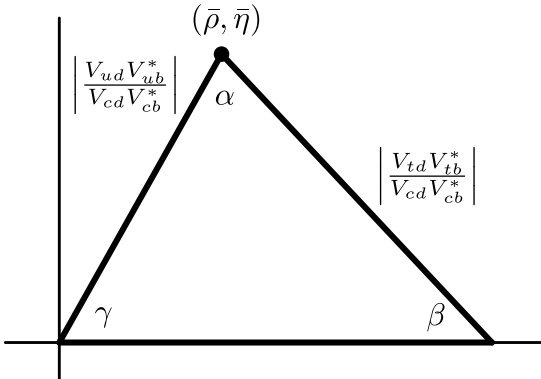


Figure 1.1. Unitarity triangle summarizing the orthogonality of the first and third columns of the CKM matrix in Eq. 1.39. The size of the sides and angles depicted are arbitrary.

The couplings of the quarks to the neutral Z^0 boson are flavor-diagonal by definition—the terms with the neutral boson have the form $\bar{u}_L \gamma^\mu u_L Z_\mu$, and therefore there are no tree-level *Flavor-Changing Neutral Currents* (FCNC) in the Standard Model. FCNC can only occur at higher orders in perturbation theory, in loop processes, such as the *penguin* [49] and *box* diagrams shown in Fig. 1.3, collectively known as *effective flavor-changing neutral currents*.

For example, in Fig. 1.3a, the $b \rightarrow s\gamma$ transition contains contributions from the three up-type quarks, scaled by the appropriate CKM matrix elements, and therefore the amplitude can be written as

$$\mathcal{A}(b \rightarrow s\gamma) = V_{tb}^* V_{ts} f(m_t) + V_{cb}^* V_{cs} f(m_c) + V_{ub}^* V_{us} f(m_u), \quad (1.49)$$

where $f(m)$ is the result of the loop integration, which depends on the mass m of the intermediate up-type quark. If the masses of the up-type quarks were degenerate (and equal to m_q), the amplitude would vanish owing to the unitarity of the CKM matrix,

$$\mathcal{A}(b \rightarrow s\gamma) = f(m_q) [V_{tb}^* V_{ts} + V_{cb}^* V_{cs} + V_{ub}^* V_{us}] = 0. \quad (1.50)$$

However, the existence of mass splitting of the up- or down-type quarks leads to a finite amplitude which is related to the mass difference of the quarks.

Thus, effective FCNC processes in the SM are allowed at loop level, but at a suppressed rate due to the quark mass splitting and loop factors. Since mass splitting in the up-quark section is large, this suppression is weaker and the t quark dominates the amplitude. In the down-quark sector, however, the mass splitting between quarks is smaller and therefore the GIM suppression for FCNC processes is more effective.

1.2. Radiative B Decays in the Standard Model

The huge mass of the top quark relative to the other up-type quarks (see Table 1.1) weakens the GIM suppression in effective FCNC such as $b \rightarrow s\gamma$, shown in Fig. 1.3a. Therefore, FCNC, and in particular radiative decays, offer a testing ground of physics at high mass scales, since the top quark contribution dominates in the virtual loop.

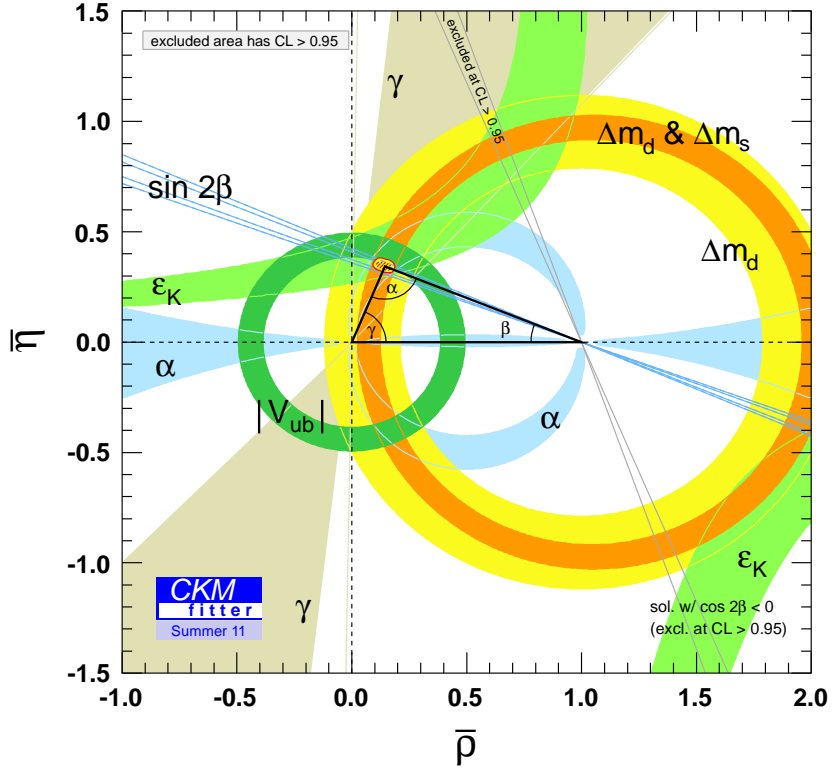


Figure 1.2. Current best fit for the unitarity triangle in the $(\bar{\rho}, \bar{\eta})$ plane by the CKM-Fitter collaboration [47].

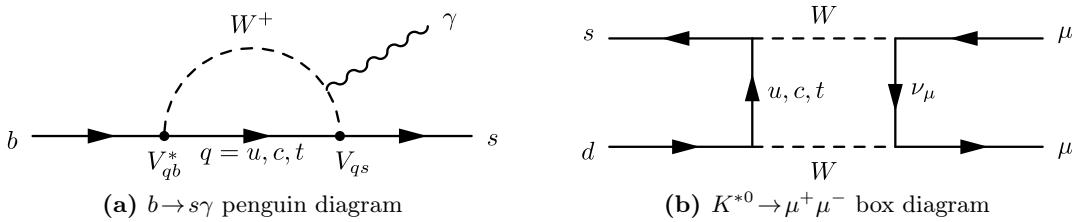


Figure 1.3. Effective flavor-changing neutral current processes.

Moreover, these processes are sensitive to any other flavor-changing particles that may circulate in the loop and that are not included by the Standard Model. Since these contributions can affect the branching ratio and CP violation, among other observables, FCNC can also be sensitive probes to new physics (NP) beyond the Standard Model, provided that reliable theoretical predictions can be made. Up to now, none of the current measurements of B meson decays have observed any unambiguous sign of NP [50]. However, there is still room for sizeable effects from new flavor structures, since FCNC processes have been tested up to only the 10% level.

Quark level FCNC processes such as $b \rightarrow s\gamma$ cannot be directly measured because the

strong interaction forms hadrons from the underlying quarks, which cannot be detected directly due to the confinement property of QCD. Therefore, in order to establish a connection between experimental observations and the CKM parameters, one needs to unfold the effects of confinement.

Inclusive $B \rightarrow X_s \gamma$ decays, which include all hadron combinations that arise from the $b \rightarrow s \gamma$ transition, are theoretically clean because they are dominated by partonic, perturbatively calculable, contributions, with small ($\sim 5\%$) non-perturbative corrections [51]. Experimentally, inclusive quantities are difficult to define due to the fact that it is not feasible to measure all possible final states; the poor knowledge of the relative branching fractions of those that are measured makes it difficult to extract reliable inclusive values. Exclusive final states with one or a few specific hadrons in the final state, *e.g.*, $B^0 \rightarrow K^{*0} \gamma$, have less predictive power due to larger non-perturbative QCD corrections. However, measurements are easier and better defined than inclusive ones, and many other useful observables beyond branching fractions can be obtained, such as CP , forward-backward, isospin, and polarization asymmetries.

To tackle the mixture of regimes of QCD behavior —perturbative and non-perturbative—, calculations are divided into two parts by making use of factorization theorems, which can be found using various techniques, such as effective field theories. *Factorization* allows to separate the contributions of perturbative QCD, occurring at scales well above the B meson mass, from the contributions from lower mass, *long distance*, scales, where perturbative calculations are no longer possible. Long distance contributions are calculated using non-perturbative techniques such as QCD sum rules or lattice calculations. QCD Factorization (QCDF) [52–54] can be used to obtain a factorization theorem which allows to put together these long distance contributions and the perturbative calculations, while the use of Soft Collinear Effective Theory (SCET) [55–58] allows to reach a deeper understanding of this factorization.

1.2.1. Effective Field Theories

Effective field theories [59, 60] are used to express a full, complete theory as an effective Hamiltonian constructed from a set of local operators O_i in which the high energy degrees of freedom, defined with respect to a mass scale Λ , have been integrated out. The amplitude for a given weak process $i \rightarrow f$ is expressed as a sum of matrix elements of the local operators:

$$\langle f | \mathcal{H}_{\text{eff}} | i \rangle = \frac{G_F}{\sqrt{2}} \sum_i V_i C_i(\mu) \langle f | O_i(\mu) | i \rangle, \quad (1.51)$$

where G_F is the Fermi constant characterizing the strength of the underlying weak processes, V_i are the suitable CKM matrix elements for the quark transitions, C_i are the *Wilson coefficients* and O_i are the local operators forming a complete set for a given transition. The Wilson coefficients C_i are the numerical coefficients associated with these effective transitions expressed with the local operators O_i . Therefore, the amplitude of the effective Hamiltonian is expressed as a sum of local operator amplitudes scaled by their Wilson coefficients.

The Wilson coefficients include the effects of interactions at scales higher than μ , and the operators absorb all the effects below. While the choice of μ is arbitrary, it is usually chosen to be $\mathcal{O}(m_b)$ for the study of B decays; this is well above the Λ_{QCD} scale where perturbative QCD starts to break down.

Wilson coefficients are calculated by *matching* the prediction of the effective theory with the full theory (with all degrees of freedom) at a high mass scale, typically m_W ; at this scale the relevant diagrams and their QCD corrections can be calculated perturbatively and evolved down to the relevant energy scale —the previously mentioned m_b in our case—by making use of the renormalization group equations. After renormalization, the local operators O_i can be identified within the full calculation and their corresponding Wilson coefficients extracted.

In general, there are several operators of the same dimension which mix under renormalization.

$$\langle O_i \rangle_B = \sum_i Z_{ij}(\epsilon, \mu) \langle O_j \rangle_R, \quad (1.52)$$

where the subscript B (R) denotes the *bare* (*renormalized*) operator. This operator mixing can affect the decay rate: in $b \rightarrow s\gamma$, this can result in a three-fold enhancement [61, 62].

Effective Weak Hamiltonian for $B \rightarrow V\gamma$ Transitions

Following the convention by Becher, Hill and Neubert [63], in the Standard Model, the effective weak Hamiltonian mediating FCNC $b \rightarrow s$ processes has the form

$$\mathcal{H}_{\text{weak}} = \frac{G_F}{\sqrt{2}} \sum_{p=u,c} V_{ps}^* V_{pb} \left[C_1 O_1^p + C_2 O_2^p + \sum_{i=3}^8 C_i O_i \right], \quad (1.53)$$

with the operators

$$\begin{aligned} O_1^p &= \bar{s}\gamma^\mu(1-\gamma_5)p\bar{p}\gamma_\mu(1-\gamma_5)b & O_2^p &= \bar{s}^i\gamma^\mu(1-\gamma_5)p^j\bar{p}^j\gamma_\mu(1-\gamma_5)b^i \\ O_3 &= \bar{s}\gamma^\mu(1-\gamma_5)b \sum_q \bar{q}\gamma_\mu(1-\gamma_5)q & O_4 &= \bar{s}^i\gamma^\mu(1-\gamma_5)b^j \sum_q \bar{q}^j\gamma_\mu(1-\gamma_5)q^i \\ O_5 &= \bar{s}\gamma^\mu(1+\gamma_5)b \sum_q \bar{q}\gamma_\mu(1+\gamma_5)q & O_6 &= \bar{s}^i\gamma^\mu(1+\gamma_5)b^j \sum_q \bar{q}^j\gamma_\mu(1+\gamma_5)q^i \\ O_7 &= -\frac{e}{8\pi^2}m_b\bar{s}\sigma^{\mu\nu}(1+\gamma_5)bF_{\mu\nu} & O_8 &= -\frac{g}{8\pi^2}m_b\bar{s}\sigma^{\mu\nu}(1+\gamma_5)T^a b G_{\mu\nu}^a, \end{aligned} \quad (1.54)$$

where i, j are color indices. The effective weak Hamiltonian for $b \rightarrow d$ transitions is obtained by replacing s with d in the above expressions.

The most relevant operators are the four-quark operator O_1^p , the electromagnetic penguin operator O_7 , and the chromomagnetic penguin operator O_8 , specially for CP studies. The matrix elements of the QCD penguin operators O_2^p, \dots, O_6 contributes at $\mathcal{O}(\alpha_s)$ and are multiplied by small Wilson coefficients, while the contribution from O_2^p starts at $\mathcal{O}(\alpha_s)$.

At one-loop order, the decay is mediated entirely by the O_7 electromagnetic penguin without mixing with the four-quark operators, which occurs at higher orders. The rate of the inclusive $B \rightarrow X_s\gamma$ transition can be written [64] at one-loop as

$$\Gamma(B \rightarrow X_s\gamma) = \frac{\alpha G_F^2 m_b^5}{128\pi^4} \left| \sum_{p=u,c} V_{ps}^* V_{pb} C_7(m_b) \right|^2. \quad (1.55)$$

1.2.2. Exclusive Radiative Decays

The Wilson coefficients of the effective weak Hamiltonian in Eq. 1.51 are process-independent and therefore can be used directly in the description of exclusive modes. The theoretical precision is thus limited by the difficulty of computing the hadronic matrix elements between meson states, $\langle f | O_j | i \rangle$.

In the case of radiative decays, Heavy Quark Effective Theory (HQET) [65, 66] has been extensively used, specially in the prediction of inclusive B decays. HQET was constructed as a general framework in which to explore heavy quark physics by performing an expansion in Λ_{QCD}/m , where m is the mass of the heavy quark. In it, all light degrees of freedom must have momenta of the order Λ_{QCD} , *i.e.*, the momentum p_{heavy} of the heavy quark inside a heavy meson moving with velocity $v = p_{\text{meson}}/M_{\text{meson}}$ is decomposed as $p_{\text{heavy}} = mv + k$ and all components of the residual momentum k are assumed to be of $\mathcal{O}(\Lambda_{\text{QCD}})$.

However, in a decay of a heavy quark into a light quark one may have a kinematical situation in which the light degrees of freedom carry a large energy in the rest frame of the heavy quark, and therefore $v p_{\text{light}} \sim m$. For example, one may consider a radiative decay in the corner of phase space where the energy E_γ of the photon is close to its maximal value $E_{\gamma,\text{max}} \sim M_B/2$, if we ignore the mass of the final state. In this case, the hadronic final state corresponds to a collimated “jet” of hadrons with small invariant mass but large energy in the rest frame of the decaying B meson.

At this point, one is faced with a multi-scale problem, which can be tackled by making use of SCET [55]. The three relevant energy scales are:

- The *soft scale* of $\mathcal{O}(\text{few} \times \Lambda_{\text{QCD}})$, set by the typical energies and momenta of the light degrees of freedom in the hadronic bound states.
- The *hard scale* of $\mathcal{O}(m_b)$, set by the b quark mass and the energy of the outgoing hadron in the B meson rest frame.
- The *hard-collinear scale*, $\mu = \sqrt{m_b \Lambda}$, appearing through interactions between soft and energetic modes in the initial and final states.

The dynamics of hard and hard-collinear modes can be described perturbatively in the heavy quark limit, $m_b \rightarrow \infty$. SCET then describes B decays to light hadrons with energies much larger than their masses, assuming that their constituents have momenta collinear to the hadron momentum.

Hadronic Matrix Elements for $B \rightarrow V\gamma$

The QCDF formula for the matrix element of a given operator of the effective weak Hamiltonian can be written in the form [67]

$$\langle V\gamma | O_i | \bar{B} \rangle = F^{B \rightarrow V_\perp} T_i^I + \int d\omega du \phi_+^B(\omega) \phi_\perp^V(u) T_i^{II}(\omega, u), \quad (1.56)$$

which is expected to be valid up to corrections of $\mathcal{O}(\Lambda_{\text{QCD}}/m)$.

The non-perturbative effects are contained in $F^{B \rightarrow V_\perp}$, a form factor evaluated at $q^2 = 0$, and in ϕ_+^B and ϕ_\perp^V , the light-cone distribution amplitudes (LCDAs) for the B and V mesons, respectively. The hard-scattering kernels T_i^I , related to virtual corrections to the inclusive decay rate, and T_i^{II} , related to parton exchange with the

light quark in the B meson, include only short distance effects, calculable through perturbation theory.

The derivation of the factorization formula from SCET allows to reach a deeper understanding of Eq. 1.56. In the SCET approach, the factorization formula can be written as [63]

$$\langle V\gamma|O_i|\bar{B}\rangle = \Delta_i C^A \zeta_{V_\perp} + \frac{\sqrt{m_b} F f_{V_\perp}}{4} \int d\omega du \phi_+^B(\omega) \phi_\perp^V(u) t_i^{II}(\omega, u), \quad (1.57)$$

where F and f_{V_\perp} are meson decay constants, and ζ_{V_\perp} is the SCET form factor, related to the QCD form factor through perturbative and power corrections. In SCET, the perturbative hard-scattering kernels T_i^I and T_i^{II} can be identified with the Wilson coefficients $\Delta_i C^A$ and t_i^{II} , which are completely known to next-to-leading order (NLO), $\mathcal{O}(\alpha_s)$. In addition, the hard-scattering kernels for O_7 and O_8 are further known up to next-to-next-to-leading order (NNLO), with only partial results known for O_1 [67].

Non-perturbative calculations: sum rules

Form factors, which summarize the non-perturbative effects of QCD interactions, can be calculated by making use of *light cone QCD sum rules* (LCSR) [68, 69], based on *Shifman-Vainshtein-Zakharov (SVZ) QCD sum rules* [70, 71]

SVZ sum rules are based on the idea that the quarks comprising hadronic states are, on average, close to each other, at a distance of $\mathcal{O}(\Lambda^{-1})$ [72]. Then, it is not necessary to use the full machinery of the first principles of QCD to approximately describe properties of the hadrons: their basic parameters depend on how the quarks of which they are built interact with typical vacuum fluctuations. Furthermore, it is assumed that QCD vacuum is sufficiently characterized by a small number of (low dimensional) vacuum condensates, such as the quark condensate $\langle\bar{q}q\rangle$, the gluon condensate $\langle G_{\mu\nu}^2 \rangle$, the mixed condensate $\langle\bar{q}\sigma Gq\rangle$, the four-quark condensate, among others.

SVZ sum rules allow to approximately determine the regularities and parameters of the classical mesons and baryons from a few simple condensates. To do so, they make use of the vacuum-to-vacuum correlation function (and its dispersion integral) of the quark vector current J_μ , defined as

$$\Pi(Q^2 = -q^2) = i \int d^4x e^{iqx} \langle 0 | T\{J(x)J^\dagger(0)\} | 0 \rangle = \frac{1}{\pi} \int_{s_0}^{\infty} ds \frac{\rho(s)}{s + Q^2}, \quad (1.58)$$

where $\rho(s)$ is the *spectral function* containing the information about the hadronic state, and the QCD correlation function calculated at $Q^2 \gg \Lambda_{\text{QCD}}^2$ with the help of Operator Product Expansion (OPE) [73]. In it, short distance contributions are absorbed into Wilson coefficients obtained from perturbative calculations of the vacuum condensate operators²:

$$\Pi(Q^2)_{\text{QCD}} = \sum_k C_{2k}(Q^2, \alpha_s, \mu) \frac{1}{Q^2} \langle 0 | O_{2k}(\mu) | 0 \rangle. \quad (1.59)$$

Quark-hadron duality, which states that $\Pi(Q^2) = \Pi(Q^2)_{\text{QCD}}$, allows to express the hadronic parameters—the spectral function—in terms of QCD parameters such as α_s and the quark masses.

²It is convenient to perform the expansion sorting the operators according to their *dimension*. The higher the dimension, the higher the power of $1/M$ of the corresponding Wilson coefficient.

The LCSR approach is a variant of the SVZ sum rules designed to overcome difficulties of the latter in three-point functions, *e.g.*, in the case of $A \rightarrow B C$. In them, the standard condensate expansion contains a series of operators with derivatives which give rise to the expansion parameter of type $p_C(p_A + p_B)/p_{A,B}^2 \sim 1$. Therefore, all terms in this subseries must be summed over.

This partial summation is carried out automatically if one considers the correlation function of the currents j_A and j_B sandwiched between the vacuum and state $|C\rangle$, instead of the three-point function $\langle j_A, j_B, j_C \rangle$. The vacuum expectation values of the condensates (operators) in the SVZ sum rules are substituted by the *light-cone wave functions* ϕ . The OPE is then performed with the light-cone wave functions sorted in increasing *twist*, defined as the difference of the dimension and the spin of the condensate operator. In other words, using LCSR allows the partial summation with the tradeoff that large distance dynamics are no longer parametrized by numbers, as in SVZ sum rules, but by functions —the leading twist, the next-to-leading twist, and so on. Quark-hadron duality then relates the twist expansion to the desired form factor.

1.3. Current theoretical and experimental status

While exclusive radiative decays offer a larger variety of experimentally accessible observables than the inclusive ones, the non-perturbative uncertainties in theoretical predictions are in general sizable.

Branching ratios

Large hadronic uncertainties arising from the non-perturbative input in Eq. 1.57 do not allow precise theoretical predictions of the branching fractions of exclusive radiative decays. The SCET soft function ζ_{V_\perp} is the main theoretical uncertainty, which can be reduced by improved QCD non-perturbative QCD calculations.

NNLO calculations [67], which make use of form factor calculations in LCSR from [74] are compared to the latest experimental results in Table 1.3. It can be seen that the measurements in the B^0 sector, coming from CLEO [75], BABAR [76] and Belle [77], are more precise than the theoretical calculations; measurements in the B_s^0 sector, performed in Belle through the $\Upsilon(5S)$ resonance [78], suffer from great uncertainties due to the low collected statistics.

The measure of the ratio of the branching fractions of $B^0 \rightarrow K^{*0}\gamma$ and $B_s^0 \rightarrow \phi\gamma$ is rather interesting, since in this case only uncertainties in the quantities which are different between the two decays add significant error. Ali, Pecjak and Greub find [67]

$$\frac{\mathcal{B}(B^0 \rightarrow K^{*0}\gamma)}{\mathcal{B}(B_s^0 \rightarrow \phi\gamma)} = 1.0 \pm 0.2, \quad (1.60)$$

to be compared with the experimental ratio 0.7 ± 0.3 .

Isospin Asymmetry

The isospin asymmetry ratio, given by

$$\Lambda_{0\pm}(B^0 \rightarrow K^{*0}\gamma) = \frac{\Gamma(B^0 \rightarrow K^{*0}\gamma) - \Gamma(B^\pm \rightarrow K^{0\pm}\gamma)}{\Gamma(B^0 \rightarrow K^{*0}\gamma) + \Gamma(B^\pm \rightarrow K^{0\pm}\gamma)}, \quad (1.61)$$

	$B^+ \rightarrow K^{*+} \gamma (\times 10^{-5})$	$B^0 \rightarrow K^{*0} \gamma (\times 10^{-5})$	$B_s^0 \rightarrow \phi \gamma (\times 10^{-5})$
Theory [67]	4.6 ± 1.4	4.3 ± 1.4	4.3 ± 1.4
CLEO [75]	$3.76_{-0.83}^{+0.89} \pm 0.28$	$4.55_{-0.68}^{+0.72} \pm 0.34$	—
BABAR [76]	$4.22 \pm 0.14 \pm 0.16$	$4.47 \pm 0.10 \pm 0.16$	—
Belle [77, 78]	$4.25 \pm 0.31 \pm 0.24$	$4.01 \pm 0.21 \pm 0.17$	$5.7_{-1.5}^{+1.8} {}^{+1.2}_{-1.1}$
HFAG [79]	4.21 ± 0.18	4.33 ± 0.15	$5.7_{-1.8}^{+2.1}$

Table 1.3. Current theoretical prediction by Ali, Pecjak and Greub and experimental results of the branching ratios (in units of 10^{-5}) from the BABAR, Belle and CLEO collaborations. In addition, the average of the experimental results by the Heavy Flavour Averaging Group (HFAG) [79] is included.

is also a very interesting measurement because it is very sensitive to NP effects in the penguin sector, specially to the ratio of the Wilson coefficients C_6/C_7 and the sign of C_7 [80]. It has also been shown to be more effective than inclusive radiative measurements in constraining the mSUGRA parameter space [81].

Theoretical predictions by various authors are of $\mathcal{O}(5\%)$ [53, 74, 82], consistent with the current measurements of BABAR and Belle, $(1.7 < \Delta_{0-} < 11.6)\%$ and $\Delta_{0+} = (1.2 \pm 4.4 \pm 2.6)\%$, respectively.

Direct CP asymmetries

The direct CP asymmetry in $B^0 \rightarrow K^{*0} \gamma$ is defined as

$$\mathcal{A}_{CP}(B^0 \rightarrow K^{*0} \gamma) = \frac{\Gamma(B^0 \rightarrow K^{*0} \gamma) - \Gamma(\bar{B} \rightarrow \bar{K}^{*0} \gamma)}{\Gamma(B^0 \rightarrow K^{*0} \gamma) + \Gamma(\bar{B} \rightarrow \bar{K}^{*0} \gamma)}. \quad (1.62)$$

This asymmetry is expected to be very small within the SM, because it is double Cabibbo suppressed. Its value has been computed making use of QCDF, and it suffers from large uncertainties [83],

$$\begin{aligned} \mathcal{A}_{CP}^0 &= -(0.61 \pm 0.46)\%, \\ \mathcal{A}_{CP}^+ &= -(0.57 \pm 0.43)\%. \end{aligned} \quad (1.63)$$

Measurements from BABAR and Belle also suffer from large uncertainties [76, 77],

$$\begin{aligned} \mathcal{A}_{CP}^0 &= -(1.6 \pm 2.2 \pm 0.7)\%, \\ \mathcal{A}_{CP}^+ &= (1.8 \pm 2.8 \pm 0.7)\%, \\ \mathcal{A}_{CP}^{\text{combined}} &= -(0.3 \pm 1.7 \pm 0.7)\%, \end{aligned} \quad (1.64)$$

leaving room for improvement in LHCb [84].

2

CERN and the LHC

The European Organization for Nuclear Research, known as CERN, is the world's largest particle physics laboratory, and is situated on the Franco-Swiss border, near Geneva. In its 50 years of existence, many high-energy physics experiments have been built within its facilities, usually by large international collaborations. It currently hosts the largest particle accelerator in the world, the LHC, and its six experiments: ALICE, ATLAS, CMS, LHCb, LHCf and TOTEM.

2.1. The European Organization for Nuclear Research (CERN)

CERN is the European Organization for Nuclear Research. The CERN acronym comes from the French *Conseil Européen pour la Recherche Nucléaire*, European Council for Nuclear Research. At the time of the foundation of the Organization, in the mid-1950's, the frontier for pure physics research was the inside of the atom, and hence the use of the *nuclear* in the name. This becomes also clear in the phrasing of the Convention that established CERN in 1954, which lays down the main missions for the Organization:

The Organization shall provide for collaboration among European States in nuclear research of a pure scientific and fundamental character (...). The Organization shall have no concern with work for military requirements and the results of its experimental and theoretical work shall be published or otherwise made generally available.

Although our current understanding of matter goes deeper than the nucleus, CERN's main mission remains the same.

CERN is run by 20 European Member States, but many non-European countries are also involved in different ways. The current Member States are: Austria, Belgium, Bulgaria, the Czech Republic, Denmark, Finland, France, Germany, Greece, Hungary, Italy, the Netherlands, Norway, Poland, Portugal, the Slovak Republic, Spain, Sweden, Switzerland, and the United Kingdom, while Romania is nowadays a candidate to

become a Member State of CERN. Some states (or international organizations) for which membership is either not possible or not yet feasible are Observers.

Overall, a total of 10000 visiting scientists from 608 institutes and universities from 113 countries around the world use CERN’s facilities, amounting to half of the world’s particle physicists. Moreover, CERN employs around 2400 people between scientific and technical staff.

History highlights

French physicist Louis de Broglie was the first to put forward an official proposal for the creation of a European laboratory at the European Cultural Conference in Lausanne in December 1949. At the end of 1951 the first resolution for the creation of an European Council For Nuclear Research was adopted, and a few months later 11 countries signed an agreement establishing the provisional Council —CERN. At the end of 1952 Geneva was chosen as the site of the future laboratory. On September 29th, 1954 the 12 founding Member States ratified the CERN Convention and the European Organization for Nuclear Research was created, keeping the provisional CERN acronym. CERN’s history highlights are presented in a schematic way in Fig. 2.1, and will be summarized below.

The maximum expression of CERN’s achievements is the construction of several great colliders, from the first 600 MeV *Synchrocyclotron* (SC), built in 1957 and closed down in 1990, to the 7 TeV *Large Hadron Collider* (LHC), which started up in 2008 and is currently the world’s biggest collider. In between, the first proton-proton collider —the *Intersecting Storage Rings* (ISR)— commissioned in 1971, the first proton-antiproton collider —the *Super Proton Synchrotron* (SPS)—, that led to the discovery of the W^\pm and Z^0 bosons, and the *Large Electron Positron* (LEP) collider, commissioned in 1989, which provided a detailed study of the electroweak interaction. These colliders have been at the core of CERN’s research and have provided great discoveries such as the existence of neutral currents.

During the history of CERN several Nobel Prizes in Physics have been awarded to scientists working at its facilities, which can be seen marked as yellow stars (\star) in Fig. 2.1. In 1976, the afterwards LEP experiment L3 spokesman Sam Ting, along with Burt Richter, received the Nobel prize “*for their pioneering work in the discovery of a heavy elementary particle of a new kind*”. The J/ψ had been discovered two years before, but not at CERN. In 1984, just one year after the discovery of the W^\pm and Z^0 bosons, Carlo Rubbia and Simon Van der Meer were awarded the Prize for “*their decisive contributions to the large project which led to the discovery of the field particles W and Z, communicators of the weak interaction*”. The experimental results confirmed the unification of weak and electromagnetic forces, the electroweak theory of the Standard Model. Less than a decade later, Georges Charpak, a CERN physicist since 1959, received the 1992 physics Nobel Prize for “*his invention and development of particle detectors, in particular the multi-wire proportional chamber, a breakthrough in the technique for exploring the innermost parts of matter*”. Charpak’s multi-wire proportional chamber, invented in 1968, and his subsequent developments launched the era of fully electronic particle detection. In 1988, Jack Steinberger, a CERN physicist since the late 1960s and head of the LEP ALEPH experiment at the time, was awarded the Nobel Prize, together with Leon Lederman and Mel Schwartz, “*for the neutrino beam method and the demonstration of the doublet structure of the leptons through the*

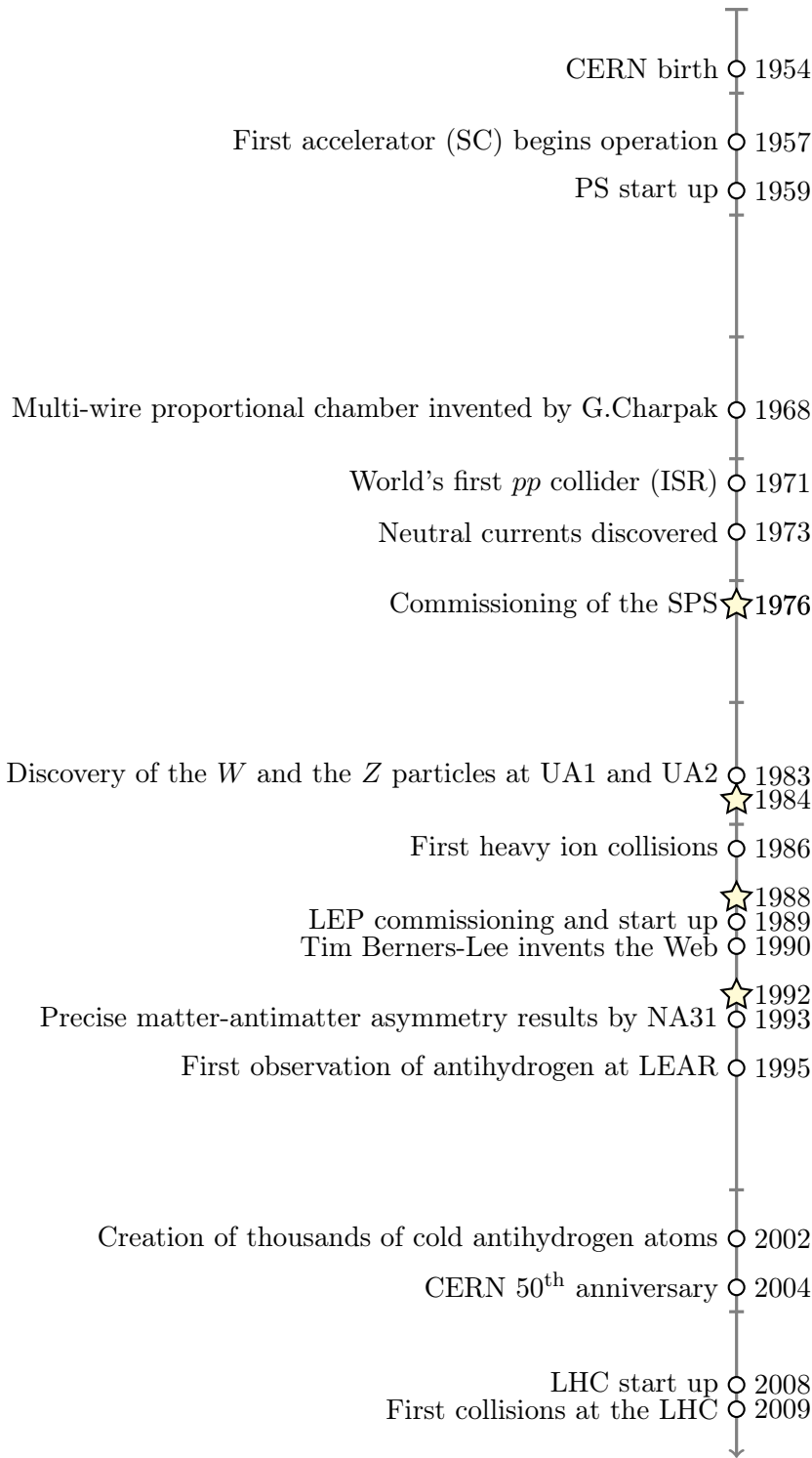


Figure 2.1. CERN history highlights, with relevant Nobel Prizes marked with a yellow star (\star).

discovery of the muon neutrino”. The discovery, made in 1962 at the US Brookhaven National Laboratory, showed that there was more than one type of neutrino.

Finally, one must not forget to mention Tim Berners-Lee, a scientist at CERN who defined the World Wide Web’s basic concepts —the URL, http and HTML— and wrote the first browser and server software in 1990. The World Wide Web was conceived and developed to meet the demand for information sharing between scientists around the world, and has changed the way we live nowadays.

2.2. The Large Hadron Collider

The Large Hadron Collider (LHC) at CERN is the most powerful tool for particle physics in the world [85]. It is a two-ring superconducting hadron accelerator and collider installed in the existing 26.7 km tunnel built between 1984 and 1989 to house the LEP machine. The tunnel has eight straight sections and eight arcs and lies between 45 m and 170 m below the surface on a plane inclined 1.4% towards the Léman lake. There are two transfer tunnels of about 2.5 km that link the LHC to the CERN accelerator complex, which acts as injector.

The LHC project was approved by the CERN council in December 1994. At that time, the plan was to build the machine in two stages, starting with a center-of-mass energy of 10 TeV, which would be upgraded to 14 TeV at a later stage. In the end, in 1996 the CERN council approved the construction of the 14 TeV machine in one stage.

The aim of the LHC and its experiments is to test or reveal the physics beyond the Standard Model. The number of events of a given type generated each second in the LHC is given by:

$$N_{\text{event}} = \mathcal{L}\sigma_{\text{event}}, \quad (2.1)$$

where σ_{event} is the cross section for the event under study and \mathcal{L} the machine luminosity. The machine luminosity solely depends on the beam parameters and can be written as [86, 87]:

$$\mathcal{L} = \frac{N_b^2 n_b f_{\text{rev}} \gamma_r}{4\pi \epsilon_n \beta^*} F, \quad [\text{cm}^{-2} \text{s}^{-1}] \quad (2.2)$$

where N_b is the number of particles per bunch, n_b the number of colliding bunches, f_{rev} the revolution frequency, γ_r the relativistic gamma factor, ϵ_n the normalized transverse beam emittance, β^* the beta function at the collision point and F the geometric luminosity reduction factor. This latter factor is has its origin in the crossing angle of the beams at the interaction point (IP), and can be expressed as

$$F = \left[1 + \left(\frac{\theta_c \sigma_z}{2\sigma^*} \right)^2 \right]^{-\frac{1}{2}}, \quad (2.3)$$

being θ_c the full crossing angle at the IP, σ_z the RMS bunch length, and σ^* the transverse RMS bunch size at the IP. Therefore, we can see that the exploration of rare events in the LHC collisions, characterized by very low cross sections, requires a high luminosity, achieved through both high beam energies and high beam intensities.

The ATLAS and CMS experiments, detailed in §2.3, are designed to run with a peak luminosity of $\mathcal{L} = 10^{34} \text{ cm}^{-2} \text{s}^{-1}$ for proton operation. Furthermore, there are two low luminosity experiments, also introduced in §2.3: LHCb, aiming at $\mathcal{L} = 10^{32} \text{ cm}^{-2} \text{s}^{-1}$, and TOTEM, aiming at a peak luminosity $\mathcal{L} = 2 \times 10^{29} \text{ cm}^{-2} \text{s}^{-1}$ with 156 colliding

bunches. The LHC has also one dedicated heavy ion experiment, ALICE, aiming at a peak luminosity of $\mathcal{L} = 10^{27} \text{ cm}^{-2} \text{ s}^{-1}$ for nominal lead-lead ion operation.

The high beam intensity required for the nominal luminosity $\mathcal{L} = 10^{34} \text{ cm}^{-2} \text{ s}^{-1}$ excludes a proton-antiproton ($p\bar{p}$) collider. Therefore, the LHC was designed as a proton-proton (pp) collider. Furthermore, since colliding two counter-rotating proton beams requires opposite magnetic dipole fields in both rings, the collider configuration with common vacuum and magnet systems for both circulating rings was excluded. The adopted configuration was thus a pp collider with separate magnetic fields and vacuum chambers in the main portion of the rings (see Fig. 2.2), with common sections only at the 4 insertion regions where the experimental detectors are located. Since there is not enough room for two separate rings of magnets in the LEP tunnel, the LHC uses twin bore magnets that consist of two sets of coils and beam channels within the same mechanical structure and cryostat. The peak beam energy depends on the integrated dipole field around the storage ring, which bends the trajectory of the proton beams. For a beam energy of 7 TeV in the LHC machine, a peak dipole field of 8.33 T is needed. These high field strengths are achieved through the use of superconducting electromagnets cooled down to a temperature of 1.9 K.

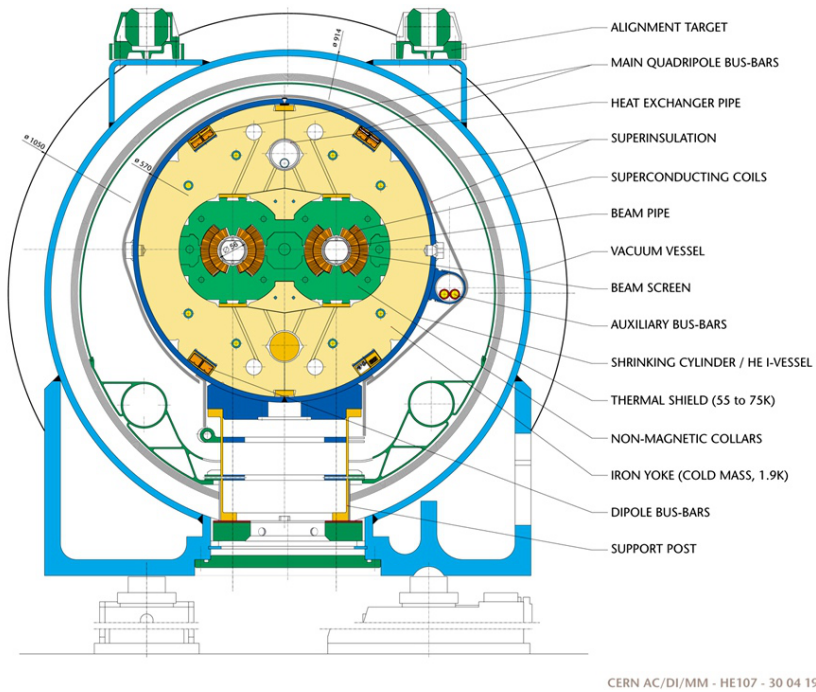


Figure 2.2. Cross-section of a LHC superconducting cryodipole [85].

The high peak luminosity of $\mathcal{L} = 10^{34} \text{ cm}^{-2} \text{ s}^{-1}$ is reached through a high number of bunches per beam, $n_b = 2808$, a high revolution rate, $f_{\text{rev}} = 11245 \text{ Hz}$, and a large number of protons per bunch, $N_b = 1.1 \times 10^{11}$. This gives a minimal distance of $\sim 7 \text{ m}$ between bunches, and a time of 25 ns between two bunch crossings, amounting to a bunch crossing frequency of 40 MHz.

Acceleration

The proton energy of 7 TeV is achieved through a chain of accelerators, shown in Fig. 2.3, of which the LHC is the last step. The protons are produced at 100 keV by an ion source, and are first accelerated by the *LINear ACcelerator 2* (LINAC 2) up to an energy of 50 MeV. They are then injected into the *Booster*, a small synchrotron that increases their energy to 1 GeV. Afterwards, the *Proton Synchrotron* (PS) boosts them to 26 GeV and injects them into a third accelerator, the *Super Proton Synchrotron* (SPS), which accelerates the protons up to 450 GeV. At this energy the proton beam is split into two beams, which are injected in a counter-rotating configuration into the LHC. The final energy of 7 TeV is reached during an acceleration process in the LHC itself.

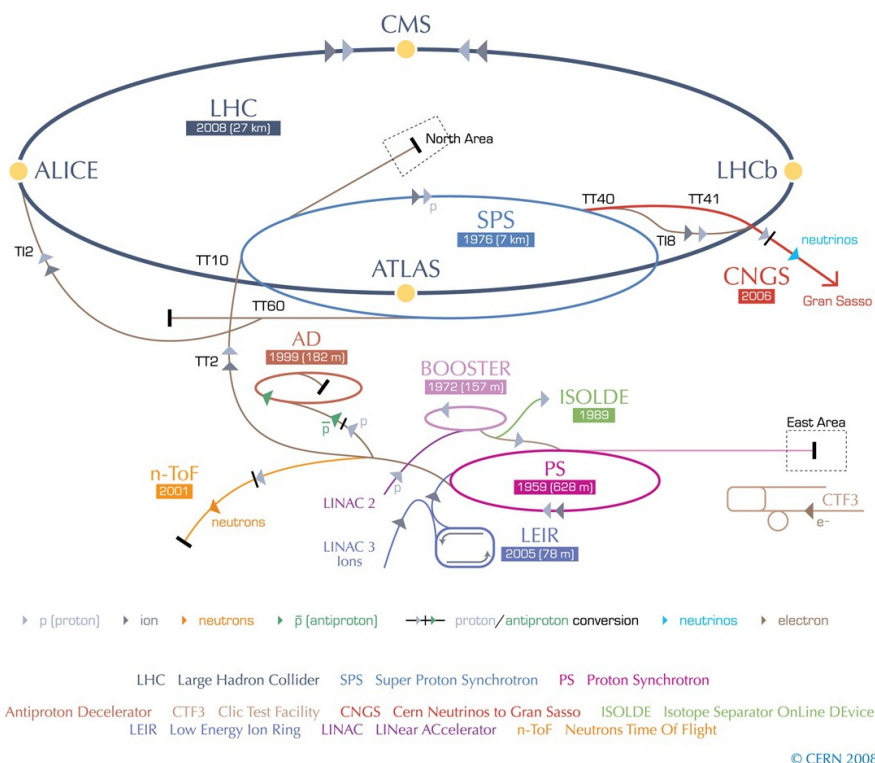


Figure 2.3. The CERN accelerator complex, with the LHC as its last step (not to scale).

A total beam current of 0.584 A corresponds to a stored energy in the beams of ~ 362 MJ, while the total energy stored in the superconducting magnets is ~ 600 MJ. Therefore, the LHC must be able to safely absorb a total energy of $\mathcal{O}(\text{GJ})$ in the event of an emergency situation. Several safety measures have been put in place, and are detailed elsewhere [85].

A very similar chain is used to accelerate the heavy lead ions ^{82}Pb to an energy of 574 TeV, which corresponds to a center-of-mass energy of 2.76 TeV/nucleon, in Pb-Pb collisions.

2.3. The experiments at the LHC

Four big detectors (ALICE, ATLAS, CMS, LHCb) and two smaller experiments in size and staff (LHCf, TOTEM) are placed around the four interaction points of the LHC ring. A brief description of the six experiments is included below:

ALICE [88] *A Large Ion Collider Experiment* is dedicated to the study the physics of strongly interacting matter and the quark-gluon plasma (QGP) at extreme values of energy density and temperature in heavy nuclei (Pb-Pb) collisions. Its design, shown in Fig. 2.4a is optimized for studying hadrons, electrons, muons, and photons produced in the nucleus-nucleus collisions up to the highest multiplicities produced in the LHC. An example collision from the 2010 Pb-Pb run is shown in Fig. 2.4b.

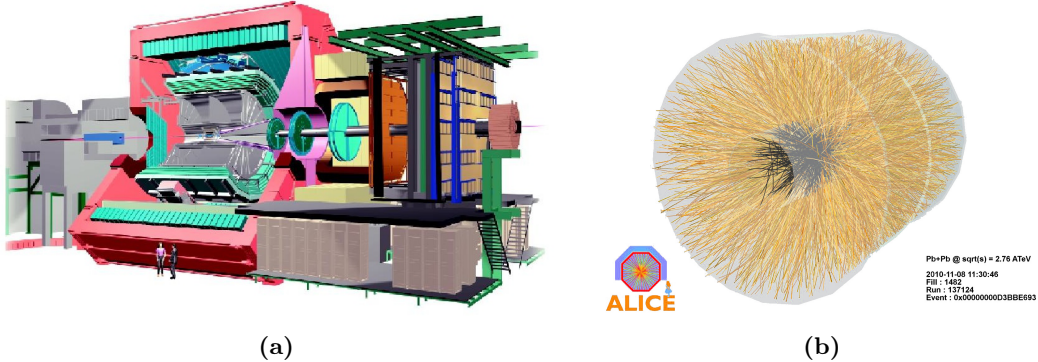


Figure 2.4. (a) The ALICE apparatus and (b) an example Pb-Pb collision from the 2010 run.

ATLAS [89] *A Toroidal LHC ApparatuS* is a general purpose experiment with the objective to test de Standard Model at the TeV scale, and to search for the Higgs boson and physics beyond the Standard Model. ATLAS is the biggest 4π detector built on the LHC, with a diameter of 22 m and a length of 40 m (see Fig. 2.5b), and weights 7000 tons. Its solenoidal magnetic field of 2 T is achieved through three superconducting toroidal magnets arranged with an eight-fold azimuthal symmetry around the calorimeters. This design decision affects the whole design of the rest of the detector. A sample collision with a muon candidate in the ATLAS detector is shown in Fig. 2.5b.

CMS [90] The *Compact Muon Solenoid* is a multi-purpose apparatus with the main aim of elucidating the nature of electroweak symmetry breaking for which the Higgs mechanism is presumed to be responsible, as well as testing the mathematical consistency of the Standard Model at energy scales above 1 TeV. The choice of the magnetic field configuration for the measurement of the momentum of muons is what conditioned the design of this 13 m long, 6 m inner-diameter apparatus (see Fig. 2.6a). A 4 T superconducting solenoid was chosen to provide the large bending power needed. A CMS sample event is presented in Fig. 2.6b.

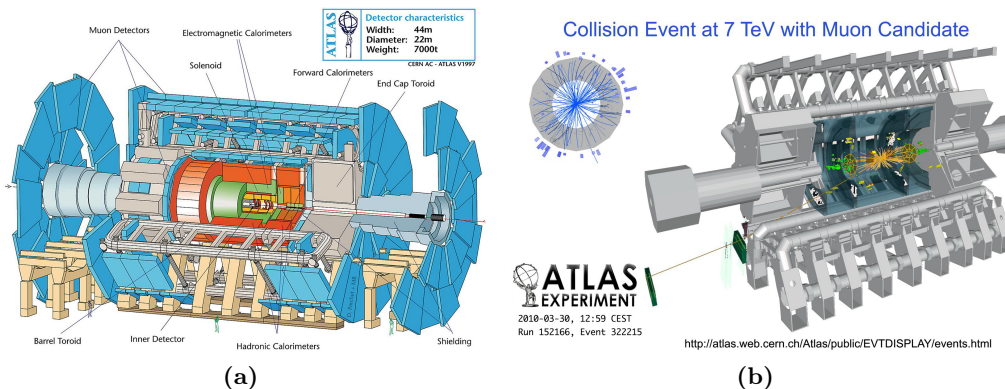


Figure 2.5. (a) The ATLAS apparatus and (b) an example collision from the 2010 run with a muon candidate.

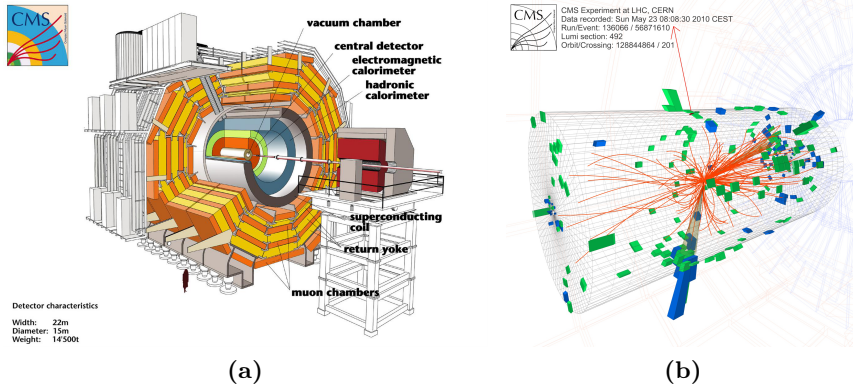


Figure 2.6. (a) The CMS apparatus and (b) a sample collision from the 2010 run.

LHCb [91] The *Large Hadron Collider beauty* experiment is dedicated to the study of CP violation and rare decays in the b -sector. It is a single-arm forward spectrometer, and it will be described in detail in Chap. 3. Its layout is presented in Fig. 2.7a, along with a $B_s^0 \rightarrow \mu\mu$ candidate event of the 2011 LHC run in Fig. 2.7b.

LHCf [92] The *Large Hadron Collider forward* experiment is the smallest of all of the LHC experiments. Its aim is to perform a measurement of the very forward production cross sections and energy spectra of neutral pions and neutrons. This will help to verify hadronic models at very high energy for the understanding of ultra-high energy cosmic rays. It consists of two small detectors, placed 140 m on both sides of the ATLAS interaction point.

TOTEM [93] The TOTEM experiment —small in size compared to the four big experiments at the LHC— is dedicated to the measurement of the total pp cross section with a luminosity-independent method based on the Optical Theorem. Moreover, its physics programme aims at obtaining a deeper understanding of the proton structure by studying elastic scattering processes with large momentum

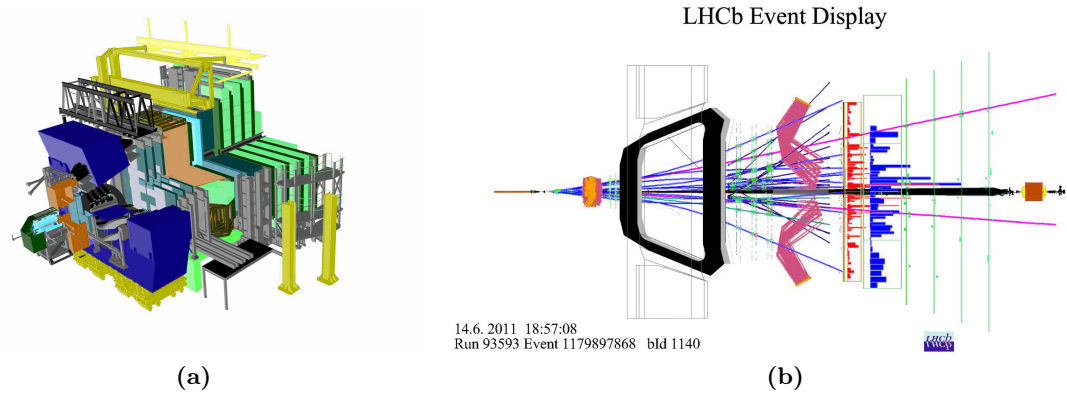


Figure 2.7. (a) The LHCb apparatus and (b) a $B_s^0 \rightarrow \mu\mu$ candidate event from the 2011 run.

transfers, and via diffractive processes. It is located around CMS, as can be seen in Fig. 2.8, with detectors placed at different distances from the interaction point in the very forward region.

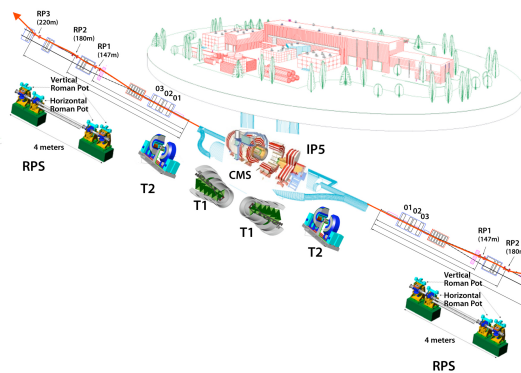


Figure 2.8. The TOTEM setup around the CMS detector.

2.4. Computing resources for the LHC

When the LHC accelerator is running optimally, it produces ~ 15 PB of data annually. Access to these data needs to be provided for the thousands of scientists in hundreds of institutes involved in the LHC experiments, not only when it is produced but also during all the estimated lifespan of the LHC project. Furthermore, the analysis of these data requires a huge amount of computing power. The *LHC Computing Grid Project* (LCG) was constituted on 2001 with the mission to develop, build and maintain a data storage and analysis infrastructure for the entire high energy physics community related to the LHC [94].

Instead of the traditional approach of centralizing the computing capacity at one

2. CERN and the LHC

location near the experiments, a novel globally distributed model—a computing Grid—was chosen for the LHC. This model allows, on one side, to share the maintenance and upgrade costs of the computing resources by distributing them in smaller computing centers run by the individual institutes. On the other side, a distributed model has no single points of failure as long as multiple copies of data and automatic reassigning of computational tasks to available resources is provided.

The *Worldwide LHC Computing Grid* (WLCG) is now the world's largest computing grid. It is based on the two main global grids currently in operation—the *European Grid Infrastructure* (EGI) and the USA *Open Science Grid* (OSG)—, as well as many associated regional and national grids across the world, such as the *Taiwan Grid* and the *EU-IndiaGrid*.

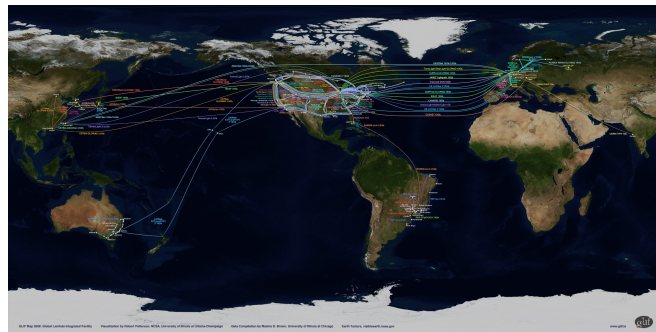


Figure 2.9. Overview of the WLCG connections.

3

The LHCb experiment

The LHCb experiment is dedicated to the study of heavy flavor physics at the LHC [91, 95, 96]. Its main aim is to make precise measurements of CP violation and rare decays of beauty and charm hadrons. It is located at Interaction Point 8 of the LHC accelerator, previously used by the DELPHI experiment from LEP.

The LHC is the most extensive source of b -hadrons in the world, including B_s^0 , B^0 and B_c mesons, and b -baryons such as Λ_b . The LHCb detector must be able to exploit this large number of b -hadrons in a high track multiplicity hadronic environment, *i.e.*, it must be able to trigger, reconstruct and correctly identify the b -hadrons coming from $b\bar{b}$ pairs generated by pp interactions. Events with multiple pp interactions are more difficult to analyze since secondary vertices coming from the b -hadron decay are harder to distinguish from primary vertices coming from different pp interactions.

As Fig. 3.1 shows, the probability for multiple interactions increases with the luminosity. In order to simplify B decay identification, the LHCb design target luminosity is lower than the LHC peak luminosity $\mathcal{L}_{\text{LHC}} = 10^{34} \text{ cm}^{-2} \text{ s}^{-1}$, effectively reducing the mean number of pp interactions per event. With the 2011 target luminosity of $\mathcal{L}_{\text{LHCb}} = 3.5 \times 10^{32} \text{ cm}^{-2} \text{ s}^{-1}$, and a measured $b\bar{b}$ cross section at $\sqrt{s} = 7 \text{ TeV}$ of $\sigma(pp \rightarrow b\bar{b}X) = (284 \pm 20 \pm 49) \mu\text{b}$ [97] (see Fig. 3.2 for predictions at different LHC luminosities), the number of produced $b\bar{b}$ pairs in a nominal year is expected to be $\sim 10^{12}$. They hadronize into b -hadrons —charged B_u , neutral B^0 , neutral B_s^0 and b -baryons— with proportions depending on the kinematics of the event [98]:

$$\begin{aligned} \frac{f_{B_s^0}}{f_{B^0} + f_{B_u}} &= 0.134 \pm 0.004^{+0.011}_{-0.010} \\ \frac{f_{\Lambda_b}}{f_{B^0} + f_{B_u}} &= (0.404 \pm 0.110) \times [1 - (0.031 \pm 0.005) \times p_T(\text{GeV})] \\ \frac{f_{B_s^0}}{f_{B^0}} &= 0.267^{+0.021}_{-0.020} \end{aligned} \quad (3.1)$$

Roughly speaking, at $p_T = 10 \text{ GeV}$, B_u and B^0 are produced $\sim 35\%$ of the times, while B_s^0 and Λ_b are produced $\sim 10\%$ and $\sim 20\%$ of the times, respectively.

The physics requirements for LHCb, combined with the LHC running conditions, give rise to a specific set of detector requirements:

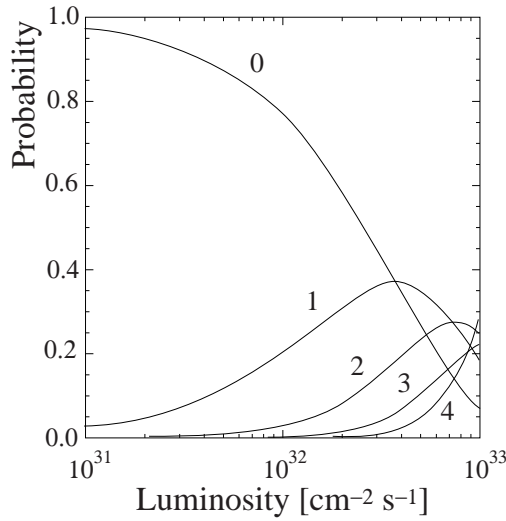


Figure 3.1. Probability to observe N $p\bar{p}$ interactions per bunch crossing as a function of the luminosity of the LHC.

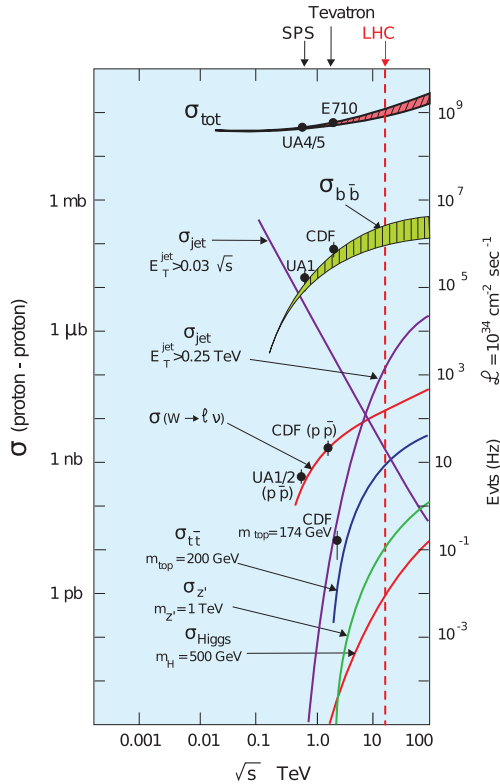


Figure 3.2. Production cross sections as a function of the center-of-mass energy of $p\bar{p}$ collisions. The left axis displays the inelastic cross sections while the right axis shows the expected number of events for the peak $\mathcal{L}_{LHC} = 10^{34} \text{ cm}^{-2} \text{ s}^{-1}$. The $b\bar{b}$ cross section has a predicted value between $200 \mu\text{b}$ and $500 \mu\text{b}$ at $\sqrt{s} = 7 \text{ TeV}$.

- An efficient, robust and flexible trigger is essential. It must be sensitive to many different final states and it must be able to adapt to varying LHC running conditions.
- Excellent vertex and momentum resolution are essential for good B decay time resolution, necessary to study the $B_s^0 - \bar{B}_s$ system—with very rapid oscillation—, and for good mass resolution, required to reduce the high combinatorial background.
- Identification of a very wide range of particle types—electrons, muons, photons, protons, kaons, and pions, both charged and neutral—is crucial in order to cleanly reconstruct many B -meson decay final states.
- A data acquisition system with high bandwidth and powerful online data processing capability is needed to optimize the data taking.

In a proton-proton collision, b quarks are always produced through the strong interaction. The partons involved in the inelastic scattering of the pp interaction exchange a great fraction of momentum. Since the exchanged momentum increases with the center-of-mass energy, the $b\bar{b}$ pairs are boosted in the direction of the most energetic parton, following the direction of the beam. Therefore the b -hadrons coming from $b\bar{b}$ pairs are produced in a very large proportion in the same direction, either in the forward or the backward direction. Fig. 3.3 shows the angular correlation between the produced b - and \bar{b} -hadrons. This distribution is crucial in the design of the detector, which will be detailed in §3.2.

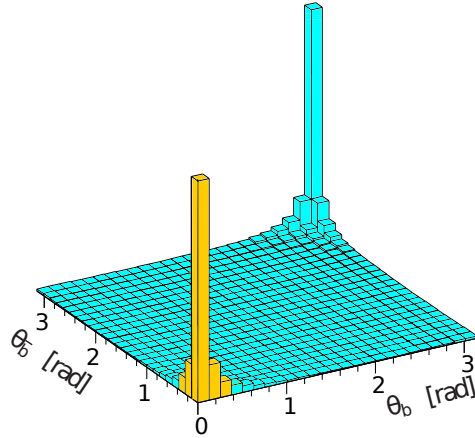


Figure 3.3. Polar angle correlation of the b -hadron and the \bar{b} -hadron produced by a $b\bar{b}$ pair, as calculated by the PYTHIA event generator. The yellow area marks the LHCb acceptance region.

3.1. LHCb 2011 running conditions

The design running conditions for LHCb require a luminosity of

$$\mathcal{L} = \sum_{i=1}^{n_b} \frac{f_{\text{rev}} N_i^1 N_i^2 S}{4\pi\epsilon\beta^*} = 2 \times 10^{32} \text{ cm}^{-2}\text{s}^{-1}, \quad (3.2)$$

where

- $n_b = 2622$ is the number of colliding bunches per beam,
- $f_{\text{rev}} = 11254 \text{ kHz}$ is the bunch revolution frequency around the LHC,
- $N_i^{1,2} \sim 10^{11}$ is the number of protons per bunch,
- $S \sim 673 \text{ mrad}$ is the beam crossing angle at LHCb,
- $\epsilon = 3.75 \mu\text{m}$ is the normalized emittance for $E_{\text{beam}} = 7 \text{ TeV}$, and
- $\beta^* = 10 \text{ m}$ is the beta function [99].

With these nominal values, the expected average number of visible pp interactions per bunch crossing in the LHCb acceptance is $\mu \sim 0.4$, and therefore the collected data would be dominated by single-interaction events.

In 2010, the LHC delivered 37 pb^{-1} to LHCb and managed to achieve 80% of the design luminosity. However, this luminosity was achieved with $\sim 10\%$ of the nominal number of colliding bunches per beam ($n_b \sim 344$) and $1/3$ of the nominal value of β^* , $\beta^* = 3.5 \text{ m}$, leading to an increase of the number of visible interactions. Fig. 3.4 compares the design value for μ and its behavior from July 2010 to the end of the 2010 data taking period.

An increase in μ means more interactions —and thus, vertices— per bunch crossing, an increase in the readout rate per bunch crossing, and an increase of the event size and processing time. A high μ also affects greatly the trigger working conditions, but the LHCb trigger has shown a great flexibility to adapt to LHC running conditions during 2010 and 2011 (see §3.5 for more details).

In 2011, the LHC has delivered $\sim 1.2 \text{ fb}^{-1}$ to LHCb, of which $\sim 1.1 \text{ fb}^{-1}$ have been recorded, as shown in Fig. 3.5. This corresponds to an efficiency of 91%.

Except for the ramp up period during the month of April, the 2011 data taking conditions have been very stable at LHCb. Data have been collected with n_b in the range $1000 - 1300$ ($n_b = 1296$ in the July-October period in which most of the data were recorded) and a target luminosity of $3.5 \times 10^{32} \text{ cm}^{-2} \text{ s}^{-1}$. That means that LHCb has been running at $\mathcal{O}(150\%)$ of the design luminosity with $\mathcal{O}(35\%)$ of the bunches per beam. As a consequence, the average number of inelastic pp collisions has been above the design value, as can be seen in Fig. 3.6, but substantially lower than the values from 2010.

The trigger configuration during the 2011 data taking period has been more stable than during the 2010 data taking, in which 18 different TCKs were used. Only a handful of Trigger Configuration Keys (TCKs, see §3.7.1) have contributed significantly to the bulk of the recorded luminosity, as summarized in Table 3.1.

3.2. Detector layout

LHCb is a single-arm spectrometer with a forward coverage from approximately 10 mrad to 300 (250) mrad in the horizontal bending (non-bending) plane. In terms of *pseudorapidity*,

$$\eta = -\ln \tan \left(\frac{\theta}{2} \right), \quad (3.3)$$

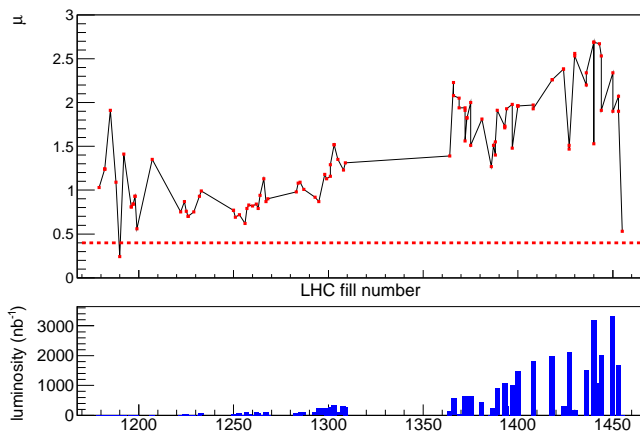


Figure 3.4. Evolution of μ per fill from end of June 2010 to the end of 2010, compared to the design value (dashed line).

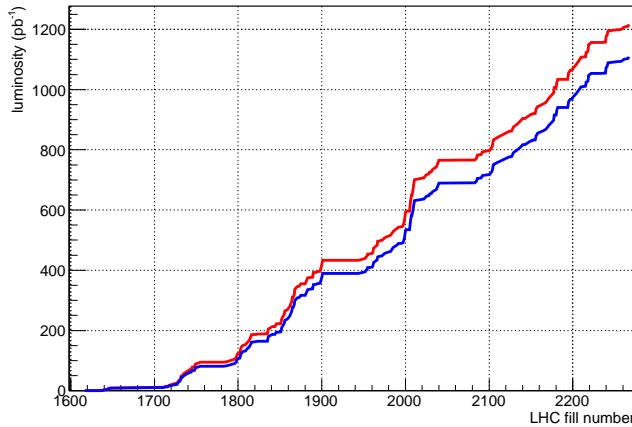


Figure 3.5. Accumulated delivered (red) and recorded (blue) luminosity in 2011.

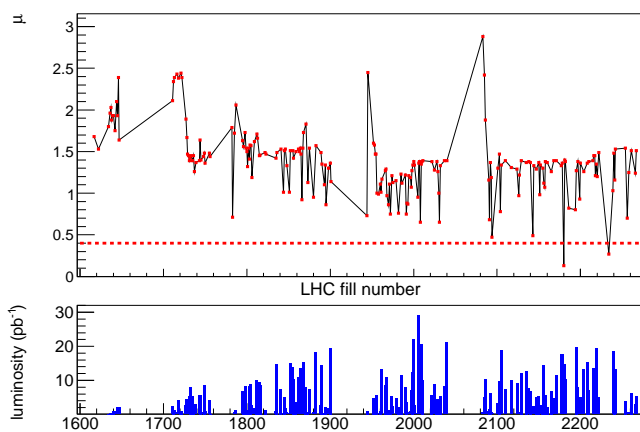


Figure 3.6. Evolution of μ per fill during the 2011 data taking, compared to the design value (dashed line).

TCK	$\int \mathcal{L} (\text{pb}^{-1})$	
	Magnet Up	Magnet Down
0x360032	—	3.36
0x480032	—	2.00
0x4A0033	—	2.09
0x561710	—	0.03
0x5A0032	38.63	28.45
0x5B0032	2.20	0.03
0x5D0033	2.25	—
0x6D0032	—	100.33
0x700034	—	1.14
0x710035	—	0.90
0x730035	134.35	61.83
0x740036	5.18	—
0x760037	107.11	191.64
0x790037	39.30	—
0x790038	153.97	209.43

Table 3.1. Trigger settings used in the 2011 data taking, with their corresponding integrated luminosity split by magnet polarity.

the acceptance of LHCb is $1.9 < \eta < 4.9$.

The choice of this detector geometry, as previously discussed, is motivated by the fact that at high energies both b -hadrons coming from a $b\bar{b}$ pair are mainly produced in the same forward or backward cone, and comes as a compromise between budget, available space in the cavern, and efficiency to detect b -hadrons. A modification of the LHC optics, displacing the interaction point by 11.25 m from the center, has permitted an optimal use of the existing cavern for the LHCb components.

The layout of the LHCb spectrometer is shown in Fig. 3.7. A right-handed coordinate system is defined with its origin at the nominal interaction point (on the left side of the detector in Fig. 3.7), z axis along the beam —positive downstream and negative downstream—, and x and y axes respectively as the horizontal —looking downstream, positive to left and negative to the right— and vertical —positive up and negative down— coordinates in the beam axis transverse plane. The detector is 20 m long (z -axis), 12 m wide in the horizontal direction (x -axis) and 10 m high (y -axis).

The LHCb detector is composed of six subdetectors, which are grouped in three interdependent systems:

- The Tracking System, described in §3.3, consists in:
 - the VErtex LOcator (VELO) [100].
 - the Tracker Turicensis (TT) [95].
 - three tracking stations —T1, T2, and T3—, each composed of a central Inner Tracker station (IT) [101] surrounded by an Outer Tracker station (OT) [102].
 - the LHCb Magnet [103].

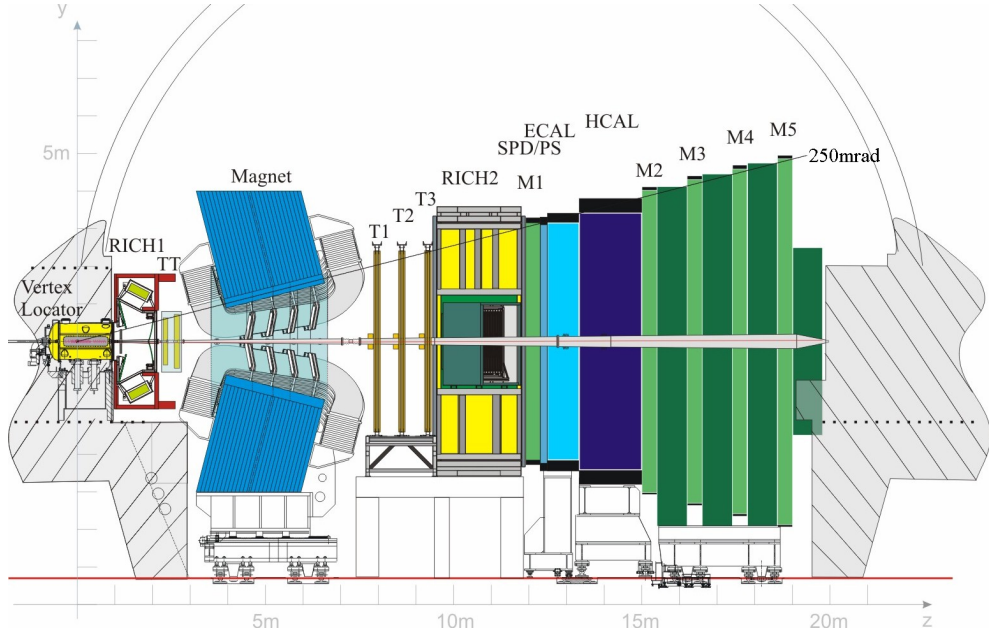


Figure 3.7. View of the LHCb detector.

- The Particle Identification System, described in §3.4, consists in
 - two Ring and Imaging Cherenkov detectors (RICH1 and RICH2) [104].
 - the Calorimeters [105], composed by the Scintillating Pad Detector (SPD), the Pre-Shower detector (PS), the Electromagnetic CALorimeter (ECAL) and the Hadronic CALorimeter (HCAL).
 - five muon stations —M1, M2, M3, M4, and M5— which compose the Muon Detector [106].
- The Trigger System, described in §3.5, is composed by some of the already mentioned subdetectors plus the pile-up detector, dedicated exclusively to triggering.

Furthermore, the Online System [107] is used to manage all data taking activities and detector operation, from the frontend electronics to the storage system. It will be discussed in §3.6.

The beampipe

The beampipe (see Fig. 3.8) is designed to minimize its contribution to the material budget in the detector acceptance. This is specially important in the high-rapidity region (see Fig. 3.9 for a summary of the material budget before the calorimeters), where the particle density is higher. Since the number of secondary particles depends on the amount of material seen by incident primary particles, the presence of the beampipe, along with its flanges and bellows, has a direct influence on the occupancy, in particular for the tracking chambers and RICH detectors.

The first 12 m out of 19 m of the beampipe are composed of beryllium, a material with long radiation length and resistant enough for the vacuum in the region of the detector. Beryllium is, however, a very toxic, fragile and costly material, and these drawbacks

3. The LHCb experiment

had to carefully be taken into account in the design, installation and operation phases. The last 7 m of beampipe, placed outside the critical zone in terms of transparency, are made of stainless steel, a material with good mechanical and vacuum properties.

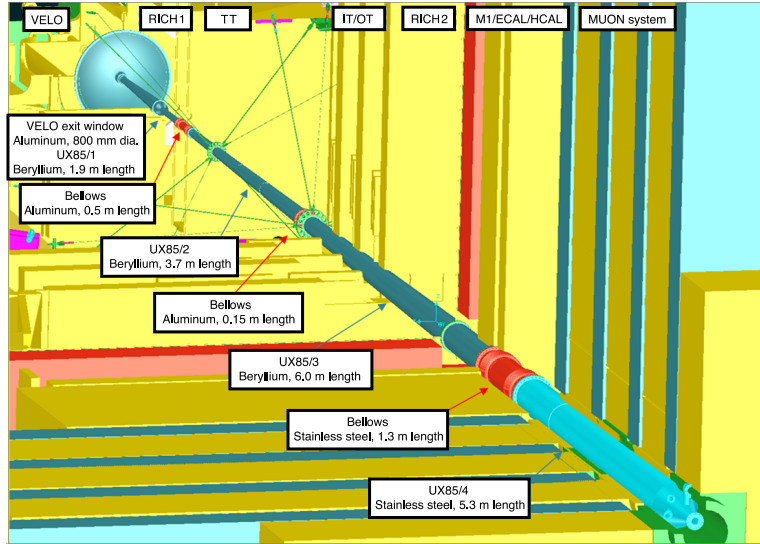


Figure 3.8. The beampipe layout through LHCb, with the interaction point at the top left part of the image.

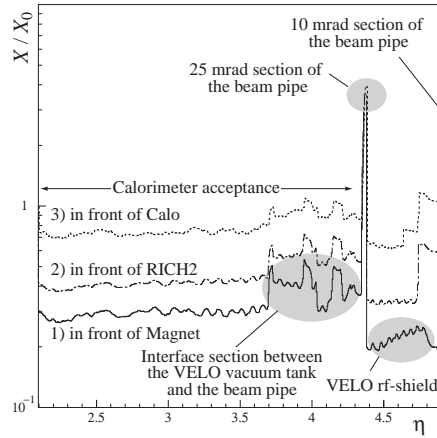


Figure 3.9. Material seen by a neutral particle from the nominal position of the interaction point as a function of the pseudorapidity at three different z positions before the calorimeter (1 – 3), averaged over the azimuthal angle.

3.3. The Tracking System

CP violation and rare decay studies require a precise knowledge of the lifetime of the B mesons. It is therefore a strong requirement for LHCb to be able to accurately measure the distance of flight and momentum of particles: to achieve several of the

key measurements of the LHCb physics program [84] it is important that the detector provides an excellent momentum resolution of $\delta p/p \approx 0.4\%$.

The Tracking System, depicted in Fig. 3.10, is dedicated to the reconstruction of the trajectories of charged particles that pass through the LHCb detector. It consists of the VELO (see §3.3.1), the Magnet (see §3.3.2), and four planar tracking stations: TT upstream the dipole magnet and T1–T3 downstream of the magnet. The VELO and TT use silicon microstrip detectors. In T1–T3, silicon microstrips are used in the region close to the beampipe —the IT— and straw-tubes are used in the outer region of the stations —the OT, see (see §3.3.4). The TT and the IT were developed in a common project called the Silicon Trackers (ST), detailed in §3.3.3.

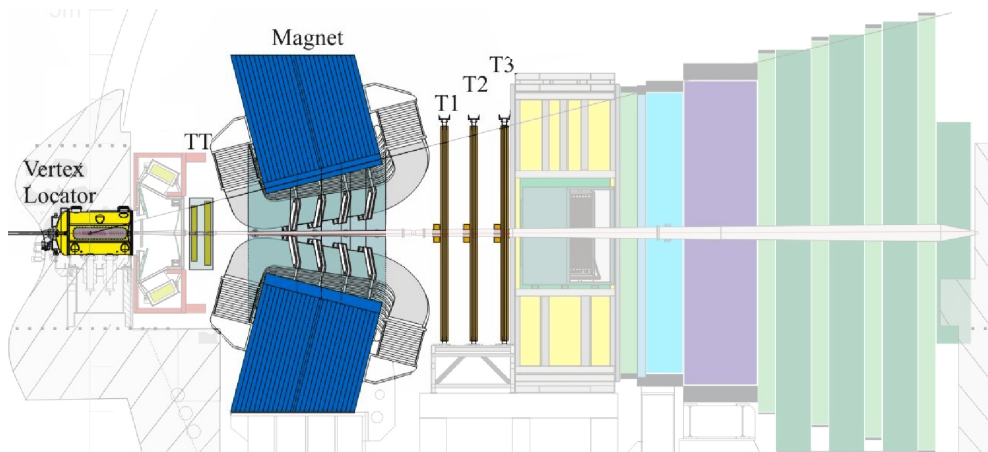


Figure 3.10. The Tracking System of the LHCb detector.

3.3.1. VErtex LOocator

The VELO is designed to provide precise measurement of track coordinates close to the interaction region, which are used to identify the distinctive displaced secondary vertices of b - and c -hadron decays¹ [100]. The VELO is able to detect particles with $1.6 < \eta < 4.9$ and emerging from interactions in the range $|z| < 10.6$ cm.

Most b -hadrons decay inside the VELO, in a so-called *secondary vertex* (SV). In a secondary vertex, the b -hadron daughter tracks converge to a point displaced from the interaction point or *primary vertex* (PV). Detached (secondary) vertices play a vital role in the High Level Trigger (HLT, see §3.5.2) and are used to enrich the b -hadron content of selected data. Therefore, a precise track reconstruction in this region is needed in order to separate primary from secondary vertices.

The VELO layout, shown in Fig. 3.11, has been optimized to minimize the amount of material in the acceptance region while providing good geometrical acceptance. It consists of a series of 21 stations arranged in the beam direction, which provide

¹The typical distance traveled by b -hadrons coming from the interaction vertex is a few centimeters. Their proper time is $\tau_B \sim 1.5 \times 10^{-12}$ s, and they come with a Lorentz boost of $\gamma \sim 10 - 100$. Therefore, their distance of flight is

$$d_B = \gamma c \tau_B \approx 458.7 \mu\text{m}$$

3. The LHCb experiment

a measure of the r and ϕ coordinates. They are mounted in a vessel that maintains vacuum around the sensors and is separated from the machine vacuum by a thin walled corrugated aluminum sheet. The use of a cylindrical geometry ($r\phi$) was chosen in order to enable fast 2D (rz) reconstruction of tracks and vertices in the LHCb trigger. Two planes perpendicular to the beam line are located upstream of the VELO sensors and constitute the *pile-up system*, which is a part of the Level-0 Trigger (L0, see §3.5.1).

Each of the 21 VELO stations is composed by one r -sensor and one ϕ -sensor, with the configuration shown in Fig. 3.12. The sensitive part of VELO sensors starts at a radius of about 8 mm, which is the smallest possible for safety reasons. During injection, however, the aperture required by the LHC machine increases, so the VELO is retracted up to a distance of 3 cm.

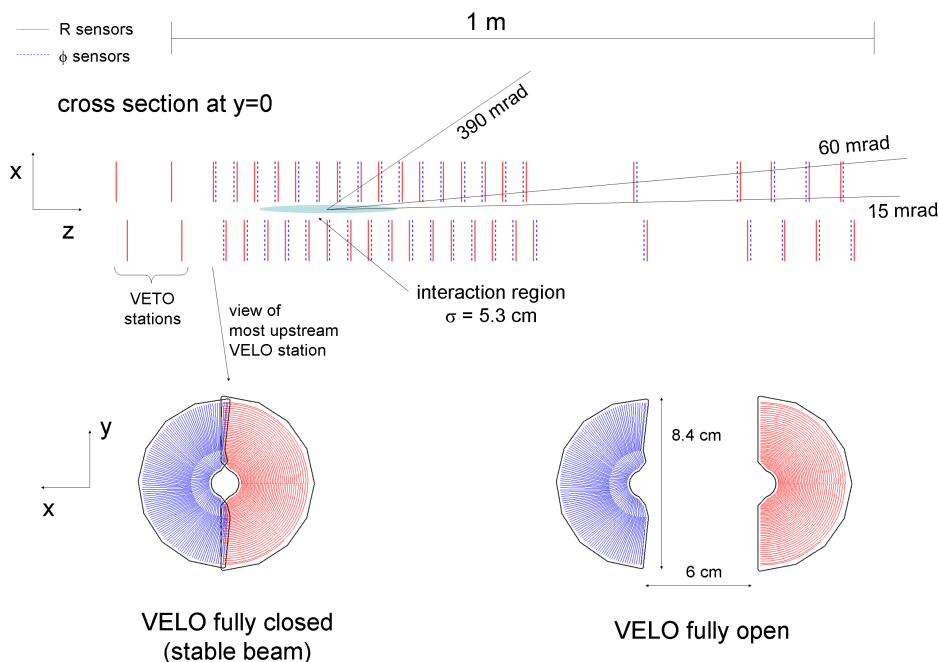


Figure 3.11. Cross section in the $x - z$ plane of the VELO sensors at $y = 0$ with the detector in the fully closed position. The front face of the first modules in the $x - y$ plane is also illustrated in both closed (left) and open (right) position.

The r -sensors are made of concentric semicircular strips (4×512 strips) centered on the nominal LHC beam position. In order to minimize the occupancy, each strip is subdivided into four 45 deg regions. The minimum pitch at the innermost radius is of 32 μm , increasing linearly to 101.6 μm at the outer radius.

The ϕ -sensors are subdivided into two regions, inner and outer, with 683 and 1365 strips, respectively. This allows to avoid unacceptably high strip occupancies in the innermost edge and too large strip pitch at the outer edge of the sensor. A skew of 20° (10°) is introduced in the inner (outer) region to improve pattern recognition, with reversed skew between the inner and the outer regions. Furthermore, the modules are placed so that adjacent ϕ -sensors have opposite skew with respect to each other,

achieving a traditional *stereo* configuration.

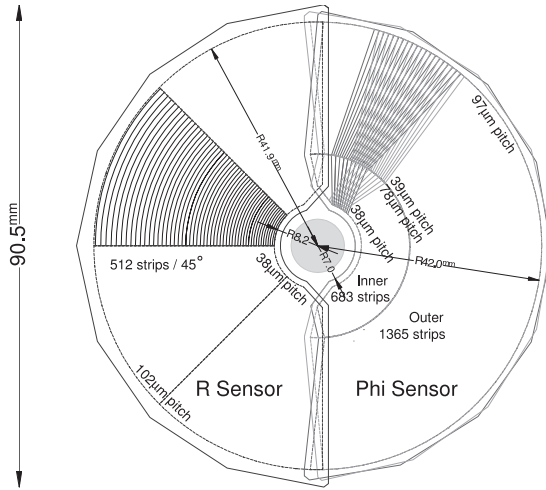


Figure 3.12. Schema of the $r\phi$ geometry of the VELO sensors, only showing one portion of the strips. In the ϕ -sensor (right), strips of two adjacent modules are shown to highlight the stereo angle.

The track definition within the LHCb acceptance ($1.6 < \eta < 4.9$) requires hits in at least three modules and are reconstructed with the polar coordinates collected in these modules. The spatial resolution on the primary vertex depends on the number of tracks, but on average it is found to be $\sim 42 \mu\text{m}$ on the z -axis direction and $\sim 10 \mu\text{m}$ in the $r - \phi$ plane.

3.3.2. Dipole Magnet

The trajectory of a charged particle is bent in the presence of a magnetic field, and thus the ratio between its electric charge and its momentum ($q/|\vec{p}|$) can be computed. Hence, the LHCb dipole magnet is used to measure the momentum of charged particles, covering a forward acceptance of ± 250 mrad vertically and ± 300 mrad vertically.

A warm magnet design was adopted over that in [96] due to budget and time reasons [103, 108, 109], with saddle-shaped coils in a window-frame yoke with sloping poles in order to match the required detector acceptance. The two identical coils, which weigh 54 tons, are of conical saddle and are placed mirror-symmetrically to each other in the 1500-ton magnet yoke. Each coil consists in of fifteen pancakes arranged in five triplets and produced of pure Al-99.7 hollow conductor in an annealed state. The full magnet schema can be found in Fig. 3.13.

The design of a magnet with an integrated magnetic field of 4 Tm for tracks of 10 m length had to accommodate two contrasting needs: on one hand, the need of a field level inside the RICHs envelope of less than 2 mT, and on the other hand a field as high as possible in the regions between the VELO and the TT. Furthermore, in order to achieve the required momentum resolution for charged tracks, the magnetic field integral $\int B(l) dl$ must be measured with a precision of a few millimeters. The final magnetic field, superimposed on the LHCb schema, is found in Fig. 3.14.

3. The LHCb experiment

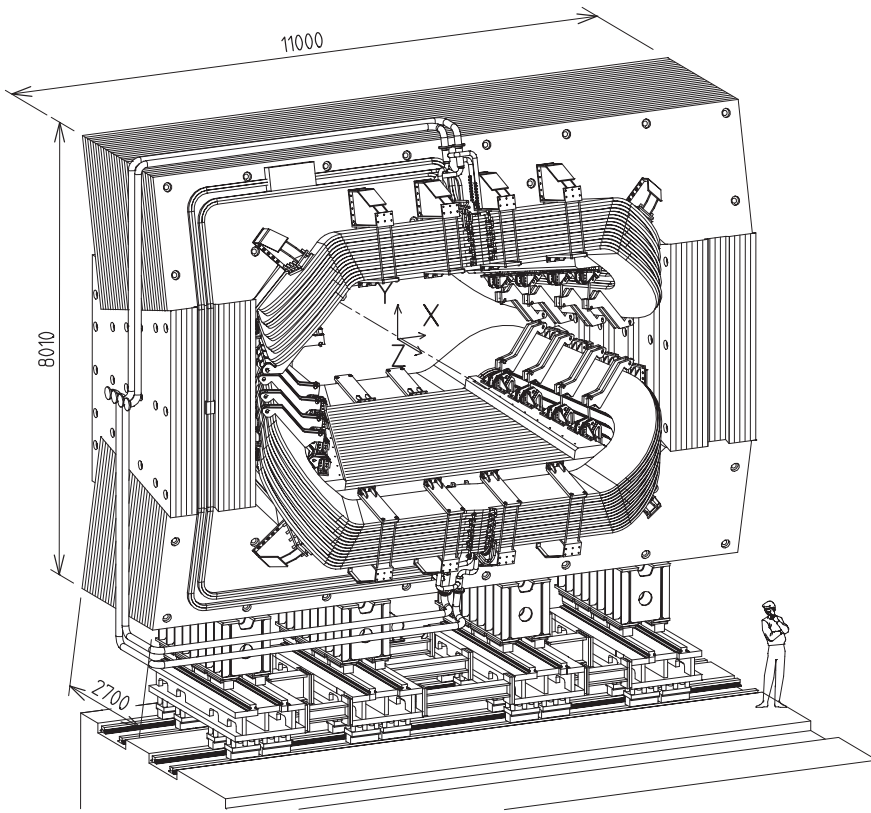


Figure 3.13. Perspective of the LHCb dipole magnet with its current and water connections.

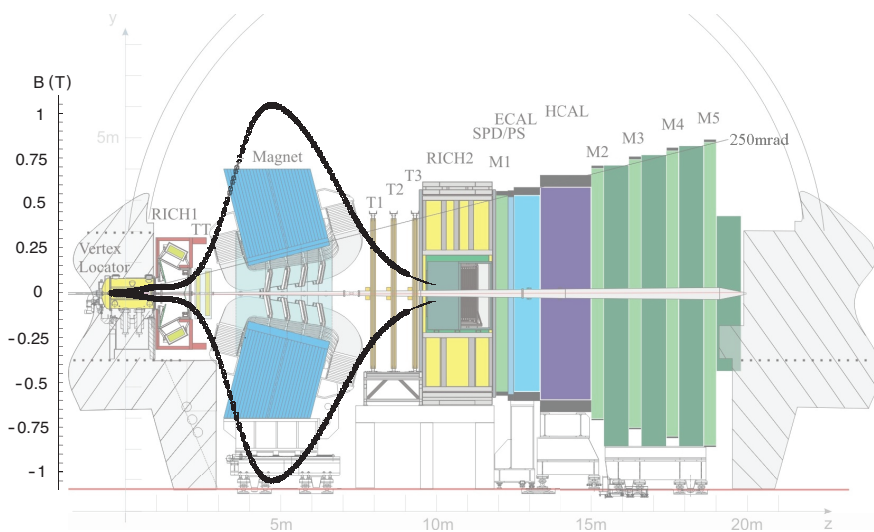


Figure 3.14. The magnetic field along the z -axis, superimposed on the LHCb layout.

3.3.3. Silicon Tracker

The ST is made up of two detectors: the Tracker Turicensis, located upstream of the dipole magnet and covering the full LHCb acceptance, and the Inner Tracker [101], a cross-shaped region located at the center of the three tracking stations T1–T3, downstream the magnet. Both the TT and IT detectors use microstrip sensors with a strip pitch of about 200 μm . Furthermore, each of the four ST stations has four detection layers in an x - u - v - x arrangement with vertical strips in the first and last layers and strips rotated by a stereo angle of -5° and $+5^\circ$ in the second and third layers (see Fig. 3.15a), respectively.

Tracker Turicensis

The TT is a 150 cm wide and 130 cm high planar tracking station placed just before the magnet with four layers that cover the full LHCb acceptance. It has an active area of 8.4 m^2 with more than 140k readout strips of up to 38 cm in length. To aid track reconstruction algorithms, the four detection layers are arranged in two pairs, (x, u) and (v, x), that are separated approximately 27 cm along the z -axis.

Each detection layer is composed by half-modules that cover half the height of the LHCb acceptance, as shown in Fig. 3.15a. A module, shown in Fig. 3.15b, consists of a row of seven silicon sensors organized into either two or three readout sectors. The regions above and below the beampipe are covered by one such half module each. The regions to the sides of the beampipe are covered by rows of seven (for the first two detection layers) or eight (for the last two detection layers) 14-sensor long full modules. Furthermore, adjacent modules within a detection layer are staggered by about 1 cm in z and overlap by a few millimeters in x to avoid acceptance gaps and to facilitate the relative alignment of the modules. In the u and v detection layers, each module is individually rotated by the respective stereo angle.

A sensor is 500 μm thick, 9.64 cm wide and 9.44 cm long. It carries 512 readout strips with a pitch of 183 μm .

With a maximal strip occupancy of $\sim 3.5\%$ in the region close to the beampipe, the TT has a spatial resolution of about 50 μm .

Inner Tracker

The IT covers a 120 cm wide and 40 cm high cross shaped region at the center of the T1–T3 stations, located after the dipole magnet. Each of the three IT stations consists of four individual detector boxes arranged around the beampipe as shown in Fig. 3.16a.

The detector boxes are light tight, and electrically and thermally insulated, with a temperature below 5°C inside them. Each detector box contains four detection layers and each detector layer consists of seven detector modules. Adjacent modules are staggered by 4 mm in z and overlap by 3 mm in x to avoid acceptance gaps and to facilitate the relative alignment of the modules.

Detector modules in the boxes above and below the beampipe consist of a single 320 μm thick silicon sensor and a readout hybrid, while detector modules in the boxes to the left and right of the beampipe consist of two 410 μm thick silicon sensors and a readout hybrid (see Fig. 3.16b). Different widths of the sensors have been chosen to ensure sufficiently high signal-to-noise ratios while minimizing the material budget

3. The LHCb experiment

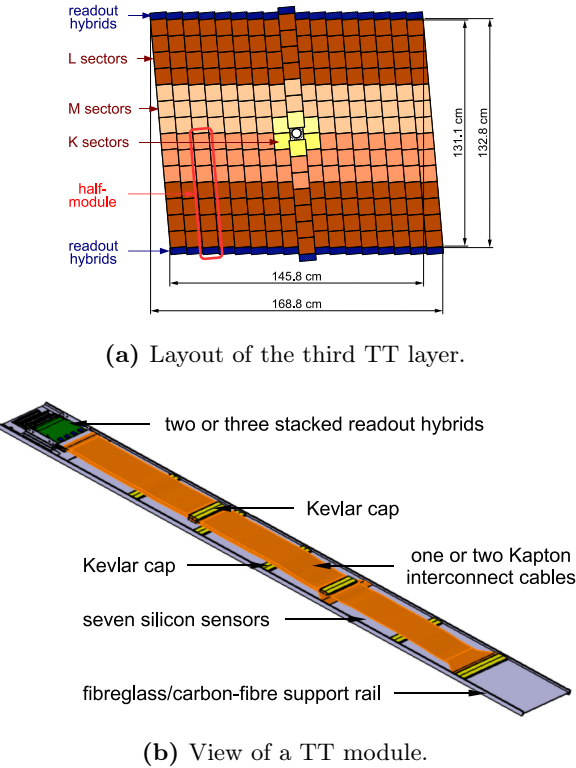


Figure 3.15. Views of the Tracker Turicensis detector.

of the detector. The sensors are 11 cm long and 7.6 cm wide, and contain 384 silicon strips with a pitch of 198 μm .

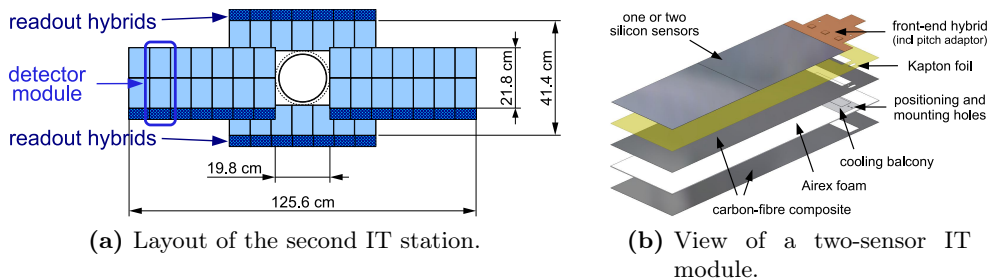


Figure 3.16. Views of the Inner Tracker detector.

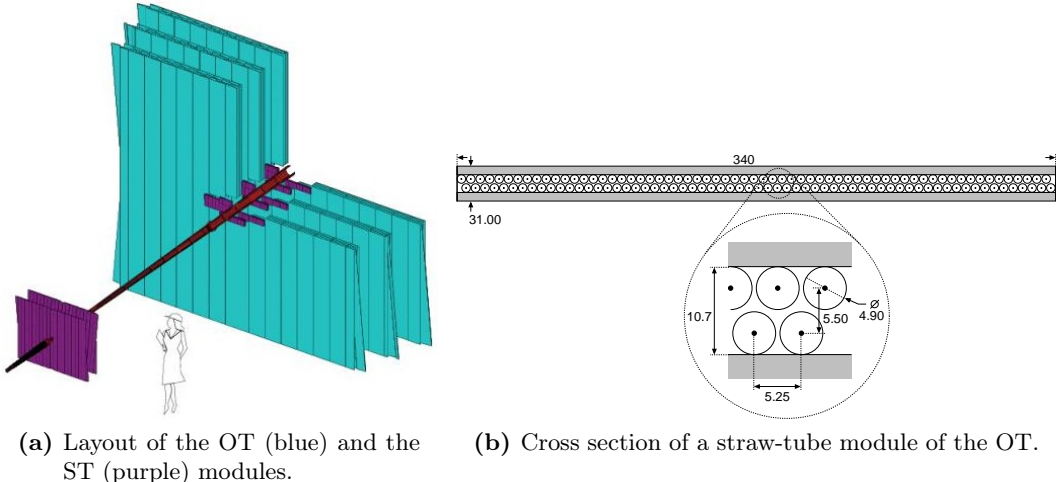
The Inner Tracker has a spatial resolution of about 57 μm .

3.3.4. Outer Tracker

The OT is a drift-time detector [102] for the tracking of charged particles and the measurement of their momentum over a large acceptance area in the outer region of the LHCb detector. Each module contains two staggered monolayers of drift-tubes with inner diameters of 4.9 mm, shown in Fig. 3.17b. A mixture of Argon (70%) and

CO_2 (30%) is chosen as a counting gas in order to guarantee a drift time below 50 ns and a drift-coordinate resolution of 200 μm .

The detector modules are arranged in three stations, as shown in Fig. 3.17a, located in the T1–T3 trackers and surrounding the IT stations. Each of the OT stations consists in four layers, arranged in a x - u - v - x geometry: modules in the x -layers are oriented vertically, whereas those in the u and v layers are tilted by $\pm 5^\circ$, respectively. The total active area of a station is $5971 \times 4850 \text{ mm}^2$ covering all the LHCb acceptance not covered by the IT stations.



(a) Layout of the OT (blue) and the ST (purple) modules. (b) Cross section of a straw-tube module of the OT.

Figure 3.17. Views of the Outer Tracker detector.

The Outer Tracker has a spatial resolution of about 200 μm .

3.3.5. Track reconstruction

The LHCb track reconstruction consists in combining the hits in the VELO, the TT, the OT and the IT detectors to form particle trajectories from the interaction region to the calorimeters, regardless of their origin. Depending on their trajectories through the tracking system, the following classes of tracks, illustrated in Fig. 3.18, are defined:

Long tracks cross the full tracking system from the VELO to the T stations. These have the most precise momentum determination and therefore are the most commonly used set of tracks for physics analyses.

Upstream tracks transverse only the VELO and the TT stations. These are low momentum tracks that are bent out of acceptance by the magnetic field, and usually have poor momentum resolution. However, they may generate Cherenkov photons in the RICH1 and maybe used for background studies in the RICH particle identification algorithms.

Downstream tracks only transverse the TT and T stations. They are relevant in the cases of long-lived particles which decay outside the VELO, such as K_s^0 and Λ .

VELO tracks are measured in the VELO only and are usually large angle or backward tracks, useful for primary vertex reconstruction.

T-tracks are only measured in the T stations, and are typically produced in secondary interactions. They are useful for global pattern recognition in RICH2.

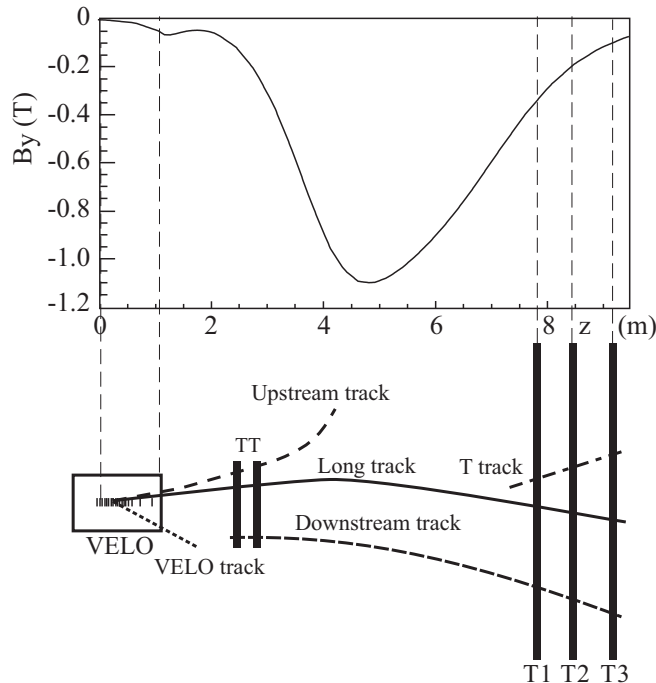


Figure 3.18. Schematic illustration of the various types of tracks: long, upstream, downstream, VELO and T tracks. The B_y magnetic field component responsible for their bending is plotted for reference.

The track reconstruction starts with a search for track *seeds*, the initial track candidates, in the VELO and the T stations where the magnetic field is low. These track seeds, the so-called *VELO track seeds* and *T track seeds*, should be almost aligned. After tracks have been found, their trajectories are refitted with a Kalman filter in order to account for multiple scattering and correct for dE/dx energy loss. This algorithm then tries to associate hits in the other parts of the tracking system to form track candidates. The quality of the reconstructed tracks is monitored by the χ^2 of the fit and the pull distribution of the track parameters.

The performance of the tracking algorithm has been evaluated on a Monte Carlo (MC) sample of $B^0 \rightarrow J/\psi K_s^0$ events in terms of two quantities [91]:

Reconstruction efficiency is defined as the fraction of the possible reconstructible tracks that have been actually reconstructed. To be considered as *reconstructed*, a track must have at least 70% of its associated hits coming from the same single MC particle.

Ghost rate is the fraction of the tracks reconstructed with hits that do not correspond to a single particle.

The efficiency to reconstruct a long track from a particle with a momentum larger than $10 \text{ GeV}/c$ is on average $\sim 94\%$. The corresponding average ghost fraction is $\sim 9\%$, but most ghost tracks have a low reconstructed p_T .

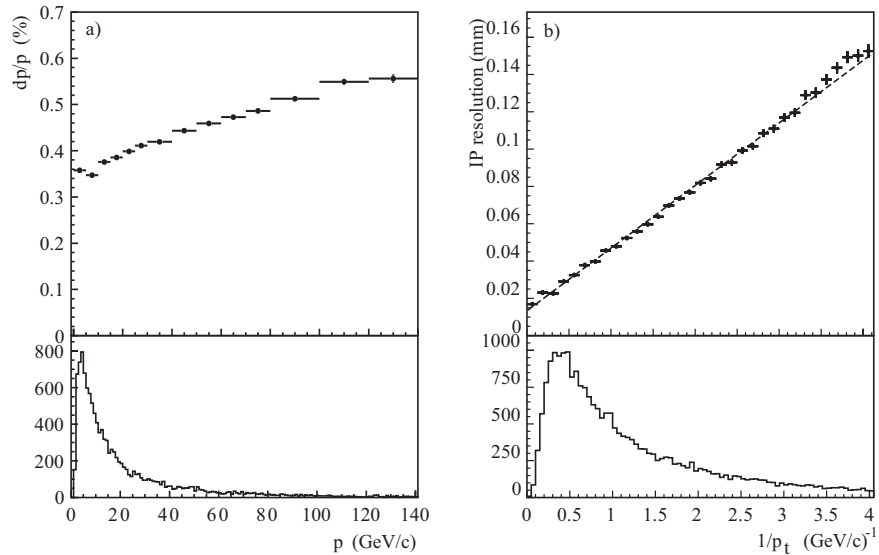


Figure 3.19. Momentum (left) and IP (right) resolution as a function of track momentum and $1/p_T$, respectively. For comparison, the p and p_T spectra of B decay particles is shown in the lower part of the plots.

Another measure of the performance of the LHCb tracking system is the resolution of the momentum and the *impact parameter* — the perpendicular distance between the track and its PV— of the reconstructed long tracks, which are shown in Fig. 3.19:

- The momentum resolution increases from $\delta p/p = 0.35\%$ for low momentum tracks to $\delta p/p = 0.55\%$ for tracks in the high end of the spectrum.
- The impact parameter (IP) resolution can be parametrized as

$$\delta_{\text{IP}} = 14 \mu\text{m} + \frac{35 \mu\text{m}}{p_T} \quad (p_T \text{ in } \text{GeV}/c) \quad (3.4)$$

The efficiency of upstream track finding for particles with $p > 1 \text{ GeV}/c$ is $\sim 75\%$, with a corresponding ghost rate of 15%. The momentum resolution is very poor, $\delta p/p = 15\%$, due to the small value of the total magnetic field integral in the track region.

The efficiency of finding downstream tracks with $p > 5 \text{ GeV}/c$ is $\sim 80\%$, with a corresponding ghost rate of 15%. Since downstream tracks transverse most of the magnetic field, their momentum resolution is relatively good with $\delta p/p = 0.43\%$ for pions originating from K_S^0 decays.

K_S^0 candidates are reconstructed through their decay to $\pi^+ \pi^-$. For K_S^0 from $B^0 \rightarrow J/\psi K_S^0$ decays, about 25% decay inside the active region of the VELO, 50% decay outside the active region of the VELO but upstream of TT, and the rest decay after TT, and will therefore be difficult to reconstruct. The K_S^0 decaying outside (inside) the VELO are reconstructed using pairs of oppositely charged downstream (long) tracks. The corresponding mass plots for MC are shown in the left part of Fig. 3.20.

The prompt K_S^0 production in $6.8 \pm 1.0 \mu\text{b}^{-1}$ in pp collisions at $\sqrt{s} = 0.9 \text{ TeV}$ was the first paper published by LHCb [110], thanks to the excellent performance of

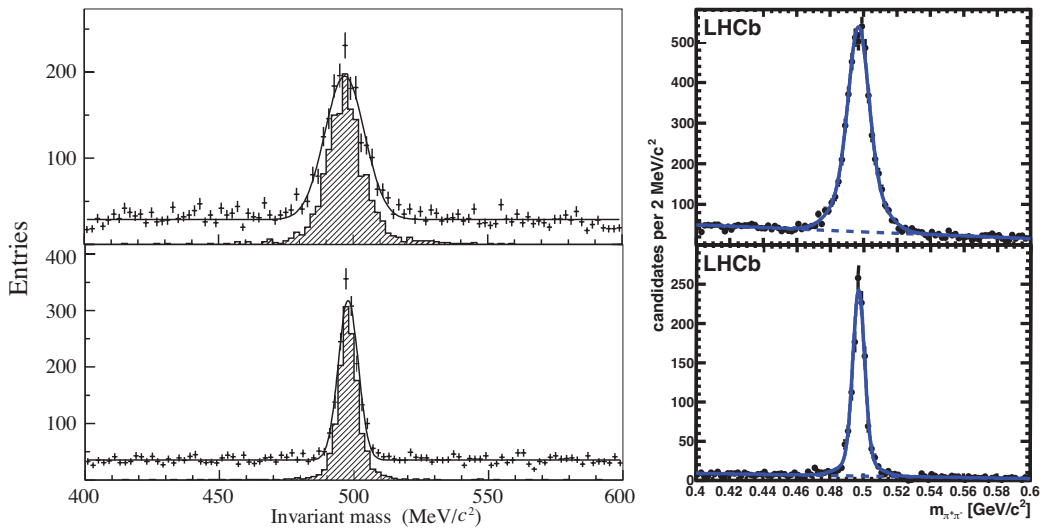


Figure 3.20. Reconstruction of $K_s^0 \rightarrow \pi^+\pi^-$ using downstream-downstream tracks (up) and long-long tracks (bottom). The used data samples are $B^0 \rightarrow J/\psi K_s^0$ MC (left) and 2009 data at $\sqrt{s} = 0.9$ TeV (right)

the tracking system. The downstream-downstream and long-long mass plots are shown in the right of Fig. 3.20, and show very good agreement with the corresponding plots from MC.

3.4. The Particle Identification System

In order to reconstruct and tag b -hadrons with the best efficiency and accuracy the LHCb experiment needs excellent Particle IDentification (PID).

The purpose of the Particle Identification system is to provide a means of distinguishing the different particle types that are produced in b -hadron decays by collecting information from the detectors shown in Fig. 3.21: two Ring Imaging Cherenkov counter detectors RICH1 and RICH2 (described in §3.4.1), the Calorimeters (detailed in §3.4.2), and the Muon Detector at the far end of the detector (see §3.4.3).

3.4.1. Ring Imaging Cherenkov Detectors

It is essential for the physics goals of the LHCb experiment to separate pions from kaons in selected B decays. LHCb uses Ring Imaging Cherenkov Detectors (RICH), which use the Cherenkov effect [111] to distinguish these two mesons. When a charged particle crosses a medium with a speed v greater than the speed of light in that medium, c/n , it emits electromagnetic radiation. Cherenkov photons are emitted within a cone whose aperture angle θ is given by

$$\cos \theta = \frac{c}{n \cdot v} = \frac{1}{\beta \cdot n} \quad (3.5)$$

Since the momentum spectrum at large polar angles is softer than at small polar angles, the particle identification system uses two RICH detectors with different radiators to cover the full momentum range (see Fig. 3.22).

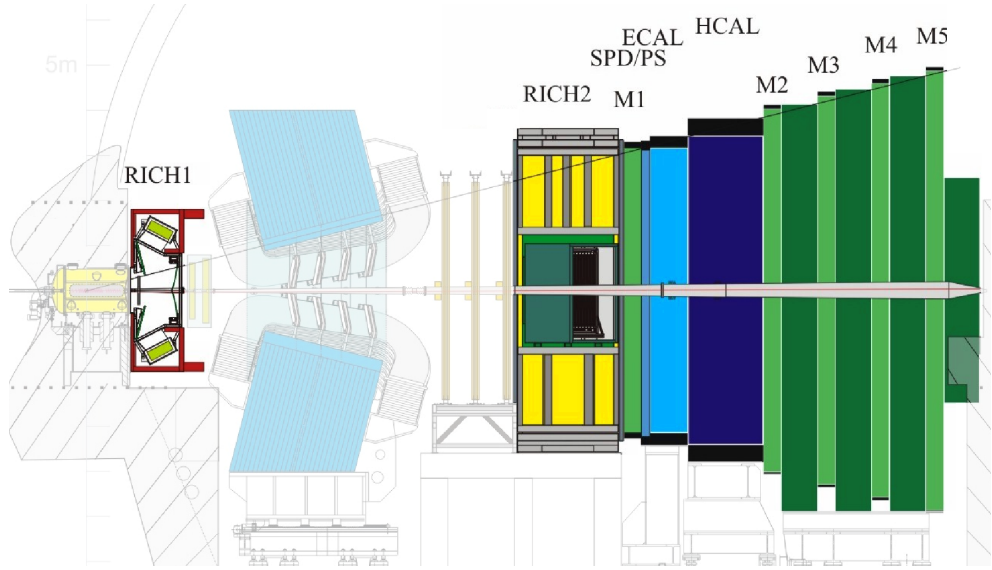


Figure 3.21. The PID System of the LHCb detector.

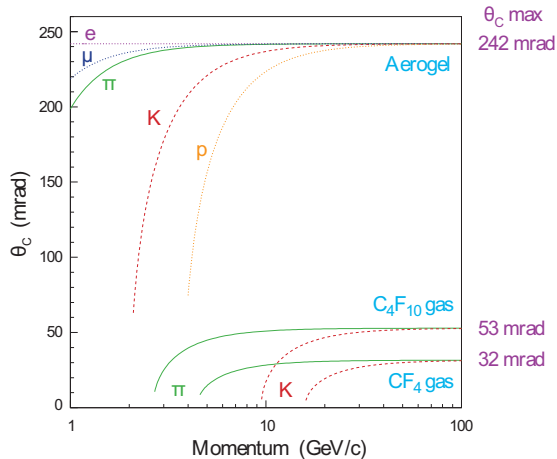


Figure 3.22. Cherenkov angle θ_C versus particle momentum for the RICH radiator materials.

The RICH1 detector [104, 112] is located upstream of the magnet, at the end of the VELO, covering the full LHCb acceptance. It covers the low momentum range, from $1\text{ GeV}/c$ to $60\text{ GeV}/c$ with the use of a C_4F_{10} ($n = 1.0014$) gas radiator and aerogel ($n = 1.03$). Its schematic view can be seen in Fig. 3.23a.

The RICH2 detector [104, 113], is located downstream of the magnet, between the T Stations and the SPD/PS, and has a limited angular acceptance of $\sim \pm 15$ mrad to ± 200 mrad in the bending plane and ± 100 mrad in the non-bending plane. RICH2 is designed to separate charged particles with a momentum between ~ 15 GeV/c and 100 GeV/c, and thus its coverage is limited to the inner region where high momentum particles are produced. It uses CF₄ as radiator, which has a tunable refractive index n between 1.01 and 1.10. The RICH2 side view can be found in Fig. 3.23b.

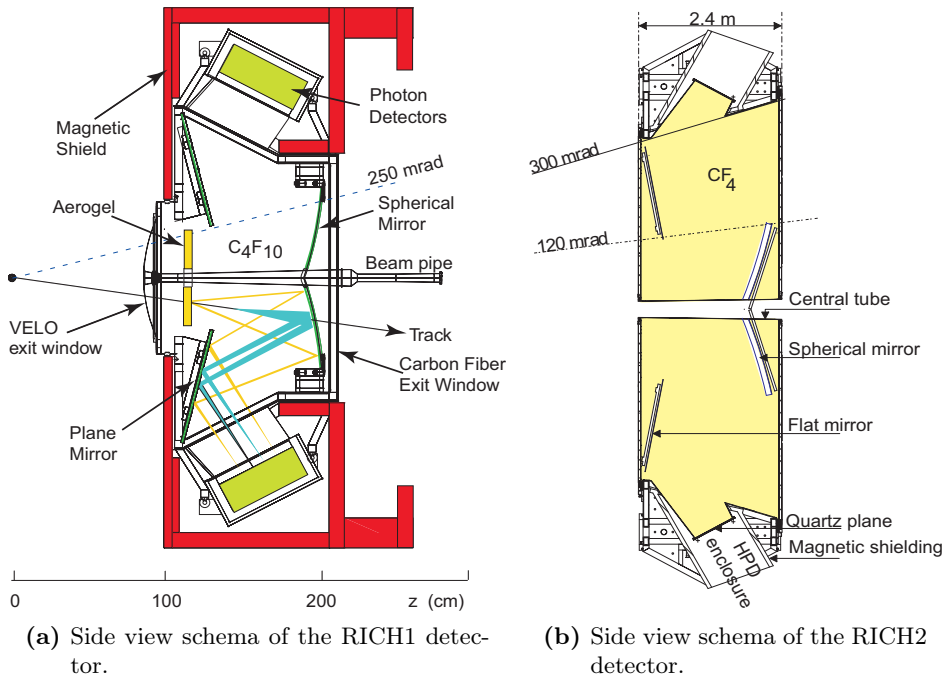


Figure 3.23. The RICH detectors at LHCb.

In both RICH detectors the focusing of the Cherenkov light is accomplished using a combination of spherical and flat mirrors to reflect the image out of the spectrometer acceptance. This light is captured using Hybrid Photon Detectors (HPDs), which capture the Cherenkov photons in the wavelength range of 200–600 nm. The 196 HPDs of RICH1 and the 288 HPDs of RICH2 are isolated from the magnetic field and have 1024 pixels each. On average, a charged particle with $n\beta > 1$ produces 6.7 Cherenkov photons in aerogel, 30.3 in the C_4F_{10} and 21.9 in the CF_4 .

The information from the HPD pixels is used to reconstruct the light cones from the Cherenkov radiation, and this information is used by the particle identification algorithms explained in §3.4.4 to distinguish between the different types of charged particles going through the RICH detectors. A typical (simulated) LHCb event in RICH1 is shown in Fig. 3.24, in which the reconstructed rings can be clearly identified.

3.4.2. The Calorimeter

The LHCb Calorimeter [105] is used for particle identification of electrons, photons and hadrons, as well as for their energy and position measurement. Accurate reconstruction of π^0 and prompt photons is essential in the study of radiative B decays, and also in flavor tagging. Furthermore, the calorimeter is in charge of selecting high transverse energy hadron, electron and photon candidates for the Level-0 trigger (L0, see §3.5.1), which makes a decision 4 μs after the interaction.

The Calorimeter is composed of the pad/preshower Detector (SPD/PS), the Electromagnetic CALOrimeter (ECAL) and the Hadronic CALOrimeter (HCAL), as shown in Fig. 3.21.

The use of the calorimeter in the L0 trigger imposes strong constraints on its design:

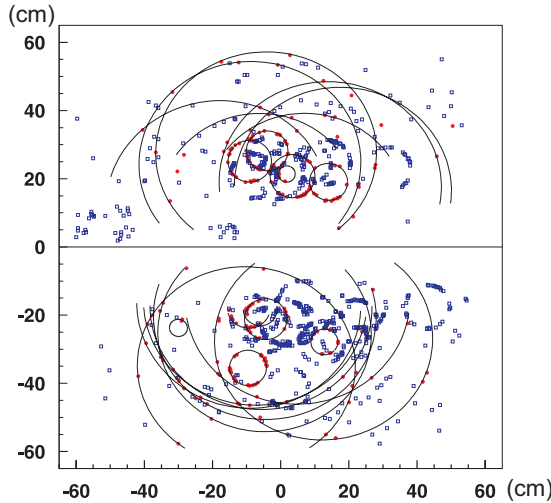


Figure 3.24. Simulation of a typical LHCb event in RICH1.

- For the separation of the electromagnetic and hadronic particles —mainly electrons from charged pions— the longitudinal profile of the electromagnetic showers constitutes an excellent factor of discrimination. For that purpose a preshower detector (PS) is located in front of the ECAL just after a layer of lead absorber.
- In order to provide good rejection of background π^0 with high E_T in the L0 electron trigger, the Scintillating Pad Detector (SPD) is located just before the layer of lead in front of the PS. Furthermore, the SPD is used to provide an estimate of the number of charged tracks at the L0 level.
- The segmentation is approximately projective in the direction of the interaction point to get a fast evaluation of the trigger candidates.

The SPD/PS, ECAL and HCAL have variable lateral segmentation (shown in Fig. 3.25) to avoid a large range of cell occupancy, as the hit density varies by two orders of magnitude as a function of the distance to the z -axis. A segmentation into three different sections with different cell sizes was chosen for the ECAL, and projectively for the SPD/PS. Given the dimensions of hadronic showers, the HCAL is segmented in two zones with larger cell sizes.

All the calorimeter subdetectors are based on the same basic concept: scintillating light is transmitted to PhotoMultiplier Tubes (PMT) by wavelength-shifting (WLS) fibers. The single fibers for the SPD/PS cells are read out using MultiAnode Photo-Multiplier Tubes (MAPMT), while the fiber bunches in the ECAL and HCAL require individual phototubes. In order to have a constant transverse energy (E_T) scale over the whole detector acceptance, the gain in the ECAL and HCAL phototubes is set as a function of their distance to the beampipe. Furthermore, since the light yield delivered by the HCAL modules is a factor 30 less than that of the ECAL, the HCAL tubes operate at a higher gain.

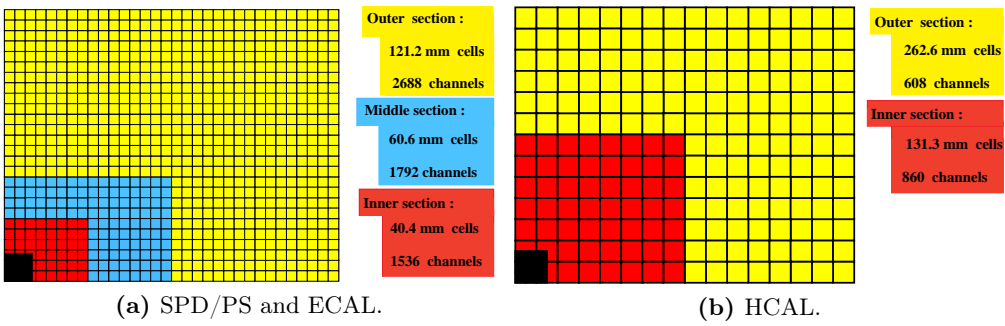


Figure 3.25. Transverse segmentation of the LHCb Calorimeters.

The Pad/Preshower detector

The Pad/Preshower (SPD/PS) detector consists of a 15 mm, $2.5 X_0$ thick, lead converter sandwiched between two almost identical planes of rectangular scintillator pads of high granularity—the SPD before the lead layer, and the PS after—with a total of 12032 detection channels. The sensitive area of the detector is 7.6 m wide and 6.2 m high, and the centers of the two scintillator planes are separated by 56 mm. In order to achieve a one-to-one projective correspondence with the ECAL segmentation (see Fig. 3.25a), each of the subdetectors is subdivided into inner (1536 cells), middle (1792 cells) and outer (2688 cells) sections with approximately 4×4 , 6×6 and 12×12 cm 2 cell dimensions, with the SPD cells being smaller than those of the PS by $\sim 0.45\%$.

The SPD is used to separate photons from electrons at the L0 trigger by making use of the fact that it is a binary—and therefore very fast—detector. Charged particles deposit energy in the scintillator material, while neutral particles do not interact. The amount of deposited energy is converted to a binary 0 or 1 depending on a cell-by-cell threshold value set to minimize photon misidentification while keeping good charged particle identification. Misidentification comes mainly from photon conversion in the material before the SPD, but also can come from interactions in the SPD that produce charged particles inside it, and backwards moving charged particles, the so-called *backsplash*, that are generated in the lead absorber or in the ECAL. Test beams showed that photons arriving at the SPD with an energy between 20 and 50 GeV have a misidentification probability of 0.8% when applying a threshold of 0.7 Minimum Ionizing Particles (MIPs).

The distinction between charged pions and electrons is done by making use of the electromagnetic shower dispersion measured in the PS. Test beam results show that with a threshold of 4 MIPs, charged pion rejection factors of 99.6%, 99.6% and 99.7% with electron retentions of 91%, 92% and 97% are achieved for 10, 20 and 50 GeV/c momentum particles, respectively.

The Electromagnetic CALorimeter

The ECAL thickness, $25 X_0$, was chosen so it would contain the full electromagnetic shower of high energy incoming photons in order to ensure optimal energy resolution. The choice of using shashlik calorimeter technology, *i.e.*, a sampling scintillator/lead structure read out by plastic WLS fibers perpendicular to the scintillator, was made

taking into account modest energy resolution, fast response time, acceptable radiation resistance and the reliability of this technology, used in other experiments such as HERA-B or PHENIX. Its design energy resolution is given by

$$\frac{\sigma_E}{E} = \frac{10\%}{\sqrt{E}} \oplus 1\% \quad (E \text{ in GeV}) \quad (3.6)$$

where the first term is the statistical fluctuation of the shower while the second comes from the systematic uncertainties of the calibration.

The ECAL is placed at 12.5 m from the interaction point. Its dimensions match projectively those of the tracking system, $\theta_x < 300$ mrad and $\theta_y < 250$ mrad, but its inner acceptance is limited to $\theta_{x,y} > 25$ mrad due to the substantial radiation dose level in that region. Since the ECAL was designed for b -hadron physics, the maximum transverse energy per cell was limited by the possible gain applied to the PMTs and is optimized for $0 < E_T < 10$ GeV. Measures of E_T beyond this point are saturated.

The energy resolution and the uniformity of the ECAL were studied at the calorimeter test beam [114]. Module response was found to be uniform within 8%. The energy resolution was also studied, and the results are shown in Fig. 3.26. The experimental curve was parametrized as

$$\frac{\sigma_E}{E} = \frac{a}{\sqrt{E}} \oplus b \oplus \frac{c}{E} \quad (3.7)$$

where a , b and c stand for the stochastic, constant and noise terms respectively. Depending on the module type and the test beam conditions the stochastic and constant terms were measured to be $8.5\% < a < 9.5\%$ and $b \sim 0.8\%$, in good agreement with the design resolution in Eq. 3.6.

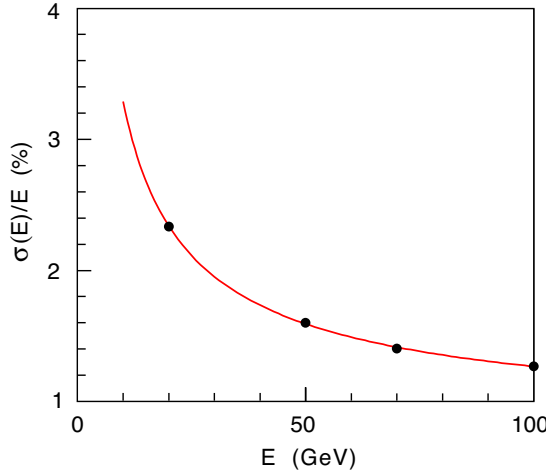


Figure 3.26. Energy resolution as measured in the test beam with electrons on a surface of $(\pm 15 \text{ mm}, \pm 30 \text{ mm})$ in an outer module.

The performance of each of the cells of the ECAL can be slightly different, and they may suffer aging at different rates. Therefore, it is necessary to regularly perform a calibration procedure to obtain a set of calibration coefficients, one per cell, in order to provide the best possible operation from the whole calorimeter.

In a first calibration stage, the energy flow technique [115] allows to even out the differences between neighboring cells by making use of the smoothness of the sum of

transverse energy depositions in the calorimeter. While this method allows to achieve a 5% calibration level, it cannot provide a global energy scale for the calorimeter energy.

Starting from the energy flow calibration constants, the decay of resolved neutral pions into two photons is used to iteratively attain a calibration level of 2%, including a global energy scale [116]. Still, this method doesn't allow to calibrate the calorimeter at high energies, since for $E_T > 3 \text{ GeV}$ all π^0 are merged. Also starting from the energy flow calibration constants, the E/p ratio of electrons, where E is the calorimeter energy and p is the particle momentum measured by the tracking system, has also been used to achieve a fine calibration up to higher energies than the π^0 method.

Hadronic CALorimeter

The HCAL is used mainly for trigger and particle identification. It is a sampling device made from iron and scintillating tiles, as absorber and active material respectively. The special feature of this sampling structure is the orientation of the scintillating tiles that run parallel to the beam axis (see Fig. 3.27). In the lateral direction tiles are interspersed with 1 cm of iron, while in the longitudinal direction the length of tiles and iron spacers corresponds to the hadron interaction length in steel.

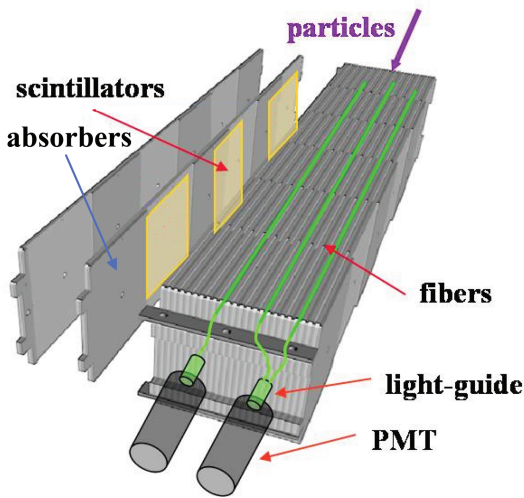


Figure 3.27. Schematic of the HCAL internal cell structure. The exploded view of two scintillator-absorber layers illustrates the elementary structure of an HCAL module.

The overall HCAL structure is built at a distance of 13.33 m from the interaction point, with dimensions of 8.4 m in height, 6.8 m in width and 1.65 m in length. Due to limited space in the cavern, the HCAL thickness is only $5.6 X_0$, which is not enough for containing the full hadronic shower. Therefore, it gives only an estimation of the hadron energy with a design resolution of

$$\frac{\sigma_E}{E} = \frac{80\%}{\sqrt{E}} \oplus 10\% \quad (E \text{ in GeV}) \quad (3.8)$$

It is segmented transversely into square cells of 131.3 mm (inner) and 262.6 mm (outer), as illustrated in Fig. 3.25b.

The energy resolution and uniformity of the HCAL were measured at the calorimeter test beam [114]. From a lateral scan of a particle beam across the prototype front surface the uniformity in response was measured to be well within $\pm 3\%$. Test beam results for energy resolution were compared with expected results from different software packages for the simulation of the hadronic shower development, as illustrated in Fig. 3.28. The resolution extracted from a fit to the data at several energies is

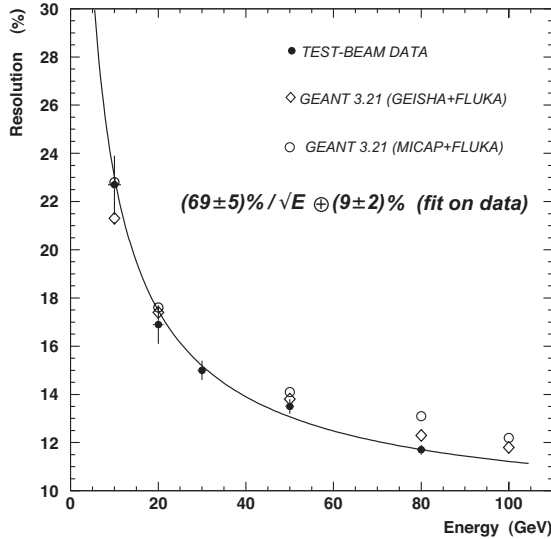


Figure 3.28. Energy resolution as measured in the test beam with $50\text{ GeV}/c$ pions, as well as for three different hadronic simulation codes.

$$\frac{\sigma_E}{E} = \frac{(69 \pm 5)\%}{\sqrt{E}} \oplus (9 \pm 2)\% \quad (E \text{ in GeV}) \quad (3.9)$$

also in agreement with the design values.

3.4.3. Muon Detector

Muon triggering and offline muon identification are fundamental requirements of the LHCb experiment. Muons are present in the final states of many CP -sensitive B decays, such as $B^0 \rightarrow J/\psi(\mu^+\mu^-)K_s^0$ and $B_s^0 \rightarrow J/\psi(\mu^+\mu^-)\phi$, and also play a major role in CP asymmetry and oscillation measurements in semileptonic decays, in which the muon can be used to provide the tag of the initial flavor of the accompanying B meson. Furthermore, muons are involved in rare B decays such as the flavor-changing neutral current $B_s^0 \rightarrow \mu^+\mu^-$, which could provide a hint to new physics beyond the Standard Model [84].

The muon detector provides fast information for the high- p_T muon trigger at the Level-0, and muon identification for the High Level Trigger (HLT, see §3.5.2) and offline analysis.

Muons have a long lifetime $\tau_\mu \approx 2.2\,\mu\text{s}$, which means $c\tau_\mu \approx 659\,\text{m}$, and a low interaction probability, and thus they fly through the whole detector. Therefore, muon chambers are installed at the end of the detector, where all other possible charged particles have been filtered. The muon detector, shown in Fig. 3.29, is composed of

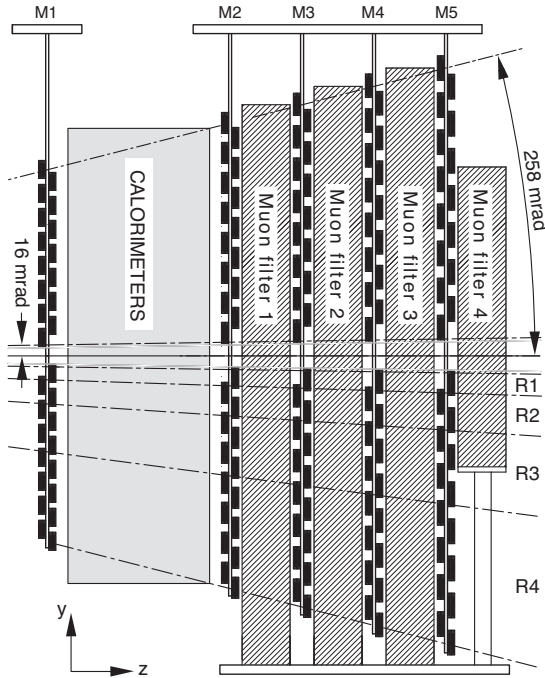


Figure 3.29. Side view of the muon chambers location, with the calorimeter between the M1 and M2–M3.

five stations, M1–M5, of rectangular shape, with a total of 1380 chambers covering a total area of 435 m^2 . The inner and outer angular acceptances of the muon detector are 20 (16) mrad and 306 (258) mrad in the bending (non-bending) plane, respectively, resulting in an acceptance of about 20% for muons from inclusive b semileptonic decays. The geometry of the stations is projective, so all their transverse dimensions scale with the distance to the interaction point.

The five muon stations consist of Multi-Wire Proportional Chambers (MWPC) with their planes perpendicular to the beam axis. Station M1 is located in front of the calorimeters and is used to improve the p_T measurement in the trigger. Stations M2–M5 are placed downstream the calorimeters and are interleaved with iron absorbers 80 cm thick to select penetrating muons. The minimum momentum of a muon to cross M1–M5 is $6\text{ GeV}/c$ since the total absorber thickness of M1–M5 and the calorimeter is ~ 20 interaction lengths.

The detectors provide space point measurements of the tracks, and binary information is passed on by partitioning the detector into rectangular *logical pads* whose dimensions define the x , y resolution. These are shown in Fig. 3.30. The muon trigger is based on standalone muon track reconstruction and p_T measurement and requires aligned hits in all five stations. Stations M1–M3 are used to rapidly ($< 25\text{ ns}$) define the track direction with a design efficiency of 95%, and to calculate the p_T of the muon candidate with a resolution of 20%. Stations M4 and M5 have limited spatial resolution, and their main purpose is the identification of very penetrating particles.

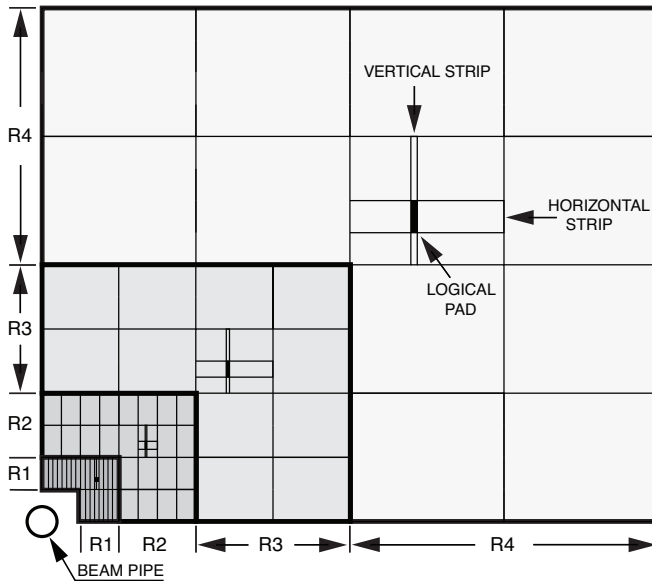


Figure 3.30. Front view of a quadrant of a muon station, with logical pads marked as dark rectangles.

3.4.4. Particle Identification

Each particle type has a different signature in the LHCb detector, as illustrated in Fig. 3.31. The information from the two RICH detectors, the calorimeters and the muon detector is combined for the identification of charged particle types (e , μ , π , K , p), while neutral particles (γ and π^0) are identified using the ECAL.

For each type of charged particle, the different particle identification contributions are combined into a log-likelihood difference (DLL) between a given PID hypothesis and the pion hypothesis. The DLL for a particle of type a is then given by

$$\text{DLL}_a = \Delta \ln \mathcal{L}_{a\pi} = \ln \mathcal{L}_a - \ln \mathcal{L}_\pi = \ln \left[\frac{\mathcal{L}_a}{\mathcal{L}_\pi} \right], \quad (3.10)$$

where \mathcal{L}_a is the combination of the information of the various subdetectors used for the identification. Therefore, the DLL between two particle hypotheses a and b is given by

$$\text{DLL}_{ab} = \Delta \ln \mathcal{L}_{ab} = \Delta \ln \mathcal{L}_{a\pi} - \Delta \ln \mathcal{L}_{b\pi} = \ln \left[\frac{\mathcal{L}_a}{\mathcal{L}_b} \right], \quad (3.11)$$

Hadron identification

Particle identification with the RICH is performed by an algorithm based on a log-likelihood approach which matches the observed pattern of hit pixels in the photodetectors to that expected from the reconstructed tracks under a given set of particle hypotheses [117]. The likelihood is maximized by varying the particle hypothesis of each track in turn, through electron, muon, pion, kaon and proton. This method, which considers all found tracks in the event and all three RICH radiators simultaneously, is referred to as *global pattern-recognition*. Its output is a best hypothesis for each track,

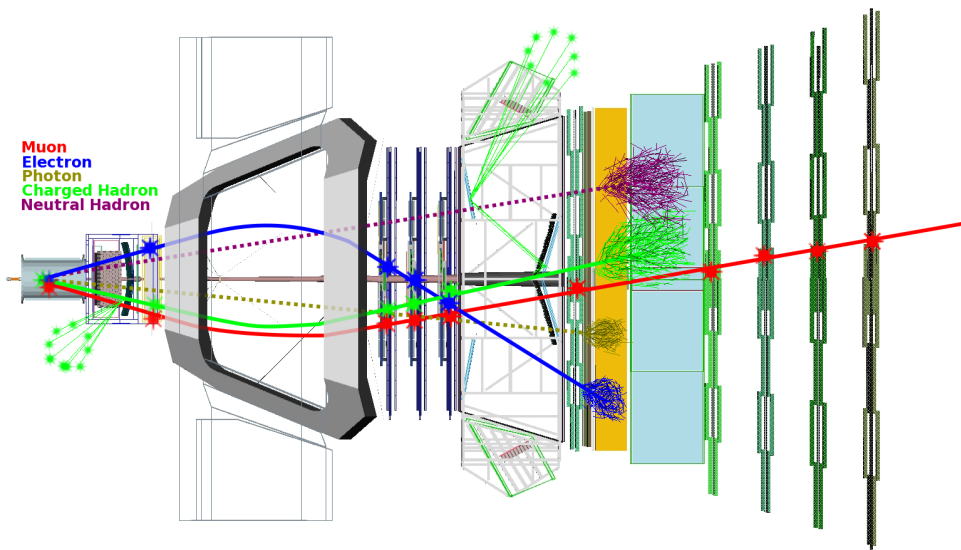


Figure 3.31. Schematic view of the different particle signatures in the LHCb detector, with corresponding hits in the tracking system and muon stations, rings in the RICH and showers in the calorimeter.

and the decrease in log-likelihood when changing from this best hypothesis to another one.

For physics analyses and detector diagnostics the performance of the RICH particle identification algorithms must be understood independently of simulation studies. The dominant $D^{*+} \rightarrow D^0(K^+\pi^-)\pi^+$ decay (and its complex conjugate) provides a very high statistics unbiased sample of pions and kaons that can be used to measure the RICH performance (see §5.6.7).

The RICH system provides excellent particle identification over the entire momentum range. The average efficiency for kaon identification for momenta in the $2 - 100 \text{ GeV}/c$ is $\sim 95\%$, with an average pion misidentification rate of $\sim 5\%$. The RICH performance has been studied both on MC and data, and the results can be compared in Fig. 3.32 [118, 119].

Muon identification

Muon identification is performed by extrapolating well reconstructed tracks with $p > 3 \text{ GeV}/c$ —particles with $p < 3 \text{ GeV}/c$ do not reach the M2–M5 detectors—into the muon stations. In order to be selected as a muon, a track must be matched to hits in a number of muon stations that depend on its momentum [120, 121], as illustrated in Table 3.2. Around 50% of muons with $p > 3 \text{ GeV}/c$ arrive to the M3 station. A hit is considered to match a track if it is within a Field Of Interest (FOI) around the extrapolation in the M2–M5, parametrized as a function of momenta for each station and region.

Using a Monte Carlo sample of $B^0 \rightarrow J/\psi K_s^0$ the muon identification efficiency was measured to be $\epsilon(\mu \rightarrow \mu) \sim 94\%$, with a corresponding misidentification $\epsilon(\pi \rightarrow \mu) \sim 3\%$. The efficiency is a flat function of the momentum above $10 \text{ GeV}/c$.

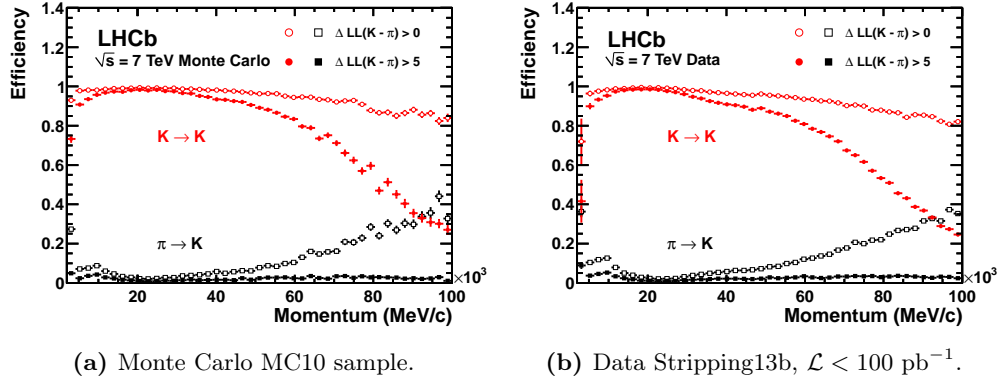


Figure 3.32. Kaon/pion separation as a function of the particle momentum.

Track momentum (GeV/c)	Required stations
$3 < p < 6$	M2+M3
$6 < p < 10$	M2+M3+(M4 or M5)
$p > 10$	M2+M3+M4+M5

Table 3.2. Stations required to have a hit within FOI for tracks at different momentum ranges.

For each track, two likelihoods, one for the muon and one for the non-muon hypothesis, are built using information from the tracking system and the muon stations. These likelihoods are built from the comparison of slopes in the muon detector and the tracking, and from the average track-hit distance of all hits in FOI associated to the track. Then the log-likelihood difference $DLL_{\mu\pi}$ is determined, and summed with the values from the RICH and calorimeter systems (if available). By doing this the pion misidentification rate can be reduced to $\sim 1\%$, while maintaining a muon efficiency of $\sim 93\%$ for muons above $3 \text{ GeV}/c$.

The high purity that can be achieved with such cuts is illustrated in one of the early results of the LHCb collaboration [122]. In the early stages of the experiment, with an integrated luminosity of $\mathcal{L} = 5.2 \text{ pb}^{-1}$, the J/ψ cross section was measured by building $J/\psi \rightarrow \mu^-\mu^+$ taking oppositely charged pairs of tracks that pass the muon identification requirements. The J/ψ mass peak is reconstructed with a resolution of $12.3 \pm 0.1 \text{ MeV}/c$, as shown in Fig. 3.33.

Electron Identification

Electron identification [123] is performed using a combination of $\Delta \ln \mathcal{L}_{e/\text{non-}e}^{\text{calo}}$ based on the information of different subdetectors:

ECAL. All reconstructed tracks in the event are extrapolated to the ECAL plane and an all-to-all matching with the reconstructed clusters is performed. A χ^2_γ is constructed based on the distance of the extrapolated tracks and the clusters, and it is used to discriminate between charged and neutral clusters. A χ^2_e estimator is build and minimized using the matching between the corrected barycenter

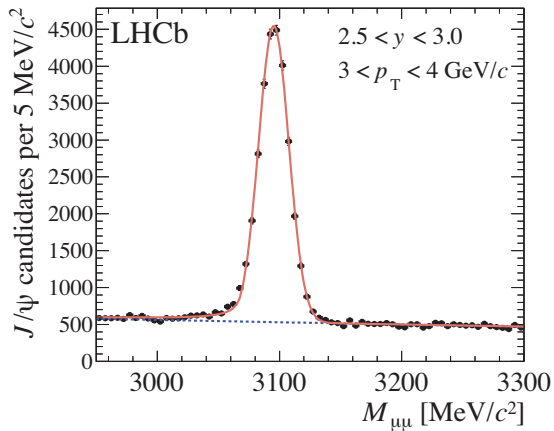


Figure 3.33. Dimuon mass distribution for the $3 < p_T < 4 \text{ GeV}/c$ and $2.5 < y < 3$ bin obtained with 5.2 pb^{-1} of data from the 2010 LHC run. The mass resolution is $12.3 \pm 0.1 \text{ MeV}/c$.

position of the cluster with the extrapolated track impact point, as well as on the balance of track momentum and energy of the charged cluster in the ECAL, shown in Fig. 3.34a. For each track the difference of log likelihood for electron and non-electron hypotheses, $\Delta \ln \mathcal{L}_{e/h}^{ECAL}$, is computed by using reference two-dimensional histograms of $\tanh \chi_e^2$ versus $\tanh p$.

PS. Since the PS detector is placed just after $2.5 X_0$ of lead absorber, a significant part of electrons start an electromagnetic shower in it, while hadrons and muons are visible as minimum ionizing particles (MIP), as illustrated in Fig. 3.34b. The log likelihood for electron and non-electron hypotheses $\Delta \ln \mathcal{L}_{e/h}^{PS}$ is computed in a similar manner as $\Delta \ln \mathcal{L}_{e/h}^{ECAL}$, on a basis of two-dimensional distributions of $\tanh E_{PS}$ versus $\tanh p$.

HCAL. Due to the thickness of ECAL, very small leakage of the electromagnetic shower into HCAL is expected. Therefore, the energy deposited in the HCAL along the particle trajectory can be used to compute $\Delta \ln \mathcal{L}_{e/h}^{HCAL}$, based on a two-dimensional distribution of $\tanh E_{HCAL}$ versus $\tanh p$.

Bremsstrahlung. Since there is no material in the region of magnetic field, the electron can emit Bremsstrahlung photons only before or after the region with sizeable magnetic field. The position of possible Bremsstrahlung photons can be predicted by a linear extrapolation of the reconstructed track segment before the magnet to an ECAL face plane. The distance of this prediction and the corrected barycenter position of all reconstructed photons can be used to build a χ^2_{brem} , which is minimized and used as a discriminating variable. $\Delta \ln \mathcal{L}_{e/h}^{\text{brem}}$ is built based on a two-dimensional $\tanh \chi^2_{\text{brem}}$ versus $\tanh p$ distribution.

In the same simulated $B^0 \rightarrow J/\psi K_S^0$ sample used for muon identification efficiency studies, efficiency is measured to be $\epsilon(e \rightarrow e) \sim 95\%$, with a corresponding misidentification $\epsilon(\pi \rightarrow e) \sim 0.7\%$.

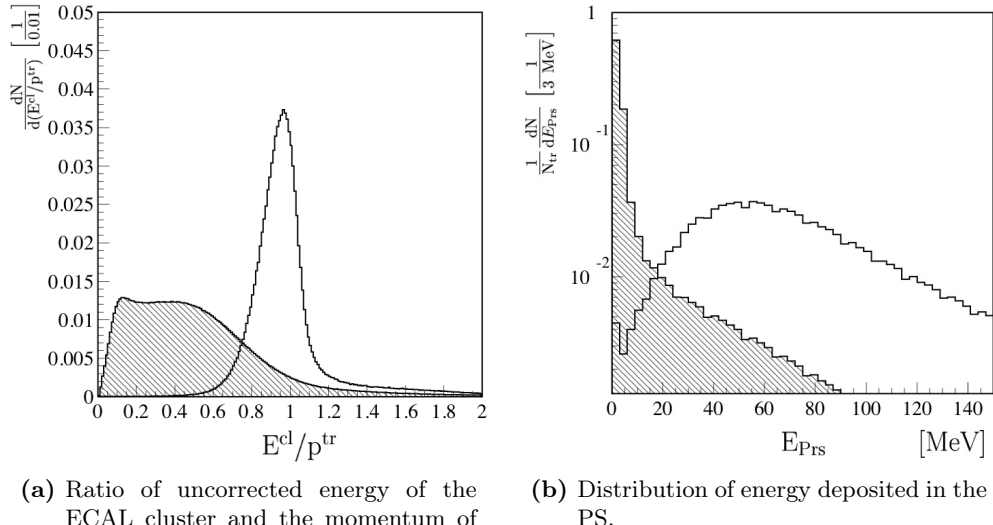


Figure 3.34. Comparison of main electron PID discriminating variables for (a) ECAL and (b) PS, for electrons (open histogram) and hadrons (shaded histogram).

Neutral Particle Identification

Neutral particles in the detector are identified according to their isolation with respect to charged tracks [124] by using the χ^2_γ described above.

Neutral clusters are associated with photons. *Converted* —photons that produced an e^+e^- pair before the PS lead absorber—and *unconverted* photons are distinguished using SPD information by analyzing the number of hits in the SPD cells in front of the ECAL cluster.

Neutral pions decay into a pair of photons. Below a transverse energy of $E_T < 2.5 \text{ GeV}$, π^0 are mostly reconstructed as a resolved pair of separated photons, and thus are called *resolved* π^0 . However, a large fraction of photon pairs coming from high energy π^0 cannot be resolved as a separate pair of clusters given the ECAL granularity. These are called *merged* π^0 .

Resolved π^0 are reconstructed by looping over the photon candidates with $E_T > 200 \text{ MeV}$, pairing them and comparing their invariant mass with the nominal π^0 mass. The π^0 identification efficiency strongly depends on the transverse momentum: on the lower p_T side, because of the minimum E_T cut in the photons, necessary in order to reduce the huge combinatorial background; on the upper p_T spectrum, because high- p_T π^0 are more likely to be merged and therefore are not identified by this pairing method. The good performance of the resolved π^0 identification is illustrated in Fig. 3.35, where the invariant mass of $\pi^0 \rightarrow \gamma\gamma$ for the first data in 2009 shows a clear π^0 peak with a very good resolution.

The procedure to reconstruct merged π^0 consists in splitting each cluster in two interleaved subclusters and iteratively recalculating the energy of each of the subclusters using the expected transverse energy shape of photon showers. The identification is performed by requiring that the π^0 energy is compatible with a pair of merged photons,

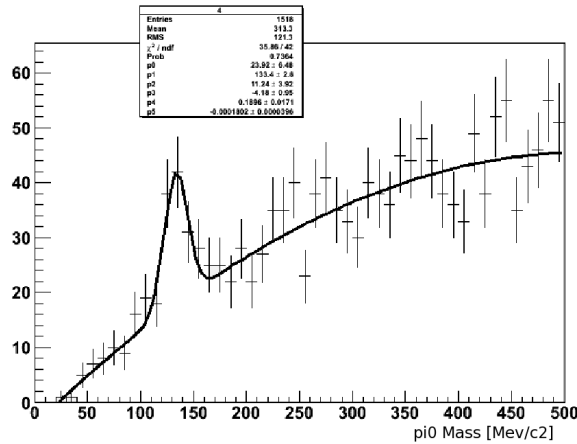


Figure 3.35. Invariant mass of $\pi^0 \rightarrow \gamma\gamma$ for November 2009 data. A peak at $133 \pm 3 \text{ MeV}/c^2$, with $\sigma = 11 \pm 4$, can be clearly distinguished.

i.e., the distance between the two photons is kinematically allowed for π^0 , and that the invariant mass of the pair of merged photons is compatible with the π^0 mass.

The global reconstruction efficiency for π^0 that give photons inside the geometrical acceptance is summarized in Fig. 3.36.

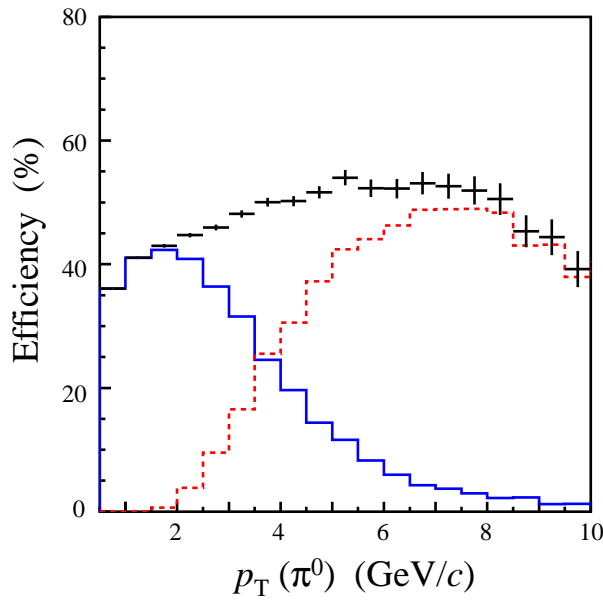


Figure 3.36. Reconstruction efficiency for π^0 decaying into photons with $E_{\text{T}} > 200 \text{ MeV}$ versus the π^0 transverse momentum for resolved (solid blue) and merged (dashed red) π^0 .

3.5. The Trigger System

The rate of visible pp interactions, defined as those collisions that produce at least two charged particles with enough hits in the VELO and T1–T3 to allow them to be reconstructible, is too high to store all of them. The trigger system aims to reduce

this high rate of visible collisions to a rate of events at which they can be written to storage for offline analysis, selecting those of higher interest for the physics goals of the experiment.

While the rate of visible interactions that contain $b\bar{b}$ pairs is about 1/200 of the total visible interaction rate, only 15–20% of them contain at least one B meson with all its decay products inside the detector acceptance. Furthermore, the branching ratios of the key B decays used in CP violation studies are typically below 10^{-3} . Triggering criteria must keep the largest fraction possible of the events necessary for offline analysis, while keeping the background event rate as low as possible.

An important feature of the LHCb trigger system is its flexibility. The number of interactions per bunch crossing at the design configuration was expected to be dominated by single interaction due to the relatively low LHCb luminosity of $2 \times 10^{32} \text{ cm}^{-2}\text{s}^{-1}$, which facilitates triggering and reconstruction due to low channel occupancy. In this case, a visible interaction rate of 10 MHz has to be reduced by a factor 5000, down to 2 kHz. However, as it has been explained in §3.1, the running conditions in 2010 and 2011 have been substantially different than those considered in the design of the trigger system: running at $3.5 \times 10^{32} \text{ cm}^{-2}\text{s}^{-1}$ with a low β^* , the experiment is not dominated by single interactions and the visible collision rate is 12–15 MHz; this causes the event size to become larger than designed, further changing the trigger working conditions and the storage requirements. The LHCb trigger has been able to adapt remarkably well to these significant modifications of its running conditions thanks to its flexibility, and has provided excellent performance throughout the data taking periods of 2010 and 2011. The output of the trigger in 2011 has been 3 kHz of very clean samples of b and c decays, exceeding the design value of 2 kHz. The output of the trigger planned for 2012 is ~ 4.5 kHz.

The trigger system is divided in two levels [125], shown in Fig. 3.37: the Level-0 Trigger (L0), detailed in §3.5.1, and the High Level Trigger (HLT), described in §3.5.2. The L0 uses custom electronics operating synchronously with the 40 MHz bunch crossing frequency, while the HLT is executed asynchronously on a processor farm, the Event Filter Farm, made up with commercially available equipment.

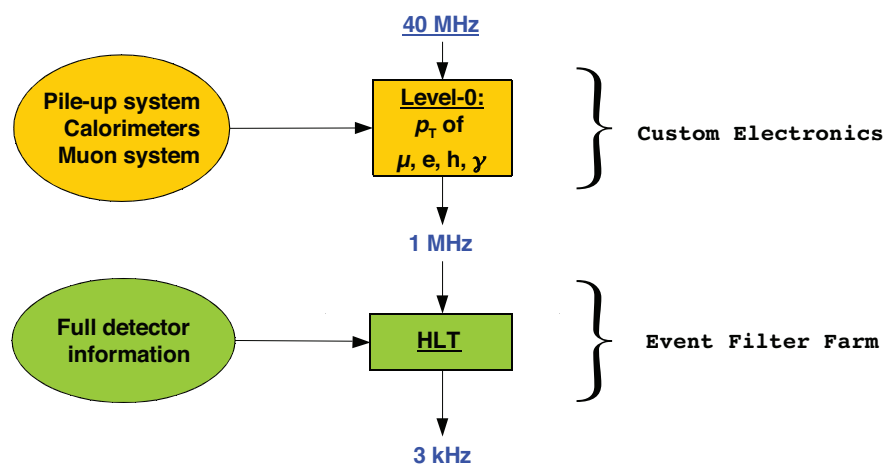


Figure 3.37. Schema of the event flow in the LHCb trigger system.

3.5.1. Level-0 Trigger

The first level of trigger (Level-0) is designed to reduce the visible event rate to the 1 MHz at which the whole detector can be read out. It is implemented using custom made hardware, running synchronously with the LHC clock. Since B meson decay products are usually particles with a large transverse momentum and transverse energy, high p_T and E_T objects constitute a very clear signature to trigger on. Therefore, the Level-0 trigger focuses on the reconstruction of:

- The highest E_T hadron, electron and photon clusters in the calorimeters.
- The two highest p_T muons in the muon chambers.

Furthermore, events with high particle multiplicity are rejected in order to reduce the processing time in the HLT.

The Level-0 Trigger is subdivided in three components: the L0 calorimeter trigger, the L0 muon trigger and the pile-up system. Each component is connected to one detector and to the Level-0 Decision Unit (L0 DU), which collects the information provided by the three L0 components to produce a final decision as a logical OR of its inputs.

The L0 DU has to release its decision 4 μs after each collision, which corresponds to the buffer length implemented in the front-end read-out chips. Furthermore, the time-of-flight of the particles, plus the cable delays, plus the front-end electronics delay leave only 2 μs for processing the data in the L0 DU and delivering a decision.

The L0 Calorimeter Trigger looks for high E_T electron, photon, neutral pion or hadron candidates. It forms clusters by summing the E_T of 2×2 cells and selects those which have the highest E_T . Then the information from the SPD/PS, ECAL and HCAL is combined to tag the clusters as electron, photon or hadron. In addition, the total E_T in the HCAL is used to reject crossings without any visible interaction and to reject events triggered by halo muons.

The total number of cells of the SPD which have a hit is used to evaluate the charged track multiplicity and to reject high occupancy events. In 2010, events with more than 900 hits in the SPD were rejected in order to keep the OT occupancy at $\sim 20\%$ and allow a good performance. In 2011, the running conditions allowed to lower the SPD multiplicity cut 600 hits, as a balance between the calorimeter occupation, the muonic triggers and the output rate.

The L0 Muon Trigger uses a fast stand-alone reconstruction of muon tracks with a $\sigma p_T \sim 20\%$. A track is found if hits in the five muon chambers can form a straight line pointing to the interaction region. The two highest- p_T muon candidates of each quadrant of the muon chambers are selected for the decision.

The Pile-Up System was designed to distinguish between single interactions from multiple ones. Four r -sensors, similar to the ones used in the VELO, are located before the interaction region to measure the radial position of the backward tracks. Since the average number of interactions in 2010 and 2011 is higher than one, and therefore the collected events are not dominated by single interactions, this system is currently only used to trigger beam-gas interactions.

3.5.2. High Level Trigger

The High Level Trigger (HLT) filters events using a software application. It uses the Online Event Filter Farm (EFF), which contains up to 20,000 CPU cores, to process and reduce the rate at which events are kept down to $\sim 3\text{ kHz}$.

The high rate of incoming events from the Level-0 Trigger and the computing power limitation of the EFF do not allow the up-front use of the full event data information in the decision-making process. Thus, the HLT is divided in two stages: the first stage (HLT1) uses only a partial reconstruction to reduce the rate by a factor of ~ 20 so that the second stage (HLT2) is able to perform full event reconstruction to further discriminate signal events.

HLT1

The HLT1 is designed to minimize the impact of varying running conditions on its performance. It is based around a single track trigger [126], which searches for a single track with high momentum, a large impact parameter with respect to all primary vertices in the event, and a good track quality. In addition to this, lifetime unbiased muon [127] and electron triggers are used for analyses which are sensitive to the presence of lifetime biases. These latter triggers are based around the confirmation of the L0 trigger decision by matching tracks reconstructed in the HLT to the objects used in the L0 decision, *i.e.*, muon segments or calorimeter clusters.

HLT1 takes $\sim 15\text{ ms}$ to process a L0-accepted minimum bias event, and accepts $\sim 5\%$ of such events with an efficiency of more than 80% on signal events for most of LHCb’s benchmark B decay modes [126, 127]. The $\sim 50\text{ kHz}$ selected by HLT1 are passed to HLT2.

HLT2

The HLT2 input rate is sufficiently low to perform an almost-full-offline reconstruction, the main difference being that in the HLT2 only tracks with $p_{\text{T}} > 500\text{ MeV}/c$ and $p > 5000\text{ MeV}/c$ are reconstructed. Having fully reconstructed events allows the HLT2 trigger lines to use event selection criteria more in line with those used in offline analyses. Furthermore, Global Event Cuts (GEC), such as the reconstructed track multiplicity, are used to reject complex events which require a big amount of processing time.

The HLT2 trigger is made up of a mixture of inclusive, which search for generic B decay features such as displaced vertices or dilepton pairs, and exclusive trigger lines, which select specific decays using similar selections to those used offline. In 2011 [128], $\sim 1/3$ of the bandwidth was taken by the inclusive topological trigger [129], which allows to obtain a high efficiency and low background retention on almost all n -body B decays. Muon triggers, which select high- p_{T} single or dimuons, used up about another third of the bandwidth. Charm decays accounted for $\sim 1/3$ of the HLT2 bandwidth, while the rest was used by several exclusive lines, such as the radiative lines [130], and inclusive lines such as the ϕ trigger [131].

3.6. The Online System

The job of the Online system is to ensure the transfer of data from the front-end electronics of the LHCb detector to permanent storage in a known and controlled fashion [107, 132]. This involves moving the data themselves, and the configuration and monitoring of all operational parameters of the detector, such as temperatures, voltages and pressures. Furthermore, the Online system must ensure the proper synchronization of all detector channels, both among themselves and with the LHC clock.

The Online System can be divided into three different subsystems, illustrated in Fig. 3.38: the Data Acquisition System (DAQ), the Timing and Fast Control System (TFC) and the Experiment Control System (ECS).

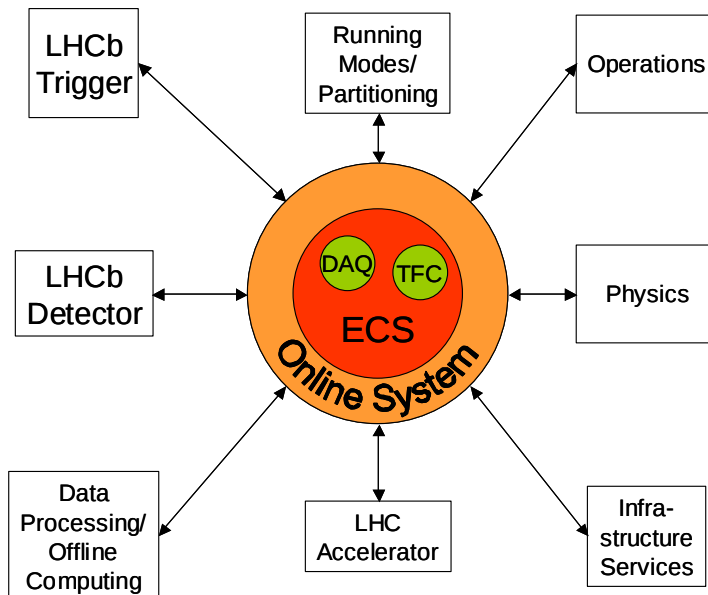


Figure 3.38. Architecture of the Online System

3.6.1. Data Acquisition System

The goal of the Data Acquisition (DAQ) system is the transport of the L0-accepted data belonging to a given bunch crossing from the detector front-end electronics to permanent storage.

In order to construct a reliable and robust system, several basic principles were observed in its design: simplicity, scalability, usage of point-to-point links to connect components, and usage of commercial off-the-shelf products wherever possible. Furthermore, the adopted design is flexible enough to cope with possible new requirements, motivated by experience with real data.

Data arrive to the front-end electronics (on/near-detector electronics) and are buffered to LHCb-wide standardized readout boards (TELL1) [133], which are placed outside the irradiated area, using optical or analog links. All subdetector DAQ systems use the TELL1 board, aside from the RICH, which use the UKL1 boards, with a very similar functionality to the TELL1. These boards make use of *Field Programmable Gate Arrays* (FPGA) technology and are designed to use simple protocols, a small

number of components, and are able to react to changing system parameters. The data are zero-suppressed, compressed, packed, buffered and sent via Gigabit-Ethernet links to the Event Builder, which collects the data coming from all the subdetectors for a single event. These data are sent forward to the HLT, that selects which events—corresponding to physically interesting interactions—are sent to permanent storage. The storage system has a capacity of ~ 40 TB, which offer enough buffer space to cope with possible interruptions of the transfer of the data to permanent storage at CERN. Gigabit-Ethernet is used throughout the Online system as link technology.

3.6.2. Timing and Fast Control System

The TFC system is in charge of driving all stages of the data readout of the LHCb detector between the front-end electronics and the Event Filter Farm by distributing the beam-synchronous clock, the L0 trigger, synchronous resets and fast control commands. The system is a combination of electronics components common to all LHC experiments and LHCb custom electronics. It is formed by three main parts: the TFC distribution network transmits the beam synchronous clock, featuring a low-latency trigger channel and a second channel used to encode control commands; the optical throttle network is used to transmit a trigger inhibit from the asynchronous parts of the readout system to the Readout Supervisor in case of congestion of the data path; the Readout Supervisor (ODIN), the most important part of the system, implements the interface between the LHCb trigger and the readout chain, synchronizing trigger decisions and beam-synchronous commands to the LHC clock. Furthermore, the Readout Supervisor is able to perform load balancing among the nodes in the EFF by dynamically selecting the destination node for the incoming events, and to provide a wide variety of auto-triggers for calibration and test purposes.

3.6.3. Experiment Control System

The Experiment Control System (ECS) ensures the control and monitoring of the entire LHCb detector, including traditional detector control domains, such as voltages, temperatures, gas flows, or pressures, and the trigger, TFC and DAQ systems. The LHCb ECS is based on the PVSS II [134, 135], a commercial SCADA (*Supervisory Control and Data Acquisition*) system, also used in other LHC experiments, that provides features such as the management of databases, the communication between distributed components, graphical libraries and an alarm system.

The LHCb ECS is a hierarchical and distributed system which allows the control of the whole detector from the top level, but also a finer control of any given subtree, which can be released from the top control and operated in standalone mode. Commands are propagated down the hierarchy, while states and alarms go upwards. This command and state/error flow is managed using a Finite State Machine package based on SMI++ [136, 137], which allows the creation of the complex logic needed, for example, in the implementation of elaborate sequencing or automated error recovery.

3.7. Computing and resources

The LHCb computing model allows to perform an efficient processing of the collected data, an accurate alignment and calibration of the subdetectors and an efficient selec-

tion of events of interest, and also provides facilities for extracting physics results from the selected data samples. Each physics working group relies heavily on a full central processing chain from the raw data to the pre-selected reconstructed data sample used for physics analyses: individual analyses generally only deal with small samples while the manipulation of larger datasets is handled centrally by the LHCb production team.

Similar algorithms need to be executed in very different contexts, from the Online Event Filter Farm to a physicist’s laptop, and therefore a high level of standardization of the software is needed. Furthermore, the large amounts of data and of computing power needs imply that data processing must be performed in a distributed manner, taking best advantage of all resources available in computing facilities around the world. These resources (CPU and storage) are accessible through a standard set of services provided to all LHC experiments —and also to the larger HEP community and beyond— by the WLCG project [94].

3.7.1. LHCb software

The LHCb software is based on the GAUDI [138, 139] architecture, which provides an Object Oriented framework for all the applications used within the experiment [140]. It has the flexibility needed for running the LHCb chain from the Monte Carlo generation to the real data analysis using the same tools. Data persistency is based on the ROOT software [141, 142], a set of object-oriented frameworks designed to handle and analyze large amounts of data.

The main software applications used in LHCb are:

GAUSS. The validation of physics analyses or reconstruction schemes need to be performed using Monte Carlo simulation. The simulation of the physical aspects of pp collisions in the LHCb detector is handled by the GAUSS software [143, 144]. In a first step, the PYTHIA software [145] is used to simulate the proton collisions, the generated particles and their corresponding momentum four-vectors. The decays of the produced particles are handled either with PYTHIA or through an LHCb-tuned EVTGEN package [146] in the case of B hadrons, with the final state radiation handled by PHOTOS [147, 148]. The particle-detector interaction is handled by the GEANT package [149], which is used to transport the particles through the detector. Detector geometry and materials are stored in a database.

BOOLE. The BOOLE software package [150] simulates the digitization of the energy depositions in the LHCb detector and the L0 trigger. This digitization takes into account the interference from previous pp events —the *spillover*. After a BOOLE pass, the simulated and the real data can be reconstructed and analyzed using the same software.

MOORE. The MOORE package [151] is used to run the HLT in the Online System, processing real data from the LHCb DAQ system, or offline starting from real data or from the output of BOOLE. The trigger is configured via a unique key, called a Trigger Configuration Key (TCK), which defines the sequence of algorithms and their cuts. It is represented by a 32-bit number, with the lower 16 bits reserved for the L0 configuration² and the higher 16 bits for the HLT. Each of

²For simplicity purposes, when dealing with TCKs for 2010 and 2011, the first 6 bits of the L0 configuration will be omitted because they are 0, *i.e.*, TCK 0x00360032 will be referred to as 0x360032.

these TCKs needs to be processed with a specific version of the MOORE software to ensure the correct reproduction of the algorithms and configuration that was run in the Online during data taking; version details for the TCKs from Table 3.1 are summarized in Table 3.3.

TCK	MOORE version
0x00360032	v12r3
0x00480032	v12r4
0x004A0033	v12r4
0x00561710	v12r8
0x005A0032	v12r5
0x005B0032	v12r5
0x005D0033	v12r5
0x006D0032	v12r6p1
0x00700034	v12r6p1
0x00710035	v12r6p1
0x00730035	v12r6p1
0x00740036	v12r6p1
0x00760037	v12r8
0x00790037	v12r9p1
0x00790038	v12r9p1

Table 3.3. Version of MOORE used to process each of the 2011 TCKs listed in Table 3.1.

BRUNEL. The reconstruction of real or Monte Carlo events, *i.e.*, the conversion from hits and calorimetric depositions into tracks and, eventually, particles, is performed by BRUNEL [152], using the algorithms described in §3.3.5, among others. The output data are saved in ROOT-based files which can be used by analysis software.

DAVINCI. The analysis and selection tools are contained within the DAVINCI software package [153]. The particle identification algorithms, described in §3.4.4, are included in this package, as well as functions for vertex fitting. It also includes several frameworks, written both in C++ and PYTHON, that allow users to extract information from the physics events and store it in ROOT tuple format.

3.7.2. Computing resources

The LHCb computing model [140, 154] is based on a distributed multi-tier regional center model. This model includes multiple data replication and is robust against single points of failure.

A schema of the organization of the LHCb computing model can be seen in Fig. 3.39. CERN is the central production center, the Tier-0, and is responsible for distributing the raw data in quasi-real time to the Tier-1 centers: CNAF (Italy), GRIDKA (Germany), IN2P3 (France), NIKHEF/SARA (The Netherlands), PIC (Spain), RAL (United Kingdom), and CERN itself, which also takes the role of a Tier-1 center. Furthermore, there is a number of Tier-2 centers. The Tier-1 centers are responsible for

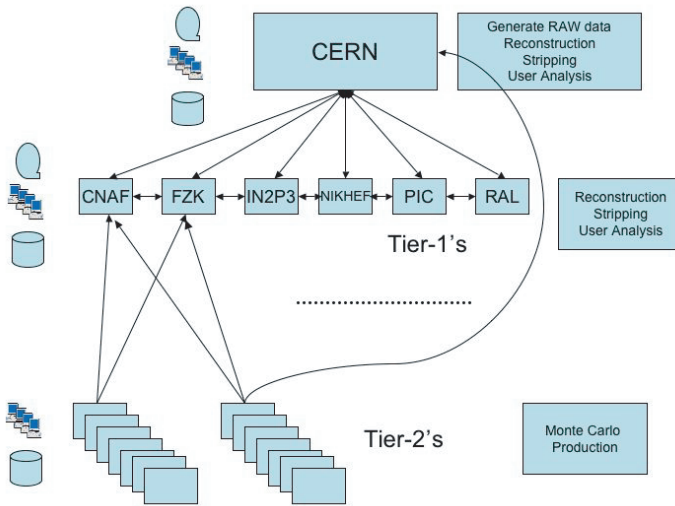


Figure 3.39. Overview of the Tier structure of the LHCb computing model.

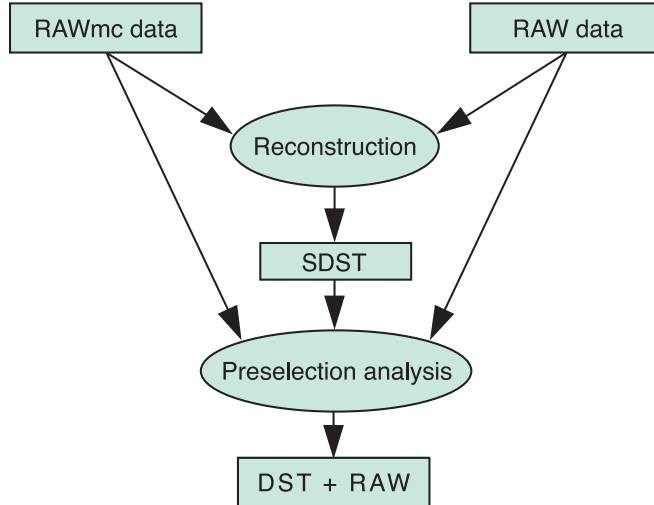


Figure 3.40. LHCb computing logical data flow model.

all the production-processing phases associated with real data, as well as user analyses. The Tier-2's are reserved for Monte Carlo simulation tasks, which have less strict storage requirements, with the Tier-1 centers acting as central repositories for the simulated data; recently they have also been used to provide extra CPU power to deal with the reprocessing of the full 2011 dataset.

3.7.3. Data flow in LHCb

The raw data of the events selected by the trigger system coming from the experiment are transferred to the CERN Tier-0 for further processing and archiving. These unprocessed data are then used to reconstruct the physical particles, made up from tracks and particle identification information, by making use of the raw information such as the hits or the calorimeter cluster energies. This reconstruction process is performed in the Tier-1's. Reconstructed events are saved in a Stripping Data Summary

Tape (SDST) file, which contains the necessary information for further event filtering without including the raw data.

The SDST files are analyzed in order to further filter events for physical analyses by making use of the full reconstructed information and with looser timing constraints than in the HLT. This sequence is known as *Stripping*, and finally produces a Data Summary Tape (DST) file, to which the raw data event information is attached. DSTs are the files accessible to scientists for physics analyses.

A summary of the data flow within the LHCb computing model is given in Fig. 3.40. The data are reprocessed several times a year with the improvement of the reconstruction, alignment and stripping software and algorithms.

4

Trigger strategies for radiative B decays at LHCb

During 2010 and 2011, the HLT2 trigger for radiative decays has been based on loose exclusive selections for the $B^0 \rightarrow K^{*0}\gamma$ and $B_s^0 \rightarrow \phi\gamma$ decays, which provide a high efficiency for signal candidates passing the selection requirements of the analyses, referred to as *offline-selected* signal. This approach fails to provide good efficiencies for other radiative decays, such as $B^+ \rightarrow \phi K^+\gamma$ or $B^+ \rightarrow K^{*0}\pi^+\gamma$, and thus limits the ability to perform measurements outside the two main radiative channels.

Inclusive HLT2 triggers, mainly the topological trigger, took more than 1/3 of the LHCb trigger bandwidth in 2011 and are used in a wide variety of analyses. While these generic triggers provide a uniform selection efficiency for many radiative channels, they only make use of tracks as generic B signatures, and this leads to compromises in order to keep the rate within acceptable boundaries. In the case of radiative B decays, the presence of the photon in the final state provides an extra signature that can be used in inclusive lines to relax some of the adopted requirements for the tracks, leading to a better trigger efficiency.

The adoption of an inclusive strategy would allow to expand the radiative decays program to many radiative channels besides $B^0 \rightarrow K^{*0}\gamma$ and $B_s^0 \rightarrow \phi\gamma$ and would open the possibility of exploring a wide range of analysis options in the future, provided that good signal efficiencies can be achieved at an acceptable rate.

4.1. Data samples

For the trigger studies in this chapter, data from the full 2011 LHCb dataset have been used. These data include a mixture of the TCKs detailed in Table 3.1.

The signal Monte Carlo samples for the $B^0 \rightarrow K^{*0}\gamma$, $B_s^0 \rightarrow \phi\gamma$, $B^+ \rightarrow \phi K^+\gamma$ and $B^+ \rightarrow K^{*0}\pi^+\gamma$ channels have been generated simulating the 2011 running conditions (see §5.1 for details). Unless specifically stated, the 0x790038 TCK, corresponding to $\sim 30\%$ of the 2011 data set, has been applied to these datasets.

Data, both real and simulated, have been offline selected with the criteria specified in Table 4.1. Details of the individual cuts and their meaning can be found in §5.2. It

can be observed that many of the selection criteria are the same, and some of these similarities are precisely what is exploited in inclusive trigger selections.

4.2. Methods for determining trigger efficiencies

In MC simulation, it is possible to evaluate the trigger efficiency of an offline-selected sample by counting how many events pass the trigger requirements and dividing between the size of the offline-selected sample.

However, this procedure cannot be applied on data because the available data samples have already been selected by some trigger, and therefore its effect cannot be directly estimated. For this reason, the trigger efficiencies are computed using an alternative method: the TISTOS method [155, 156] provides a means of determining trigger efficiencies directly from data, and can be used on MC as well. It is based on the idea of obtaining the most unbiased event sample possible from the offline-selected, triggered sample, and from it extract the trigger efficiency.

In order to describe the main concepts related to the TISTOS method, two types of objects need to be defined:

- A *signal object* is the collection of tracks and calorimeter objects used to build the offline reconstructed B candidate.
- A *trigger object* is the collection of tracks and calorimeter objects responsible for firing a particular trigger line.

The study of signal and trigger objects and their relation for a given trigger line leads to define the following types of events:

Trigger Independent of Signal (TIS). Events which are triggered by a given line independently of the presence of the signal object. In order for an event to be TIS, there must exist at least one trigger object which does not overlap with the signal object. The overlap between signal and trigger objects is checked by comparing the identifiers (LHCbIDs) of the detector elements that were hit by each track or photon that is part of the signal or the trigger object. Two tracks don't overlap if they share less than 1% of their hits; since tracks in LHCb can have around 60 hits, this requirement means that the tracks may not share a single hit. Similarly, two ECAL objects do not overlap if they share less than 0.99% of their hits. TIS events are trigger unbiased saving correlations between the signal B decay and the rest of the event.

Trigger On Signal (TOS). Events which are triggered by a given line on the signal object, independently of the rest of the event. The TOS criterion is satisfied if there exists at least one trigger object all of whose tracks and calorimeter objects have overlap with the signal object. Two tracks (calorimeter objects) overlap when they share more than 70% (1%) of their hits, 60% in the case of muon segments.

Trigger On Both (TOB). Events which are neither TIS nor TOS, *i.e.*, they require both the signal and the rest of the event in order to be triggered by a given line. In HLT2, typical TOB events are those where the trigger is fired because of a signal track combined with a ghost to form a displaced vertex. Even in the

		$B^0 \rightarrow K^{*0} \gamma$	$B_s^0 \rightarrow \phi \gamma$	$B^+ \rightarrow \phi K^+ \gamma$	$B^+ \rightarrow K^{*0} \pi^+ \gamma$
Track χ^2		< 5	< 5	< 5	< 5
Track IP χ^2		> 25	> 25	> 25	> 25
Track p_T	(MeV/c)	> 500	> 500	> 500	> 500
Max track p_T	(MeV/c)	> 1200	> 1200	> 1000	> 1000
Kaon DLL $_{K\pi}$		> 5	> 5	> 5	> 5
Kaon DLL $_{Kp}$		> 2	> 2	> 2	> 2
Pion DLL $_{K\pi}$		< 0	–	–	< 0
Vector meson vertex $\Delta\chi^2$		< 9	< 9	< 9	< 9
Vector meson ΔM_{PDG}	(MeV/ c^2)	< 50	< 9	< 9	< 9
Photon E_T	(MeV)	> 2600	> 2600	> 2600	> 2600
Photon CL		> 0.25	> 0.25	> 0.25	> 0.25
π^0/γ separation		> 0.5	> 0.5	> 0.5	> 0.5
Candidate p_T	(MeV/c)	> 3000	> 3000	> 3000	> 3000
Candidate IP χ^2		< 9	< 9	< 9	< 9
Candidate DIRA	(mrad)	< 20	< 20	< 20	< 20
Candidate FD χ^2		> 100	> 100	> 100	> 100
Candidate ΔM_{PDG}	(MeV/ c^2)	< 700	< 700	< 700	< 700
Candidate $ \cos\theta_H $		< 0.8	< 0.8	–	–
Candidate isolation $\Delta\chi^2$		> 2	> 2	> 2	> 2

Table 4.1. Selection criteria for the radiative channels used for trigger analysis.

case of the HLT1 single track trigger, it is also possible to have a TOB event, *e.g.*, the VELO segment of the signal track is combined with a T-station ghost. TOB events are problematic because their efficiency cannot be defined without constructing a model for the trigger efficiency on background events. Hence, TOB events are of limited use to any analysis which needs to know the trigger efficiency or acceptance.

With these definitions, the TOS efficiency can be calculated as

$$\epsilon_{\text{TOS}} = \frac{\mathcal{N}_{\text{TIS\&TOS}}}{\mathcal{N}_{\text{TIS}}}, \quad (4.1)$$

and, likewise for the TIS efficiency:

$$\epsilon_{\text{TIS}} = \frac{\mathcal{N}_{\text{TOS\&TIS}}}{\mathcal{N}_{\text{TOS}}}. \quad (4.2)$$

All trigger efficiencies quoted in this chapter are TOS efficiencies, unless specifically stated. In the case of MC samples, the TOS efficiency can also be obtained directly by counting events that pass the given TOS requirement and dividing between the size of the offline-selected sample.

The TISTOS method allows to estimate the TOS efficiency of a signal by normalizing the number of TOS events with the TIS requirement. The precision of the efficiencies obtained with this procedure is limited by the statistics of TIS events available, since these constitute a small fraction of the total offline-selected signal. Furthermore, since there may exist a correlation between the signal B and the other B in the event, efficiencies computed using the TISTOS method have to be determined as a function of variables of interest, such as the B momentum, the B transverse momentum and the B meson lifetime.

4.3. L0 channels

The relevant L0 channels for radiative decays are those included in the L0 Calorimeter Trigger [125]. The idea behind this set of L0 channels is to search for high E_{T} objects and identify them as electrons, photons, π^0 or hadrons. Since showers are relatively narrow, their corresponding E_{T} is computed in a 2×2 cells zone, which is wide enough to contain most of the energy and small enough to reduce significantly the probability of overlap between different particles. Furthermore, at each stage of the process only the candidate with the highest E_{T} is kept, thus reducing the number of candidates to process. The selection of these L0 candidates is performed as following:

1. High E_{T} deposits are selected by the Front-End (FE) cards, which handle ECAL and HCAL information. Each of these handles 32 cells, and the highest E_{T} over the 32 sums of 2×2 cells is selected. To calculate these sums it is essential to have access to neighboring cells in other cards.
2. Information from the SPD and PS is added in the Validation Cards in order to identify the type of electromagnetic candidate. L0 candidates are distinguished as *electromagnetic* by making use of the PS information of the cells in front of them: a certain energy deposit is required in order to ascertain that the electromagnetic

shower has begun in the lead absorber. The SPD information (hit/no hit) is then used to distinguish between electron (`L0Electron`) and photon (`L0Photon`) candidates. Only one candidate per card and per type is selected and forwarded to the Selection Crate. The types are not exclusive, *i.e.*, the same 2×2 cluster can be selected by different L0 calorimeter triggers. Finally, the ECAL transverse energy is added to the relevant HCAL 2×2 clusters for hadron (`L0Hadron`) candidates.

3. The candidate with the highest E_T for each type is selected in the Selection Crate. In addition, the total E_T in the HCAL and the total SPD multiplicity are computed as a measure of the activity in the event.

While the `L0Photon` and `L0Electron` thresholds were high and not completely stable during 2010, 3.2 GeV and 4.4 GeV for the bulk of the data, in 2011 they have been very stable and almost all data have been collected with a lower threshold of 2.5 GeV. In the case of the `L0Hadron`, during 2010 the threshold was placed at 3.6 GeV almost for all the data taking, while in 2011 the cut was lowered to 3.5 GeV throughout most of the year.

L0 trigger on the photon

It has been shown on simulation that using only `L0Photon` candidates is an ineffective way to trigger photons for radiative decays [157]. On one side, the requirement of PS energy to identify electromagnetic energy depositions rejects 20% of the photon clusters. On the other side, the SPD only identifies as photon $\sim 60\%$ of these electromagnetic clusters due to the fact that 40% of the photons convert before the SPD, mostly in the M1 ($\sim 0.265X_0$).

Therefore, incorporating the `L0Electron` to the definition of photon at the L0 level helps recovering part of those photons lost due to conversion, as can be seen in Fig. 4.1, at the cost of an increased rate. This rate can be controlled by tightening the E_T cut for both `L0Photon` and `L0Electron`, and doing so results in better efficiency (at a given rate) than keeping a looser E_T cut and using only `L0Photon`. For this reason, two further L0 channels have been added to the `L0`, `L0PhotonHi` and `L0ElectronHi`, which correspond to `L0Photon` and `L0Electron` but with a tightened E_T cut, $E_T > 4.2$ GeV. These high E_T channels can be used in the HLT1 to provide a performance boost for decays with photons.

L0 trigger on hadrons

In order to add robustness to the L0 trigger strategy, the `L0Hadron` requirement, which relies on the HCAL estimation of the transverse energy of the hadrons, can be added in order to trigger, for example, on the daughter tracks of the K^{*0} or the ϕ . This opens the possibility of loosening the photon E_T cut in the offline selections, since events not triggered by the photon could be recovered if they were selected due to the hadrons.

4.4. HLT1 lines

Commissioning of the HLT1 in 2010 showed that hadronic triggers suffered from contamination by *ghost tracks* (reconstructed tracks with no real counterpart, produced by

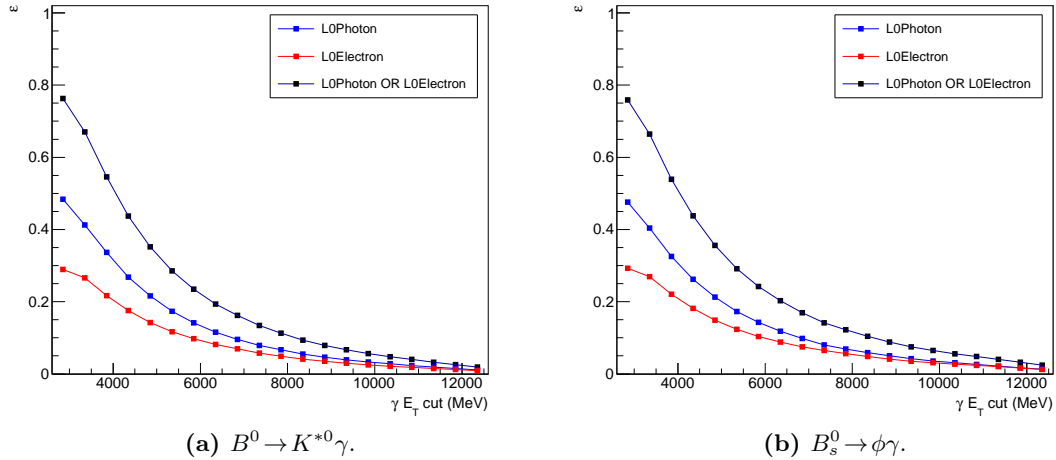


Figure 4.1. Efficiency on the signal photon of the LOPhoton (blue) and LOElectron (red) requirements, or the combination of both (black) on offline-selected $B^0 \rightarrow K^{*0} \gamma$ and $B_s^0 \rightarrow \phi \gamma$ MC11 signal as a function of the E_T cut on the offline-reconstructed photon.

spurious track hit combinations). To solve this problem, the L0 confirmation strategy, where the HLT1 line “confirms” the corresponding L0 candidate by adding tracking information, was abandoned, and the HLT1 alleys¹ were replaced by the single track [126] and muon triggers [127].

The HLT1 trigger strategy for radiative decays in 2011 revolves around the single track trigger. In it, a single detached high momentum track is searched for in a region of interest defined by a straight VELO track segment and its assumed momentum, without confirmation of the L0 trigger decision. The track used for triggering is required to have:

- Good track reconstruction in the VELO, which is measured by the number of VELO hits, the difference between the number of VELO hits and the expected number of hits given the track direction and its first measured point, and by its corresponding impact parameter.
- A minimum momentum p and transverse momentum p_T , since the B average momentum at the LHC is high, $\sim 100 \text{ GeV}/c$. Furthermore, only tracks over a given p and p_T threshold are considered at this stage in order to reduce the search windows in the tracker stations, resulting in low timing requirements and a reduced dependency of the reconstruction time on μ .
- Detachment of the track, measured by its IP χ^2 .
- Good quality of the track, measured by its χ^2 .

¹See [158] for a review of the HLT1 Electromagnetic Alley, which was the alley responsible for triggering on electromagnetic objects, such as the photon.

Although no L0 confirmation is performed, the L0 information is used in these lines to trigger more effectively in some specific decay types, resulting in three single track lines:

- The *All L0* line (`Hlt1TrackAllL0`), which runs on all L0 `Physics`-passed events.
- The *Muon* line (`Hlt1TrackMuon`), which runs on L0`Muon`- or L0`DiMuon`-passed events, and benefits from the extra muonID cut to loosen most of the cuts applied on the track.
- The *Photon* line (`Hlt1TrackPhoton`), which runs on those events passing the L0`PhotonHi` or L0`ElectronHi` channels, and makes use of the L0 photon requirement to relax the p and p_T requirements on the track. This line was specially added to aid in the trigger of radiative decays.

The gain obtained when adding a requirement B as the logical OR over a requirement A is quantified by calculating

$$g_A^B = \frac{\mathcal{N}_{A \text{ OR } B}}{\mathcal{N}_A} - 1. \quad (4.3)$$

With this definition, we can use MC to estimate the gain of adding the HLT1 Photon line requirement to the HLT1 All L0 line,

$$g_{\text{Hlt1TrackAllL0}}^{\text{Hlt1TrackPhoton}} \approx 13\%, \quad (4.4)$$

for both the $B^0 \rightarrow K^{*0}\gamma$ and $B_s^0 \rightarrow \phi\gamma$.

Discarding the HLT1 Muon line, which does not provide any intrinsic gain, radiative decays have two possible (non-exclusive) trigger paths in HLT1, the *All L0* and the *Photon* lines, the cuts of which are detailed in Table 4.2. On one side, the *All L0* line allows to trigger on harder tracks while keeping relatively low E_T requirements on the photon. On the other side, some of the efficiency lost by the *All L0* line due to the p_T and p requirements on the track can be recovered by making use of the *Photon* line, which loosens the requirements on the track at the cost of requiring a harder photon. The combination of these two lines allows to cover a bigger phase space for triggering radiative decays, as shown in Fig. 4.2.

Furthermore, adding L0`Hadron` to the L0 requirements would allow access to the top-left region in Fig. 4.2. If we compute the gain, defined in Eq. 4.3, of adding the L0`Hadron` requirement on offline-selected MC11 events with the photon E_T cut loosened to $E_T > 2$ GeV and the HLT1 TOS selection, we obtain

$$g_{\text{LOPhoton OR LOElectron}}^{\text{L0Hadron}} \approx 12\%, \quad (4.5)$$

for both $B^0 \rightarrow K^{*0}\gamma$ and $B_s^0 \rightarrow \phi\gamma$. Thus, $\mathcal{O}(10\%)$ more events would be available to HLT2, but the effects of lowering the photon E_T on the S/B ratio would have to be assessed.

4.5. HLT2 lines

The majority of trigger work in radiative decays in 2011 has been made on the HLT2, resulting in an optimized set of lines which greatly exceed the performance of those used in 2010.

	<i>All L0 line</i>	<i>Photon line</i>
L0 channel	L0 physics	L0PhotonHi or L0ElectronHi
Implicit photon E_T	(GeV)	> 2.5
VELO track IP	(μm)	> 100
VELO track hits		> 9
Missed VELO hits		< 3
Track p	(GeV/c)	> 10.0
Track p_T	(GeV/c)	> 1.7
Track χ^2		< 2
Track IP χ^2		> 16

Table 4.2. Cut values for the HLT1 single track lines relevant to radiative decays for 2011. The implicit photon E_T cut corresponds to the photon cut in the L0 channels on which the given HLT1 line runs.

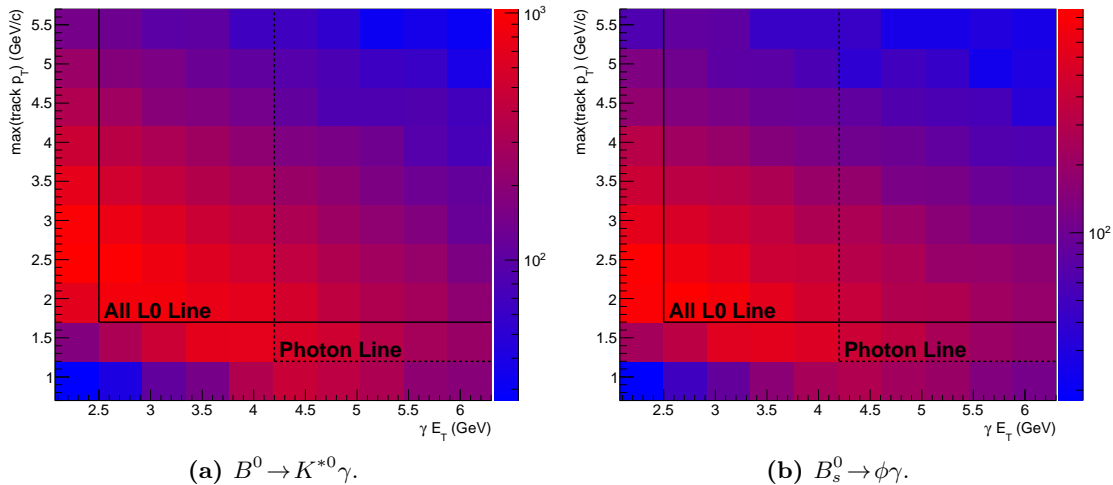


Figure 4.2. Distribution of the maximum p_T of the vector meson daughter versus the photon E_T on MC11 offline-selected events (the track p_T and photon E_T cuts have not been included) for $B^0 \rightarrow K^{*0}\gamma$ (left) and $B_s^0 \rightarrow \phi\gamma$ (right). Superimposed, the p_T - E_T cuts of the HLT1 All L0 single track line (solid line) and the Photon single track line (dotted line), combined with the implicit L0 photon cuts.

On one side, the HLT2 exclusive lines used in 2010 were optimized from their original version in order to improve their signal selection efficiency. On the other side, an inclusive approach has been tested by studying a set of already existing lines, the HLT2 Topological trigger, by introducing a new set of lines, the HLT2 Radiative Topological trigger, and by improving the useful inclusive ϕ line. Furthermore, a new procedure for reconstruction of the calorimeter in the HLT2 has been developed in order to diminish the timing problems of those lines that make use of photons.

4.5.1. Calorimeter Reconstruction in HLT2

As it has already been discussed, timing is critical when dealing with trigger algorithms due to the limited time available to make a decision. For this reason, the only reconstruction performed upfront in the HLT2 is the tracking, limited to long tracks with $p_T > 500 \text{ MeV}/c$. All other reconstruction algorithms, such as the PID or the calorimeter, are triggered on demand when needed by specific lines. Therefore, one must be very careful to trigger on-demand reconstruction as efficiently as possible in order to avoid excessive CPU consumption, *e.g.*, filtering the tracks by making use of kinematic criteria before making any RICH PID requirement.

Dealing with trigger lines that make use of photons implies dealing with calorimeter reconstruction. Reconstruction of the calorimeter in the HLT2 has been a long standing problem in LHCb owing to the fact that it was not optimized for online running. In fact, the online calorimeter reconstruction mainly consisted in the offline code with the necessary software tweaks to allow it to run in the Online context.

The offline calorimeter reconstruction takes $\sim 56 \text{ ms}/\text{event}$, the slowest parts being:

- *Clusterization*, in which energy deposits in the individual ECAL cells are grouped together using a Cellular Automaton algorithm [159] to form clusters. This clustering algorithm is based on finding local energy maxima in the calorimeter, defining them as the cluster seed and iteratively adding neighboring cells to it. Having to perform the clustering procedure for the full calorimeter is thus a slow process in HLT2 timing terms.
- *Track matching for Calorimeter PID*, in order to separate charged from neutral calorimeter particles. As detailed in §3.4.4, the distance of each of the tracks to the energy cluster needs to be calculated, and doing this for each track and each cluster results in the use of a large number of CPU cycles.

To reduce the time consumption of the calorimeter reconstruction, these two issues need to be addressed. Namely, steps need to be taken to reduce the number of clusters being built and to eliminate the need for track matching. Given these premises, a new calorimeter reconstruction procedure for the HLT2 was designed and introduced after the June 2011 LHC technical stop.

In the new procedure, clusters are only searched for in 3×3 regions of interest defined by L0 calorimeter candidates (*L0CaloCandidates*) above a certain E_T threshold and the CaloPID of the associated particle is defined by the type of L0 candidate. This method presents three main advantages in the HLT context:

- Fewer clusters are built due to E_T cut on the *L0CaloCandidates*.
- Better scalability with the number of visible interactions due to the fact that there is only one *L0CaloCandidate* per Validation Card and per *L0Calo* type, and thus the maximum number of *L0CaloCandidates* per type is equal to the number of Validation Cards, 28. Therefore, processing time is less affected by event multiplicity.
- No need for track matching.

Moreover, this procedure can be used not only for photons, but also for electrons and π^0 , using the following inputs for clusterization:

- *Photons* are built from **L0Electron** or **L0Photon** L0CaloCandidates with $E_T > 2000$ MeV.
- *Electrons* are built from **L0Electron** L0CaloCandidates with $E_T > 300$ MeV.
- *Neutral pions* are built from **L0Electron** or **L0Photon** L0CaloCandidates with $E_T > 300$ MeV.

The clustering process is therefore performed three times, albeit using a very limited number of calorimeter cells, and the resulting objects are stored in three different locations. While this adds some inefficiencies due to duplication of cluster reconstruction, having three separated containers allows to have a much faster CaloPID assignment since the track matching step is no longer necessary.

The timing and performance of L0-based calorimeter reconstruction have been tested on simulated $B^0 \rightarrow K^{*0}\gamma$ events, and compared to the previous offline-like reconstruction. The results of this comparison can be seen in Table 4.3. Tasks performed in both cases, like the unpacking of the RAW event, which takes 0.9 ms/event, are not taken into account because there is no improvement to be made in that respect. In total, the L0-based reconstruction takes 9.3 ms/event while the offline-like reconstruction takes 27.5 ms/event, *i.e.*, the new reconstruction procedure is 3 times faster. More specifically, there is a ten-fold and a four-fold speed increase in clustering and particle reconstruction, respectively.

	Offline-like reconstruction				L0-based reconstruction			
	γ	e^\pm	π^0	Total	γ	e^\pm	π^0	Total
Clustering (ms/evt)	—	—	—	3.1	0.08	0.13	0.07	0.28
Particle reco (ms/evt)	8.4	1.7	4.4	14.5	0.3	1.5	1.6	3.4

Table 4.3. Timing comparison of the clustering and particle reconstruction parts between the offline-like and the L0-based calorimeter reconstruction.

Having only one L0CaloCandidate per Validation Card and type has the downside that some efficiency is lost. The new HLT2 calorimeter reconstruction produces a 7.5% lower rate, and the TOS efficiency for photons is reduced by $\sim 6\%$.

4.5.2. Exclusive radiative lines

The *exclusive HLT2 lines* for radiative decays consist in one line for $B^0 \rightarrow K^{*0}\gamma$ (**Hlt2Bd2KstGamma**) and one for $B_s^0 \rightarrow \phi\gamma$ (**Hlt2Bs2PhiGamma**), plus several prescaled monitoring lines. In each of them, the target decay is reconstructed using roughly the same procedure as it is done for offline analysis: two oppositely-charged tracks are combined to build the vector meson V , which is then combined with a photon to build a B candidate.

At the end of the 2010 data taking period, several changes were introduced to the lines in [130] in order to cope with the running conditions, adapt the HLT2 strategy to the HLT1 changes, and to increase the overall signal retention:

- The HLT2 lines were running on the output of the HLT1 Photon line of the HLT1 Electromagnetic alley, which performed the confirmation of **L0Photon** candidates.

Therefore, following the ideas discussed in §4.3, to increase the global trigger efficiency of radiative decays events coming from the L0Electron channel were been included in the trigger path. Thus, events entering the HLT2 radiative exclusive lines are required to have fired either L0Photon or L0Electron.

- The replacement of the HLT1 alleys, including the Electromagnetic alley, by the single track lines, triggered the removal of the explicit dependence on any HLT1 lines, leaving only a requirement that events should have been trigger by any HLT1 physics line. As can be seen in Fig. 4.2, explicitly requiring the single track trigger removes a sizeable amount of events that would otherwise be selected offline. Therefore, removing the HLT1 single track requirement from the HLT2 lines allows to select more signal events, even if they are TIS; this helps in those analyses that don't require any knowledge of the trigger efficiency, such as the CP asymmetry for $B^0 \rightarrow K^{*0}\gamma$.
- The HLT2 lines were completely rewritten before the 2011 run, adding a cut in the quality of both charged tracks and improving their speed by applying the cuts in the correct order —fastest, more discriminant, first. The value of the B candidate IP χ^2 , K^{*0} mass window and V vertex χ^2 cuts were relaxed, adapting to the experience with 2010 data. The final cuts used to filter the candidates, looser than their offline counterparts, are summarized in Table 4.4.
- The use of the new calorimeter reconstruction was adopted after the June technical stop, greatly improving the timing budget of these lines.

The changes in the L0 and HLT1 dependency, combined with the optimized code, result in half the execution time, approximately one third of the rate and double the efficiency with respect to 2010.

In addition, the monitoring lines for $B^0 \rightarrow K^{*0}\gamma$ and $B_s^0 \rightarrow \phi\gamma$ were optimized in order to help in the estimation of possible biases produced by the trigger cuts, prescaled to 1/20 and 1/10, respectively:

- Wide B and B_s^0 invariant mass window lines, `Hlt2Bd2KstGammaWideBMass` and `Hlt2Bs2PhiGammaWideBMass`, which can be used for checking for the appearance of structures in the background mass distribution.
- A wide K^{*0} invariant mass window line, `Hlt2Bd2KstGammaWideKMass`, to see the full line shape of the resonance, since the mass window cut in the non-prescaled line must be kept tight, at twice the natural width of the K^{*0} , to keep the rate under control. The analogous line for the ϕ is not necessary, because its narrow width allows to have a wide cut of 5σ while keeping a reasonable rate.

The efficiency of these improved exclusive lines on simulated data is shown in Table 4.5. The table showcases that the exclusive lines are very effective in selecting those events for which they were designed, particularly when taking into account that these efficiencies include a 6% loss of efficiency due to the new HLT2 calorimeter reconstruction. Furthermore, it can be seen that the $B^+ \rightarrow \phi K^+\gamma$ and $B^+ \rightarrow K^{*0}\pi^+\gamma$ decays have a fairly high TOS efficiency with the exclusive line that contains the same vector meson, mainly due to the loose IP and DIRA cuts on the B candidate.

	$B^0 \rightarrow K^{*0}\gamma$ line	$B_s^0 \rightarrow \phi\gamma$ line
Track p	(MeV/ c)	> 5000
Track p_T	(MeV/ c)	> 500
Track χ^2		< 5
Track IP χ^2		> 10
$V \Delta M_{\text{PDG}}$	(MeV/ c^2)	< 100 (200)
V vertex χ^2		< 16
Photon E_T	(MeV)	> 2600
B IP χ^2		< 25
B DIRA	(mrad)	< 63 (140)
B ΔM_{PDG}	(MeV/ c^2)	< 1000 (2000)
L0 channel	L0Photon or L0Electron	L0Photon or L0Electron
HLT1 lines	HLT1 Physics	HLT1 Physics

Table 4.4. Cuts applied in the HLT2 exclusive lines for $B^0 \rightarrow K^{*0}\gamma$ and $B_s^0 \rightarrow \phi\gamma$, separated in track cuts, vector meson V cuts, photon cuts, B candidate cuts and trigger filters. Cut values for the monitoring lines can be found in parentheses, when applicable.

	Hlt2Bd2KstGamma (%)	Hlt2Bs2PhiGamma (%)
$B^0 \rightarrow K^{*0}\gamma$	85.6 ± 0.3	0.002 ± 0.004
$B_s^0 \rightarrow \phi\gamma$	35.4 ± 0.4	89.4 ± 0.2
$B^+ \rightarrow \phi K^+\gamma$	17.5 ± 0.8	18.0 ± 0.8
$B^+ \rightarrow K^{*0}\pi^+\gamma$	42.2 ± 1.8	0.5 ± 0.2

Table 4.5. TOS efficiency of the HLT2 exclusive lines over L0 and HLT1 TOS, defined as L0Photon TOS or L0Electron TOS and Hlt1TrackAllL0 TOS or Hlt1TrackPhoton TOS, respectively, in offline-selected simulated samples with TCK 0x790038.

4.5.3. HLT2 Topological lines

The *HLT2 topological* trigger family is a group of lines designed to trigger inclusively on 2-,3- and 4-body B decays, regardless of the B flavor, keeping a high efficiency on signal data and a very low background retention [129]. To achieve inclusiveness, cuts on variables such as the B candidate mass, the DIRA or the IP of such candidate cannot be used; instead, cuts on quantities that preserve inclusiveness are employed.

Furthermore, if a trigger candidate only contains a subset of its daughter particles, the mass of the candidate will be less than the mass of the corresponding B meson, and therefore mass cuts need to be avoided. The *corrected mass* variable, defined as

$$m_{\text{corrected}} = \sqrt{m^2 + |p_{T,\text{missing}}|^2} + |p_{T,\text{missing}}|, \quad (4.6)$$

where $p_{T,\text{missing}}$ is the missing momentum transverse to the direction of flight of the B candidate, can be used to account for missing daughters of a decay without knowing

how many there are or of which type they are, as shown in Fig. 4.3. The value of $m_{\text{corrected}}$ corresponds exactly to the mass of the B candidate if the missing particle is massless.

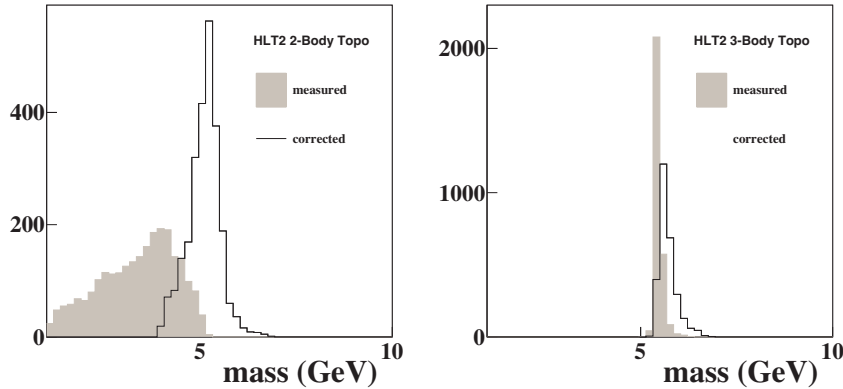


Figure 4.3. Masses from $B \rightarrow K\pi\pi$ decays for the 2-body (left) and 3-body (right) topological trigger candidates. In each plot, the measured mass of the 2- or 3-body object is shown shaded, while the corrected mass obtained using Eq. 4.6 is shown as a solid line. This figure has been taken from [129].

The HLT2 topological lines were introduced in 2010 as a set of cut-based lines, providing very good performance with good signal retention and high background rejection. However, with 2011 conditions —more colliding bunches— the background rejection needed to be three times higher in order to keep the same rate, and this could not be achieved with simple cuts without compromising the signal efficiency. For this reason a multivariate approach was introduced, using the Bagged Bonsai Decision Tree (BBDT) method [160], a discretized version of the Bagged Decision Tree [161]. This method performs simple few-dimensional cuts in regions of the phase space with low background, and complex many-dimensional cuts in regions with high levels of background.

In the 2011 topological lines, the following strategy was used:

1. Upfront cuts in track χ^2 , p_T , p , IP χ^2 and candidate mass are performed.
2. Regions with low background are factored out of the BBDT and simple cuts are applied.
3. The full 7-dimensional BBDT cut is performed in high background regions. The variables included are the sum of p_T of the tracks, the minimum track p_T , the candidate mass and corrected mass, the distance of closest approach (DOCA) between the tracks, defined as the minimum distance between the vectors defined by the momentum of the tracks, their IP χ^2 , and the flight distance χ^2 of the candidate.

A cut-based version of the topological, so-called *Simple*, is also kept to provide cross checks of the multivariate decision. However, its cuts have been tightened to keep up with the rate budget, and therefore its signal efficiency is significantly lower.

While very effective for many of the key channels in LHCb [162], it can be seen in Table 4.6 that the HLT2 topological lines are not as effective with radiative decays, mainly due to the presence of the photon, which is not used as an input object in these lines. However, as expected, it can be seen that a significant efficiency is obtained for the three-body decays, both in the 2-body and 3-body lines.

If the 2- and 3-body BBDT lines are combined, efficiencies of $(50.1 \pm 1.1)\%$ and $(48.8 \pm 1.8)\%$ are obtained for $B^+ \rightarrow \phi K^+ \gamma$ and $B^+ \rightarrow K^{*0} \pi^+ \gamma$, respectively. Therefore, the combined efficiency of the BBDT-based topological is slightly higher for the 3-body decays, and thus some of the efficiency lost by the exclusive HLT2 lines can be recovered.

	2-body		3-body	
	Simple (%)	BBDT (%)	Simple (%)	BBDT (%)
$B^0 \rightarrow K^{*0} \gamma$	9.8 ± 0.3	33.1 ± 0.4	0.026 ± 0.014	0.018 ± 0.012
$B_s^0 \rightarrow \phi \gamma$	18.5 ± 0.3	47.1 ± 0.4	0.050 ± 0.017	0.052 ± 0.017
$B^+ \rightarrow \phi K^+ \gamma$	6.7 ± 0.5	42.1 ± 1.1	8.9 ± 0.6	36.3 ± 1.0
$B^+ \rightarrow K^{*0} \pi^+ \gamma$	9.5 ± 1.0	43.2 ± 1.8	4.1 ± 0.7	28.7 ± 1.6

Table 4.6. TOS efficiency of the HLT2 topological lines over L0 and HLT1 TOS, defined as LOPhoton TOS or L0Electron TOS and Hlt1TrackAllL0 TOS or Hlt1TrackPhoton TOS, respectively, in offline-selected simulated samples with TCK 0x790038.

4.5.4. HLT2 Radiative Topological lines

The *HLT2 radiative topological* lines have been designed to efficiently trigger on any B decay with at least two tracks and one high- E_T photon, and their goal is to improve the efficiency provided by regular topological lines to radiative decays. This is achieved by adopting an inclusive strategy very similar to that used by the cut-based topological trigger and making use of the photon information to lower the rate.

In the radiative topological lines the B candidates are built as follows:

1. Tracks are selected following usual momentum and quality criteria, as shown in the first section of Table 4.7.
2. A 2-body object is built using two selected tracks, with cuts detailed in the second section of Table 4.7. This *di-track* object is filtered according to the DOCA of the two tracks, the quality of its vertex and its p_T . The mass of this object is also limited in order to avoid selecting too-heavy intermediate particles. In addition, it is required that at least one of the tracks of the combination has a lower χ^2 than in the previous step.
3. The di-track object is then combined with a photon with $E_T > 2.5 \text{ GeV}$ to build a 3-body object, the B candidate. Candidates are selected with similar criteria as the HLT2 topological lines, that is, requiring a minimum p_T , a corrected mass range, a minimum flight distance of the candidate and a sum of the p_T of the daughters greater than $5 \text{ GeV}/c$ (see the fourth section of Table 4.7 for details). The mass is not used in this case in order to maintain inclusiveness.

Track p	(MeV/c)	> 5000
Track p_T	(MeV/c)	> 700
Track χ^2		< 5
Track IP χ^2		> 10
Min track χ^2		< 3
Di-track DOCA	(mm)	< 0.15
Di-track vertex χ^2		< 10
Di-track mass	(MeV/ c^2)	< 2000
Di-track p_T	(MeV/c)	> 1500
Photon E_T	(MeV)	> 2500
Candidate p_T	(MeV/c)	> 1000
Candidate $m_{\text{corrected}}$	(MeV/ c^2)	> 4000, < 7000
Candidate FD χ^2		> 64
Daughters Σp_T	(MeV/c)	> 5000
# of forward tracks with $p_T > 500 \text{ MeV}/c$		< 120

Table 4.7. Selection criteria for the HLT2 radiative topological lines, divided in sections. The first section details the cuts on input tracks, the second the di-track combination cuts, the third the photon cuts, the fourth cuts on the B candidate and the last one is the GEC.

In addition, a Global Event Cut (GEC) on the track multiplicity is applied in order to reject events with a high level of background.

Furthermore, in order to achieve robustness under possible changes of the L0 trigger, two different radiative topological lines, with different L0 and HLT1 requirements, have been introduced:

- *L0 photon line* (`Hlt2RadiativeTopoPhotonL0`): this line runs on those events that have passed either the `L0Photon` or the `L0Electron` lines, and any HLT1 physics line. The requirements are similar in this case to the exclusive lines, but the efficiency of the line is highly dependent on the `L0Photon` and `L0Electron` threshold, *i.e.*, a higher cut on the E_T would imply a sizeable loss of efficiency.
- *HLT1 Track TOS line* (`Hlt2RadiativeTopoTrackTOS`): this line requires the event to pass one of the HLT1 Track lines and requires that one of the used tracks was actually responsible for firing the HLT1 track trigger —this is the so-called *TOS track filter*. Thus, this line allows to recover those events that haven't been triggered on the photon by triggering on one of the daughter particles of the 2-body object. It is thought of as backup of the L0 photon line in the event that the L0 thresholds were to be increased, but it will also be useful in the scenario where the photon E_T requirement of the radiative selections is lowered and the `L0Hadron` is added to the current TOS selection.

To assess the effect of the *HLT1 Track TOS* line, trigger efficiencies with SPD multiplicity < 600 and thresholds of `L0Photon` and `L0Electron` set at 4.2 GeV —a possible scenario for a high luminosity TCK— have been considered. The effect of increasing

the threshold of `L0Photon` and `L0Electron` is a $\sim 30\%$ efficiency drop in the exclusive lines —and similarly in the radiative L0 Photon TOS line. In this case, the HLT1 Track TOS line only loses $\sim 10\%$ of its efficiency thanks to the `L0Hadron` channel.

As explained previously, the HLT2 topological lines used in the 2011 data taking period include a multivariate-based selection (BBDT) that allows to achieve a very high efficiency on signal while rejecting most of the background. At the end of the 2011 data taking period, two extra lines for radiative decays have been incorporated to the topological trigger to benefit from this multivariate technique:

- A 2-body BBDT line (`Hlt2TopoRad2BodyBBDT`) which runs on the output of `L0Photon` and `L0Electron`. This line builds the 2-body object from a track and a photon, and therefore cuts need to be very tight in order to reject combinatorics.
- A 3-body BBDT line (`Hlt2TopoRad2plus1BodyBBDT`) in which one of the bodies is forced to be a photon; it is therefore a 2 track plus one photon line. This line benefits from the presence of the photon, which allows to loosen the BBDT cut while keeping a reasonable rate.

Both lines apply a TOS track filter.

The efficiency of the HLT2 radiative topological lines has been assessed on MC simulation and documented in Table 4.8. In it we can see that, in general, the BBDT-based lines outperform the cut-based lines, specially in the case of $B^0 \rightarrow K^{*0}\gamma$ and $B_s^0 \rightarrow \phi\gamma$. When comparing to other HLT2 lines, the radiative topological provides efficiencies only slightly lower than the exclusive lines for $B^0 \rightarrow K^{*0}\gamma$ and $B_s^0 \rightarrow \phi\gamma$, but the improvement with respect to the regular topological lines ranges is approximately two-fold.

	Cut-based (%)	BBDT-based (%)
$B^0 \rightarrow K^{*0}\gamma$	75.6 ± 0.4	80.5 ± 0.4
$B_s^0 \rightarrow \phi\gamma$	77.3 ± 0.3	84.4 ± 0.3
$B^+ \rightarrow \phi K^+\gamma$	90.0 ± 0.6	91.4 ± 0.6
$B^+ \rightarrow K^{*0}\pi^+\gamma$	89.3 ± 1.1	91.5 ± 1.0

Table 4.8. TOS efficiency of the cut- and BBDT-based HLT2 radiative topological lines over L0 and HLT1 TOS, defined as `L0Photon` TOS or `L0Electron` TOS and `Hlt1TrackAllL0` TOS or `Hlt1TrackPhoton` TOS, respectively, in offline-selected simulated samples.

A detail on the individual performance of the BBDT-based lines is shown in Table 4.9. The 2-body radiative line, which uses one track and one photon as input, does not add any significant efficiency, and thus its removal should be considered.

4.5.5. Inclusive ϕ line

The inclusive ϕ trigger provides a robust and transversal trigger for radiative decays involving ϕ vector mesons, such as $B_s^0 \rightarrow \phi\gamma$ and $B^+ \rightarrow \phi K^+\gamma$. It looks for detached ϕ mesons built from pairs of oppositely charged tracks identified as kaons by making use of RICH information.

	2-body BBDT (%)	3-body BBDT (%)
$B^0 \rightarrow K^{*0} \gamma$	51.0 ± 0.4	80.2 ± 0.4
$B_s^0 \rightarrow \phi \gamma$	66.4 ± 0.4	84.0 ± 0.3
$B^+ \rightarrow \phi K^+ \gamma$	63.2 ± 1.0	90.7 ± 0.6
$B^+ \rightarrow K^{*0} \pi^+ \gamma$	62.4 ± 1.7	91.1 ± 1.0

Table 4.9. Detailed TOS efficiency of the 2- and 3-body BBDT-based HLT2 radiative topological lines over L0 and HLT1 TOS, defined as L0Photon TOS or L0Electron TOS and Hlt1TrackAllL0 TOS or Hlt1TrackPhoton TOS, respectively, in offline-selected simulated samples.

The current implementation, which has been running throughout 2010 and 2011, has been designed based on the DC06 inclusive ϕ stream [131]. In it, ϕ candidates are built in a three step process, with the corresponding cuts listed in Table 4.10:

1. Reconstructed tracks with RICH information are filtered according to their p_T , IP χ^2 and quality. A cut in $DLL_K\pi$ is also applied to improve the kaon purity of the track sample.
2. Opposite sign tracks are combined to build ϕ candidates. Prior to the vertex fit, a cut in the DOCA of the two tracks is applied, and afterwards the p_T and the vertex quality are used for filtering bad combinations.
3. ϕ candidates are further filtered by applying a HLT1 Track TOS requirement.

Before this process is performed, a GEC on the number of tracks is also applied. This cut, along with the TOS filter applied in the third step, was added in order to reduce the rate of the ϕ lines, which was ~ 575 Hz at the beginning of 2011, to ~ 36 Hz [163].

Track p_T	(MeV/c)	> 800
Track χ^2		< 5
Track IP χ^2		> 6
Track DLL_K		> 0
ϕ tracks DOCA	(mm)	< 0.2
ϕ vertex χ^2		< 20
ϕ mass window	(MeV/ c^2)	± 20
ϕp_T	(MeV/c)	> 1800
# of forward tracks with $p_T > 500$ MeV/c		< 120

Table 4.10. Selection criteria for the HLT2 inclusive ϕ line, divided in sections. The first section details the cuts on input tracks, the second on the ϕ candidate and the last one is the GEC.

The performance of the inclusive ϕ lines has been evaluated on the offline-selected MC $B_s^0 \rightarrow \phi \gamma$ and $B^+ \rightarrow \phi K^+ \gamma$ samples. Considering a TOS selection of L0Electron or L0Photon, and HLT1TrackAllL0 or HLT1TrackPhoton, the efficiencies of this line on the relevant radiative decays are detailed in Table 4.11. While the efficiency on

the $B_s^0 \rightarrow \phi\gamma$ is the highest among the studied lines —even the exclusive one—, the performance of the inclusive ϕ trigger on $B^+ \rightarrow \phi K^+\gamma$ is lower, mainly due to the high p_T cut. In the latter case, the radiative topological lines provide a better efficiency.

Inclusive ϕ (%)	
$B_s^0 \rightarrow \phi\gamma$	95.51 ± 0.15
$B^+ \rightarrow \phi K^+\gamma$	81.4 ± 0.8

Table 4.11. TOS efficiency of the HLT2 inclusive ϕ line over L0 and HLT1 TOS, defined as LOPhoton TOS or LOElectron TOS and Hlt1TrackAllL0 TOS or Hlt1TrackPhoton TOS, respectively, on offline-selected simulated samples.

Furthermore, the gain of adding the inclusive ϕ trigger to the $B_s^0 \rightarrow \phi\gamma$ HLT2 exclusive TOS selection is found to be, in simulation,

$$g_{\text{Hlt2Bs2PhiGamma}}^{\text{Hlt2IncPhi}} \approx 9\%, \quad (4.7)$$

making it a very interesting trigger for $B_s^0 \rightarrow \phi\gamma$ analyses, such as the photon polarization, which need a sizeable amount of statistics.

4.6. Exclusive strategy

The exclusive trigger approach for radiative decays relies on selecting the photon at L0 and performing a loose selection for $B^0 \rightarrow K^{*0}\gamma$ and $B_s^0 \rightarrow \phi\gamma$ in HLT2. In the case of those $B^0 \rightarrow K^{*0}\gamma$ and $B_s^0 \rightarrow \phi\gamma$ analyses that need to account for trigger efficiencies, such as the one in Chap. 5, it is required that the signal photon has fired L0, one of the daughter tracks of the V meson has fired HLT1, and finally that offline B candidate matches the one that has been built in HLT2. In other words, the offline-selected signal is either LOPhoton TOS or LOElectron TOS in L0, Hlt1TrackAllL0 TOS or Hlt1TrackPhoton TOS in HLT1 and TOS in the corresponding HLT2 exclusive line, either Hlt2Bd2KstGamma TOS or Hlt2Bs2PhiGamma TOS.

Detailed trigger MC efficiencies per TCK with this TOS selection are shown in Table 4.12. In it one can see that the TOS efficiency for the 2011 trigger has been very uniform except for two TCKs:

- 0x360032 corresponds the 2010 trigger configuration: in it, the HLT2 exclusive lines run on the output of the `Hlt1.*Photon.*` lines, predecessors of the HLT1 track trigger. The low efficiency of this TCK highlights the sizeable improvement achieved with respect to 2010 thanks to the changes detailed in §4.5.
- 0x740036 is a test TCK with a LOPhoton and LOElectron cut of $E_T > 3 \text{ GeV}$ and the SPD multiplicity cut decreased to 450.

However, as one can see in Table 3.1, the contribution of these two TCKs is not relevant to the total luminosity, as they only contain 38.8 pb^{-1} of the $\sim 1 \text{ fb}^{-1}$ of data that have been collected in 2011.

Furthermore, it can also be identified the decrease in efficiency of $\sim 6\%$ caused by the introduction of the new L0-based calorimeter reconstruction for the HLT2, as discussed in §4.5.1, since TCK 0x760037.

TCK	$B^0 \rightarrow K^{*0}\gamma$ (%)	$B_s^0 \rightarrow \phi\gamma$ (%)
0x360032	26.5 ± 0.2	28.3 ± 0.2
0x480032	51.5 ± 0.3	55.5 ± 0.3
0x4A0033	51.4 ± 0.3	55.3 ± 0.3
0x5A0032	51.3 ± 0.3	55.2 ± 0.3
0x5B0032	51.3 ± 0.3	55.3 ± 0.3
0x5D0033	51.3 ± 0.3	55.4 ± 0.3
0x6D0032	51.3 ± 0.3	55.3 ± 0.3
0x700034	51.2 ± 0.3	55.2 ± 0.3
0x710035	51.2 ± 0.3	55.3 ± 0.3
0x730035	51.3 ± 0.3	55.3 ± 0.3
0x740036	41.3 ± 0.3	44.9 ± 0.3
0x760037	48.3 ± 0.3	52.2 ± 0.3
0x790037	48.4 ± 0.3	52.3 ± 0.3
0x790038	48.3 ± 0.3	52.2 ± 0.3

Table 4.12. Full exclusive for $B^0 \rightarrow K^{*0}\gamma$ and $B_s^0 \rightarrow \phi\gamma$ TOS efficiencies by TCK, computed as the ratio between the events that pass the trigger TOS requirements over the total number of events on the MC offline-selected sample.

Having exclusive trigger lines for each of the radiative channels has the obvious benefit that the selection strategy and cuts in each line can be tailored to the specific decay being studied. This strategy allows to extract the best possible signal efficiencies for these channels, but it does not provide a significant triggering efficiency for other decays: the trigger efficiency for $B^0 \rightarrow K^{*0}\gamma$ and $B_s^0 \rightarrow \phi\gamma$ with the exclusive strategy is around 50%, while the efficiencies for $B^+ \rightarrow \phi K^+\gamma$ and $B^+ \rightarrow K^{*0} \pi^+\gamma$ are $\sim 16\%$ and $\sim 25\%$, respectively. These two last channels benefit from their similarity to the main $B^0 \rightarrow K^{*0}\gamma$ and $B_s^0 \rightarrow \phi\gamma$, but decays like the baryonic $\Lambda_b \rightarrow \Lambda^0\gamma$ do not benefit from such effects and thus their trigger efficiency is significantly lower.

Therefore, while providing excellent efficiency for the included lines, the exclusive approach in trigger presents the following disadvantages:

- The efficiency on channels that are not selected by one of the exclusive lines is low. A sizeable fraction of events are lost —and cannot be recovered— while a specific channel doesn't have its own exclusive line and hence there is no real possibility for data-mining.
- More maintenance is needed to keep up with the needs of the experiment and the analyses, *i.e.*, modifying cuts and adding new lines as they are needed.
- Background retention and timing increase with the number of lines.

To mitigate these problems, the solution is to move to an inclusive strategy, in which generic signatures of B decays (displaced vertices, pairs of high- p_T tracks, *etc.*) are searched for, provided that the efficiency for signal events can be kept at a similar level.

4.7. Inclusive strategy

The inclusive trigger approach for radiative decays aims at selecting those events which contain the typical signatures of B decays with the addition of the distinct high- E_T photon signal. Robustness is provided by triggers not relying in the photon, namely the inclusive ϕ trigger, which relies on online PID cuts for selecting a pure kaon sample, and the HLT2 topological trigger.

Three sets of HLT2 inclusive lines have been considered in §4.5:

- The topological lines, widely tested and used in LHCb, which have provided the base ground for subsequent inclusive trigger studies.
- The radiative topological lines, inspired in the previous lines, have been tailored for radiative decays by requiring the presence of a high- E_T photon.
- The inclusive ϕ line, which selects events containing a detached ϕ vertex, provides robustness to the trigger strategy of radiative decays containing a ϕ .

The L0 and HLT1 TOS strategies are the same as in the exclusive case, *i.e.*, LOPhoton or LOElectron TOS for L0 and Hlt1TrackAllL0 or Hlt1TrackPhoton TOS for HLT1. The inclusion of the L0Hadron TOS requirement only adds efficiency in the case of considering a photon E_T cut lower than the L0 electromagnetic transverse energy cut of 2.5 GeV. Since neither the Stripping nor the offline selection has been optimized for this situation and hence contain a cut in the photon E_T , the addition of the L0Hadron requirement will be considered during 2012, as will be discussed in §4.9.

The MC efficiencies of the different trigger paths defined by the different inclusive HLT2 requirements are summarized in Table 4.13.

The highlighted trigger lines in the table easily show that the best performance is obtained by using the BBBDT-based radiative topological lines, except in the case of $B_s^0 \rightarrow \phi\gamma$, where the inclusive ϕ trigger offers a better efficiency. Furthermore, comparing these results with those in Table 4.12 we can conclude that the inclusive approach outperforms the exclusive one in three of the four studied channels, being $B^0 \rightarrow K^{*0}\gamma$ the only exception.

	BBBDT-based Topo (%)	Cut-based Radiative (%)	BBBDT-based Radiative (%)	Inclusive ϕ (%)
$B^0 \rightarrow K^{*0}\gamma$	18.7 ± 0.3	42.7 ± 0.3	45.5 ± 0.3	–
$B_s^0 \rightarrow \phi\gamma$	27.5 ± 0.3	45.1 ± 0.3	49.2 ± 0.3	55.7 ± 0.3
$B^+ \rightarrow \phi K^+\gamma$	30.4 ± 0.8	54.7 ± 0.8	55.6 ± 0.8	49.5 ± 0.8
$B^+ \rightarrow K^{*0}\pi^+\gamma$	28.3 ± 1.2	51.8 ± 1.3	53.1 ± 1.3	–

Table 4.13. Full inclusive TOS efficiencies for radiative B decays, computed for the 0x790038 TCK as the ratio between the events that pass a given TOS requirement over the total number of events on the MC offline-selected sample. The L0 and HLT1 requirements are the same in all cases, LOPhoton or LOElectron TOS for L0 and Hlt1TrackAllL0 or Hlt1TrackPhoton TOS for HLT1, and the HLT2 TOS requirement is added on top of that. The most efficient trigger for each decay has been highlighted.

However, the comparison between exclusive and inclusive approaches is still missing the study of the background rejection for each line, *i.e.*, the signal-over-background ratio, S/B . This last piece will be studied directly on data in the next section.

4.8. Performance in 2011

The performance of the trigger strategies defined in the previous sections has been evaluated on Monte Carlo and using the 2011 data. Two aspects of the performance of the lines have been studied: the efficiency on offline-selected signal has been evaluated on both data and Monte Carlo, and the event retention (*rate*) has been determined from real data, both running offline and by making use of the instantaneous rate monitors in the Online System.

Performance for channels not included in the exclusive set of lines, such as $B^+ \rightarrow \phi K^+ \gamma$ and $B^+ \rightarrow K^{*0} \pi^+ \gamma$, will not be shown due to the lack of suitable Stripping lines in the `Stripping17` configuration. At the time of writing, this deficiency has been solved and they have been added to the `Stripping17b` configuration, but data have still not been processed with it.

4.8.1. Efficiency

The TISTOS method detailed in §4.2 can be used to evaluate the TOS efficiencies of the different HLT2 lines on 2011 data. However, the real data sample contains a mixture of signal and background events, which needs to be disentangled in order to correctly evaluate the signal TOS efficiency. The *sPlot* technique [164], a statistical tool which can be used to unfold the different contributions of different sources to the distribution of a data sample in a given variable, can be used to separate the signal from the background contribution.

However, applying the TIS criteria on the offline selected sample produces a sizeable reduction of the available statistics. Given the available statistics, the adopted TIS criteria are the most general possible, `LOGlobal`, `Hlt1Global` and `Hlt2Global`, meaning that an event will be considered TIS if there is at least one TIS decision in L0, one in HLT1 and one in HLT2.

In the case of $B^0 \rightarrow K^{*0} \gamma$, the size of the signal sample obtained with the *sPlot* technique is reduced from 6106 events to 160 TIS events for the full 1.0 fb^{-1} of data recorded in 2011; for $B_s^0 \rightarrow \phi \gamma$, the number of TIS events is 20, from a 781 event sample. The low number of TIS events available for $B^0 \rightarrow K^{*0} \gamma$ and $B_s^0 \rightarrow \phi \gamma$, 160 and 20 events, respectively, greatly limits the possibilities of applying the TISTOS method to extract the trigger efficiencies from data.

Exclusive lines

The global TOS efficiency for the $B^0 \rightarrow K^{*0} \gamma$ exclusive lines, calculated on TIS events, is found to be

$$\epsilon_{\text{TOS}}^{B^0 \rightarrow K^{*0} \gamma} = (57 \pm 4)\%, \quad (4.8)$$

which is higher than the value found in simulation, shown in Table 4.12. The calculation of the TOS efficiency of the HLT2 $B^0 \rightarrow K^{*0} \gamma$ exclusive line on events passing the TIS

requirement and the L0 and HLT1 TOS requirement is found to be

$$\epsilon_{\text{HLT2 TOS}}^{B^0 \rightarrow K^{*0} \gamma} = (84 \pm 3)\%, \quad (4.9)$$

compatible with the value computed from MC, $(85.6 \pm 0.3)\%$, as shown in Table 4.5. The reason for the inconsistency in the global TOS efficiency can be traced to the L0 TOS efficiency. In particular, of the L0 TOS efficiencies,

$$\epsilon_{\text{LOPhoton TOS}}^{B^0 \rightarrow K^{*0} \gamma} = (50 \pm 4)\% \quad \text{and} \quad \epsilon_{\text{LOElectron TOS}}^{B^0 \rightarrow K^{*0} \gamma} = (42 \pm 4)\%, \quad (4.10)$$

the LOElectron channel shows a higher efficiency than anticipated from MC (see Fig. 4.1a).

Further insight can be gained without using the TISTOS method. The invariant mass distributions for offline-selected $B^0 \rightarrow K^{*0} \gamma$ and $B_s^0 \rightarrow \phi \gamma$ can be directly studied and their respective yields extracted through unbinned maximum likelihood fits. While this procedure doesn't allow to calculate any absolute efficiency, it allows to assess the relative efficiencies between the different trigger requirements by comparing their yields and to determine their background rejection performance by comparing their S/B ratios; this is precisely the type of information that is needed to shape the trigger strategies for the future data taking. The invariant mass distributions will be described by a Crystal Ball function for the signal (see §5.3 for a motivation and details for this distribution) and an exponential for the background.

Regarding the exclusive trigger strategy detailed in §4.6, one might wonder how much is lost by applying the TOS requirement. For analyses that don't need to account for trigger efficiencies, dropping the L0 and HLT1 requirements may help to recover events with low- E_T photons or low- p_T tracks which have been triggered by the other B in the event. However, this comes with a cost in terms of the background level. In the case of offline-selected $B^0 \rightarrow K^{*0} \gamma$ data, removing the TOS requirement produces a gain in signal yield of $\sim 15\%$, as can be seen in Fig. 4.4, but the S/B ratio is reduced by 30%. In the case of $B_s^0 \rightarrow \phi \gamma$, the presence of the inclusive ϕ trigger, with has a high efficiency, slightly accentuates the difference between no trigger requirement and the exclusive TOS requirement, which is $\sim 20\%$ as shown in Fig. 4.5. However, removing the exclusive TOS selection induces a 40% decrease in the S/B ratio.

Inclusive ϕ line

It is also worth it to compare the yield for $B_s^0 \rightarrow \phi \gamma$ events with an exclusive TOS requirement, in Fig. 4.5b, with what is obtained replacing the HLT2 requirement for a TOS requirement in the inclusive ϕ line, as shown in Fig. 4.6a. This comparison showcases the importance of a line like the inclusive ϕ , which is able to provide great efficiency with a completely different—and somewhat transversal—triggering strategy, adding robustness to the $B_s^0 \rightarrow \phi \gamma$ selection. Even further, the inclusive ϕ trigger benefits from adding the LOHadron in the L0 TOS requirement, as shown in Fig. 4.6b, and would allow to lower the E_T cut on the photon in the selection to recover some events with high- p_T ϕ daughters².

²Unfortunately, the current Stripping for radiative decays contains a 2.5 GeV cut in the photon transverse energy, and therefore it is not possible to study these kind of events.

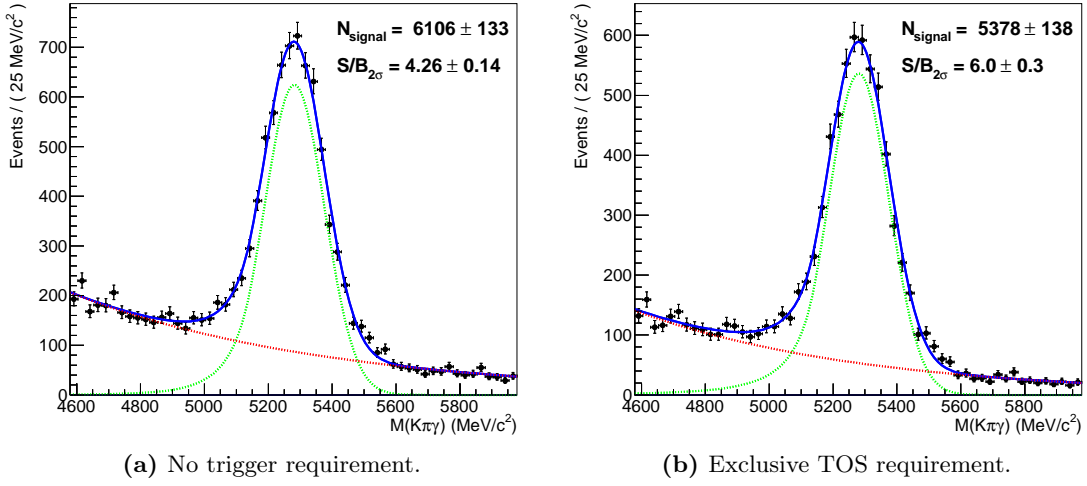


Figure 4.4. Mass distribution for offline-selected $B^0 \rightarrow K^{*0}\gamma$ events without any trigger requirement and with TOS requirement on the exclusive lines.

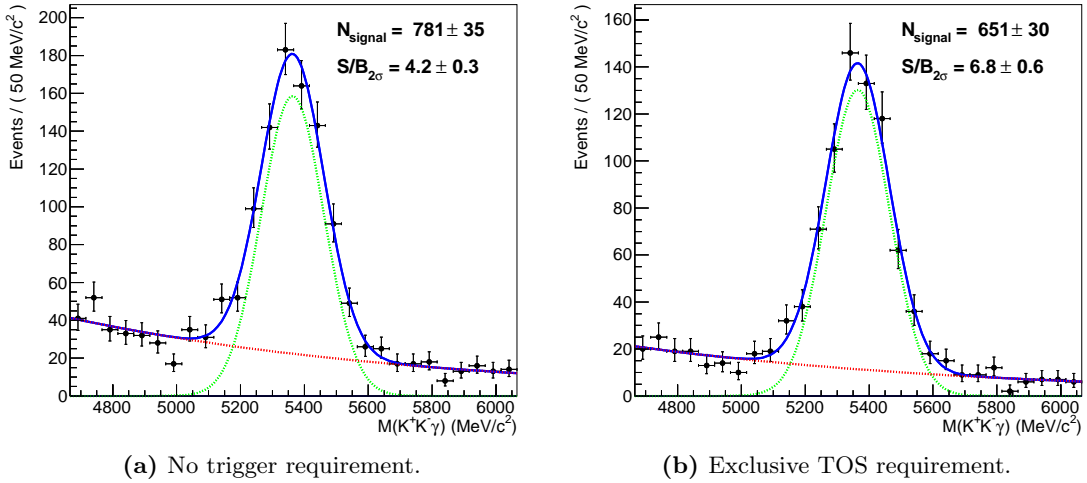


Figure 4.5. Mass distribution for offline-selected $B_s^0 \rightarrow \phi\gamma$ events without any TOS requirement and with TOS requirement on the exclusive lines.

Cut-based radiative topological lines

The cut-based radiative topological lines were added to the trigger after the LHC technical stop in June, 2011. Therefore, in order to compare their performance with the exclusive lines we have to restrict to a subset of the full data sample; specifically, events from the 0x760037 TCK onwards are considered, adding up to $\sim 700 \text{ pb}^{-1}$. Comparison between the exclusive lines and the cut-based radiative topological lines is presented in Fig. 4.7. As predicted by the MC studies summarized in Table 4.12 and Table 4.13, the exclusive lines are slightly more efficient: the ratio between the signal yields in Fig. 4.7a and Fig. 4.7b, corresponding to $B^0 \rightarrow K^{*0}\gamma$, is 1.05 ± 0.05 , while the

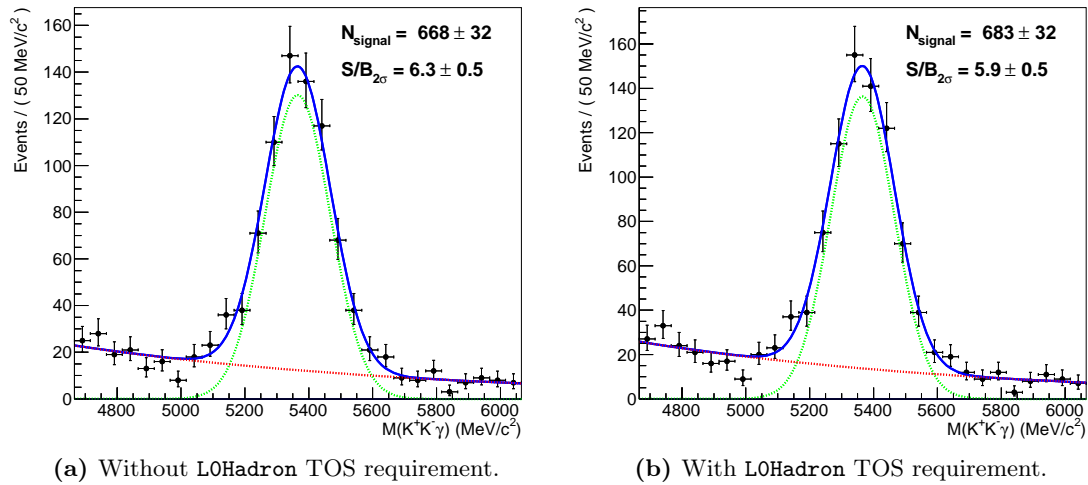


Figure 4.6. Mass distribution for offline-selected $B_s^0 \rightarrow \phi\gamma$ events with Hlt2IncPhi TOS requirement, with and without TOS requirement in the LOHadron line.

ratio of $B_s^0 \rightarrow \phi\gamma$ yields for Figs. 4.7c-4.7d is 1.13 ± 0.09 . However, it must be taken into account the HLT2 exclusive lines are built the same way as the offline selection, and therefore they offer the maximum possible signal efficiency; if the inclusive trigger approach were to be adopted, both stripping and offline selections for radiative decays would need to be adapted.

The other side of the coin in the comparison is the background retention, where the radiative topological lines perform better, removing almost completely the high-mass combinatorial background.

In summary, the cut-based radiative topological lines perform almost as good as the exclusive lines, yield-wise, while providing at the same time an improved background rejection. Furthermore, the track TOS line is free from any L0 requirements, and it can eventually allow to access a lower E_T for the photon with the same rate by tightening the p_T track requirement; this would allow to take advantage of the signal events that pass through the LOHadron.

BBDT-based radiative topological lines

In order to assess the performance of the BBDDT-based radiative topological lines, introduced after the end-of-August technical stop, only data taken with the 0x790038 TCK, corresponding to $\sim 360 \text{ pb}^{-1}$, can be considered. The comparison between the exclusive TOS, the cut-based radiative topological, and the BBDDT-based topological for $B^0 \rightarrow K^{*0}\gamma$ can be found in Fig. 4.8, while the analogous plots for $B_s^0 \rightarrow \phi\gamma$, plus the inclusive ϕ TOS, can be found in Fig. 4.9. Several conclusions can be extracted from these figures:

- The BBDDT-based radiative topological lines offer a performance almost up-to-par with the exclusive lines, providing at the same time an excellent combinatorial background rejection. The price that needs to be paid for this improvement is the introduction of a multivariate method that performs complex cuts which cannot

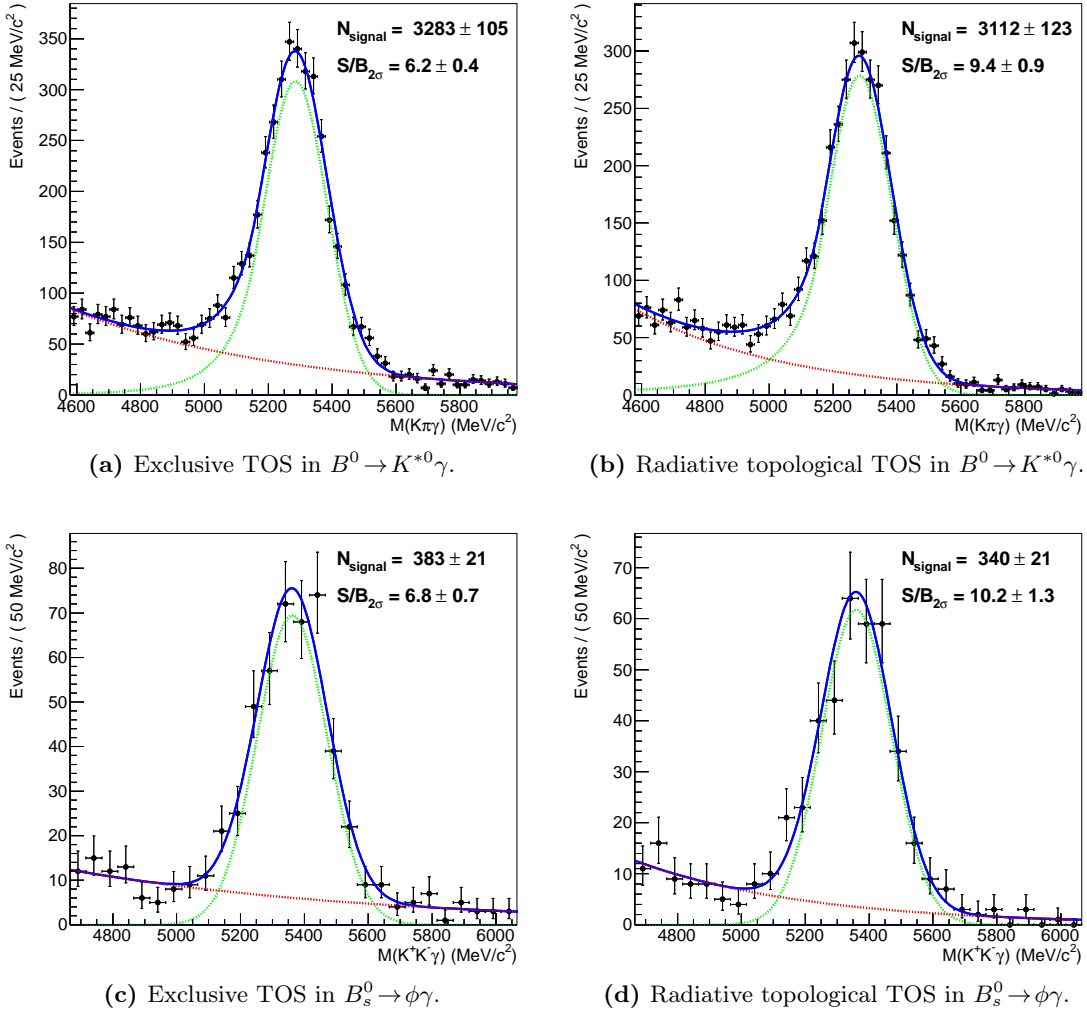


Figure 4.7. Mass distribution for offline-selected $B^0 \rightarrow K^{*0}\gamma$ (top) and $B_s^0 \rightarrow \phi\gamma$ (bottom) events with HLT2 exclusive TOS requirement (left) and HLT2 cut-based radiative topological TOS requirement (right). The data sample corresponds to a luminosity of $\sim 700 \text{ pb}^{-1}$, collected from June to the end of the 2011 run.

be easily understood.

- The BBDDT-based radiative topological lines have big overlap with the regular topological lines because they are built together using the same machinery. Therefore, adding the regular topological to the BBDDT-based radiative topological TOS, as done in Figs. 4.8e-4.9f, does not improve the efficiency. This is not the case with the cut-based radiative topological, in which the addition of the regular topological TOS requirement shown in Figs. 4.8c-4.9d allows to recover part of the efficiency and puts them at the level of the BBDDT-based radiative topological.
- In the case of $B_s^0 \rightarrow \phi\gamma$, the performance of the inclusive ϕ trigger is outstanding:

it provides the best efficiency with a good background rejection. Furthermore, if it is added to the HLT2 TOS requirement, it pushes the radiative topological lines to the same efficiency level as the exclusive line, as shown in Fig. 4.10.

4.8.2. Rate

The rate taken by the radiative HLT2 lines has been tested on a real minimum-bias data sample with 284k L0-Physics-passed (Routing Bit 11) events. Several trigger configurations have been simulated with MOORE: the trigger configuration from October 2011, and the same configuration without the radiative exclusive lines, without the cut-based radiative topological lines and without neither. Afterwards, the number of events that pass each line have been converted to HLT2 rate by assuming a L0 rate of 1 MHz.

A summary of the obtained results can be found in Table 4.14. In it, the rate of the individual lines is given as the estimation obtained by simulating the trigger on minimum-bias data and as the instantaneous online rate in real running conditions [128]. Furthermore, the rate added to the HLT2 by the exclusive and radiative topological lines is displayed.

	Events	Estimated rate (Hz)	Online rate (Hz)
$B^0 \rightarrow K^{*0} \gamma$ exclusive	10	35 ± 11	27.501
$B_s^0 \rightarrow \phi \gamma$ exclusive	2	7 ± 5	6.01389
Extra from exclusive lines	12	42 ± 12	–
Rad. topological L0 photon	76	268 ± 31	254.335
Rad. topological Track TOS	59	208 ± 27	175.323
Extra from rad. topological	52	183 ± 25	–
H1t2TopoRad2BodyBBDT	78	275 ± 32	268.246
H1t2TopoRad2plus1BodyBBDT	129	454 ± 59	449.785
Inclusive ϕ	19	66 ± 21	55.2732

Table 4.14. Rate of the radiative lines, comparing $\mu > 2$ minimum-bias data and the online rate in run 102422 (HLT2 at 2864 Hz, HLT2 topological rate ~ 1500 Hz). The rate added to the HLT2 by the inclusion of both the exclusive and the radiative topological is also shown.

The cut-based HLT2 radiative topological adds $\sim 15\%$ of rate to the regular topological trigger, 4 times more than the exclusive lines, with the benefit that many new radiative decays are included. This is a crucial point because if an event is not triggered, it is lost. Therefore, the cost of the adoption of the inclusive strategy is acceptable because it greatly opens the analysis possibilities for radiative decays, both in the present and in the future.

4.9. Prospects for 2012

The LHCb trigger strategy in 2011 was inclined towards inclusiveness, as can be clearly seen from the fact that the majority of the HLT2 bandwidth was dedicated to inclusive

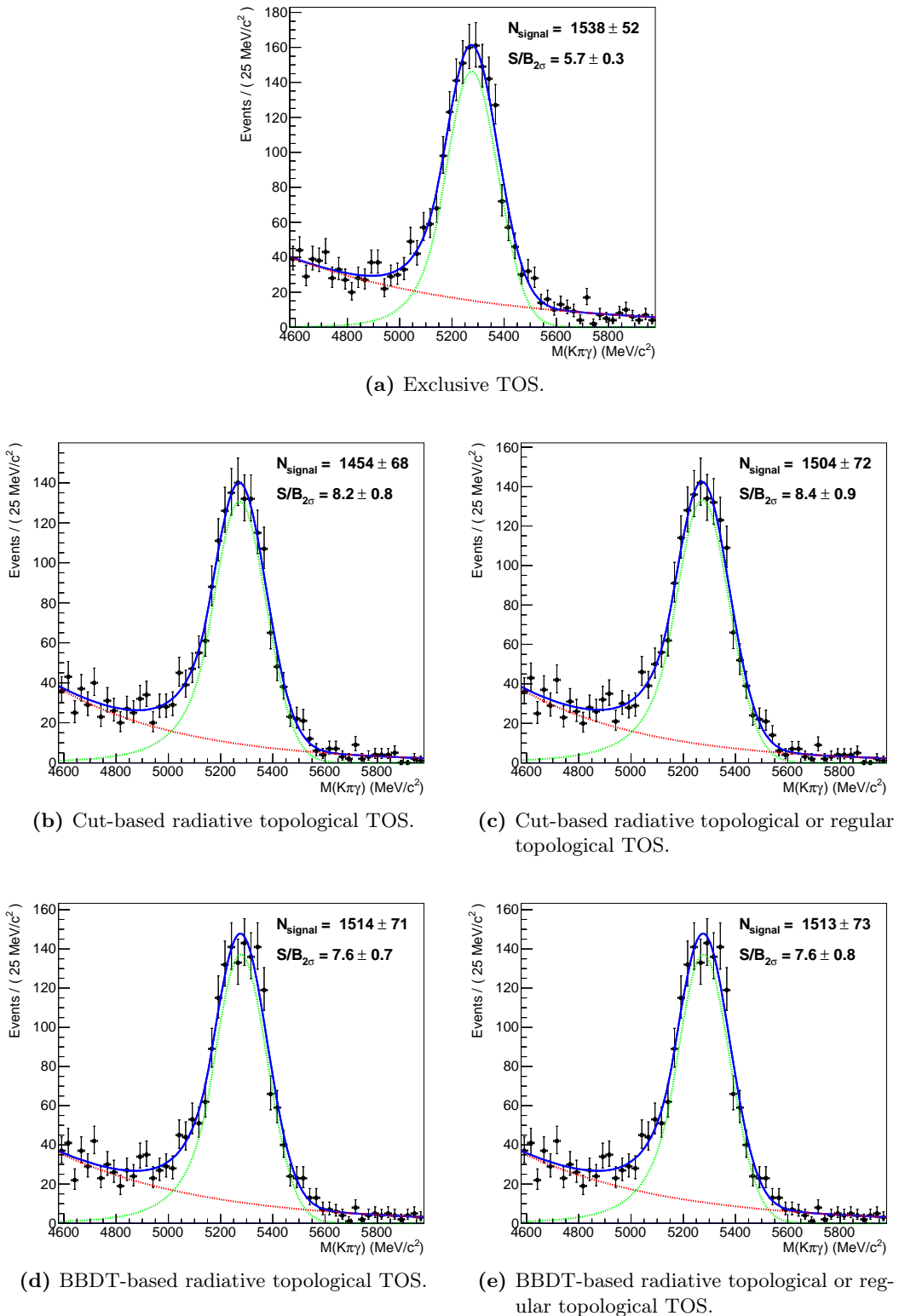


Figure 4.8. Mass distribution for offline-selected $B^0 \rightarrow K^{*0}\gamma$ events with HLT2 exclusive TOS (top), HLT2 cut-based radiative topological TOS (middle) and HLT2 BBTD-based radiative topological TOS (bottom) requirements. The data sample corresponds to a luminosity of $\sim 360 \text{ pb}^{-1}$, collected from the end of August to the end of the 2011 run.

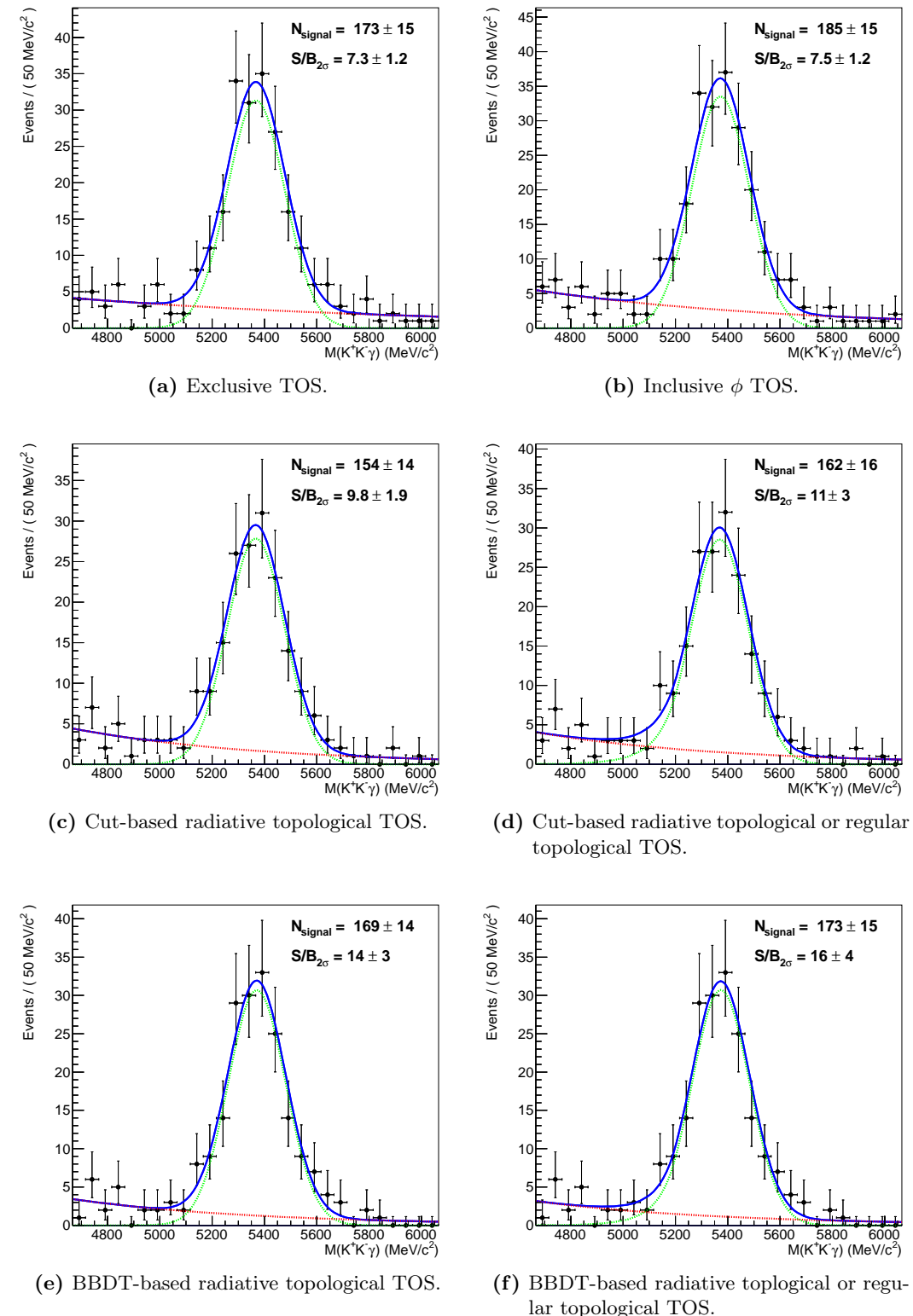


Figure 4.9. Mass distribution for offline-selected $B_s^0 \rightarrow \phi\gamma$ events with HLT2 exclusive TOS (top left), HLT inclusive ϕ (top right), HLT2 cut-based radiative topological TOS (middle), and HLT2 BBDT-based radiative topological TOS (bottom) requirements. The data sample corresponds to a luminosity of $\sim 360 \text{ pb}^{-1}$, collected from the end of August to the end of the 2011 run.

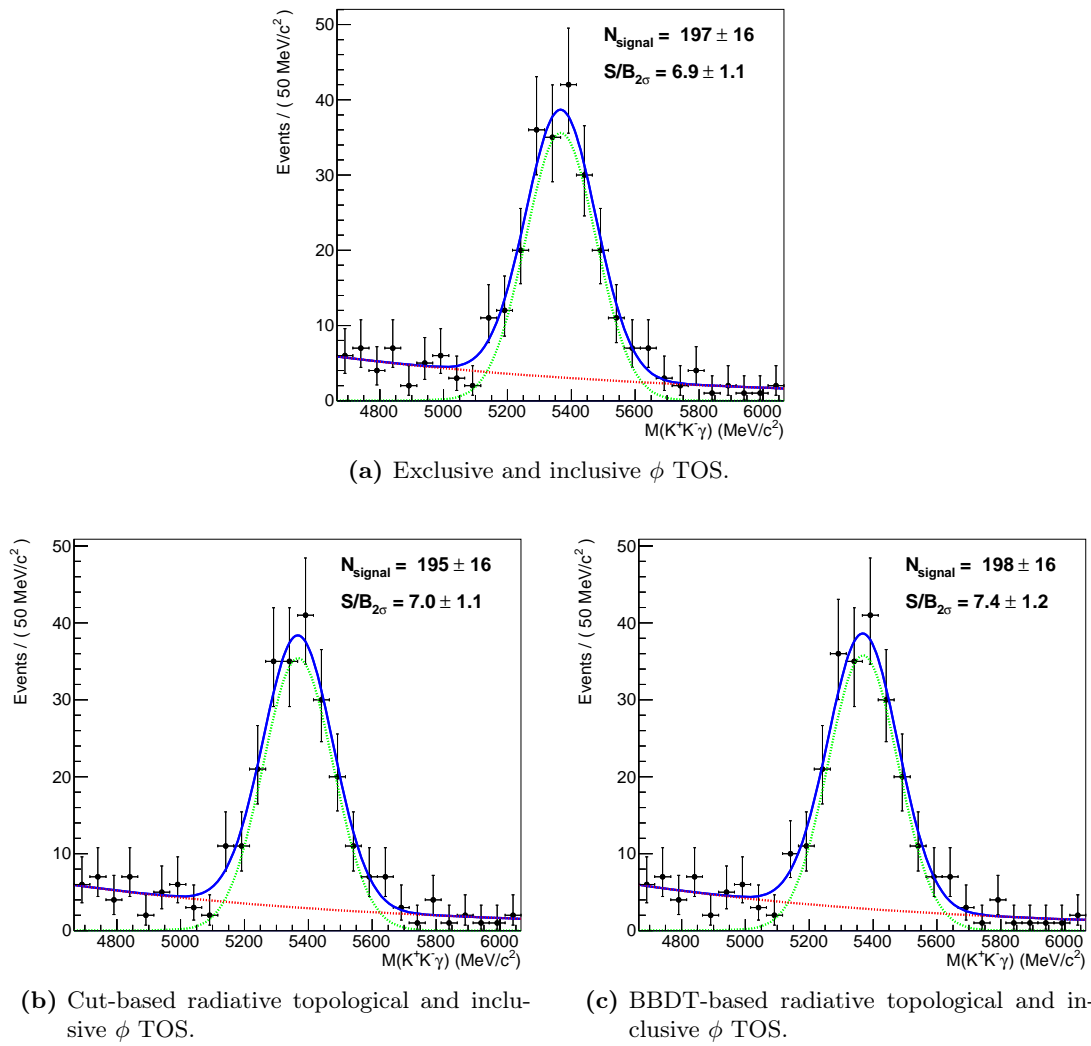


Figure 4.10. Mass distribution for offline-selected $B_s^0 \rightarrow \phi\gamma$ events with HLT2 exclusive (top), HLT2 cut-based radiative topological (bottom left), and HLT2 BBBDT-based radiative topological (bottom right), plus inclusive ϕ TOS requirement. The data sample corresponds to a luminosity of $\sim 360 \text{ pb}^{-1}$, collected from the end of August to the end of the 2011 run.

lines such as the HLT2 topological trigger. The usage of exclusive lines has been reduced to those cases where it is completely necessary because the inclusive triggers don't provide enough efficiency, and always with the requirement of a low bandwidth.

Following this path, and given the excellent performance provided by the HLT2 radiative topological trigger at the end of 2011, the radiative decays trigger strategy for 2012 will be also inclusive. Besides the fact that this strategy better accommodates the experiment-wise trigger strategy, this decision is also motivated by the start of several new analyses, such as the CP -asymmetry studies for $B^+ \rightarrow \phi K^+\gamma$ and $B^+ \rightarrow K^{*0}\pi^+\gamma$, or the study of radiative decays of Λ_b baryons, which were not favored by the exclusive lines. Further studies involving other channels, such as the $B^0 \rightarrow K^{*0}\gamma$ isospin-asymmetry, or the CP asymmetry of $b \rightarrow d\gamma$ transitions such as $B \rightarrow \rho\gamma$, will

also be possible in the future because these decays will have already been triggered with significant efficiency.

Based on the 2011 performance studies described in the previous section, the HLT2 cut-based radiative topological lines have been modified to decouple the L0 Photon and the Track TOS lines. The idea behind the changes is to use the L0 Photon line to select radiative events based on the distinct photon signature and use the Track TOS line to recover radiative events with low E_T photons. To achieve this goal, the E_T cut in the photon has to be lowered, and a cut in the maximum p_T of the two used tracks needs to be introduced to keep a reasonable rate. Exact values of these cuts are still to be determined during the 2012 HLT commissioning period, but working values are $E_T > 2\text{ GeV}$ for the photon and $\max(p_T) > 3.5\text{ GeV}/c$ for the tracks, following the transverse energy cut in L0Hadron channel, which would imply a $\sim 10\%$ gain in efficiency with a similar rate. If this improvement was indeed possible, stripping and offline selection changes would need to follow this change.

The decision of which inclusive lines to use in 2012 will depend on the running conditions and the necessary background rejection. Since cuts in the radiative topological lines are currently placed at the limit of the phase space where no substantial efficiency is lost, a need for further background rejection could imply a sizeable loss in performance. In this scenario, the BBDT-based lines have the potential to provide a better performance than cut-based ones, as it has already been shown in LHCb [160]. If no further reduction is necessary, and the modifications of the cut-based radiative topological lines provide a similar performance as the BBDT-based ones, it would be advisable to keep the cut-based lines because they are easier to interpret. In the case of $B_s^0 \rightarrow \phi\gamma$ and $B^+ \rightarrow \phi K^+\gamma$, the inclusive ϕ line provides robustness and extra efficiency.

In addition, it is interesting to keep the exclusive trigger lines as a way to cross check the results obtained by making use of the radiative topological lines, specially de BBDT-based ones, which may be hard to interpret. However, to do that their impact on the overall HLT2 rate needs to be negligible. Therefore, the exclusive lines for $B^0 \rightarrow K^{*0}\gamma$ and $B_s^0 \rightarrow \phi\gamma$ have been modified to lower their rate to an acceptable level of $\mathcal{O}(1\text{ Hz})$. This rate reduction has been achieved by tightening the cuts in the lines, effectively turning them into quasi-offline selections performed in the trigger, as shown in Table 4.15.

The new, tighter exclusive lines have been tested with two minimum bias testing samples, one with a higher μ and the other with a low μ , with 85,417 and 81,635 L0-Physics events, respectively; in addition, the tracking conditions in the HLT2 have been modified to add downstream tracking and $p_T > 300\text{ MeV}/c$ and $p > 3000\text{ MeV}/c$ as the requirements for a track to be reconstructed³. It has been found that no events pass the exclusive radiative triggers in the high μ sample, while one event passes the `Hlt2Bd2KstGamma` line in the case of the low μ sample; this is equivalent to a rate of 5 Hz with almost a 100% uncertainty.

Given the big uncertainty on their rate, these new lines will be checked during the HLT commissioning work at the beginning of the 2012 run in order to determine with more precision their rate and to make the proper adjustments. Possible modifications to lower the rate include the addition of a track TOS filter or a GEC on the number of tracks.

Summing up, an inclusive trigger strategy for radiative decays has been prepared for

³At the time of writing, these were the working conditions for the HLT2 trigger optimization for 2012.

	$B^0 \rightarrow K^{*0} \gamma$ line	$B_s^0 \rightarrow \phi \gamma$ line	
Track p	(MeV/c)	> 3000	> 3000
Track p_T	(MeV/c)	> 300	> 300
Track χ^2		< 5	< 5
Track IP χ^2		> 20	> 20
$V \Delta M_{\text{PDG}}$	(MeV/ c^2)	< 100	< 20
V vertex χ^2		< 16	< 25
Photon E_T	(MeV)	> 2600	> 2600
$B p_T$	(MeV/c)	> 3000	> 3000
B IP χ^2		< 12	< 12
B DIRA	(mrad)	< 63	< 45
$B \Delta M_{\text{PDG}}$	(MeV/ c^2)	< 1000	< 1000
L0 channel	LOPhoton or LOElectron	L0Photon or LOElectron	
HLT1 lines	HLT1 Physics	HLT1 Physics	

Table 4.15. Cuts applied in the 2012 HLT2 exclusive lines for $B^0 \rightarrow K^{*0} \gamma$ and $B_s^0 \rightarrow \phi \gamma$, separated in track cuts, vector meson (V) cuts, photon cuts, B candidate cuts and trigger filters.

the 2012 LHC run, replacing the exclusive strategy used so far. Furthermore, all new lines have been tested and checked at the end of the 2011 run, and have shown good performance. However, it will be necessary to perform a thorough commissioning of both the inclusive and the exclusive lines in order to adjust to possible changes in the tracking conditions in HLT2, which could largely affect the retention rates.

5

Measurement of the ratio $\mathcal{B}(B^0 \rightarrow K^{*0}\gamma) / \mathcal{B}(B_s^0 \rightarrow \phi\gamma)$

The main aim of this analysis is to extract the ratio of branching fractions of $B^0 \rightarrow K^{*0}\gamma$ with $K^{*0} \rightarrow K^\pm\pi^\mp$ and $B_s^0 \rightarrow \phi\gamma$ with $\phi \rightarrow K^+K^-$, and their complex conjugates¹. From this result, and using the well-measured value of $\mathcal{B}(B^0 \rightarrow K^{*0}\gamma)$, the branching fraction of $B_s^0 \rightarrow \phi\gamma$ can be extracted. This is the first analysis of radiative B decays performed at LHCb, and as such it requires a detailed study of elements, such as signal shapes and associated backgrounds, which will be extremely helpful in future analyses.

The heart of the measurement is the extraction of the signal yields for each channel. To do that, the line shape of the mass distributions of the selected B^0 and B_s^0 candidates has to be determined, including a detailed account of all possible background contributions. These yields need to be corrected for the efficiency of the selection and the relative abundance of both B species in LHC collisions.

In this analysis, the B^0 and B_s^0 candidates are built by combining a vector meson candidate, either a K^{*0} or a ϕ , and a photon. The vector meson candidates are built from pairs of oppositely charged tracks, a kaon and a pion in the case of the K^{*0} and two kaons in the case of the ϕ . Those track pairs with an invariant mass located within the defined mass window for each of vector mesons are combined with a photon to calculate the invariant mass of the B candidates.

In order to obtain the best possible measurement, the selection is carried out following the same procedure for both channels. In this way, most systematical effects cancel out in the calculation of the ratio of efficiencies, resulting in a reduced uncertainty. For a complete cancellation, both decays should have:

- The same photon efficiency.
- The same kinematics.
- The same topology.

However, this is not completely true in our case due to the different nature of the

¹Throughout this chapter, whenever a mode is given, the charge conjugate is also implied.

	m (MeV/ c^2)	Γ (MeV/ c^2)
K^{*0}	895.94 ± 0.22	48.7 ± 0.8
ϕ	1019.455 ± 0.020	4.26 ± 0.04

Table 5.1. Mass and natural width of the K^{*0} and ϕ resonances [21].

daughters of the vector mesons —and of the vector mesons themselves. Thus, the main differences between the two decays are:

- Since the $B^0 \rightarrow K^{*0}\gamma$ contains one pion and one kaon in the final state and the $B_s^0 \rightarrow \phi\gamma$ contains two kaons, different particle identification requirements are needed.
- Due to the different width of the two resonances, as shown in Table 5.1, different mass window requirements of the vector mesons need to be applied. The K^{*0} mass window —the mass difference to the nominal K^{*0} mass peak position starting from which candidates are rejected— must be tighter than that of the ϕ in order to reduce the contamination from random kaon-pion pairs.
- The difference between the masses of the ϕ meson and its daughters is very small compared to the difference between the masses of the K^{*0} and its daughters. Kaons coming from a ϕ are closer as there is few extra momentum that they can take, whereas the kaon and pion coming from a K^{*0} can take a larger fraction of momentum. This implies that the vertex reconstruction efficiency is different for the two vector mesons.

The photon E_T spectrum for both decays is very similar, as it will be seen in Fig. 5.18. Therefore, the systematics associated to the photon cancel out if the selection and reconstruction criteria are the same in both channels.

5.1. Data samples and software versions

5.1.1. Real data

The analysis is performed on events from the LHCb 2011 March-November running period at $\sqrt{s} = 7$ TeV, corresponding to a luminosity of 1.0 fb^{-1} . This number differs from the recorded luminosity quoted in §3.1 because the previous number comes from the online measurement, and the number quoted in analyses comes from an offline analysis procedure, which allows for a more precise luminosity estimation [165, 166].

The branching fractions of the two channels of interest are of the order of 10^{-5} , as seen in Table 1.3. Therefore, given the luminosity collected, and using the measured $b\bar{b}$ cross section documented in early LHCb publications [97], the approximate number of events in each channel produced in the LHCb acceptance before trigger, reconstruction and selection is given in Table 5.2.

Data have been recorded with the Trigger Configuration Keys (TCK) detailed in Table 3.1, each with its corresponding MOORE version, going from v10r2 to v10r9. Data have been reconstructed using the `Reco12` configuration with BRUNEL v41r1 and stripped with the `Stripping17` configuration with DAVINCI v29r1.

Events in acceptance	
$B^0 \rightarrow K^{*0} \gamma$	$\mathcal{O}(3M)$
$B_s^0 \rightarrow \phi \gamma$	$\mathcal{O}(740k)$

Table 5.2. Approximate number of events within the LHCb acceptance before (trigger, reconstruction and selection) for an integrated luminosity of 1.0 fb^{-1} at the center of mass energy of $\sqrt{s} = 7 \text{ TeV}$, using the measured $b\bar{b}$ cross section $(75.3 \pm 5.4 \pm 13.0) \mu\text{b}^{-1}$ [97].

5.1.2. Monte Carlo simulation

Many of the signal and background studies have been performed on simulated Monte Carlo data samples. In LHCb, Monte Carlo (MC) simulation samples are produced centrally, organized in coherent campaigns. Since the 2010 running conditions were noticeably different than anticipated, the MC samples that had been used for physics performance studies, belonging to the DC06 simulation campaign, did not provide an accurate description of the collisions collected by LHCb. Therefore, a simulation campaign, called MC10, was started at the end of that year to produce a dataset consistent with the 2010 data. Similarly, at the end of 2011 a new campaign, called MC11, started to produce simulated data consistent with the observed conditions in 2011. This campaign is still ongoing at the time of writing.

Signal and background studies have been performed on simulated samples corresponding to the MC11 Monte Carlo campaign, unless stated otherwise. In some cases, data from the MC10 simulation campaign have been used due to the lack of the corresponding MC11 sample; in addition, loosely selected truth-matched MC10 signal samples, consisting in reconstructed signal with no further cuts other than the requirement of a match with the MC truth, has been used in some studies. The size of each Monte Carlo sample is summarized in Table 5.3.

The MC11 samples are being produced with the following software versions:

- GAUSS v41r1 with $\nu = 2$ to reproduce the average visible number of interactions in 2011 running (see Fig. 3.6).
- BOOLE v23r1.
- MOORE v12r8g1 with the 0x40760037 TCK, a special version of the 0x00760037 TCK specially crafted for Monte Carlo. The trigger is run in flagging mode, *i.e.*, not rejecting events, but only flagging the ones that would pass the trigger.
- BRUNEL v41r1p1 running the `Reco12` configuration.
- DAVINCI v29r1p1 running the `Stripping17` stripping pass, also in flagging mode.

The used MC10 samples were produced under the following conditions:

- GAUSS v39r0 with $\nu = 2.5$, which roughly corresponds to the average number of visible interactions in the 2010 data sample.
- BOOLE v21r9.
- MOORE v10r2, used to run the trigger algorithms with the 0x002e002a TCK in flagging mode.

	MC10 (Mevts)	MC11 (Mevts)
$B^0 \rightarrow K^{*0}\gamma$	10.18	6.99
$B_s^0 \rightarrow \phi\gamma$	4.05	3.98
$B^+ \rightarrow K^{*0}\pi^+\gamma$	—	2.01
$B^+ \rightarrow \phi K^+\gamma$	0.10	2.01
$B^0 \rightarrow K^+\pi^-\pi^0$	2.01	0.22
$B_s^0 \rightarrow K^+\pi^-\pi^0$	2.01	—
$B^0 \rightarrow \pi^+\pi^-\pi^0$	—	1.01
$B^0 \rightarrow K^{*0}e^+e^-$	1.03	3.98
$B^0 \rightarrow D^-\rho^+$	—	0.22
$B^0 \rightarrow D_s^*(\pi\pi\pi^0)\pi$	1.00	—
$B^0 \rightarrow D^0(K\pi\pi^0)K^{*0}$	2.52	—
$B^+ \rightarrow K^{*+}(K^+\pi^0)K^+K^-$	0.10	—
$B^+ \rightarrow K^{*+}(K^+\pi^0)\pi^+\pi^-$	1.10	—
$B^+ \rightarrow D^0(K\pi\pi^0)\pi^+$	0.10	—
$B^+ \rightarrow J/\psi(\rho^0\pi^0)K^+$	0.10	—
$B_s^0 \rightarrow \rho^+(\pi^+\pi^0)K^-$	0.06	—
$\Lambda_b \rightarrow \Lambda^0\gamma$	—	0.50
$\Lambda_b \rightarrow \Lambda(1520)\gamma$	—	1.00
$\Lambda_b \rightarrow \Lambda(1670)\gamma$	—	1.16

Table 5.3. Statistics of the MC10 and MC11 datasets used in this study, with radiative signal in the top section and background in the bottom one. Each of the samples is split in two halves of approximately the same size, corresponding to the two polarities of the magnetic field.

- BRUNEL v37r8p5, with the `Reco08` configuration.
- DA VINCI v28r2p2 running the `Stripping12` stripping pass, also in flagging mode.

When producing the ROOT NTuples for analysis from the MC10 DSTs, an extra reconstruction pass was applied with DA VINCI v29r1 to reproduce the `Reco12` calorimeter configuration from 2011.

5.2. Event selection

As already mentioned, the main point in the analysis strategy is try to benefit from the cancellations of most uncertainties in the ratio of efficiencies. In particular, the cancellations are maximized by adopting the same selection strategy for both channels. B meson candidates are constructed through the following process:

1. Vector meson candidates are built from pairs of oppositely charged tracks.
2. Photon candidates are built from the clusters in the ECAL.
3. Vector meson and photon candidates are combined to build the B candidate.

Common cuts for the tracks and the photon are used to minimize the impact of systematic effects. However, some inevitable differences appear in the selection of the

vector meson candidate, especially in the particle identification of its decay products and in its mass window cut.

As explained in §3.7.3, events used in analysis have been selected through the following steps:

1. *Trigger*. Data taken by LHCb are filtered by the L0 and HLT trigger stages, and only those events that are selected by the trigger are kept.
2. *Stripping*. Stored raw data are reconstructed and selected to produce reduced data samples for physics analyses. In the case of this analysis, the Radiative Stripping stream is used.
3. *Offline selection*. B candidates are built from stripped events and are selected using tight cuts in order to achieve the best possible signal significance; these are the candidates used in the physics analyses.

Details on these three steps follow, with an explanation of the most relevant triggers in §5.2.1, the Radiative Stripping stream in §5.2.2 and the offline selection used for the $B^0 \rightarrow K^{*0}\gamma$ and $B_s^0 \rightarrow \phi\gamma$ decays in §5.2.3.

5.2.1. Trigger

The exclusive trigger strategy, defined in Chap. 4, has been chosen for this analysis, and therefore the required trigger lines are the following:

- In L0, `L0Electron` and `L0Photon` select those events with an electromagnetic deposition in the ECAL with a transverse energy with respect to the beam direction, E_T , greater than the thresholds detailed in Table 5.4. Additionally, a subset of the events that pass these two lines also pass the `L0ElectronHi` and `L0PhotonHi` lines, which require a higher E_T cut.
- In the HLT1, the relevant lines are `Hlt1TrackAllL0` and `Hlt1TrackPhoton` single track lines. They select events based on the transverse momentum and impact parameter of the tracks with respect to the beam direction. `Hlt1TrackAllL0` selects low- E_T photons with a harder cut in the required track, while `Hlt1TrackPhotonL0` allows to lower the p_T requirement for the track at the cost of a harder E_T cut on the photon, as illustrated in Table 5.4.
- In HLT2, the exclusive radiative lines, `Hlt2Bd2KstGamma` and `Hlt2Bs2PhiGamma`, which only run on events that pass the `L0Electron` and `L0Photon` lines. Events are selected by building the vector meson, combining it with a high- E_T photon and applying loose cuts in the same direction as the stripping and offline selections. Details of the E_T and p_T cuts can be found in Table 5.4.

In order to extract the ratio of branching fractions the exclusive TOS requirement is made, *i.e.*, it is required that the signal tracks and photon are responsible of firing the corresponding trigger lines. This requirement is essential for a better understanding of the trigger efficiencies and for enforcing the similarity of the trigger path of the $B^0 \rightarrow K^{*0}\gamma$ and $B_s^0 \rightarrow \phi\gamma$, which will ensure the cancellation of the systematic effects induced by the trigger. With that consideration in mind, the trigger TOS selections for each channel are those given in §4.6:

	photon E_T (MeV/c)	track p_T (MeV/c)
L0Electron	2500	—
L0Photon	2500	—
L0ElectronHi	4200	—
L0ElectronHi	4200	—
Hlt1TrackAllL0	(2500)	1700
Hlt1TrackPhoton	(4200)	1200
Hlt2Bd2KstGamma	2600	500
Hlt2Bs2PhiGamma	2600	500

Table 5.4. Transverse energy/momenta thresholds for the relevant trigger lines in the 2011 TCKs. Values in parentheses indicate that the threshold is not explicitly applied, but a consequence of a previous cut.

- L0 TOS is defined as L0Electron TOS or L0Photon TOS.
- HLT1 TOS is defined as Hlt1TrackAllL0 TOS or Hlt1TrackPhoton TOS.
- HLT2 TOS is defined as Hlt2Bd2KstGamma TOS and Hlt2Bs2PhiGamma TOS for $B^0 \rightarrow K^{*0}\gamma$ and $B_s^0 \rightarrow \phi\gamma$, respectively.

No explicit TOS in the L0 LOXHi lines is required since it is implied by the regular L0Photon or L0Electron lines TOS.

The decision to use the exclusive trigger TOS strategy is justified by several arguments:

- The efficiency of the radiative exclusive lines is twice that from the inclusive HLT2 topological lines, and the overlap between these two HLT2 requirements is very high. Thus, the small gain obtained by adding the HLT2 topological requirement to the exclusive one would bring an unknown systematic effect arising from the fact that the two decays are topologically different.
- While the efficiency of the radiative topological lines is at par with the exclusive lines, they were not introduced in the trigger until June 2011. Furthermore, they suffered from several modifications from this date until the end of the 2011 data taking period, making them less stable than the exclusive lines.
- The inclusive ϕ line offers a moderate efficiency gain for $B_s^0 \rightarrow \phi\gamma$, as shown in Table 4.13. However, introducing this line in the analysis implies a full source of systematic effects that don't cancel, since it only triggers with significant efficiency on one of the decays of interest. This goes against the analysis strategy outlined previously, so the gain of a few % is not enough to justify its inclusion in this particular case.

5.2.2. Stripping

After having been triggered and stored, the events are reconstructed and stripped in order to keep under control both the computing time spent needed for physics analyses and the storage requirements.

The Radiative stream of the LHCb Stripping is designed as a sum of lines, each of which performs an exclusive selection of a radiative B decay following the procedure outlined at the beginning of §5.2. In Stripping17, only the $B^0 \rightarrow K^{*0}\gamma$ and $B_s^0 \rightarrow \phi\gamma$ decays are included, performing an offline-like selection with looser cuts. In addition, several monitoring lines have been devised, allowing to access, with a prescale, parts of the dataset that would otherwise be cut out in the Stripping selection, *e.g.*, the sidebands of the K^{*0} or the B particles. The used cuts are summarized in Table 5.5, with the monitoring line cuts in parentheses.

5.2.3. Offline selection

Reconstructed candidates are filtered through a cut-based selection. The values of the cuts have been optimized in order to maximize the significance ξ [167]:

$$\xi = \frac{S}{\sqrt{S + B}}, \quad (5.1)$$

where S and B are the number of signal and background events, respectively. The optimization of ξ was done using simulated $B^0 \rightarrow K^{*0}\gamma$ and $B_s^0 \rightarrow \phi\gamma$ Monte Carlo from DC06.

At the same time, special care has been taken to keep the cuts and their values the same for both decays whenever possible. Table 5.5 shows the Stripping and offline selection cuts for both decays, and it can be seen that only the PID and vector meson mass window cuts differ.

Following the B candidate building procedure outlined at the beginning of §5.2, the motivation of the cuts detailed in Table 5.5 follows. In the first step of building the B candidates, in both the $B^0 \rightarrow K^{*0}\gamma$ and $B_s^0 \rightarrow \phi\gamma$ cases a vector meson (K^{*0} or ϕ) is built from two oppositely charged tracks. The requirements applied on these tracks, corresponding to the first two sections of Table 5.5, are the following:

- Tracks are built by minimizing a χ^2 function of the difference between the hit position and what is expected from the track model [168]. Track quality is ensured by requiring the track to have $\chi^2 < 5$.
- In order to make sure that the track does not come from the primary vertex, PV, a cut on its impact parameter, IP, is applied. Instead of a direct cut in this distance, the error on its determination is taken into account. Thus, the applied cut is $\text{IP } \chi^2 > 25$.
- In order to reduce combinatorial background coming from soft tracks, a loose $p_T > 500 \text{ MeV}/c$ cut is applied. Furthermore, the maximum p_T of the two charged tracks is required to be above $1200 \text{ MeV}/c$.
- Tracks are identified as kaons or pions by evaluating the change in log likelihood under different particle ID hypotheses [118]. Proton and pion hypotheses against kaon hypothesis are used for the kaon identification, $\text{DLL}_{K\pi} > 5$ and $\text{DLL}_{Kp} > 2$, and the kaon hypothesis against the pion hypothesis is used to identify the latter, $\text{DLL}_{K\pi} < 0$.

The invariant mass distributions after the track selection are shown in Fig. 5.1a.

The vector meson candidates are filtered with very simple criteria, corresponding to the third section of Table 5.5, to remove background coming from random track combinations, and their effect is shown in Fig. 5.1b:

- The quality of the vertex is ensured by cutting in the χ^2 resulting from the vertex fit, $\chi^2 < 9$.
- The background coming from non-resonant $K^\pm\pi^\mp$ and K^+K^- combinations can be reduced by applying strict cuts to the mass window around the vector meson mass. As can be seen in Table 5.1, the K^{*0} resonance is much wider than the ϕ . Adding this to the fact that the K^{*0} has more combinatorial background than the ϕ because it has one pion in its decay products, it becomes clear that the mass window cut must be tighter for the K^{*0} than for the ϕ . Indeed, the mass window for the K^{*0} is cut at ~ 1 width, $\Delta M_{K^\pm\pi^\mp, \text{PDG}} < 50 \text{ MeV}/c^2$, while the ϕ mass window is set at ~ 2 widths, $\Delta M_{K^+K^-, \text{PDG}} < 9 \text{ MeV}/c^2$.

The photon that is combined with the vector meson needs to be filtered to avoid contamination from other calorimetric particles, specially electrons and merged π^0 , as detailed in the fourth section of Table 5.5:

- Background coming from low- E_T photons, such as *bremsstrahlung* photons, is removed with the requirement that $E_T > 2600 \text{ MeV}/c$.
- As detailed in §3.4.4, discrimination between photons and electrons is done by an anti-coincidence between the ECAL cluster and the extrapolation of the reconstructed tracks up to the calorimeter. The $\Delta \ln \mathcal{L}$ between the photon and non-photon hypotheses is extracted, and this is transformed to a value $\text{CL} \in [0, 1]$ with the following transformation

$$\text{CL} = \frac{\tanh(\Delta \ln \mathcal{L}) + 1}{2}. \quad (5.2)$$

The optimal cut for photon identification is found to be $\text{CL} > 0.25$.

- Discrimination between photons and merged π^0 is done using the electromagnetic cluster shape [169, 170]. Several cluster shape variables are combined in a multivariate discriminator, and the optimal cut for identifying photons is found to be > 0.5 .

The invariant mass distribution obtained after applying these cuts on the photon is shown in Fig. 5.1c.

Combinations of one vector meson and a photon are selected to obtain the final set of B candidates in the mass window of $1 \text{ GeV}/c^2$ around the nominal mass of the corresponding meson. The cuts shown in the last section of Table 5.5 are applied in order to remove as much combinatorial and physical background as possible, improving the significance ξ :

- To make sure that the B candidate is well reconstructed, two cuts are applied. One on one side, its IP with respect to its PV must be small, $\text{IP } \chi^2 < 9$. On the other side, the DIRA, *i.e.*, the angle between the momentum of the B candidate and the direction defined by the vector between the PV and the decay vertex of the B must also be small, and the cut is set at $< 0.02 \text{ rad}$.

- As stated before, B mesons have $c\tau = 455.4 \mu\text{m}$. Due to their boost, they fly an average of $\sim 1 \text{ cm}$ in the detector before they decay. To remove the contamination from random combinations, B candidates are required to be at a significant distance from their corresponding PV, *i.e.*, their flight distance χ^2 must be higher than 100.
- B candidates from random combinatorics have a lower p_T spectrum. A cut in this variable is implemented in order to reduce this contamination, $p_T > 3000 \text{ MeV}/c$.
- To remove B candidates coming from partially reconstructed decays, extra tracks compatible with the B vertex are looked for: the χ^2 of the vertex is compared with the χ^2 of the vertex obtained when adding an extra track from the event, and the difference between them, $\Delta\chi^2$, is computed. The minimum value of $\Delta\chi^2$ is an indicator of the B candidate isolation, with smaller values meaning that the B candidate could be coming from a partially reconstructed B decay. Therefore, a $\Delta\chi^2 > 2$ cut is applied in the event selection.
- Contamination from decays with a π^0 misidentified as a single photon can be reduced by exploiting the polarization of the vector meson. In particular, the angular distribution of the helicity angle θ_H , *i.e.*, the angle between one of the daughters of the vector meson and the B candidate in the rest frame of the vector meson, is used. This angle is expected to follow a $\sin^2 \theta_H$ distribution for signal, a $\cos^2 \theta_H$ for the π^0 background, and to be flat for combinatorial background, as detailed in Appendix A. The optimized value for the cut in θ_H is $|\cos \theta_H| < 0.8$.

The invariant mass distribution obtained after applying the kinematical cuts on the B candidate is illustrated in Fig. 5.1d, while the vertex isolation effect on the partially reconstructed background is shown in Fig. 5.1e. The final invariant mass distributions, obtained after applying the TOS criteria, are shown in Fig. 5.1f.

5.3. Signal shape

Using the MC11 signal samples from Table 5.3, the shape of the mass peaks for the B meson and the vector mesons, K^{*0} and ϕ , has been studied. In the case of the vector mesons, the MC11 signal is compared to the distributions obtained from data.

Vector meson mass shape

The K^{*0} and ϕ resonances can be described by a relativistic P -wave Breit-Wigner distribution [171, 172]:

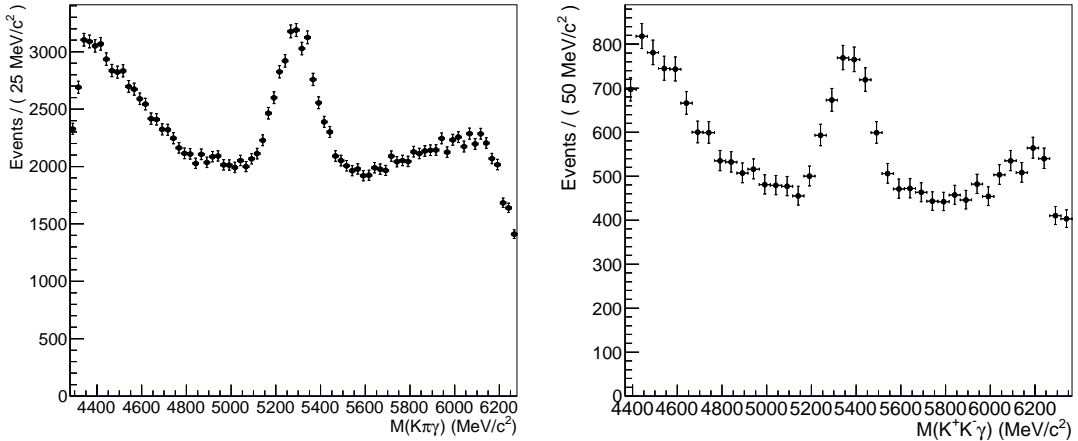
$$BW(m) = \frac{m_0 m \Gamma(m)}{(m_0^2 - m^2)^2 + (m \Gamma(m))^2} \quad (5.3)$$

$$\Gamma(m) = \Gamma_0 \left(\frac{q}{q_0} \right)^{(2l+1)} \frac{m_0}{m}, \quad (5.4)$$

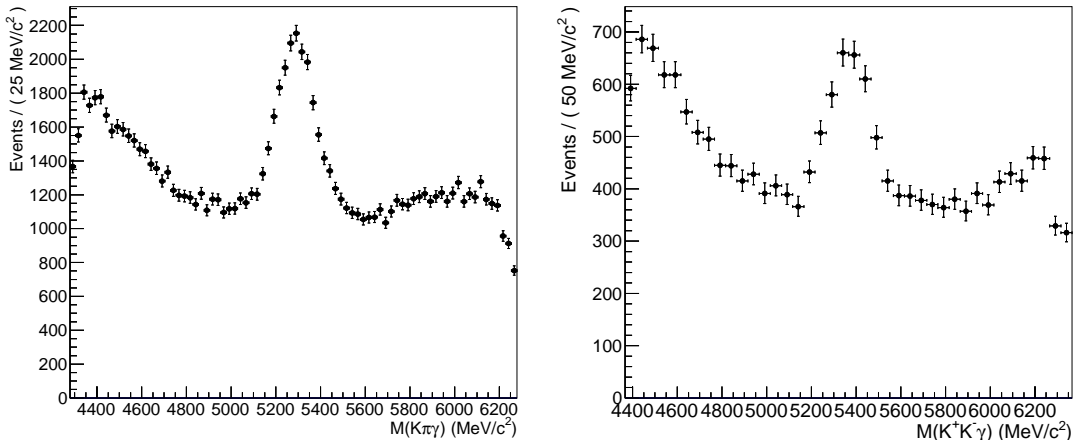
where m_0 is the resonance mass, $\Gamma_0 \equiv \Gamma(m_0)$ its natural width, $l = 1$ the transferred angular momentum, and $q(m)$ the momentum of the decay products in the rest frame

	$B^0 \rightarrow K^{*0}\gamma$		$B_s^0 \rightarrow \phi\gamma$	
	Stripping	Offline	Stripping	Offline
Track χ^2	< 5	–	< 5	–
Track IP χ^2	> 10	> 25	> 10	> 25
Track p_T	(MeV/c)	> 500	–	> 500
Max track p_T	(MeV/c)	–	> 1200	–
Kaon DLL $K\pi$	> -5	> 5	> -5	> 5
Kaon DLL Kp	–	> 2	–	> 2
Pion DLL $K\pi$	–	< 0	–	–
V meson vertex $\Delta\chi^2$	< 15	< 9	< 15	< 9
V meson ΔM_{PDG}	(MeV/ c^2)	< 100 (150)	< 50	< 15
Photon E_T	(MeV)	> 2600	> 2600	> 2600
Photon CL	–	> 0.25	–	> 0.25
π^0/γ separation	–	> 0.5	–	> 0.5
B candidate p_T	(MeV/c)	–	> 3000	–
B candidate IP χ^2		< 15	< 9	< 15
B candidate DIRA	(mrad)	< 20 (60)	< 20	< 20 (60)
B candidate FD χ^2		–	> 100	–
B candidate ΔM_{PDG}	(MeV/ c^2)	< 1000 (2000)	< 1000	< 1000 (2000)
B candidate $ \cos\theta_H $	–	< 0.8	–	< 0.8
B candidate isolation $\Delta\chi^2$	–	> 2	–	> 2

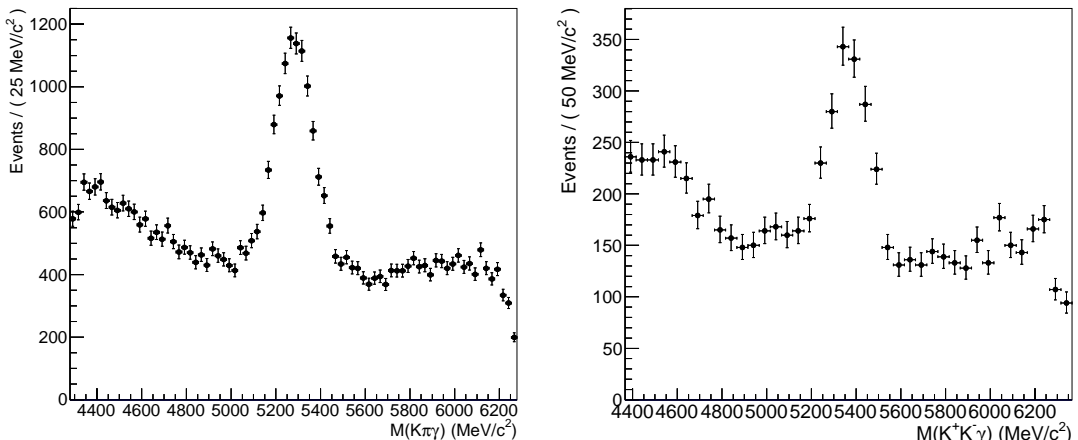
Table 5.5. Selection cuts for the $B^0 \rightarrow K^{*0}\gamma$ and $B_s^0 \rightarrow \phi\gamma$ decays. For each cut, the stripping (with the monitoring line value in parentheses, if different) and offline values are shown. The cuts are separated in sections, which are, in order, track cuts, PID cuts, vector meson cuts, photon cuts, and B candidate cuts.



(a) $B^0 \rightarrow K^{*0}\gamma$ and $B_s^0 \rightarrow \phi\gamma$ after applying the track requirements.



(b) $B^0 \rightarrow K^{*0}\gamma$ and $B_s^0 \rightarrow \phi\gamma$ after applying the vector meson requirements.



(c) $B^0 \rightarrow K^{*0}\gamma$ and $B_s^0 \rightarrow \phi\gamma$ after applying the photon requirements.

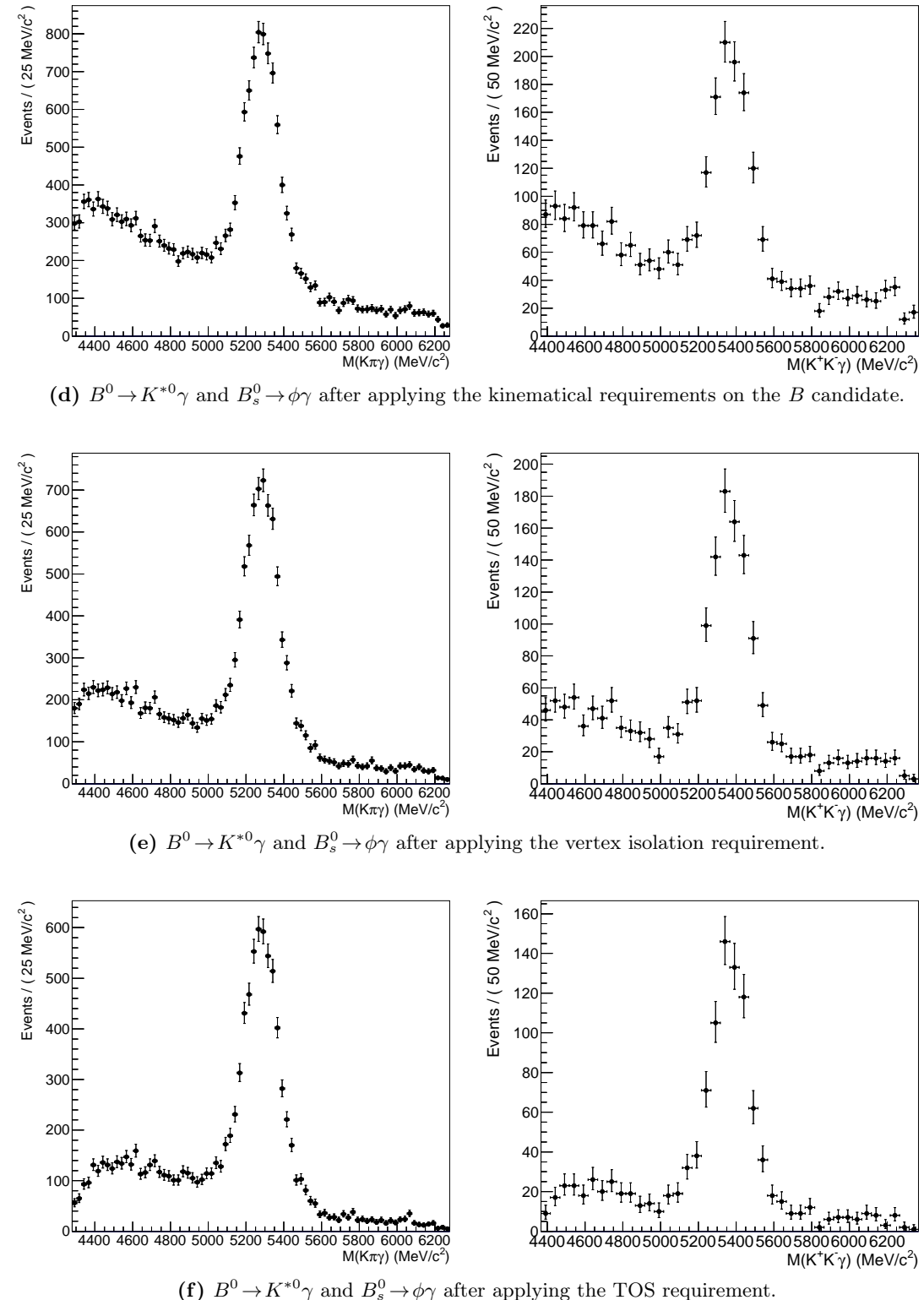


Figure 5.1. Effect of the cuts in Table 5.5 on the $B^0 \rightarrow K^{*0}\gamma$ (left) and $B_s^0 \rightarrow \phi\gamma$ (right) samples from 2011 data. Each of the consecutive subfigures contains the cuts in the previous one, plus de ones detailed in its caption.

of the mother particle:

$$q(m)_{K^{*0}} = \frac{\sqrt{(m^2 - (m_K + m_\pi)^2)(m^2 - (m_K - m_\pi)^2)}}{2m} \quad (5.5)$$

$$q(m)_\phi = \frac{\sqrt{m^2 - 4m_K^2}}{2}. \quad (5.6)$$

To take into account the detector resolution, the Breit-Wigner distribution has been numerically convoluted with a Gaussian distribution of width σ . The resulting PDF has been fitted to the vector meson invariant mass distributions, as shown in Fig. 5.2, with Γ_0 fixed to the corresponding values in Table 5.1.

While the chosen PDF for describing the vector mesons is shown to be very accurate for ϕ , the used line shape fails to exactly reproduce the K^{*0} simulation, specially at the regions more than $2\Gamma_0$ away from the nominal mass peak position. The high statistics of the used MC sample highlight all those elements that have not been taken into account in the description, such as the efficiency dependency on the mass (higher masses tend contain less slow pions, which are very inefficient), the resolution dependency with the mass, or the presence of final state radiation.

However, these effects are not visible in the data sample, which has less statistics and is polluted by the presence of combinatorial background, as shown in Fig. 5.2c. Furthermore, it can be seen that the lack of a wider mass window for the K^{*0} doesn't allow a good determination of the resolution parameter. Still, data and MC show good agreement both on the K^{*0} and the ϕ .

B meson mass shape

The width of the shape of the B meson mass distribution is dominated by the calorimeter energy resolution of the photon. In addition, two contributions in the signal mass shape have been considered:

- In the low mass region, possible losses in the photon energy due to the fiducial volume of the calorimeter have been accounted for by making use of a Crystal Ball (CB) distribution [174]. This distribution consists of a Gaussian core and a power-law low-end tail below a certain threshold, and is given by

$$CB(x; \alpha, n, \bar{x}, \sigma) = N \times \begin{cases} \exp\left(-\frac{(x - \bar{x})^2}{2\sigma^2}\right) & \text{for } \frac{x - \bar{x}}{\sigma} > -\alpha \\ A \times \left(B - \frac{x - \bar{x}}{\sigma}\right)^{-n} & \text{for } \frac{x - \bar{x}}{\sigma} \leq -\alpha \end{cases}, \quad (5.7)$$

where A and B are

$$A = \left(\frac{n}{|x|}\right)^n \exp\left(-\frac{\alpha^2}{2}\right), \quad (5.8)$$

$$B = \frac{n}{|\alpha|} - |\alpha|, \quad (5.9)$$

and N is the normalization factor.

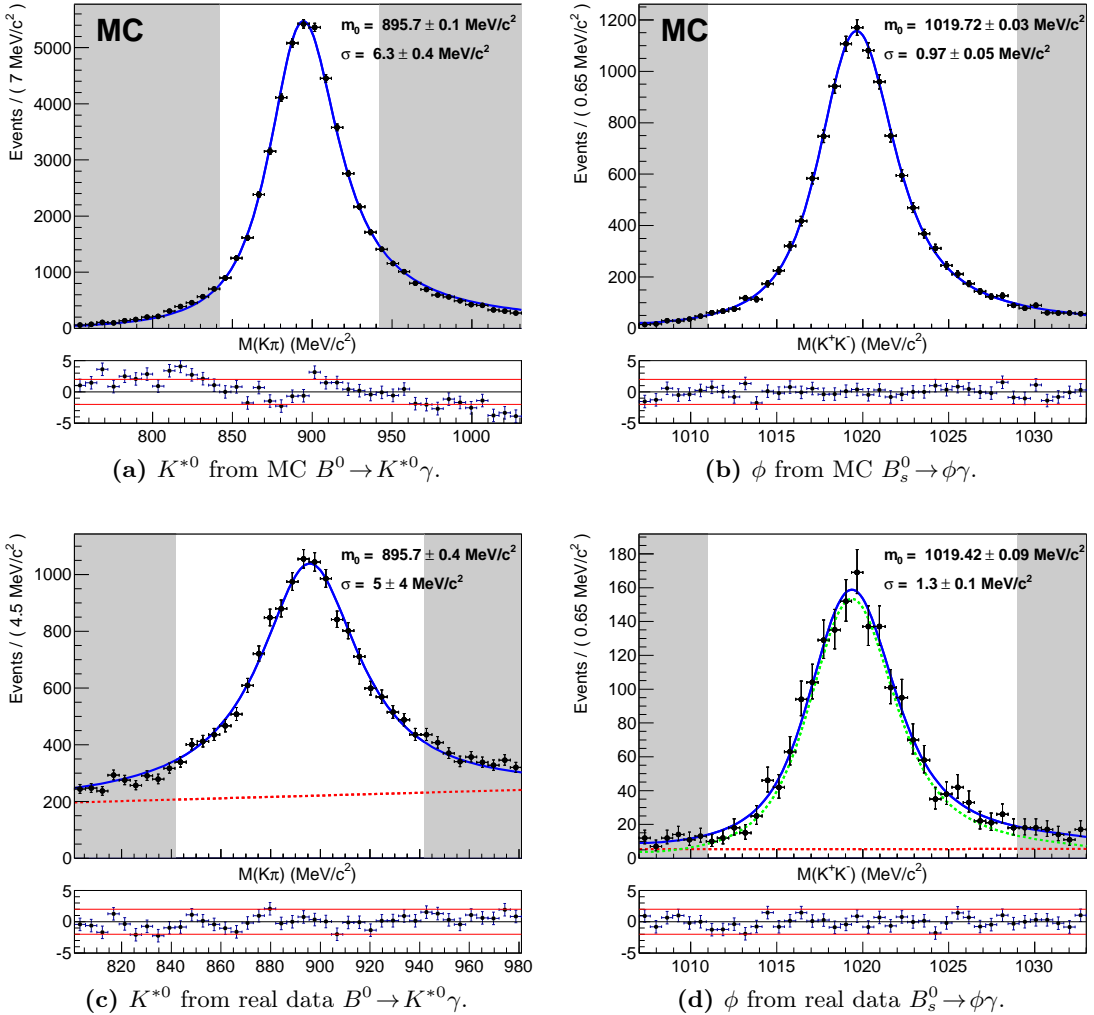


Figure 5.2. Mass distribution of the vector meson for simulated events from the MC10 loose sample (up) and 2011 data (down). The offline selection has been applied except for the vector meson mass window cut, but the areas rejected by this cut appear shaded. The χ^2 residuals for Poisson-distributed histograms, as detailed by Baker and Cousins [173], are included in the lower part of the plot to give a visual hint of the goodness-of-fit. However, it must be taken into account that binned χ^2 tests are not the optimal method for the determination of the goodness-of-fit in the case of unbinned fits, as this one.

- The tail at high masses can be partially explained by the spread in the error of the reconstructed B meson, and has been observed in several analyses in LHCb [175, 176]. Toy MC studies show that, while the high mass tail forms naturally from a B mass with per-event error distribution, there are other effects contributing to the tail that have yet to be determined. Namely, it has been observed that there exists a correlation between events in the high mass tail and events with a large error on the B mass. This high mass tail can be parametrized by a CB distribution with $\alpha < 0$.

Taking these contributions into account, the B meson signal shape is parametrized as the sum of two CB distributions with common mean position μ and width σ , and relative fraction f . The subscripts L and H are used to denote the CB with $\alpha > 0$ and $\alpha < 0$, respectively. The results of fitting the MC data for $B^0 \rightarrow K^{*0}\gamma$ and $B_s^0 \rightarrow \phi\gamma$ can be seen in Fig. 5.3, with the values of the parameters detailed in Table 5.6. It can be seen that, due to wide width of the peak and the strong fall of the high-mass tail, the n_H parameter cannot be defined with precision.

		$B^0 \rightarrow K^{*0}\gamma$		$B_s^0 \rightarrow \phi\gamma$	
		no smearing	2% smearing	no smearing	2% smearing
μ	(MeV/ c^2)	5278.6 ± 0.5	5279.4 ± 0.6	5365.3 ± 0.5	5365.1 ± 0.6
σ	(MeV/ c^2)	75.8 ± 0.4	92.8 ± 0.5	75.5 ± 0.5	93.3 ± 0.6
α_L		2.15 ± 0.05	2.14 ± 0.06	2.13 ± 0.05	2.19 ± 0.05
n_L		0.92 ± 0.06	0.99 ± 0.07	0.74 ± 0.05	0.75 ± 0.06
α_H		-1.0 ± 0.1	-1.1 ± 0.2	-1.0 ± 0.1	-0.87 ± 0.08
n_H		7 ± 1	7 ± 2	9 ± 2	20 ± 19
f		0.71 ± 0.04	0.72 ± 0.07	0.65 ± 0.06	0.79 ± 0.03

Table 5.6. Summary of fit parameters obtained when using the sum of two CB contributions to parametrize the mass shape of $B^0 \rightarrow K^{*0}\gamma$ and $B_s^0 \rightarrow \phi\gamma$ on MC, with no smearing of the photon energy and with a 2% smearing to reproduce the signal width observed in data.

The width of the signal in MC, ~ 75 MeV/ c^2 , is narrower than the width of the data shown in Fig. 5.1f, ~ 95 MeV/ c^2 , even though the simulated samples have been produced with assuming a 1% residual miscalibration in the ECAL. In order to reproduce the signal data resolution, a 2% Gaussian smearing is applied to the energy of the photon, and the fit results are shown in Fig. 5.4. This additional miscalibration is in good agreement with the performance achieved by the ECAL π^0 -based calibration procedure in 2011 [116]. It can be seen in Table 5.6 that, as expected, all fitted parameters are stable when applying the smearing procedure, except for the width of the CB .

5.4. Background composition

As will be discussed in §5.6, the $B^0 \rightarrow K^{*0}\gamma$ and $B_s^0 \rightarrow \phi\gamma$ yields are extracted from the signal fit of the $K^\pm\pi^\mp\gamma$ and $K^+K^-\gamma$ mass distributions of the selected B candidates. However, these mass distributions contain a mixture of signal and background events, since the offline selections from Table 5.5 are not able to completely remove

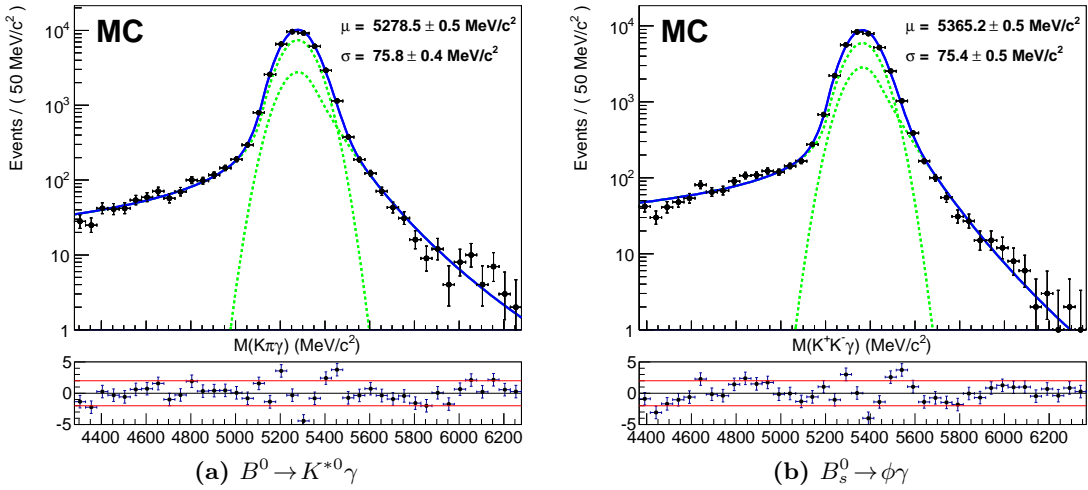


Figure 5.3. Mass distribution for offline-selected MC events, with the corresponding fit with two CB's (solid blue line). The individual CB distributions are shown as green dashed lines.

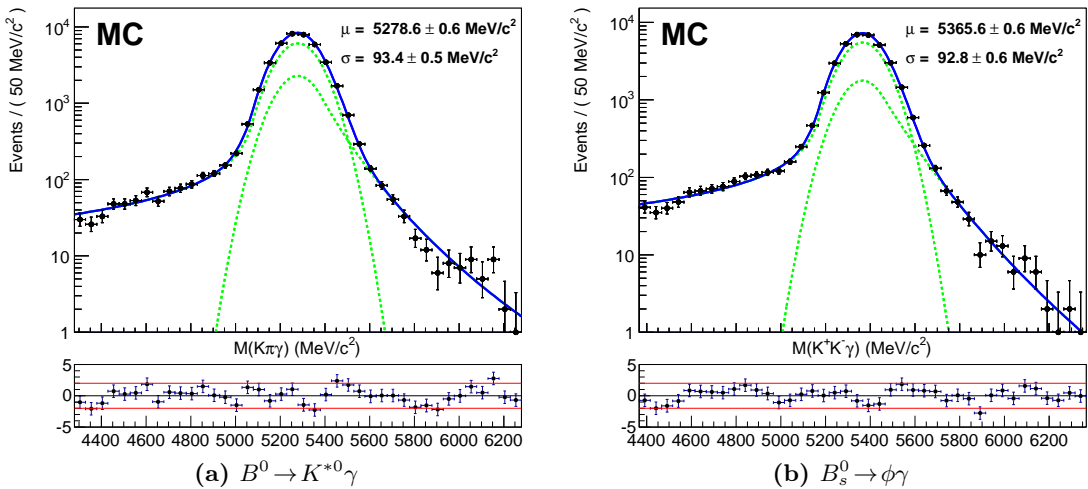


Figure 5.4. Mass distribution for offline-selected MC events with a photon energy smear of 2%. The corresponding fit with two CB's is shown as solid blue line, with the individual CB distributions represented as green dashed lines.

the background events. The background contributions to the $B^0 \rightarrow K^{*0}\gamma$ and $B_s^0 \rightarrow \phi\gamma$ mass distributions can be condensed in the following groups:

- Combinatorial background.
- Contamination from merged π^0 .
- Contamination from partially reconstructed B decays.
- Contamination from baryonic radiative decays.
- Signal cross-feed.

A detailed study of the aforementioned backgrounds is performed in the following sections. The contamination to the signal from each of the backgrounds to the signal is calculated as

$$C_{\text{bkg}}^{\text{data}} \equiv \frac{\mathcal{N}_{\text{bkg}}}{\mathcal{N}_{\text{sig}}} = \frac{\epsilon_{\text{sig}}^{\text{MC}}}{\epsilon_{\text{bkg}}^{\text{MC}}} \frac{\epsilon_{\text{sig}}^{\text{acc}}}{\epsilon_{\text{bkg}}^{\text{acc}}} \frac{\mathcal{B}_{\text{sig}}}{\mathcal{B}_{\text{bkg}}} \frac{f_{\text{sig}}}{f_{\text{bkg}}} C_{\text{sig}}^{\text{MC}}. \quad (5.10)$$

Whenever MC samples are used, PID cuts are not applied directly because of the bad description of the PID variables in the simulation, as will be explained in §5.6.7. Instead, a data-based reweighing has been applied to better model their behavior and extract the correct efficiencies and contaminations. Furthermore, a 2% Gaussian smearing has been applied to the photon energy in order to account for the ECAL performance in data.

5.4.1. Combinatorial background

A check of the mass shape for the $K\pi\gamma$ combinatorial background in $B^0 \rightarrow K^{*0}\gamma$ can be performed by making use of the K^{*0} mass sidebands. The $B^0 \rightarrow K^{*0}\gamma$ monitoring trigger and stripping selections, with the K^{*0} mass window extended to $150 \text{ MeV}/c^2$ and a prescaling of $1/20$ to match the data flow budget, have been used to get a better access to these sidebands.

However, as can be seen in Fig. 5.2a, the distribution of the K^{*0} invariant mass in the MC signal sample still contains a sizeable fraction of signal events for $|\Delta M_{K\pi,\text{PDG}}| > 100 \text{ MeV}/c^2$ (~ 2 times the K^{*0} natural width), specially at higher masses. Thus, in order to reduce the presence of signal when studying the shape of the combinatorial background, only the low mass sideband of the K^{*0} has been used. The distribution of the $K\pi\gamma$ invariant mass in the low mass sideband, $\Delta M_{K\pi,\text{PDG}} < -100 \text{ MeV}/c^2$, for the events passing the wide K^{*0} mass window monitoring Stripping line is displayed in Fig. 5.5.

Even within the limited statistics, a hint of a signal mass peak is observed, as expected. The shape of the combinatorial background is well defined, nonetheless; it has been fitted with an exponential function excluding 2σ around the nominal B^0 mass peak position, *i.e.*, in the range $[4479, 5079] \cup [5479, 6079] \text{ MeV}/c^2$. The decay constant of the exponential is found to be

$$\tau_{B^0,\text{SB}} = -1.5 \pm 0.8 \text{ GeV}^{-1}c^2. \quad (5.11)$$

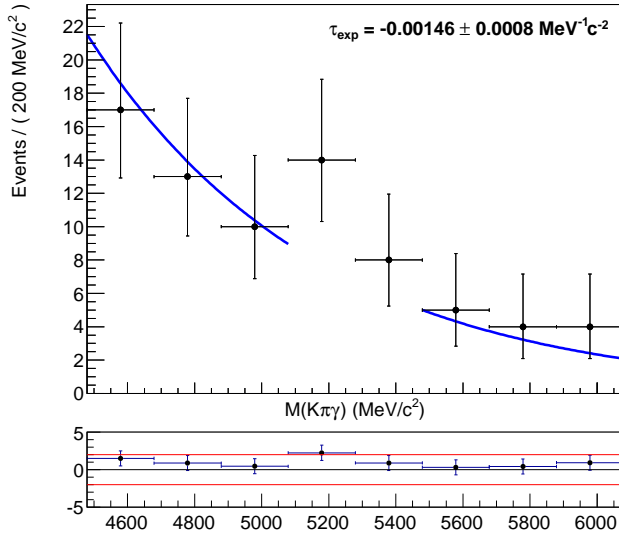


Figure 5.5. $K\pi\gamma$ mass shape for the combinatorial background selected in the low K^{*0} mass sideband. It has been modeled with a single exponential excluding the $[5079, 5479] \text{ MeV}/c^2$ range.

5.4.2. Contamination from merged π^0

As discussed in §3.4.4, high energy π^0 s likely mimic a single photon when the two electromagnetic showers of the $\pi^0 \rightarrow \gamma\gamma$ decay cannot be resolved in the ECAL granularity. Such configuration, called *merged* π^0 , starts occurring when the transverse momentum of the neutral pion exceeds $2 \text{ GeV}/c$. Charmless $B \rightarrow hh\pi^0$ meson decays with branching fractions of $\mathcal{O}(10^{-5})$ can thus produce a dangerous contamination to both the $B^0 \rightarrow K^{*0}(K^\pm\pi^\mp)\gamma$ and $B_s^0 \rightarrow \phi(K^+K^-)\gamma$ signal when a merged π^0 is misidentified as a photon. Several possible contributions have been investigated.

Contamination from $B_{(s)}^0 \rightarrow K^\pm\pi^\mp\pi^0$ to $B^0 \rightarrow K^{*0}\gamma$

The efficiency of the $B^0 \rightarrow K^{*0}\gamma$ selection on the $B_{(s)}^0 \rightarrow K^\pm\pi^\mp\pi^0$ decays, as well as the shape of the resulting mass distribution, has been extracted from MC10 offline-selected samples (see Table 5.3), removing the restriction in the B mass window. The selection efficiency used to extract the contamination level with respect to the signal yield has been obtained on the MC10 offline-selected sample with the TOS requirement.

The mass distributions of the $B^0 \rightarrow K^+\pi^-\pi^0$ and $B_s^0 \rightarrow K^-\pi^+\pi^0$ samples reconstructed as $B^0 \rightarrow K^{*0}\gamma$, shown in Fig. 5.6, have been fitted with a *CB* distribution, and the results can be seen in Table 5.7. They respectively produce a peaking contribution at $5.2 \text{ GeV}/c^2$ and $5.3 \text{ GeV}/c^2$ with a resolution 1.84 ± 0.13 and 1.62 ± 0.11 times wider than that of the $B^0 \rightarrow K^{*0}(K^+\pi^-)\gamma$ signal, producing a sizeable contamination under the signal peak.

The ratio of selection efficiency between $B^0 \rightarrow K^+\pi^-\pi^0$ and the signal $B^0 \rightarrow K^{*0}\gamma$ decay is found to be

$$R_{B^0 \rightarrow K^+\pi^-\pi^0} = \frac{\epsilon_{B^0 \rightarrow K^+\pi^-\pi^0}}{\epsilon_{B^0 \rightarrow K^{*0}\gamma}} = 0.8\%, \quad (5.12)$$

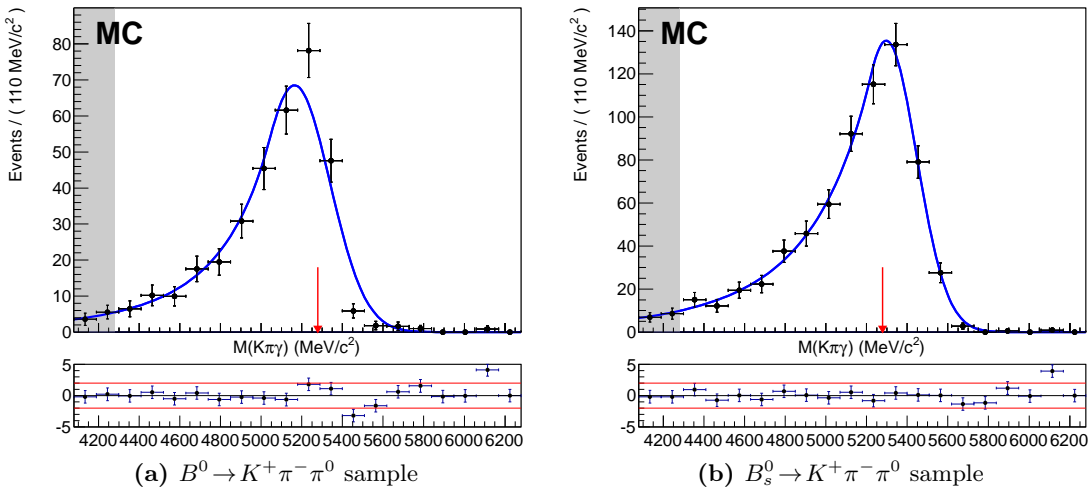


Figure 5.6. Mass distribution of the $(K^\pm\pi^\mp\gamma)$ combinations reconstructed in $B^0(s) \rightarrow K^+\pi^-\pi^0$ MC10 samples with a photon energy smearing of 2%. Each mass distribution is fit with a CB function, and the parameter values are detailed in Table 5.7. The areas outside the $\pm 1 \text{ GeV}/c^2$ B^0 mass window have been shaded.

	$B^0 \rightarrow K^+ \pi^- \pi^0$	$B_s^0 \rightarrow K^+ \pi^- \pi^0$
μ	(MeV/ c^2)	5178 ± 17
σ	(MeV/ c^2)	171 ± 12
α		0.36 ± 0.55
n		20 ± 12
		5 ± 0.4

Table 5.7. Summary of parameters obtained when fitting a CB distribution to the mass distribution of the $B_{(s)}^0 \rightarrow K^+ \pi^- \pi^0$ samples reconstructed as $B^0 \rightarrow K^{*0} \gamma$, as shown in Fig. 5.6.

The reduction factor 60 in efficiency has four causes:

- A factor ~ 12 comes from the requirement that the $K\pi$ pair falls in the K^* mass window. This number is in agreement with the contribution of the specific $B^0 \rightarrow K^{*0}\pi^0$ decay to $B^0 \rightarrow K^+\pi^-\pi^0$, measured as $(8.6 \pm 1.9)\%$ by the BABAR experiment.
 - A factor ~ 2.5 comes from the π^0 reconstructed as single ECAL cluster, *i.e.*, merged π^0 .
 - A factor ~ 2 come from the trigger selection, which rejects these events due to the γ requirement.
 - A factor ~ 3 comes from the π^0 rejection power provided by the helicity angle, γ ID and γ/π^0 separation variables used in the selection.

Taking into account that $\mathcal{B}(B^0 \rightarrow K^+ \pi^- \pi^0) = (35.9^{+2.8}_{-2.4}) \times 10^{-6}$ [79], the contamination of the $B^0 \rightarrow K^+ \pi^- \pi^0$ decay to the $B^0 \rightarrow K^{*0} \gamma$ selected signal is estimated to be

$$C_{B^0 \rightarrow K^+ \pi^- \pi^0} = \frac{N_{B^0 \rightarrow K^+ \pi^- \pi^0}^{\text{sel}}}{N_{B^0 \rightarrow K^{*0}\gamma}^{\text{sel}}} = (0.5 \pm 0.1)\%, \quad (5.13)$$

where the dominating uncertainty comes from the error on the measured branching fractions.

The $B_s^0 \rightarrow K^- \pi^+ \pi^0$ decay, not yet observed so far, proceeds via a Cabibbo-suppressed penguin diagram. Conservatively assuming the same branching ratio as for the corresponding B^0 decay and the same $K^{*0}\pi^0$ fraction, the contamination to $B^0 \rightarrow K^{*0}\gamma$ offline-selected signal is predicted to be

$$C_{B_s^0 \rightarrow K^- \pi^+ \pi^0} = \frac{N_{B_s^0 \rightarrow K^- \pi^+ \pi^0}^{\text{sel}}}{N_{B^0 \rightarrow K^{*0}\gamma}^{\text{sel}}} = (0.2 \pm 0.2)\%, \quad (5.14)$$

which is reduced with respect to the analogous B^0 decay due to the relative hadronization factor, f_s/f_d . A conservative uncertainty has been taken due to the lack of precise knowledge of the corresponding branching fraction.

Contamination from $B_s^0 \rightarrow K^\pm K^\mp \pi^0$ to $B_s^0 \rightarrow \phi\gamma$

In a similar way, the not yet observed $B_s^0 \rightarrow K^\pm K^\mp \pi^0$ decay can pollute the $B_s^0 \rightarrow \phi\gamma$ signal. Like the $B^0 \rightarrow K^{*0}\gamma$ contribution to the $B^0 \rightarrow K^+ \pi^- \pi^0$ decay discussed in [177], the dangerous $B_s^0 \rightarrow \phi\pi^0$ contribution to the $B_s^0 \rightarrow K^+ K^- \pi^0$ decay proceeds via color-suppressed $b \rightarrow s$ penguin and $b \rightarrow u$ transitions. However, these diagrams interfere with the $B_s^0 \rightarrow K^{*\mp}(K^+\pi^0)K^\pm$ tree and penguin transitions, which may have a significantly larger amplitude than the SU(2)-related mode, $B^0 \rightarrow K^{*+}(K^+\pi^0)\pi^-$.

A contamination of $0.6 \pm 0.6\%$ is assumed, corresponding to the contamination of the $B^0 \rightarrow K^+ \pi^- \pi^0$ decay to $B^0 \rightarrow K^{*0}\gamma$ signal. The large uncertainty is assigned to handle the unknown level of this contamination, allowing it to be a factor 2 larger than in the SU(2)-related mode. The line shape is also assumed to be the same as $B^0 \rightarrow K^+ \pi^- \pi^0$ reconstructed as $B^0 \rightarrow K^{*0}\gamma$, shifting the μ position by the mass difference between the B^0 and B_s^0 mesons.

Other contaminations from charmless decays with π^0

Contamination from $B^0 \rightarrow \pi^+ \pi^- \pi^0$, shown in Fig. 5.7, and $B_s^0 \rightarrow K^+ K^- \pi^0$ to the $B^0 \rightarrow K^{*0}\gamma$ invariant mass window requires a π/K misidentification and is further suppressed. The relative contribution of these two decays has found to be of $\mathcal{O}(10^{-4})$, and therefore they can be neglected. Likewise for the contamination from $B_{(s)}^0 \rightarrow K^{+(-)}\pi^{-(+)}\pi^0$ to $B_s^0 \rightarrow \phi\gamma$.

5.4.3. Contamination from partially reconstructed B decays

The partial reconstruction of a decay fragment from both charmless and charmed $B \rightarrow V(\gamma/\pi^0)X$ decays, where V denotes either K^{*0} or ϕ , may provide a sizeable contamination in the low mass side of the signal region.

As detailed in §5.2, several variables used in the signal selection are designed to fight against these partially reconstructed n -body B decays; in particular, the angle of the B candidate momentum with respect to its flight direction provided by the primary and

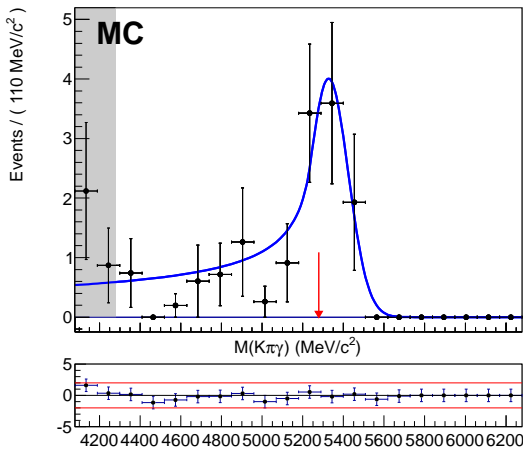


Figure 5.7. Mass distribution of the $(K^\pm\pi^\mp\gamma)$ combinations reconstructed in the $B^0 \rightarrow \pi^+\pi^-\pi^0$ MC11 sample with a photon energy smearing of 2 %. The mass distribution is fit with a CB function. The areas outside the ± 1 GeV/c^2 B^0 mass window have been shaded.

the decay vertices, the DIRA, and the isolation of the K^{*0}/ϕ decay vertex. However, there is still a sizeable remainder of partially reconstructed B decays. They can be classified in three groups, which will be studied separately:

- The charmless $B^+ \rightarrow K^{*0}\pi^+\gamma$ and $B^+ \rightarrow (\phi K^+\gamma$ decays, which can pollute the $B^0 \rightarrow K^{*0}\gamma$ and $B_s^0 \rightarrow \phi\gamma$ mass distributions, respectively.
- The $B^0 \rightarrow K^{*0}e^+e^-$ decay, where one of the electron showers is misidentified as a photon.
- Other $B \rightarrow h^+h^-\pi^0X$ decays.

Contamination from partially reconstructed radiative decays

The $B^+ \rightarrow K^{*0}\pi^+\gamma$ decay can be selected as a $B^0 \rightarrow K^{*0}\gamma$ when the π^+ has not been included as part of the signal. Given the low mass of the missing particle and its low transverse momentum, the contamination in $B^0 \rightarrow K^{*0}\gamma$ coming from this channel will be located in a very sensitive region in the low tail of the mass shape and will compete with the left tail of the $B^0 \rightarrow K^{*0}\gamma$ signal. Indeed, the mass distribution of the $B^+ \rightarrow K^{*0}\pi^+\gamma$ MC10 sample reconstructed as $B^0 \rightarrow K^{*0}\gamma$ in Fig. 5.8a shows the peak location at $\sim 3\sigma$ away from the B^0 mass. Table 5.8 shows the parameter values when fitting the obtained distribution with a CB function.

Making use of the MC sample selection efficiency and the measured branching fraction $\mathcal{B}(B^+ \rightarrow K^{*0}\pi^+\gamma) = (20^{+7}_{-6}) \times 10^{-6}$ [178], the contamination of this decay into the ± 1 GeV/c^2 mass window is estimated to be

$$C_{B^+ \rightarrow K^{*0}\pi^+\gamma} = (3.3 \pm 1.1)\%. \quad (5.15)$$

In addition, the $B^0 \rightarrow K^{*0}\pi^0\gamma$ decay, not affected by the vertex isolation cut, could contaminate the $B^0 \rightarrow K^{*0}\gamma$ up to the 5 % level. Other channels, such as $B^+ \rightarrow \rho e^+\nu$ and $B^0 \rightarrow K^{*0}\eta(\gamma\gamma)$, could also contaminate the signal with a similar shape.

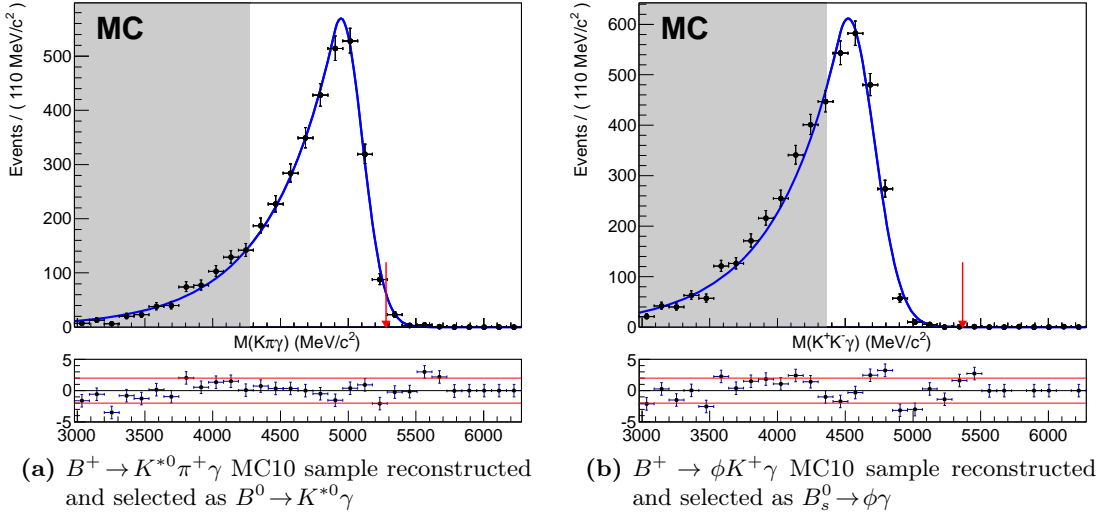


Figure 5.8. Mass distributions with a photon energy smearing of 2 %, fitted with a CB function. The fit parameter values are detailed in Table 5.8. The areas outside the B^0 and $B_s^0 \pm 1 \text{ GeV}/c^2$ mass windows, respectively, have been shaded.

	$B^+ \rightarrow K^{*0}\pi^+\gamma$	$B^+ \rightarrow \phi K^+\gamma$
μ (MeV/ c^2)	4944 ± 9	4528 ± 10
σ (MeV/ c^2)	159 ± 6	187 ± 6
α	0.331 ± 0.017	0.382 ± 0.019
n	11.10 ± 0.09	11.70 ± 0.17

Table 5.8. Summary of parameters obtained when fitting a CB distribution to the mass distribution of the $B^+ \rightarrow K^{*0}\pi^+\gamma$ sample reconstructed as $B^0 \rightarrow K^{*0}\gamma$ and $B^+ \rightarrow \phi K^+\gamma$ as $B_s^0 \rightarrow \phi\gamma$, as shown in Fig. 5.8.

In the case of the $B^+ \rightarrow \phi K^+\gamma$ contamination into $B_s^0 \rightarrow \phi\gamma$, the larger mass of the missing particle shifts the position of the fake peak at the lower edge of the mass window, as can be seen in Fig. 5.8b and Table 5.8. In this case, the abrupt fall of the mass distribution due to the kinematical constraint arising from the mass of the missing K is worse described by the used CB function. The branching fraction of this decay is $\mathcal{B}(B^+ \rightarrow \phi K^+\gamma) = (25.8 \pm 3.3) \times 10^{-6}$ [79], and the corresponding contamination to the $B_s^0 \rightarrow \phi\gamma$ mass window is expected to be

$$C_{B^+ \rightarrow \phi K^+\gamma} = (1.8 \pm 0.3)\%, \quad (5.16)$$

with a possible enhancement due to similarly shaped contributions, as in the case of $B^+ \rightarrow \phi K^+\gamma$.

Contamination from $B^0 \rightarrow K^{*0}e^+e^-$

Signal $B^0 \rightarrow K^{*0}e^+e^-$ events can be reconstructed and selected as a $B^0 \rightarrow K^{*0}\gamma$ when one of the electrons is misidentified as a photon. The mass distribution of the ($K^\pm\pi^\mp\gamma$)

combinations reconstructed in the MC11 sample of $B^0 \rightarrow K^{*0} e^+ e^-$ events is shown in Fig. 5.9. As detailed in Table 5.9, this background produces a peaking mass shape at ~ 4.8 GeV with a large tail penetrating the signal region.

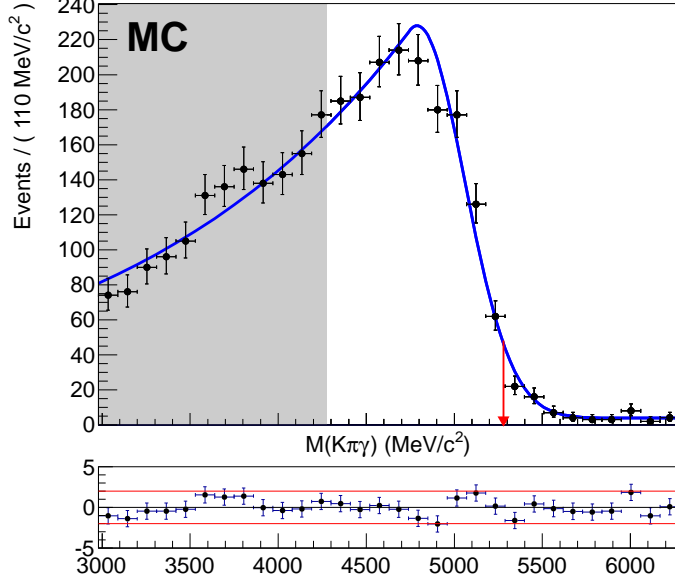


Figure 5.9. Mass distribution of the $B^0 \rightarrow K^{*0} e^+ e^-$ events reconstructed and selected as $B^0 \rightarrow K^{*0} \gamma$ with a photon energy smearing of 2 %, fitted with a CB function and an exponential to parametrize the combinatorics. The fit parameter values are detailed in Table 5.9. The areas outside the $B^0 \pm 1 \text{ GeV}/c^2$ mass window have been shaded.

$B^0 \rightarrow K^{*0} e^+ e^-$	
μ	(MeV/ c^2) 4789 ± 33
σ	(MeV/ c^2) 269 ± 21
α	0.16 ± 0.02
n	96 ± 75

Table 5.9. Summary of the CB parameters obtained when fitting the sum of a CB distribution and an exponential to the mass distribution of the $B^0 \rightarrow K^{*0} e^+ e^-$ sample reconstructed as $B^0 \rightarrow K^{*0} \gamma$, as shown in Fig. 5.9.

This channel has a sizeable relative efficiency with respect the $B^0 \rightarrow K^{*0} \gamma$ signal,

$$R_{B^0 \rightarrow K^{*0} e^+ e^-} = \frac{\epsilon_{B^0 \rightarrow K^{*0} e^+ e^-}}{\epsilon_{B^0 \rightarrow K^{*0} \gamma}} = 1.6\%, \quad (5.17)$$

twice the efficiency of the $B^0 \rightarrow K^+ \pi^- \pi^0$ background. However, the contamination to the $B^0 \rightarrow K^{*0} \gamma$ signal in the $\pm 1 \text{ GeV}/c^2$ mass window,

$$C_{B^0 \rightarrow K^{*0} e^+ e^-} = \frac{N_{B^0 \rightarrow K^{*0} e^+ e^-}^{\text{sel}}}{N_{B^0 \rightarrow K^{*0} \gamma}^{\text{sel}}} \sim 0.05\%, \quad (5.18)$$

is negligible due to the $\mathcal{O}(10^2)$ reduction factor of its branching fraction with respect to $B^0 \rightarrow K^{*0}\gamma$ [179], giving $\mathcal{B}(B^0 \rightarrow K^{*0}e^+e^-) = (1.03^{+0.19}_{-0.17}) \times 10^{-6}$.

Contamination from other $B \rightarrow h^+h^-\pi^0X$ decays

Many meson decays —other than the ones previously discussed— can exhibit a final state topology close to the $B^0 \rightarrow K^{*0}\gamma$ and $B_s^0 \rightarrow \phi\gamma$ signals when one of their decay products is not included. The K^{*0}/ϕ production from B^0/B^+ is of $\mathcal{O}(10\%)$ and therefore the branching fraction of the partially reconstructed background is potentially four orders of magnitude above the $B^0 \rightarrow K^{*0}\gamma$ and $B_s^0 \rightarrow \phi\gamma$ signals. Given the fact that the rejection of the partially reconstructed background by the offline selections is of $\mathcal{O}(10^6)$, the remaining contamination may be significant.

These potentially dangerous decays involving high energy neutral pions have been scrutinized at the simulation level by making use of a cocktail of MC10 $B \rightarrow h^+h^-\pi^0X$ decays, where X stands for a single particle or a multi-body object, including:

- $B^+ \rightarrow K^{*+}(K^+\pi^0)\pi^+\pi^-$.
- $B^+ \rightarrow J/\Psi(\pi^+\pi^-\pi^0)K^+$.
- $B^0 \rightarrow D^0(K\pi\pi^0)K^{*0}(K^+\pi^-)$.
- $B^+ \rightarrow K^+K^-K^+\pi^0$.
- $B^0 \rightarrow D^-(K^-\pi^-\pi^0)\rho^+(\pi^+\pi^0)$.

The reconstructed $K^\pm\pi^\mp\gamma$ mass in this cocktail of partially reconstructed backgrounds is shown in Fig. 5.10.

Following the ideas in [180], the shape of this background has been parametrized by a generalized Argus function [181], given by

$$A(m; m_0, c, p) = \frac{2^{-p}c^{2(p+1)}}{\Gamma(p+1) - \Gamma(p+1, \frac{1}{2}c^2)} \frac{m}{m_0^2} \left(1 - \frac{m^2}{m_0^2}\right)^p e^{-\frac{1}{2}c^2\left(1 - \frac{m^2}{m_0^2}\right)}, \quad (5.19)$$

where $\Gamma(\cdot)$ is the gamma function and $\Gamma(\cdot; \cdot)$ is the upper incomplete gamma function. The parameters m_0 , c and p represent the cutoff, curvature and power, respectively, with $0 \leq m \leq m_0$.

$B \rightarrow h^+h^-(\gamma/\pi^0)X$		
m_0	(MeV/ c^2)	5089 ± 96
c		20 ± 4
p		7.1 ± 1.7

Table 5.10. Summary of the parameters obtained when fitting the Argus distribution (with an exponential for the combinatorics) to the $K^\pm\pi^\mp\gamma$ mass distribution of the $B \rightarrow h^+h^-(\gamma/\pi^0)X$ cocktail sample reconstructed as $B^0 \rightarrow K^{*0}\gamma$, as shown in Fig. 5.10.

Unfortunately, the lack of a sizeable amount of statistics of the suitable MC samples doesn't allow to perform the same study with $B \rightarrow h^+h^-\pi^0X$ events reconstructed as $B_s^0 \rightarrow \phi\gamma$, since the narrow mass window for the ϕ rejects most of the events.

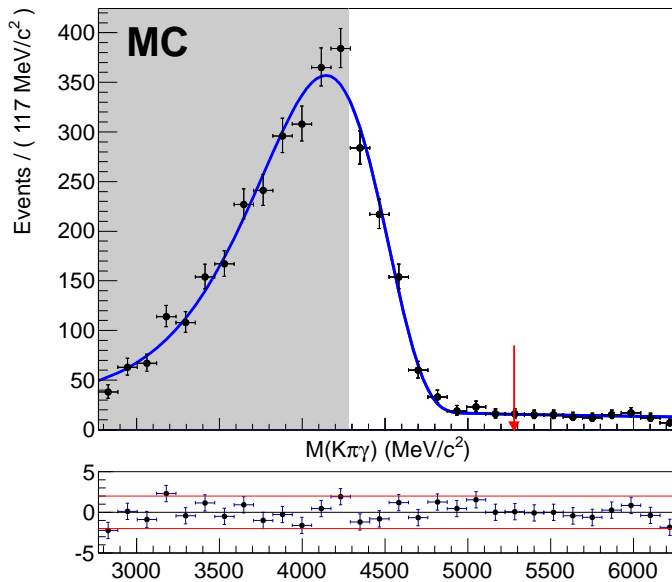


Figure 5.10. Mass distribution of the $B \rightarrow h^+ h^- (\gamma/\pi^0) X$ cocktail reconstructed and selected as $B^0 \rightarrow K^{*0}\gamma$ with a photon energy smearing of 2%, fitted with an Argus function and an exponential to parametrize the combinatorics. The fit parameter values are detailed in Table 5.10. The areas outside the $\pm 1 \text{ GeV}/c^2$ B^0 mass window have been shaded.

5.4.4. Contamination from baryonic radiative decays

The contamination coming from the radiative decays of b-baryons $\Lambda_b \rightarrow \Lambda\gamma$, where the proton has been misidentified as a kaon or pion, has also been studied. On one side, the Λ_b decay via the long-lived resonance Λ^0 decaying in a $p\pi$ final state, mostly exhibits a different topology than the $B^0 \rightarrow K^{*0}\gamma$ and $B_s^0 \rightarrow \phi\gamma$ signal and is hence found to be harmless. However, the so-far unmeasured $\Lambda_b \rightarrow \Lambda^*(Kp)\gamma$ decay, where Λ^* stands for $\Lambda(1520)$ and the further massive resonances promptly decaying into a pK final state, can contaminate the signal via the proton misidentification into pion or kaon. The p misidentification causes a shift of the Λ_b and the Λ^* (mis)reconstructed masses towards the $B_{d,s}$ and K^{*0}/ϕ mass regions, respectively.

The MC11 $\Lambda_b \rightarrow \Lambda(1520)\gamma$ and $\Lambda_b \rightarrow \Lambda(1670)\gamma$ samples have been used to obtain the shape of the contamination when they are reconstructed as $B^0 \rightarrow K^{*0}\gamma$ or $B_s^0 \rightarrow \phi\gamma$, as shown in Fig. 5.11 and Table 5.11. The shape of this contamination is modeled by a CB distribution peaked at $\sim 5300 \text{ MeV}/c^2$. From visual inspection it can already be seen that the efficiency selecting Λ_b decays is larger when reconstructing them as $B^0 \rightarrow K^{*0}\gamma$, mainly due to the effect of the wider K^{*0} mass window.

Making use of the events selected as $B^0 \rightarrow K^{*0}\gamma$, the $\Lambda_b \rightarrow \Lambda^*(Kp)\gamma$ decay has been observed in the 1.0 fb^{-1} of data collected by LHCb in 2011. The mass peak shown in Fig. 5.12 has been obtained by recalculating the invariant mass, changing the pion mass to the proton mass, and by applying the $B^0 \rightarrow K^{*0}\gamma$ offline selection, replacing the pion identification criteria with a strong proton PID requirement, $DLL_{p/\pi} > 20$. Such a strong identification criteria is needed to reduce the contamination from misidentified $K^{*0}(K^+\pi^-)\gamma$ to the $\Lambda_b \rightarrow \Lambda^*(Kp)\gamma$ candidates. This contamination is found to be at

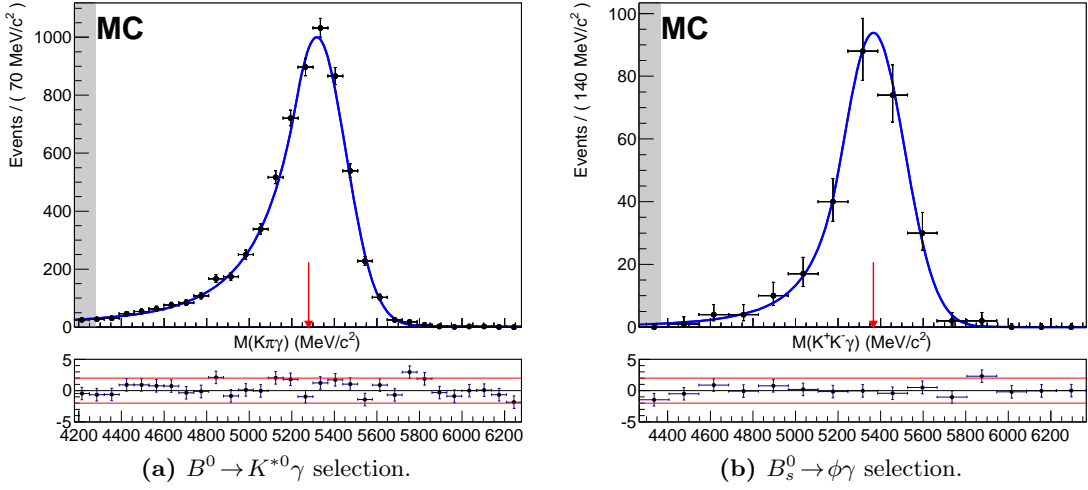


Figure 5.11. Mass distribution of the $\Lambda_b \rightarrow \Lambda(1520)\gamma$ and $\Lambda_b \rightarrow \Lambda(1670)\gamma$ MC11 samples reconstructed and offline-selected as $B^0 \rightarrow K^{*0}\gamma$ and $B_s^0 \rightarrow \phi\gamma$, with a photon energy smearing of 2 %. Each mass distribution is fit with a CB function, the parameter values of which are detailed in Table 5.11. The areas outside the B^0 and $B_s^0 \pm 1 \text{ GeV}/c^2$ mass windows, respectively, have been shaded.

	$B^0 \rightarrow K^{*0}\gamma$ selection	$B_s^0 \rightarrow \phi\gamma$ selection
μ (MeV/ c^2)	5316 ± 4	5367 ± 12
σ (MeV/ c^2)	141 ± 4	147 ± 10
α	0.77 ± 0.06	1.0 ± 0.2
n	5.0 ± 1.7	4 ± 4

Table 5.11. Summary of parameters obtained when fitting a CB distribution to the mass distribution of the $\Lambda_b \rightarrow \Lambda(1520)\gamma$ and $\Lambda_b \rightarrow \Lambda(1670)\gamma$ MC11 samples reconstructed and offline-selected as $B^0 \rightarrow K^{*0}\gamma$ and $B_s^0 \rightarrow \phi\gamma$, as shown in Fig. 5.11.

the level of $(3.2 \pm 0.5)\%$, and needs to be subtracted to the number of fitted events in Fig. 5.12, 263 ± 26 . After the correction, the number of $\Lambda_b \rightarrow \Lambda^*\gamma$ events is found to be

$$\mathcal{N}^{B^0 \rightarrow K^{*0}\gamma}(\Lambda_b \rightarrow \Lambda^*\gamma) = 255 \pm 25, \quad (5.20)$$

where the superscript in \mathcal{N} indicates that the yield has been obtained on a sample selected as $B^0 \rightarrow K^{*0}\gamma$.

As the visible branching fraction of $\Lambda_b \rightarrow \Lambda^*(Kp)\gamma$ has not been measured so far, the contamination from such decays to $B^0 \rightarrow K^{*0}\gamma$,

$$\begin{aligned} C_{\Lambda_b \rightarrow \Lambda^*\gamma} &\equiv \frac{\mathcal{N}^{B^0 \rightarrow K^{*0}\gamma}(\Lambda_b \rightarrow \Lambda^*\gamma)}{\mathcal{N}^{B^0 \rightarrow K^{*0}\gamma}(B^0 \rightarrow K^{*0}\gamma)} \\ &= \frac{\epsilon^{B^0 \rightarrow K^{*0}\gamma}(\Lambda_b \rightarrow \Lambda^*\gamma)}{\epsilon^{B^0 \rightarrow K^{*0}\gamma}(B^0 \rightarrow K^{*0}\gamma)} \frac{\mathcal{B}(\Lambda_b \rightarrow \Lambda^*\gamma)}{\mathcal{B}(B^0 \rightarrow K^{*0}\gamma)} \frac{f_\Lambda}{f_d}, \end{aligned} \quad (5.21)$$

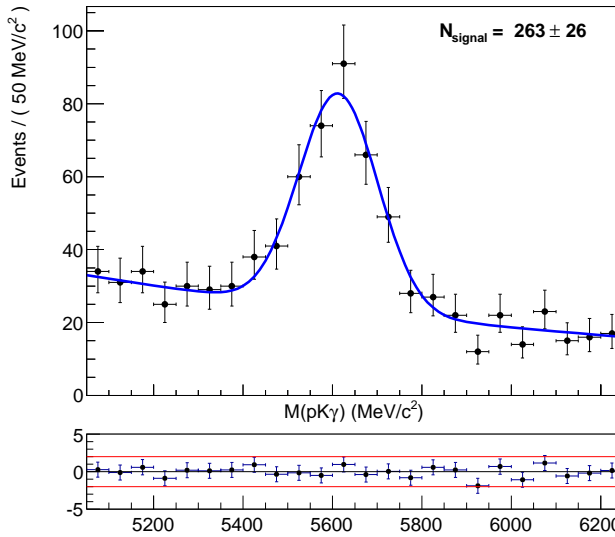


Figure 5.12. Mass distribution for $\Lambda_b \rightarrow \Lambda^*(Kp)\gamma$ extracted from $B^0 \rightarrow K^{*0}\gamma$ selected events.

has been estimated using the signal from the dedicated $\Lambda^*(Kp)\gamma$ selection normalized to a simulated sample, taking into account that

$$\frac{\mathcal{B}(\Lambda_b \rightarrow \Lambda^*\gamma)}{\mathcal{B}(B^0 \rightarrow K^{*0}\gamma)} \frac{f_\Lambda}{f_d} = \frac{\epsilon^{B^0 \rightarrow K^{*0}\gamma}(B^0 \rightarrow K^{*0}\gamma)}{\epsilon^{\Lambda_b \rightarrow \Lambda^*\gamma}(\Lambda_b \rightarrow \Lambda^*\gamma)} \frac{\mathcal{N}^{\Lambda_b \rightarrow \Lambda^*\gamma}(\Lambda_b \rightarrow \Lambda^*\gamma)}{\mathcal{N}^{B^0 \rightarrow K^{*0}\gamma}(B^0 \rightarrow K^{*0}\gamma)}, \quad (5.22)$$

and thus:

$$C_{\Lambda_b \rightarrow \Lambda^*\gamma}^{B^0 \rightarrow K^{*0}\gamma} = \frac{\mathcal{N}^{\Lambda_b \rightarrow \Lambda^*\gamma}(\Lambda_b \rightarrow \Lambda^*\gamma)}{\epsilon^{\Lambda_b \rightarrow \Lambda^*\gamma}(\Lambda_b \rightarrow \Lambda^*\gamma)} \frac{\epsilon^{B^0 \rightarrow K^{*0}\gamma}(\Lambda_b \rightarrow \Lambda^*\gamma)}{\mathcal{N}^{B^0 \rightarrow K^{*0}\gamma}(B^0 \rightarrow K^{*0}\gamma)} = r_{\text{PID}}^p \times (2.7 \pm 0.4)\% = (1.0 \pm 0.3)\%, \quad (5.23)$$

where the relative rate of the proton to pion misidentification,

$$r_{\text{PID}}^p = \frac{\epsilon_{p \rightarrow \pi}^{\text{PID}}}{\epsilon_{p \rightarrow p}^{\text{PID}}} = (38 \pm 8)\%, \quad (5.24)$$

has been determined from the data-driven PID calibration techniques that will be detailed in §5.6.7, while the rest of efficiencies have been determined from simulation.

Following a similar procedure, the $\Lambda_b \rightarrow \Lambda^*\gamma$ contamination to the $B_s^0 \rightarrow \phi\gamma$ has been estimated as

$$C_{\Lambda_b \rightarrow \Lambda^*\gamma}^{B_s^0 \rightarrow \phi\gamma} = (0.4 \pm 0.3)\%, \quad (5.25)$$

and is found to be reduced thanks to the tight ϕ mass window and to the anti proton-PID cut, $\text{PID}_{K/p} > 2$, applied to both kaons.

5.4.5. Signal cross-feeds

The so-called *signal cross-feed* category actually consists in three contributions, discussed below.

Irreducible contamination from the $B_s^0 \rightarrow K^{*0}\gamma$ radiative decay

The $B_s^0 \rightarrow K^{*0}\gamma$ decay is indistinguishable from $B^0 \rightarrow K^{*0}\gamma$ due to the width of the mass peak. The branching fraction of this suppressed $b \rightarrow d\gamma$ transition of the B_s^0 meson is predicted to be $\mathcal{B}(B_s^0 \rightarrow K^{*0}\gamma) = (1.26 \pm 0.25 \pm 0.18) \times 10^{-6}$ [67].

Since this channel has the same efficiencies as $B^0 \rightarrow K^{*0}\gamma$, its contamination to the $B^0 \rightarrow K^{*0}\gamma$ yield is given by

$$C_{B_s^0 \rightarrow K^{*0}\gamma} = \frac{f_s}{f_d} \frac{\mathcal{B}(B_s^0 \rightarrow K^{*0}\gamma)}{\mathcal{B}(B^0 \rightarrow K^{*0}\gamma)} = (0.8 \pm 0.2)\% \quad (5.26)$$

Furthermore, its line shape should be the same as that from $B^0 \rightarrow K^{*0}\gamma$ (see Table 5.6), with its mean value shifted by an amount equal to the mass difference between the B^0 and B_s^0 mesons.

$B_s^0 \rightarrow \phi\gamma$ contamination to $B^0 \rightarrow K^{*0}\gamma$, and vice-versa

Another possible source of background for both channels is the cross feed between them, when one of the kaons from the ϕ in $B_s^0 \rightarrow \phi\gamma$ is misidentified as a pion, or, on the contrary, a pion from the K^{*0} in $B^0 \rightarrow K^{*0}\gamma$ is misidentified as a kaon. By making use of the MC11 data samples, reweighed with the data-driven PID calibration tables, the contamination from cross feed between $B^0 \rightarrow K^{*0}\gamma$ and $B_s^0 \rightarrow \phi\gamma$ is found to be negligible, thanks to the tight PID cuts and the ϕ narrow mass window.

Multiple candidates reconstructed in single signal events

Selected events with several $B^0 \rightarrow K^{*0}\gamma$ or $B_s^0 \rightarrow \phi\gamma$ candidates and their possible impact on the background and signal peak shape have also been investigated using offline-selected data with trigger TOS requirements. The overall rate of such multiple candidate events is negligible in the full B meson mass window, as can be seen in Table 5.12.

	$B^0 \rightarrow K^{*0}\gamma$	$B_s^0 \rightarrow \phi\gamma$
Events in the B mass window	10483	1145
Events with multiple candidates	3	0
Contamination from multiple candidates	$(0.029 \pm 0.017)\%$	—

Table 5.12. Multiple candidate contamination per decay after the offline selection and the TOS requirement.

5.5. Fit

The yields for $B^0 \rightarrow K^{*0}\gamma$ and $B_s^0 \rightarrow \phi\gamma$ are extracted simultaneously from an extended unbinned maximum likelihood fit performed with the RooFit toolkit [182] and the MINUIT minimization routines [183]. The correlation between the $B^0 \rightarrow K^{*0}\gamma$ and $B_s^0 \rightarrow \phi\gamma$ datasets is taken into account by keeping the difference between the B meson masses gaussianly constrained at the PDG value, $\Delta m = m_{B^0} - m_{B_s^0} = 87.0 \pm 0.6$ [21].

5.5.1. Mass window

Given the sizeable width of the B mass peak discussed in §5.3, $\sim 100 \text{ MeV}/c^2$, it becomes necessary to use the widest mass window possible in order to better describe the shape of the backgrounds.

The mass window given by the trigger and the stripping is of $1 \text{ GeV}/c^2$ around each of the B mesons nominal mass. However, this mass window cannot be used naively due to the effects of calorimeter miscalibration and aging. During 2011, ECAL has suffered from noticeable aging, which has been corrected in the data reconstruction step, along with possible cell miscalibration, by applying a set of time-dependent cell-by-cell corrections. Nonetheless, this information was not available at the trigger level during most of the year, and therefore data were collected with an incomplete calibration of the ECAL.

Thus, an acceptance effect appears in the vicinity of the calibrated mass window border, and in order to consider the $1 \text{ GeV}/c^2$ mass window it is necessary to introduce an acceptance function. The *complementary error function* is used to model the threshold effect:

$$\text{erfc}(x) = 1 - \text{erf}(x) = \frac{2}{\sqrt{\pi}} \int_x^\infty e^{-t^2} dt. \quad (5.27)$$

With the help of the erfc , the *threshold acceptance function* is defined as

$$a(m_B; m_L, m_H, \sigma_t) = \text{erfc}\left(\frac{m_L - m_B}{\sigma_t}\right) \times \text{erfc}\left(\frac{m_B - m_H}{\sigma_t}\right), \quad (5.28)$$

where $m_{L,H}$ correspond to the position of low (L) and high (H) mass thresholds and σ_t corresponds to the quadratic difference between the corrected and uncorrected masses.

The $\pm 1 \text{ GeV}/c^2$ mass window can be used with the help of the threshold acceptance function. However, the lack of knowledge of the exact shape of threshold acceptance effect has to be taken into account: a fit with a tighter mass window of $700 \text{ MeV}/c^2$ will also be considered when evaluating the systematics of the measurement.

5.5.2. Fit model

The data from the $B^0 \rightarrow K^{*0}\gamma$ and $B_s^0 \rightarrow \phi\gamma$ offline selections are put together in the same dataset, marked with the corresponding *decay* category. Then, an Extended Probability Density Function (PDF), *i.e.*, a PDF with the proper normalization to match the total number of events in the samples, is built as a sum of PDFs:

$$F(m; x_i) = \delta(d = d_{B^0})a(m)N^d \left[S^d(m) + \sum_i C_i^d B_i^d(m) \right] + \\ + \delta(d = d_{B_s^0})a(m)N^d \left[S^d(m) + \sum_i C_i^d B_i^d(m) \right], \quad (5.29)$$

where m is the invariant mass of the B candidates, the δ function expresses that each of the expressions in squared parentheses is only used with data of a given decay, a corresponds to the threshold acceptance function described in Eq. 5.28, S^d and B_i^d are signal and background PDFs, respectively, the N^d correspond to the signal yield of each decay, and the C_i coefficients are the fraction of yield —the contamination— of each of the considered background PDFs.

$\mathcal{B} (\times 10^{-5})$	Contamination		
	$B^0 \rightarrow K^{*0}\gamma$	$B_s^0 \rightarrow \phi\gamma$	
$B^0 \rightarrow K^+\pi^-\pi^0$	$3.59^{+0.28}_{-0.24}$	$(0.5 \pm 0.1)\%$	$\mathcal{O}(10^{-4})$
$B_s^0 \rightarrow K^+\pi^-\pi^0$	unknown	$(0.2 \pm 0.2)\%$	$\mathcal{O}(10^{-4})$
$B_s^0 \rightarrow K^+K^-\pi^0$	unknown	$\mathcal{O}(10^{-4})$	$(0.5 \pm 0.5)\%$
$B^+ \rightarrow K^{*0}\pi^+\gamma$	$2.0^{+0.7}_{-0.6}$	$(3.3 \pm 1.1)\%$	$\mathcal{O}(10^{-4})$
$B^0 \rightarrow K^{*0}\pi^0\gamma$	4.1 ± 0.4	$\mathcal{O}(5\%)$	$\mathcal{O}(10^{-4})$
$B^+ \rightarrow \phi K^+\gamma$	2.58 ± 0.33	$\mathcal{O}(10^{-4})$	$(1.8 \pm 0.3)\%$
$B \rightarrow h^+h^-\pi^0X$	$\mathcal{O}(10^4)$	$\mathcal{O}(1\%)$	$\mathcal{O}(1\%)$
$\Lambda_b \rightarrow \Lambda^*\gamma$	unknown	$(1.0 \pm 0.3)\%$	$(0.4 \pm 0.3)\%$
$B_s^0 \rightarrow K^{*0}\gamma$	0.126 ± 0.031	$(0.8 \pm 0.2)\%$	$\mathcal{O}(10^{-4})$
$B^0 \rightarrow K^{*0}\gamma$ cross feed	4.33 ± 0.15	—	$\mathcal{O}(10^{-4})$
$B_s^0 \rightarrow \phi\gamma$ cross feed	$5.7^{+2.1}_{-1.8}$	$\mathcal{O}(10^{-4})$	—

Table 5.13. Expected relative contamination to the $B^0 \rightarrow K^{*0}\gamma$ and $B_s^0 \rightarrow \phi\gamma$ yield in the $\pm 1 \text{ GeV}/c^2$ mass window from the backgrounds considered in §5.4.

Signal shape

The shape of the signal peak for both the B^0 and the B_s^0 has been extracted from Monte Carlo simulation in §5.3. Thus, S^d consists in the sum of two CB with common σ and μ and different α and n parameters:

$$S^d(m) = CB_L(m; \mu_d, \sigma_d, \alpha_L^d, n_L^d) + CB_H(m; \mu_d, \sigma_d, \alpha_H^d, n_H^d), \quad (5.30)$$

with a Gaussian constraint on $\mu_{B_s^0}$ in the case of $B_s^0 \rightarrow \phi\gamma$.

Due to the presence of background, when performing the full fit is very difficult to obtain reliable estimations of the α and n parameters. Therefore, they are kept fixed at the values obtained from the smeared MC fit, which can be found in Table 5.6, while the μ and σ parameters are left free.

Background shapes

The different possible background sources for the $B^0 \rightarrow K^{*0}\gamma$ and $B_s^0 \rightarrow \phi\gamma$ decays have been studied in §5.4, and their expected contaminations to the signal yield are summarized in Table 5.13. In the fit, all background shapes are fixed from MC. The contamination fraction of those decays located under the mass peak, and thus indistinguishable from the signal, is also fixed from the MC estimation, while the contamination level from other backgrounds is left free.

For $B^0 \rightarrow K^{*0}\gamma$, the following background sources have been included in the fit PDF:

- Combinatorial background, parametrized by an exponential function

$$B_{\text{comb}}^{B^0}(m; \tau_{B^0}) = \exp \left\{ \frac{m}{\tau_{B^0}} \right\}. \quad (5.31)$$

- The irreducible $B_s^0 \rightarrow K^{*0}\gamma$ contamination is parametrized by the same shape as the $B^0 \rightarrow K^{*0}\gamma$ with the *CB* mean value shifted by $\Delta\mu = 87 \text{ MeV}/c^2$,

$$B_{B_s^0 \rightarrow K^{*0}\gamma}(m) = S^{B^0 \rightarrow K^{*0}\gamma}(m; \mu_{B^0} + \Delta\mu, \sigma_{B^0}, \alpha_L^{B^0}, n_L^{B^0}, \alpha_H^{B^0}, n_H^{B^0}), \quad (5.32)$$

Since this contribution is placed well under the mass peak, the contamination fraction $C_{B_s^0 \rightarrow K^{*0}\gamma}$ has been fixed from MC.

- The $B_{d(s)} \rightarrow K^\pm \pi^\mp \pi^0$ decays reconstructed as $B^0 \rightarrow K^{*0}\gamma$ also contribute well under the $B^0 \rightarrow K^{*0}\gamma$ mass peak. Their shape is fixed to a *CB* function with parameters fixed to the values detailed in Table 5.7:

$$B_{B^0 \rightarrow K^\pm \pi^\mp \pi^0}(m) = CB(m; \mu_{B^0}, \sigma_{B^0}, \alpha_{B^0}, n_{B^0}), \quad (5.33)$$

$$B_{B_s^0 \rightarrow K^\pm \pi^\mp \pi^0}(m) = CB(m; \mu_{B_s^0}, \sigma_{B_s^0}, \alpha_{B_s^0}, n_{B_s^0}). \quad (5.34)$$

Their contamination fraction has been fixed in the fit.

- The partially reconstructed $B^+ \rightarrow K^{*0}\pi^+\gamma$ contribution is parametrized by a *CB*, where the μ, σ, α, n parameters are fixed from Table 5.8:

$$B_{B^+ \rightarrow K^{*0}\pi^+\gamma}(m) = CB(m; \mu_{K^{*0}\pi^+\gamma}, \sigma_{K^{*0}\pi^+\gamma}, \alpha_{K^{*0}\pi^+\gamma}, n_{K^{*0}\pi^+\gamma}), \quad (5.35)$$

The contamination fraction $C_{B^+ \rightarrow K^{*0}\pi^+\gamma}$, is left free in the fit because other decays can produce a sizeable contribution with a similar shape.

- The baryonic $\Lambda_b \rightarrow \Lambda^*(Kp)\gamma$ decays are also taken into account as a *CB*-shaped contribution,

$$B_{\Lambda_b \rightarrow \Lambda^*\gamma}(m) = CB(m; \mu_{\Lambda_b}, \sigma_{\Lambda_b}, \alpha_{\Lambda_b}, n_{\Lambda_b}), \quad (5.36)$$

where the parameters have been fixed from Table 5.11 and the contamination fraction from Eq. 5.23.

- The partially reconstructed $B \rightarrow h^+ h^- \pi^0 X$ decays, referred to from now on as *partially reconstructed background*, are modeled by making use of an Argus function with its parameters fixed to the values obtained from MC (see Table 5.10):

$$B_{\text{partial}}^{B^0}(m) = A(m; m_0, c_{B^0}, p_{B^0}). \quad (5.37)$$

The contamination from this source, which cannot be reliably extracted from MC, is left as a free parameter in the fit.

The $B_s^0 \rightarrow \phi\gamma$ fit PDF includes the following background sources:

- Combinatorial background, parametrized by an exponential function in the same way as for the $B^0 \rightarrow K^{*0}\gamma$ combinatorics:

$$B_{\text{comb}}^{B_s^0}(m; \tau_{B_s^0}) = \exp \left\{ \frac{m}{\tau_{B_s^0}} \right\}. \quad (5.38)$$

- The π^0 -related decay to $B_s^0 \rightarrow \phi\gamma$, $B_s^0 \rightarrow K^+ K^- \pi^0$, is parametrized with the same shape as $B^0 \rightarrow K^+ \pi^- \pi^0$ with the μ parameter shifted by $\Delta M = 87.0 \text{ MeV}/c^2$:

$$B_{B_s^0 \rightarrow K^+ K^- \pi^0}(m) = B_{B^0 \rightarrow K^\pm \pi^\mp \pi^0}(m; \mu_{B^0} + \Delta M, \sigma_{B^0}, \alpha_{B^0}, n_{B^0}) \quad (5.39)$$

Its contamination fraction is fixed to $C_{B_s^0 \rightarrow K^+ K^- \pi^0} = C_{B^0 \rightarrow K^\pm \pi^\mp \pi^0} = 0.5\%$.

- The partially reconstructed $B^+ \rightarrow \phi K^+\gamma$ gives a contribution parametrized with a CB function with parameters fixed from Table 5.8:

$$B_{B^+ \rightarrow \phi K^+\gamma}(m) = CB(m; \mu_{\phi K^+\gamma}, \sigma_{\phi K^+\gamma}, \alpha_{\phi K^+\gamma}, n_{\phi K^+\gamma}), \quad (5.40)$$

and its contamination fraction is left free.

- All other partially reconstructed background sources are modeled with the same Argus function as in the $B^0 \rightarrow K^{*0}\gamma$ case, with its threshold mass shifted by $\Delta M = 87 \text{ MeV}/c^2$:

$$B_{\text{partial}}^{B_s^0}(m) = B_{\text{partial}}^{B^0}(m; m_0 + \Delta M, c, p). \quad (5.41)$$

The contamination from partially reconstructed background to $B_s^0 \rightarrow \phi\gamma$ is also left as a free parameter in the fit.

5.5.3. Simultaneous fit result

An unbinned maximum likelihood fit of the simultaneous PDF described in Eq. 5.29 has been performed on the offline-selected $B^0 \rightarrow K^{*0}\gamma$ and $B_s^0 \rightarrow \phi\gamma$ data with the exclusive trigger TOS requirement, corresponding to the full 2011 dataset.

		Fit value
$\mathcal{N}_{B^0 \rightarrow K^{*0}\gamma}$		5279 ± 92
μ_{B^0}	(MeV/c^2)	5278.4 ± 1.5
σ_{B^0}	(MeV/c^2)	92.4 ± 1.6
$\mathcal{N}_{B_s^0 \rightarrow \phi\gamma}$		691 ± 36
$\mu_{B_s^0}$	(MeV/c^2)	5365.3 ± 1.7
$\sigma_{B_s^0}$	(MeV/c^2)	97 ± 6
$\mathcal{N}_{\text{exp}, B^0}$		3928 ± 517
τ_{B^0}	($\text{GeV}^{-1}\text{c}^2$)	-1.16 ± 0.15
$C_{B^+ \rightarrow K^{*0}\pi^+\gamma}$		$(15 \pm 5)\%$
C_{partial, B^0}		$(5 \pm 4)\%$
$\mathcal{N}_{\text{exp}, B_s^0}$		400 ± 64
$\tau_{B_s^0}$	($\text{GeV}^{-1}\text{c}^2$)	-0.7 ± 0.2
$C_{B^+ \rightarrow \phi K^+\gamma}$		$(5 \pm 3)\%$
$C_{\text{partial}, B_s^0}$		$(0^{+9}_{-0})\%$
σ_t	(MeV/c^2)	125 ± 39
m_{L, B^0}	(MeV/c^2)	4342 ± 9
m_{H, B^0}	(MeV/c^2)	6239 ± 17
m_{L, B_s^0}	(MeV/c^2)	4403 ± 15
m_{H, B_s^0}	(MeV/c^2)	6285 ± 32

Table 5.14. Summary of free parameters for signal (top section), background (middle section) and acceptance function (bottom section) for the simultaneous fit.

A list of the free parameters included in the fit, as well as their final values, can be found in Table 5.14. The invariant mass distributions for $B^0 \rightarrow K^{*0}\gamma$ and $B_s^0 \rightarrow \phi\gamma$,

and the corresponding fitted curve, are shown in Fig. 5.13. On one side, $B^0 \rightarrow K^{*0}\gamma$ is observed with a yield of 5279 ± 92 events and a S/B ratio of 5.4 ± 0.4 in the 2σ mass window. On the other side, 691 ± 36 $B_s^0 \rightarrow \phi\gamma$ events have been observed with a S/B of 7.3 ± 0.7 in the 2σ mass window, constituting the largest $B_s^0 \rightarrow \phi\gamma$ sample collected.

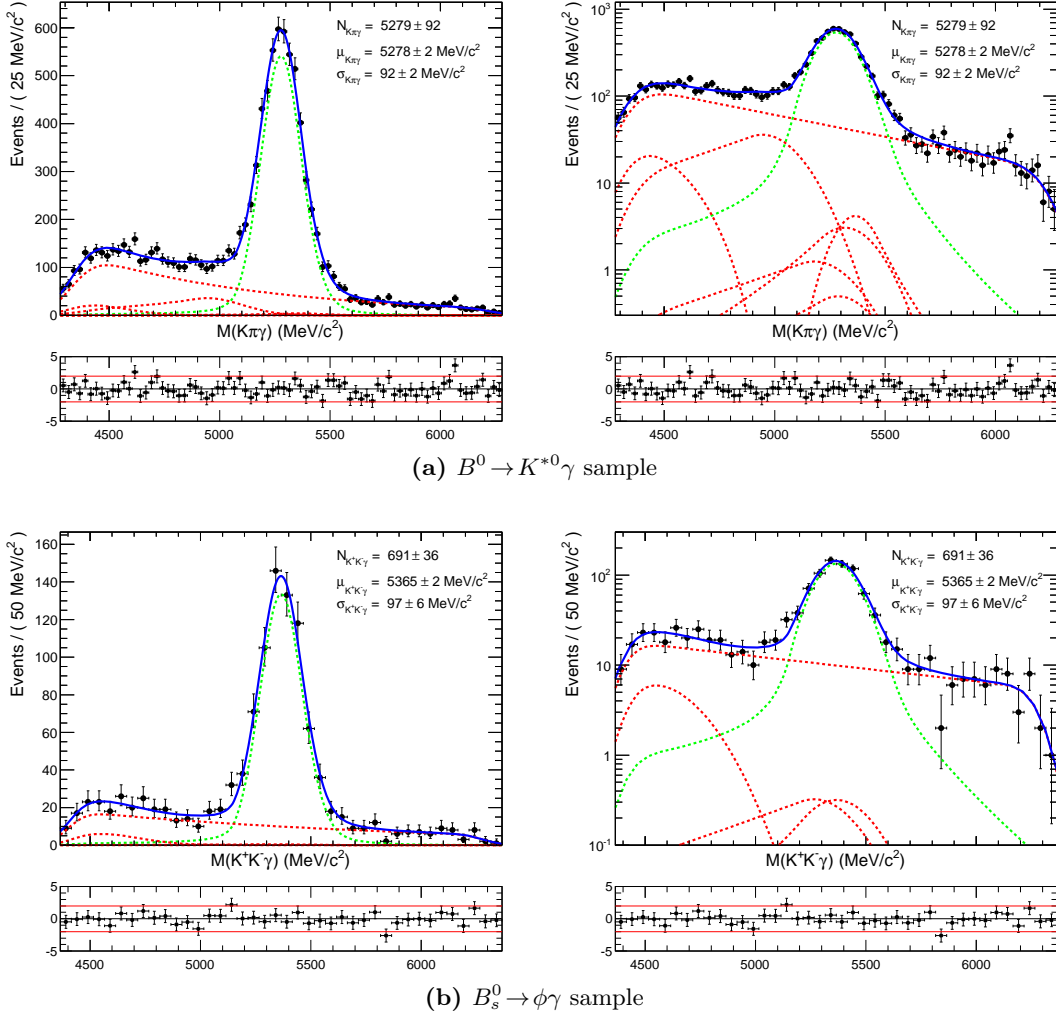


Figure 5.13. Mass distribution of the $B^0 \rightarrow K^{*0}\gamma$ and $B_s^0 \rightarrow \phi\gamma$ data samples, in linear (left) and logarithmic (right) scale. The fit model PDF is overlaid in a solid blue line, with the signal (dashed green) and background (dashed red) components. The parameter values for the PDF are detailed in Table 5.14.

The τ_{B^0} parameter is compatible with the value estimated from the K^{*0} sidebands in Eq. 5.11. However, given the big uncertainty of the decay constant extracted from the sidebands, this agreement can only be considered as a simple cross check.

The fitted contamination for $B^+ \rightarrow K^{*0}\pi^+\gamma$ and similar partially reconstructed decays is slightly higher than the sum of the predictions for $B^+ \rightarrow K^{*0}\pi^+\gamma$ and $B^0 \rightarrow K^{*0}\pi^0\gamma$. As it has been discussed earlier, several other channels can contribute in a sizeable amount to this shape, and therefore this result is within expectations. The contribution from generic partially reconstructed background is also found to be

within expectations.

5.5.4. Fit quality

In order to assess the quality of the fit, its goodness-of-fit has been evaluated with the χ^2 method, while its stability has been assessed with toy Monte Carlo samples generated following the shape of the fitted PDF.

Goodness-of-fit

Determination of the goodness-of-fit in the case of unbinned maximum likelihood fits is not as straightforward as it is with binned fits [184]. For example, it has been shown that the naive method of comparing the value of the likelihood at the maximum with the distribution of the maximum likelihood of MC-generated toy models is a flawed and should not be used [185, 186]. Thus, a usual approach to the goodness-of-fit problem consists in binning the fitted dataset and applying the χ^2 test.

The χ^2 residuals [173] located at the bottom of the invariant mass plots in Fig. 5.13 give already a visual hint about the suitability of the used PDF, since almost all of them lie within the $\pm 2\sigma$ band. To obtain a numerical value for the goodness-of-fit, the chi-square test statistic, defined as

$$X^2 = \sum_i^n \frac{(data_i - pdf_i)}{data_i}, \quad (5.42)$$

can be used to calculate a p -value by comparing the X^2 value obtained from the fit to a χ^2 distribution of the appropriate degrees of freedom. The number of degrees of freedom is equal to the number of bins n , minus the reduction in degrees of freedom, calculated as the number of parameters, minus one, to account for the fact that, once the number of events in $n - 1$ bins is known, the number of events in the last bin is known from the total number of events.

In the simultaneous fit case, however, it is difficult to define the individual number of degrees of freedom for each plot, since some of the parameters are related. A common X^2 has been extracted, $X^2 = 101.23$, and the corresponding degrees of freedom have been calculated as

$$dof = 120 \text{ bins} - (19 \text{ parameters}) - 1 - 1 = 99. \quad (5.43)$$

Therefore, a value of $X^2/dof = 101.23/99 \sim 1.0225$ is determined, which corresponds to a p -value of 42%. This result confirms the good agreement between the data and the fitted PDF.

Stability of the fit

The pull distribution \mathcal{P}_x of a given fit parameter x ,

$$\mathcal{P}_x = \frac{x_{\text{Fit}} - x_{\text{Toy}}}{\sigma_x}, \quad (5.44)$$

extracted from a set of toy MC experiments, can be used to assess the stability of the fit. If the fit is well behaved, the distribution of \mathcal{P}_x is a Gaussian with $\mu = 0$ and

$\sigma = 1$. If the mean value diverges from 0, it means that the determination of the parameter is biased, while a divergence in the width of the pull indicates that errors are not correctly estimated.

A set of 20,000 toy MC samples have been generated following the PDF from Eq. 5.29 with the values of the parameters extracted from the fit to the data. Each of the generated samples has then been fitted with the same PDF. The pull distributions for the six free signal parameters in the fit, fitted with a gaussian function, are shown in Fig. 5.14. It can be seen that these parameters are unbiased and their errors have been correctly estimated, since the means and the widths obtained from the gaussian fit are compatible with zero and one, respectively. Thus, it can be concluded that the fit is stable under variations of the input data and that the signal parameters and their uncertainties have been correctly extracted within the chosen model.

5.6. Extraction of the ratio of branching fractions

The expected yield for a given B decay is given by

$$\mathcal{N} = \mathcal{L} \times \sigma_{b\bar{b}} \times f \times \mathcal{B} \times \epsilon, \quad (5.45)$$

where \mathcal{L} is the luminosity, $\sigma_{b\bar{b}}$ the $b\bar{b}$ production cross section, f is the B meson hadronization fraction, \mathcal{B} is the visible branching fraction of the studied decay, and ϵ the acceptance, trigger, reconstruction and selection efficiencies.

Thus, the expected yield for the studied decays is

$$\begin{aligned} \mathcal{N}_{B^0 \rightarrow K^{*0}\gamma} &= \mathcal{L} \times \sigma_{b\bar{b}} \times f_d \times \mathcal{B}(B^0 \rightarrow K^{*0}\gamma) \times \mathcal{B}(K^{*0} \rightarrow K^+\pi^-) \times \epsilon_{B^0 \rightarrow K^{*0}\gamma}, \\ \mathcal{N}_{B_s^0 \rightarrow \phi\gamma} &= \mathcal{L} \times \sigma_{b\bar{b}} \times f_s \times \mathcal{B}(B_s^0 \rightarrow \phi\gamma) \times \mathcal{B}(\phi \rightarrow K^+K^-) \times \epsilon_{B_s^0 \rightarrow \phi\gamma}, \end{aligned} \quad (5.46)$$

and the ratio of branching fractions is calculated as the product of the ratio of fitted events, the inverse ratio of visible vector meson branching fractions, the ratio f_s/f_d , and the inverse ratio of selection efficiencies ϵ :

$$\frac{\mathcal{B}(B^0 \rightarrow K^{*0}\gamma)}{\mathcal{B}(B_s^0 \rightarrow \phi\gamma)} = \frac{\mathcal{N}_{B^0 \rightarrow K^{*0}\gamma}}{\mathcal{N}_{B_s^0 \rightarrow \phi\gamma}} \frac{\mathcal{B}(\phi \rightarrow K^+K^-)}{\mathcal{B}(K^* \rightarrow K^+\pi^-)} \frac{f_s}{f_d} \frac{\epsilon_{B_s^0 \rightarrow \phi\gamma}}{\epsilon_{B^0 \rightarrow K^{*0}\gamma}}. \quad (5.47)$$

The efficiency for each channel is split into trigger, acceptance, reconstruction and selection without PID requirements, and PID selection. The reason for separating the calculation of the selection efficiency from the PID efficiency is that the PID distributions are not accurately described by the simulation, and therefore cannot be extracted directly from MC. With this splitting in mind, the ratio of efficiencies between the two channels can be written as:

$$r_\epsilon \equiv \frac{\epsilon_{B_s^0 \rightarrow \phi\gamma}}{\epsilon_{B^0 \rightarrow K^{*0}\gamma}} = \frac{\epsilon_{\text{Trigger}}^{B_s^0 \rightarrow \phi\gamma}}{\epsilon_{\text{Trigger}}^{B^0 \rightarrow K^{*0}\gamma}} \times \frac{\epsilon_{\text{Acceptance}}^{B_s^0 \rightarrow \phi\gamma}}{\epsilon_{\text{Acceptance}}^{B^0 \rightarrow K^{*0}\gamma}} \times \frac{\epsilon_{\text{Reco\&SelNoPID}}^{B_s^0 \rightarrow \phi\gamma}}{\epsilon_{\text{Reco\&SelNoPID}}^{B^0 \rightarrow K^{*0}\gamma}} \times \frac{\epsilon_{\text{PID}}^{B_s^0 \rightarrow \phi\gamma}}{\epsilon_{\text{PID}}^{B^0 \rightarrow K^{*0}\gamma}}. \quad (5.48)$$

The ratio of efficiencies for trigger, acceptance, and reconstruction and selection without PID have been extracted from MC11 simulation. The ratio of efficiencies of PID cuts has been extracted by making use of a data-driven reweighting method on the Monte Carlo simulation.

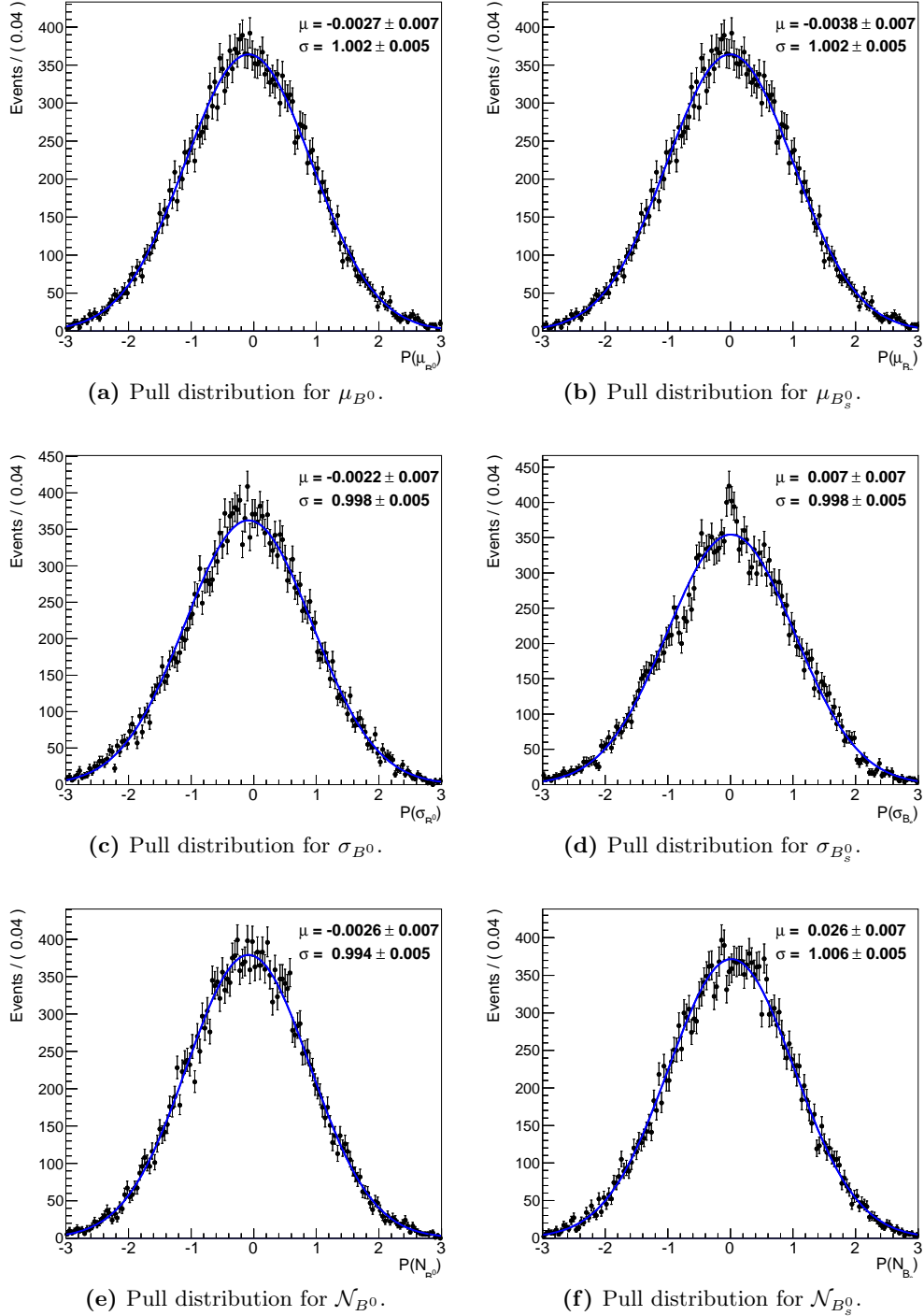


Figure 5.14. Pull distributions of the free signal parameters, obtained from fitting 20,000 toy MC samples generated with the model PDF. The fit of the pull distributions to a gaussian is shown in a blue solid line, with its parameters on the top right corner of each plot.

5.6.1. Ratio of signal yields

The signal yields $\mathcal{N}_{B^0 \rightarrow K^{*0}\gamma}$ and $\mathcal{N}_{B_s^0 \rightarrow \phi\gamma}$ have been obtained from the simultaneous fit (see Table 5.14), and their ratio is found to be

$$r_{\mathcal{N}} \equiv \frac{\mathcal{N}_{B^0 \rightarrow K^{*0}\gamma}}{\mathcal{N}_{B_s^0 \rightarrow \phi\gamma}} = 7.63 \pm 0.38 \text{ (stat)}, \quad (5.49)$$

where the given statistical error has been calculated by taking into account the correlation between the two signal yields.

Systematical uncertainties

The signal shape parameters for both $B^0 \rightarrow K^{*0}\gamma$ and $B_s^0 \rightarrow \phi\gamma$ decays have been fixed in the fit from their MC expectations found in Table 5.6. Although Table 5.6 shows that the values of the parameters are consistent when applying the photon smearing, possible discrepancies between the shapes of the signal between MC and data have been assessed by randomly varying, within 2σ of the MC fit result, the values of each of the fixed shape parameters, repeating the fit procedure and extracting r_{yields} . The $1 - \alpha$ confidence level intervals for the ratio of yields variation have been extracted from the distribution of 3500 of such fits using the *central intervals* criterion [187], *i.e.*, the probabilities excluded in the high and low limits are each $\alpha/2$ (shaded areas in Fig. 5.15). With this definition, the 95% confidence interval has been determined to be $[-1.3, +1.4]\%$.

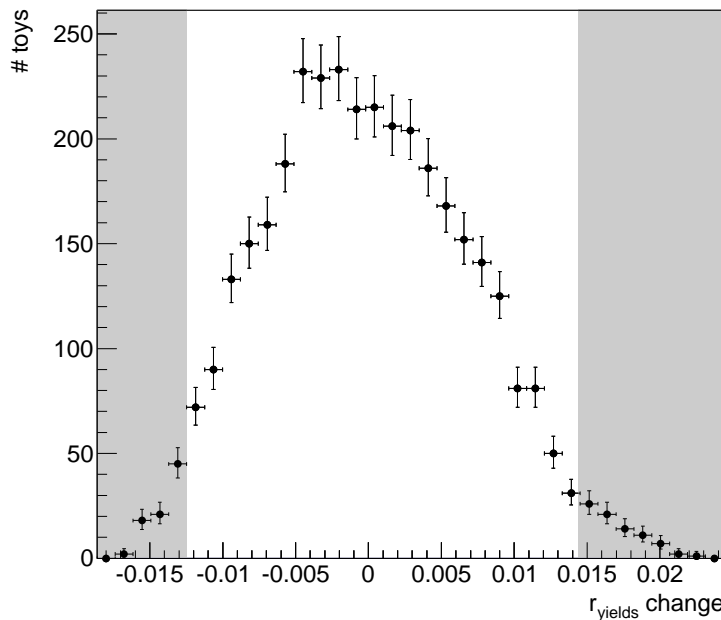


Figure 5.15. Distribution of the yield ratio variation for the 3500 experiments varying the signal CB parameters within their uncertainty. The area outside the asymmetric 95% confidence level zone has been shaded.

All background components in the fit model have their shapes fixed from the MC studies in §5.4. Some of them, specially those backgrounds the contribution of which

is under the mass peak, have their contamination fixed from the MC studies. There is, however, a big uncertainty emerging from poorly known line shapes or branching fractions —some of them have not even been measured yet. The systematic effect induced by the background models has been evaluated with a systematical exploration of the space of their fixed parameters. The fit procedure has been repeated by varying, within their uncertainty, the amplitude —when fixed— and the shape parameters of each specific background, and, for each of the 13,000 repeated fits, $r_{\mathcal{N}}$ has been extracted. The asymmetric, non-gaussian distribution of the variation of the ratio of yields is shown in Fig. 5.16. A relative variation of $[-1.2, +1.4]\%$ has been observed by making use of the central intervals criterion at 95% confidence level.

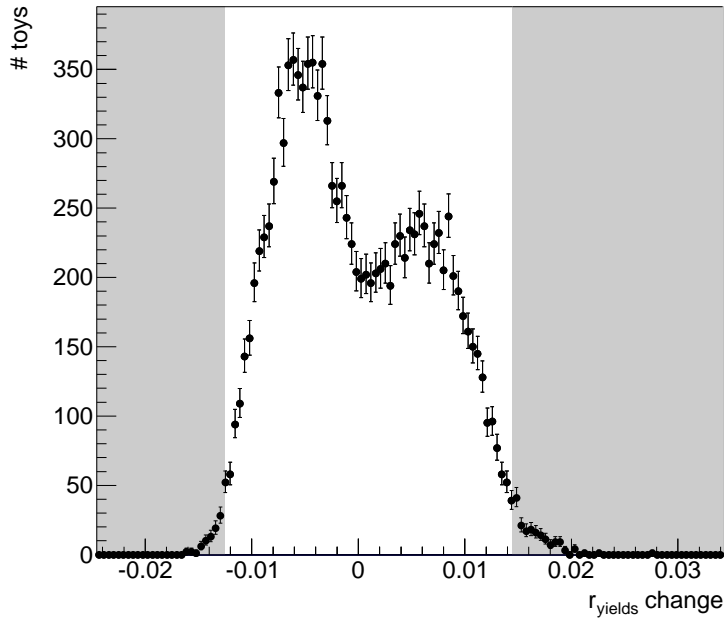


Figure 5.16. Distribution of the yield ratio variation for the toy background study, varying all the fixed parameters in the fit within their uncertainty. The area outside the asymmetric 95% confidence zone has been shaded.

The possible bias induced by the introduction of the acceptance function to model the calorimeter miscalibration and aging effects and by the chosen model of the partially reconstructed background has been determined by repeating the simultaneous fit in a tighter mass window. Given the value of σ_t and mass thresholds found from the fit, detailed in Table 5.14, the mass window has been reduced to $\pm 700 \text{ MeV}/c^2$, at approximately 2σ from the threshold. A 1% variation of the ratio of yields is observed from the fit shown in Fig. 5.17.

Combining the systematical errors of the background model, the signal model and the mass window choice, a 2.3% relative efficiency is found for the ratio of yields:

$$r_{\mathcal{N}} = 7.63 \pm 0.38 \text{ (stat)} {}^{+0.17}_{-0.16} \text{ (syst).} \quad (5.50)$$

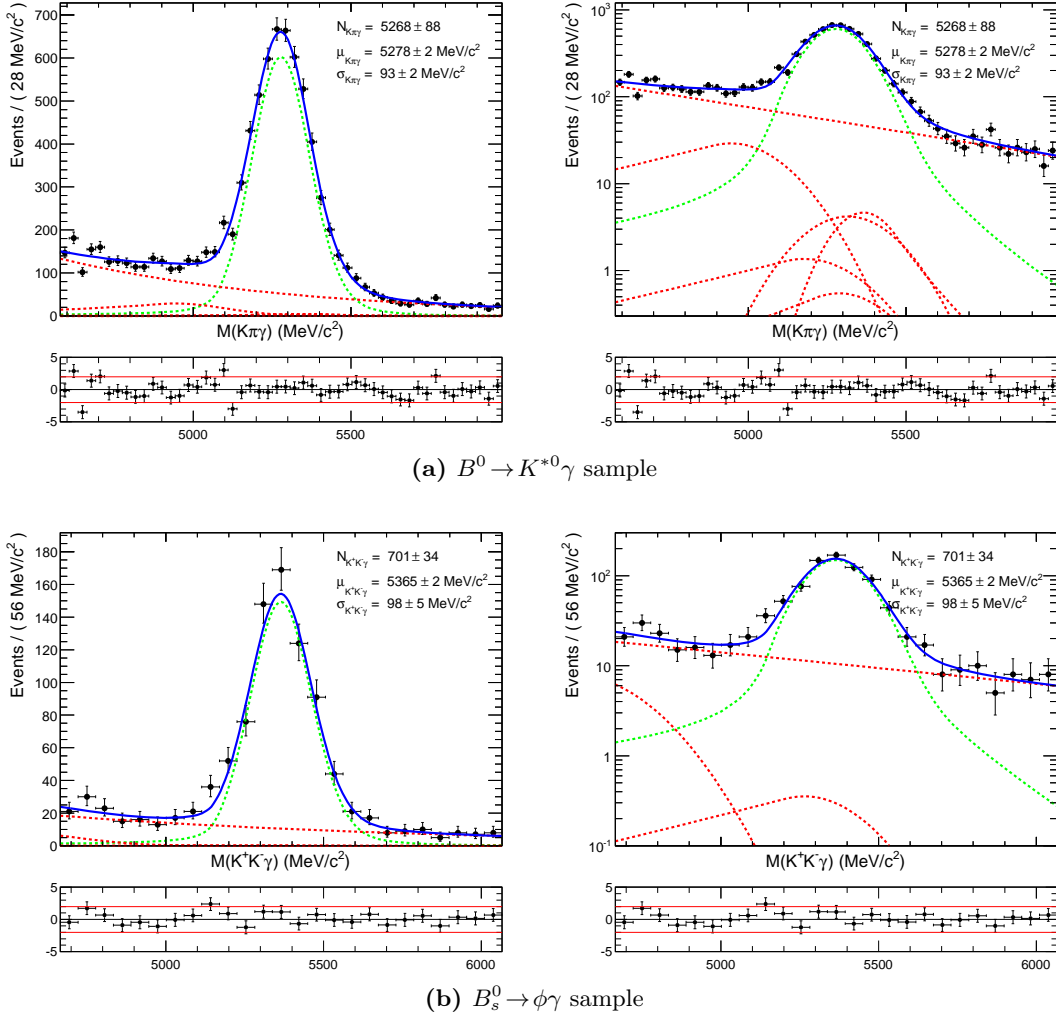


Figure 5.17. Mass distribution of the $B^0 \rightarrow K^{*0}\gamma$ and $B_s^0 \rightarrow \phi\gamma$ data samples, in linear (left) and logarithmic (right) scale, a the narrow mass window of $\pm 700 \text{ MeV}/c^2$. The fit model PDF is overlaid in a solid blue line, with the signal (dashed green) and background (dashed red) components. The χ^2/dof of the fit, obtained as detailed in §5.5.4, is found to be 1.14; this larger value is mainly due to the residual effect of the threshold acceptance in the low mass region.

5.6.2. Ratio of visible vector meson branching fractions

Since not all possible decay modes of the vector meson have been used on this the analysis, to obtain the visible cross section one needs to add the partial branching fractions of the observed modes $K^{*0} \rightarrow K^\pm\pi^\mp$ and $\phi \rightarrow K^+K^-$. In particular, the K^{*0} decay is almost a 100% isospin-conserving string decay and therefore one expects a 2/3 partial branching fraction for the charged decays (see Appendix B for more details).

The branching fractions of the vector mesons to the observed charged modes can be found in [21]:

$$\begin{aligned}\mathcal{B}(K^{*0} \rightarrow K^\pm\pi^\mp) &= (66.507 \pm 0.014) \times 10^{-2}, \\ \mathcal{B}(\phi \rightarrow K^+K^-) &= (48.9 \pm 0.5) \times 10^{-2}.\end{aligned}\quad (5.51)$$

Thus, the ratio of the visible vector meson branching fractions is

$$r_{\text{vector meson } \mathcal{B}} \equiv \frac{\mathcal{B}(\phi \rightarrow K^+K^-)}{\mathcal{B}(K^{*0} \rightarrow K^\pm\pi^\mp)} = 0.735 \pm 0.008. \quad (5.52)$$

5.6.3. Ratio of hadronization fractions

The LHCb experiment has measured the ratio $[f_s/(f_u + f_d)]$ using semileptonic decays of b -hadrons [188], as well as the ratio f_s/f_d using the relative abundance of $B_s^0 \rightarrow D_s^-\pi^+$ to $B^0 \rightarrow D^-K^+$, and $B^0 \rightarrow D^-\pi^+$ [189].

The ratio f_s/f_d is taken from the combined LHCb measurement, which has a 7.5% uncertainty [98]:

$$\frac{f_s}{f_d} = 0.267^{+0.021}_{-0.020}. \quad (5.53)$$

The contribution of f_s/f_d constitutes the main source of systematical uncertainty in the measurement.

5.6.4. Ratio of trigger efficiencies

The trigger efficiencies —including the TOS requirements detailed in §5.2.1— have been evaluated from the offline selected signal Monte Carlo sample by applying the following procedure:

1. Run the MOORE software with the studied trigger configuration on the offline-selected MC sample without trigger requirements.
2. Apply the TISTOSing algorithm with respect to the signal decay.
3. Calculate the efficiency of the TOS selection.

To obtain the trigger efficiency for data with several TCKs run one must average the individual efficiencies of each TCK, weighted by the luminosity taken with them.

For the data considered, a total number of 15 different TCKs have been used, the luminosities of which can be found in Table 3.1. Detailed TOS efficiencies per TCK are shown in Table 4.12, as well as the averaged TOS efficiency. This table can be used

to obtain the ratios of trigger efficiencies per TCK shown in Table 5.15. Calculating the luminosity-weighted average, the ratio of trigger efficiencies is found to be

$$r_{\text{Trigger}} \equiv \frac{\epsilon_{\text{Trigger}}^{B_s^0 \rightarrow \phi \gamma}}{\epsilon_{\text{Trigger}}^{B^0 \rightarrow K^{*0} \gamma}} = 1.080 \pm 0.009, \quad (5.54)$$

where the quoted uncertainty is due to the size of the used MC samples.

TCK	r_{Trigger}
0x360032	1.068 ± 0.011
0x480032	1.078 ± 0.009
0x4A0033	1.076 ± 0.009
0x5A0032	1.076 ± 0.009
0x5B0032	1.078 ± 0.009
0x5D0033	1.080 ± 0.009
0x6D0032	1.078 ± 0.009
0x700034	1.078 ± 0.009
0x710035	1.080 ± 0.009
0x730035	1.078 ± 0.009
0x740036	1.087 ± 0.011
0x760037	1.081 ± 0.009
0x790037	1.081 ± 0.009
0x790038	1.081 ± 0.009
Weighted average	1.080 ± 0.009

Table 5.15. Global trigger ratio efficiencies by TCK, considering L0 TOS, HLT1 TOS and HLT2 TOS as defined in §5.2.1.

Systematical uncertainties

As outlined in the overview of the analysis, the trigger paths enforced for the two channels through the TOS selection are almost identical in order to cancel most systematical uncertainties. In the trigger, differences between the two channels appear in the exclusive HLT2 selection, but cuts applied at HLT2 level are looser than the corresponding offline cuts, and thus the systematics related to them are included in the calculation systematical uncertainties of the selection.

A possible source of significant systematics in the trigger could come from the badly simulated L0 energies, which could affect the LOPhoton or LOElectron efficiencies. However, there is no noticeable difference in the E_T spectrum of the $B^0 \rightarrow K^{*0} \gamma$ and the $B_s^0 \rightarrow \phi \gamma$ above 2 GeV, as can be seen in Fig. 5.18. Therefore, no systematical error is expected, even if the difference between the Monte Carlo and the data spectra were sizeable.

In summary, only the systematical uncertainty related to the size of the used MC sample in the extraction of the ratio of trigger efficiencies, which amounts to 0.8%, has been included.

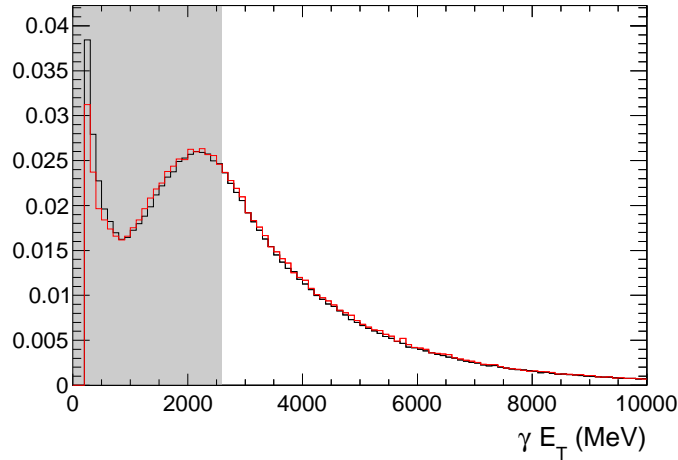


Figure 5.18. Transverse energy of reconstructed truth-matched Monte Carlo photons, for $B^0 \rightarrow K^{*0}\gamma$ (black) and $B_s^0 \rightarrow \phi\gamma$ (red). No differences are observed above $E_T > 2500$ MeV, the critical zone both for analysis and trigger. The area rejected by the offline cut of $E_T > 2600$ MeV has been shaded.

5.6.5. Ratio of acceptance efficiencies

When generating the Monte Carlo samples for a given decay channel, only those events with their final state particles inside the 400 mrad cone of LHCb acceptance are passed on to the detector simulation step. Thus, acceptance efficiencies have to be considered even before the reconstruction process takes place. They are calculated at generation time by the GAUSS software and are incorporated to the particle cut tables for MC11 [190].

	MagUp (%)	MagDown (%)	Average (%)
$B^0 \rightarrow K^{*0}\gamma$	23.41 ± 0.13	23.40 ± 0.13	23.41 ± 0.13
$B_s^0 \rightarrow \phi\gamma$	25.83 ± 0.14	25.51 ± 0.14	25.67 ± 0.14

Table 5.16. Acceptance efficiencies as given by the GAUSS software.

The acceptance efficiency is higher for the $B_s^0 \rightarrow \phi\gamma$ channel because the kaons coming from the ϕ are more likely to lie both within the detector acceptance, as they come out in a smaller angle due to the phase-space limitations of the $\phi \rightarrow K^+K^-$ decay. With the values shown in Table 5.16, the ratio of the particle cut efficiencies inside the 400 mrad LHCb acceptance cone is

$$r_{\text{Acceptance}} \equiv \frac{\epsilon_{<400\text{mrad}}^{B_s^0 \rightarrow \phi\gamma}}{\epsilon_{<400\text{ mrad}}^{B^0 \rightarrow K^{*0}\gamma}} = 1.097 \pm 0.009, \quad (5.55)$$

where the quoted uncertainty is due to the limited statistics at the generator level. The geometrical acceptance is known to be well modeled by the simulation, and therefore no further systematical uncertainty is added.

5.6.6. Ratio of reconstruction and selection efficiencies

The overall ratio of the reconstruction and selection efficiencies, without considering the PID cuts, has been extracted from the MC11 signal samples: the efficiency for each channel has been calculated by dividing the number of offline-selected events between the size of the samples, extracted from Table 5.3, and then the ratio has been computed:

$$r_{\text{Reco}\&\text{SelNoPID}} \equiv \frac{\epsilon_{\text{Reco}\&\text{SelNoPID}}^{B_s^0 \rightarrow \phi\gamma}}{\epsilon_{\text{Reco}\&\text{SelNoPID}}^{B^0 \rightarrow K^{*0}\gamma}} = 0.881 \pm 0.005, \quad (5.56)$$

where the uncertainty is statistical only. Special care has been taken to remove all PID cuts that are used in the reconstruction of kaons in order to avoid any double counting of PID effects.

The specific contribution of the reconstruction efficiencies, i.e., the ratio of the fraction of Monte Carlo events that have been reconstructed over the number of Monte Carlo events generated, has been extracted by making use of a special version of the reconstruction. On one side, as already mentioned, the soft PID cuts that are used in the reconstruction of kaons have been removed. On the other side, the IP cuts that are applied in building the loose K^{*0} particles —`StdVeryLooseDetachedKst2Kpi`— have also been removed in order to study their full effect when considering the offline selection. This reconstruction efficiency ratio is found to be

$$\frac{\epsilon_{\text{Reco}}^{B_s^0 \rightarrow \phi\gamma}}{\epsilon_{\text{Reco}}^{B^0 \rightarrow K^{*0}\gamma}} = 1.016 \pm 0.014. \quad (5.57)$$

As discussed in §5.2, the selection of both $B^0 \rightarrow K^{*0}\gamma$ and $B_s^0 \rightarrow \phi\gamma$ is identical except for the PID cuts and the vector mass window. However, there are significant differences in the efficiencies of several cuts due to the kinematical differences between the two decays. Table 5.17 illustrates the efficiency of each cut over the loosely selected MC10 sample for each of the channels. While only providing rough quantitative information (the concept of “reconstructed sample” is hard to define), the table allows to highlight the main differences between the two channels of interest:

- Owing to the fact that the ϕ daughters are closer together, the IP χ^2 cut has a bigger impact on the $B_s^0 \rightarrow \phi\gamma$.
- Due to the phase-space constraints of the ϕ decay, the ϕ vertex has worse resolution (see Fig. 5.19) and thus the DIRA, flight distance and the B isolation $\Delta\chi^2$ requirements affect the $B_s^0 \rightarrow \phi\gamma$ in a larger amount.
- Because the π of the K^{*0} has a softer p_T spectrum, the track transverse momentum cut is more restrictive on the $B^0 \rightarrow K^{*0}\gamma$ decay.
- The vector meson mass window cut is more efficient in the $B_s^0 \rightarrow \phi\gamma$ than in the $B^0 \rightarrow K^{*0}\gamma$ because the mass window of the K^{*0} has been chosen to be of 1 natural width (Γ_0) of the resonance in order to improve the $S/\sqrt{S+B}$, while the mass window of the ϕ has been left at $2\Gamma_0$.

Combining equations 5.56 and 5.57, the selection efficiency is found to be

$$\frac{\epsilon_{\text{SelNoPID}}^{B_s^0 \rightarrow \phi\gamma}}{\epsilon_{\text{SelNoPID}}^{B^0 \rightarrow K^{*0}\gamma}} = 0.867 \pm 0.013, \quad (5.58)$$

	$B^0 \rightarrow K^{*0}\gamma$	$B_s^0 \rightarrow \phi\gamma$
Kaon IP χ^2	82%	68%
Pion IP χ^2	78%	–
Track p_T	89%	97%
Max track p_T	86%	81%
V meson vertex $\Delta\chi^2$	96%	95%
V meson ΔM_{PDG}	75%	85%
Photon E_T	56%	54%
Photon CL	81%	81%
π^0/γ separation	67%	66%
B candidate p_T	68%	69%
B candidate IP χ^2	91%	92%
B candidate DIRA	68%	45%
B candidate FD χ^2	73%	59%
B candidate $ \cos\theta_H $	96%	95%
B candidate isolation $\Delta\chi^2$	82%	71%

Table 5.17. Efficiency of each of the offline cuts on reconstructed events from simulated $B^0 \rightarrow K^{*0}\gamma$ and $B_s^0 \rightarrow \phi\gamma$ samples.

where the uncertainty is due to the Monte Carlo sample statistics.

Systematical uncertainties

Several effects need to be considered when calculating the ratio of reconstruction efficiencies, mainly material budget effects. Using the tracking efficiency tables [191] a systematic of the order of 0.2% per track is obtained. However, it will be ignored because tracking efficiency systematics mostly cancel due to the fact that the spectra of the tracks are very similar in both decays.

There is a more important systematic effect due to the fact that the reconstruction efficiency for the hadrons has not been measured in LHCb. Assuming that the material budget is known within 20%, studies have shown [192] that there is an average difference of 20% interaction lengths between pions and kaons. Assuming this difference, and adding the fact that the material budget constitutes $\sim 20\%$ of the hadronic interaction length, the uncertainty in the material budget gives a systematical uncertainty of the order of 0.4%.

Another possible source of systematics are those variables which have different distributions for the $B^0 \rightarrow K^{*0}\gamma$ and the $B_s^0 \rightarrow \phi\gamma$ and, at the same time, are not well described by the Monte Carlo simulation. These variables are mainly the IP χ^2 and the vertex isolation $\Delta\chi^2$, as they are sensitive to the track multiplicity, which is known to be poorly described in the current simulation. Other variables with different distributions between the two decays, such as the flight distance χ^2 and the DIRA, are well modeled in the simulation. To deal with the systematics associated with these two variables, the data has been reweighed with the MC distribution and the ratio of yields has been recalculated. A 1% difference in the isolation $\Delta\chi^2$ is obtained, while the IP χ^2 discrepancy is found to be 0.5%.

Therefore, summing up all the contributions, including the statistical uncertainty

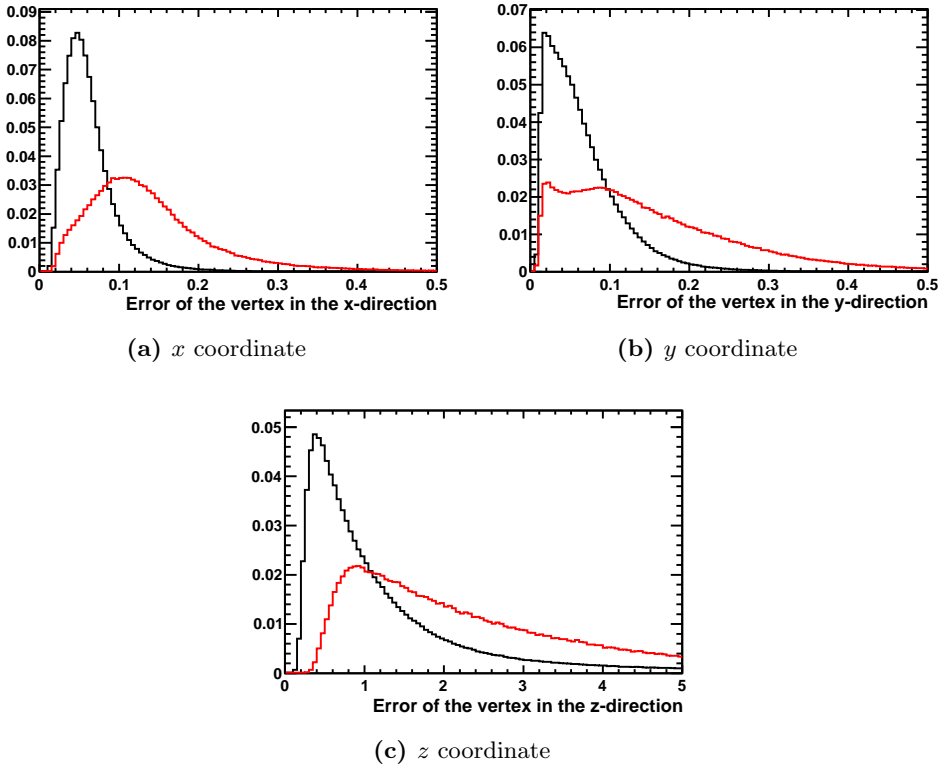


Figure 5.19. Vector meson vertex resolution in the three spatial directions for K^{*0} in $B^0 \rightarrow K^{*0}\gamma$ (black) and ϕ in $B_s^0 \rightarrow \phi\gamma$ (red) simulated events. It can be clearly seen how the ϕ vertex has a much worse resolution.

quoted in Eq. 5.56, the reconstruction and selection efficiency systematics is found to be at the level of 1.3%:

$$r_{\text{Reco\&SelNoPID}} = 0.881 \pm 0.005 \text{ (MC stat)} \pm 0.010 \text{ (syst)}. \quad (5.59)$$

5.6.7. Ratio of PID selection efficiencies

The PID efficiency ratio can be expressed as

$$r_{\text{PID}} \equiv \frac{\epsilon_{\text{PID}}^{B_s^0 \rightarrow \phi\gamma}}{\epsilon_{\text{PID}}^{B^0 \rightarrow K^{*0}\gamma}} = \frac{\epsilon_{\text{PID}}^\phi}{\epsilon_{\text{PID}}^{K^{*0}}}, \quad (5.60)$$

since the PID cuts do not affect the photon. This ϵ^ϕ and $\epsilon^{K^{*0}}$ efficiencies have to be understood as an average of the individual efficiencies that can be assigned to each event depending on its particular kinematics, *i.e.*, they are values that cannot be extracted generally because they depend on the particular kinematics of the studied sample.

As it can be seen in Table 5.5, pions from the K^{*0} are required to have $\text{DLL}_{K\pi} < 0$ and kaons, either from the K^{*0} or the ϕ , are required to fulfill at the same time the $\text{DLL}_{K\pi} > -5$ and $\text{DLL}_{Kp} > 2$ conditions².

²In a given event, it is important to keep in mind that, in general,

$$\epsilon_{\text{DLL}_{K\pi} \& \text{DLL}_{Kp}} \neq \epsilon_{\text{DLL}_{K\pi}} \times \epsilon_{\text{DLL}_{Kp}},$$

The distributions for $\Delta \ln \mathcal{L}_{\text{MC}}$ are different from $\Delta \ln \mathcal{L}_{\text{data}}$, and some examples of this situation for $B^0 \rightarrow K^{*0}\gamma$ and $B_s^0 \rightarrow \phi\gamma$ can be seen in Fig. 5.20. That means that a given PID cut will perform differently in data and in Monte Carlo, and thus MC cannot be used to estimate the PID cuts efficiency.

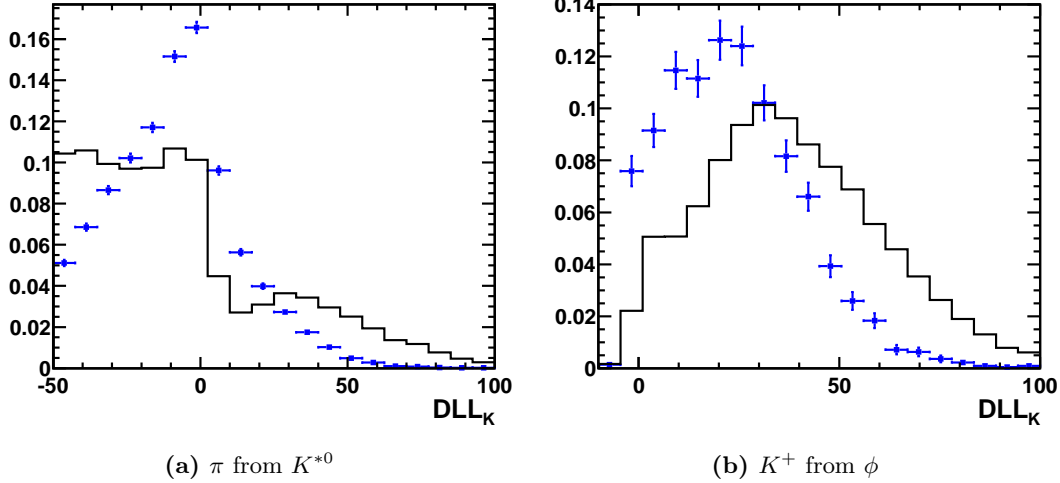


Figure 5.20. Distributions of $DLL_{K\pi}$ (DLL_K) of offline-selected (without PID cuts) real data (blue dots) and MC11 (red solid line) samples.

A way of determining PID performance from data, *i.e.*, a PID calibration procedure, has been developed by the LHCb Particle IDentification group [193, 194]. A calibration sample of prompt $D^{*\pm} \rightarrow D^0(K^+\pi^-)\pi^\pm$ is reconstructed and selected using only kinematical variables, *i.e.*, without the use of the RICH detectors; this allows to acquire calibration samples of pure pions and kaons. Then, the key idea of the data-driven calibration procedure is that if one bins in PID-dependent variables, all tracks in a given bin will have consistent RICH PID decisions, no matter their origin, and thus the efficiency per bin can be evaluated.

The chosen variables for binning by the PID group are those in which the PID algorithms are more dependent. They have been found to be:

- Number of tracks in the event.
- Track momentum, p .
- Track transverse momentum, p_T .
- Track pseudorapidity, η .

It is not necessary, however, to use all of them, specially in analyses with low statistics, and one may keep those with a dominant effect on PID efficiency. Once the binning for each specific analysis has been decided, an efficiency table for that specific binning can be obtained by reprocessing the sample efficiency tables using the PID software package.

since $DLL_{K\pi}$ and DLL_{Kp} are correlated. It is therefore mandatory to study the $DLL_{K\pi}$ and DLL_{Kp} cuts for the kaon as a unit, and not individually.

		Magnet Up	Magnet Down	Average
$B^0 \rightarrow K^{*0} \gamma$	$\epsilon_{\text{PID}}^{K^\pm}$	(70.0 ± 0.3)%	(72.2 ± 0.4)%	(71.1 ± 0.2)%
	$\epsilon_{\text{PID}}^{\pi^\mp}$	(90.0 ± 0.3)%	(92.0 ± 0.3)%	(91.0 ± 0.2)%
	$\epsilon_{\text{PID}}^{K^{*0}}$	(63.5 ± 0.4)%	(66.9 ± 0.3)%	(65.2 ± 0.2)%
$B_s^0 \rightarrow \phi \gamma$	$\epsilon_{\text{PID}}^{K^+}$	(69.4 ± 0.3)%	(72.2 ± 0.4)%	(70.8 ± 0.2)%
	$\epsilon_{\text{PID}}^{K^-}$	(69.6 ± 0.3)%	(72.2 ± 0.4)%	(70.8 ± 0.2)%
	$\epsilon_{\text{PID}}^\phi$	(52.8 ± 0.3)%	(56.5 ± 0.4)%	(54.7 ± 0.2)%
	r_{PID}	0.831 ± 0.007	0.844 ± 0.007	0.839 ± 0.005

Table 5.18. PID selection efficiencies, split in magnet polarity, obtained by reweighting the (p, η) spectrum of the kaons and pions of the $B^0 \rightarrow K^{*0} \gamma$ and $B_s^0 \rightarrow \phi \gamma$ decays with the PID calibration tables. The last line gives the ratio of the PID selection efficiencies. The quoted errors are due to the statistical errors of each bin of the PID tables, which arise from the limited size of the calibration sample.

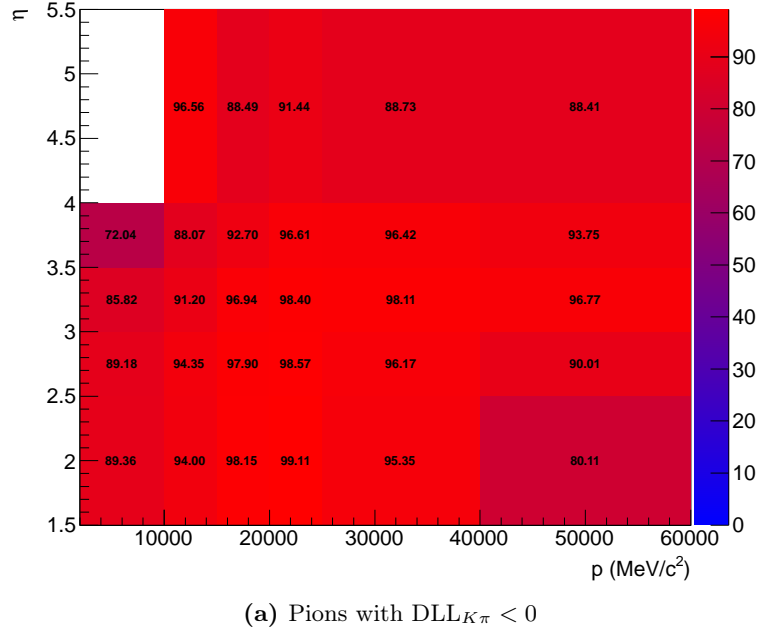
In this analysis, and given the statistics of the studied decays, seven bins in p and five in η have been used. The efficiency map for pions with $\text{DLL}_{K\pi} < 0$, extracted with the PID software package, is given in Fig. 5.21a; the corresponding efficiency map for kaons with $\text{DLL}_{K\pi} > 5$ and $\text{DLL}_{Kp} > 2$ is shown in Fig. 5.21b.

Since the ratio of branching fractions measurement is fully inclusive—not binned in any variable—, a global efficiency is obtained by integrating the full selected sample. However, as stated before, the PID efficiency for a given event is the product of the efficiencies of the daughters of the K^{*0} or ϕ , depending on which channel is being studied. Thus, one cannot consider the p and η distributions of the individual daughters of the candidate vector meson and sum over the efficiency of each bin. Instead, one must consider the PID efficiency —calculated as the product of efficiencies for each $K\pi$ and KK pair—as a per-event weight, and with that information calculate the integrated efficiency.

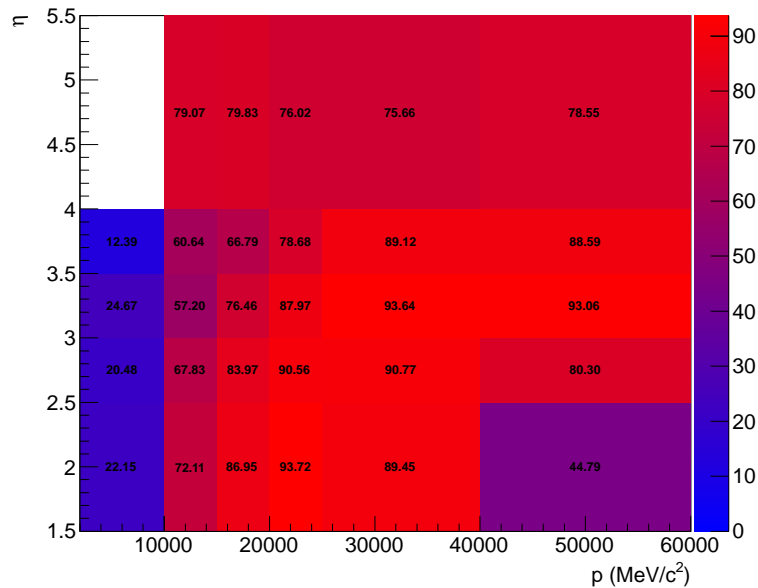
To do that, the momentum, transverse momentum and pseudorapidity of the signal tracks must be known in order to assign the correct weight to each event. However, in the data samples signal is mixed with background, and thus they cannot be used directly because the kaon and pion distribution shapes between signal and background may be different.

The $s\mathcal{P}lot$ technique could be used to extract the required distributions of the signal tracks from real data. However, the low signal statistics in the data sample would give rise to big uncertainties when determining the PID efficiencies from the PID tables. A better precision is achieved by taking advantage of the fact that the simulation describes well kinematical variables such as p , p_T and η . Thus, MC signal tracks can be used as inputs for the data-driven PID calibration procedure.

Moreover, the PID performance is different depending on the magnet polarity, and thus PID calibration tables for the up and down configurations need to be used. A summary of the PID efficiencies determined for each polarity, as well as their average, can be found in Table 5.18.



(a) Pions with $\text{DLL}_{K\pi} < 0$



(b) Kaons with $\text{DLL}_{K\pi} > 5$ and $\text{DLL}_{Kp} > 2$

Figure 5.21. Efficiency map for the PID cuts given in Table 5.5 for kaons and pions, binned in track momentum and pseudorapidity, obtained with a data-driven calibration method (the leftmost bin in p , which goes from 60 to 400 GeV/c, has been left out to improve readability). Given a bin in momentum and pseudorapidity, all tracks behave consistently regarding PID decisions. Therefore, the PID efficiency for a given event is the product of the efficiencies of its particular $K\pi$ and KK combination, obtained by making use of these tables.

Systematical uncertainties

Each of the bins of the data-based calibration table has an associated uncertainty due to the size of the $D^{*\pm} \rightarrow D^0(K^+\pi^-)\pi^\pm$ calibration sample and the remaining statistics per bin. The level of uncertainty per bin with the chosen binning scheme, shown in Fig. 5.22, is the responsible of the uncertainties quoted in Table 5.18, and it is calculated to be 0.6%.

Furthermore, the uncertainty induced by the data-driven PID method has been estimated by applying the same method on a $D^{*\pm} \rightarrow D^0(K^+\pi^-)\pi^\pm$ MC sample and comparing the resulting efficiencies, shown in Fig. 5.23, to those obtained by directly applying the PID cuts on the selected data sample. A 1.1% difference is found, and is taken as a systematic.

Thus, the ratio of PID efficiencies is

$$\frac{\epsilon_{PID}^{B_s^0 \rightarrow \phi\gamma}}{\epsilon_{PID}^{B^0 \rightarrow K^{*0}\gamma}} = 0.839 \pm 0.005 \text{ (stat)} \pm 0.009 \text{ (syst)}. \quad (5.61)$$

5.7. Result

A summary of the efficiency ratios defined in Eq. 5.48, including their systematical uncertainties, is presented in Table 5.19. All contributions to the calculation of the ratio between branching fractions, as defined in Eq. 5.47, are summarized in Table 5.20.

r_{Trigger}	1.080 ± 0.009
$r_{\text{Acceptance}}$	1.099 ± 0.004
$r_{\text{Reco\&SelNoPID}}$	0.881 ± 0.011
r_{PID}	0.839 ± 0.010
r_ϵ	0.877 ± 0.017

Table 5.19. Summary of intermediate efficiency ratios, as well as the overall ratio of efficiencies, including all systematical uncertainties.

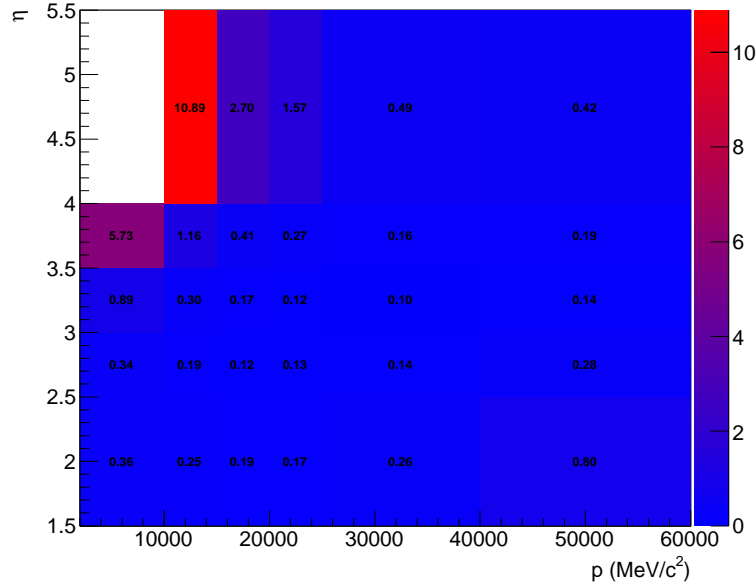
r_N	$7.63 \pm 0.38 {}^{+0.17}_{-0.16}$
$r_{\text{vector meson } B}$	0.735 ± 0.008
f_s/f_d	$0.267 {}^{+0.021}_{-0.020}$
r_ϵ	0.877 ± 0.017

Table 5.20. Summary of the various contributions to the ratio of branching fractions, as defined in Eq. 5.47.

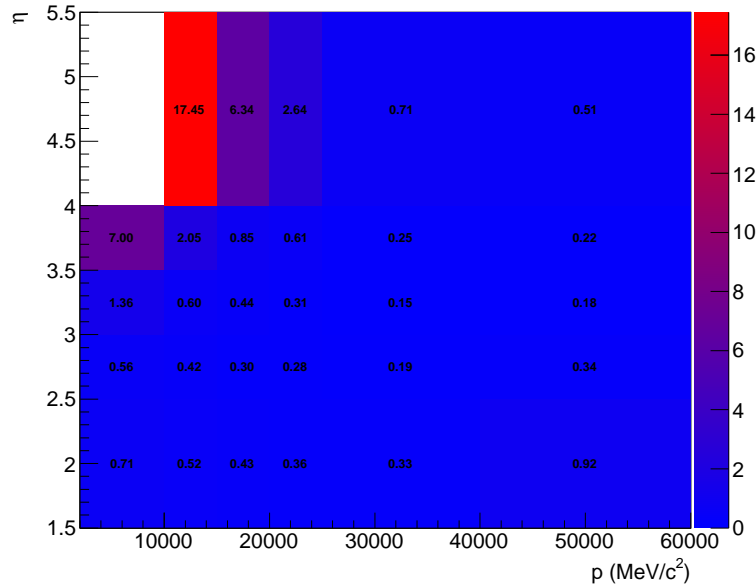
Combining the information in Table 5.20, the ratio of branching fractions between $B^0 \rightarrow K^{*0}\gamma$ and $B_s^0 \rightarrow \phi\gamma$ in 1.0 fb^{-1} of pp collisions at a center of mass energy of $\sqrt{s} = 7 \text{ TeV}$ has been measured to be

$$\frac{\mathcal{B}(B^0 \rightarrow K^{*0}\gamma)}{\mathcal{B}(B_s^0 \rightarrow \phi\gamma)} = 1.31 \pm 0.08 \text{ (stat)} \pm 0.04 \text{ (syst)} \pm 0.10 (f_s/f_d), \quad (5.62)$$

in good agreement with the theory prediction of 1.0 ± 0.2 .



(a) Pions with $DLL_{K\pi} < 0$



(b) Kaons with $DLL_{K\pi} > 5$ and $DLL_{Kp} > 2$

Figure 5.22. Efficiency uncertainties map for the PID efficiency map in Fig. 5.21. The leftmost bin in p , which goes from 60 to $400 \text{ GeV}/c$, has been left out to improve readability

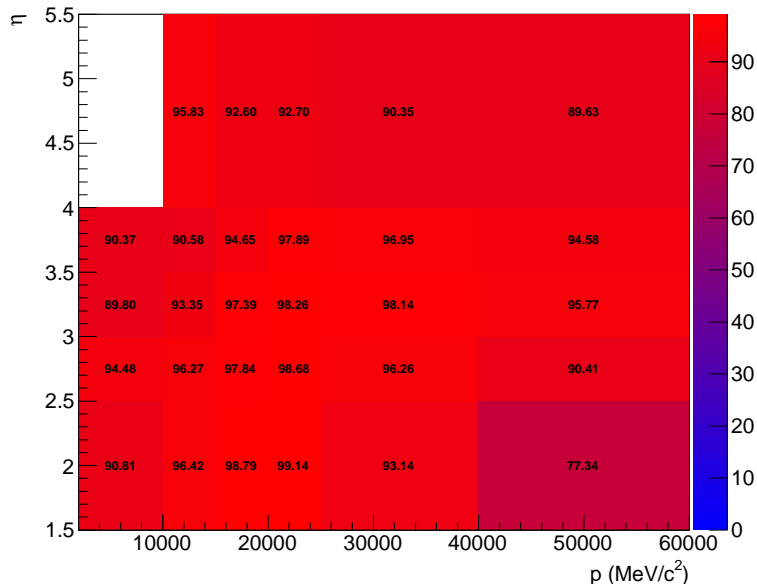
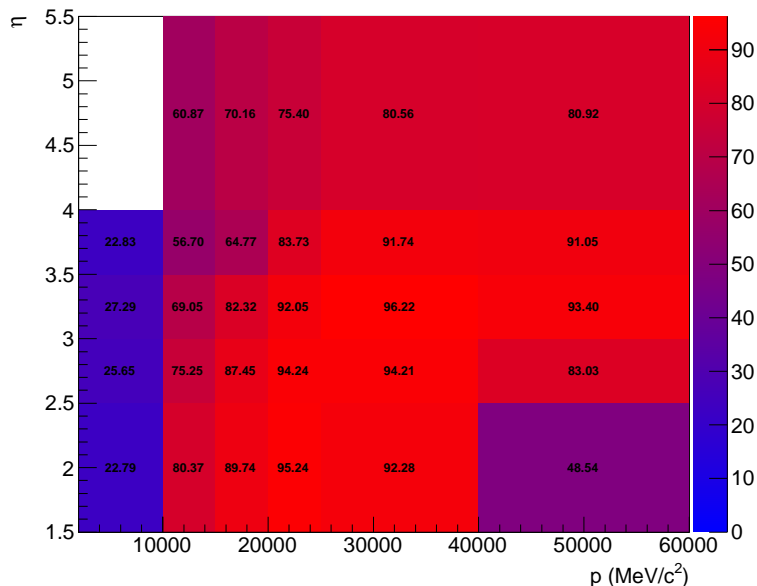
(a) Pions with $DLL_{K\pi} < 0$ (b) Kaons with $DLL_{K\pi} > 5$ and $DLL_{Kp} > 2$

Figure 5.23. Efficiency map for the PID cuts given in Table 5.5 for MC kaons and pions, binned in track momentum and pseudorapidity, obtained with a data-driven calibration method applied on a MC calibration sample (the leftmost bin in p , which goes from 60 to 400 GeV/c, has been left out to improve readability).

This ratio of branching fractions can be combined with the well-known value for $\mathcal{B}(B^0 \rightarrow K^{*0}\gamma)$, included in Table 1.3, to extract a new value for $\mathcal{B}(B_s^0 \rightarrow \phi\gamma)$,

$$\mathcal{B}(B_s^0 \rightarrow \phi\gamma) = (3.3 \pm 0.3) \times 10^{-5}, \quad (5.63)$$

which agrees with the previous experimental measurement, as well as with the theoretical prediction of $\mathcal{B}(B_s^0 \rightarrow \phi\gamma) = (4.3 \pm 1.4) \times 10^{-5}$.

6

Conclusions

This document has presented my contribution to the first steps of the radiative B decays program at LHCb.

Radiative B decays are an example of flavor-changing neutral currents, and as such they only appear in the Standard Model as loop-level processes. This feature makes them sensitive to the heavy degrees of freedom circulating in the loop, turning them into very sensitive probes for New Physics searches. While exclusive branching fractions of radiative B decays are not well predicted theoretically, other observables such as CP and isospin asymmetries, and the photon polarization provide a good handle to test models beyond the Standard Model, such as mSUGRA or the Left Right Symmetric Model.

An essential requirement for these studies is a good trigger efficiency, so a sizeable amount of events can be kept from the background-dominated pp collisions at LHC. The optimizations introduced to the trigger lines for $B^0 \rightarrow K^{*0}\gamma$ and $B_s^0 \rightarrow \phi\gamma$ have been detailed, and their performance has been assessed both on simulated and real data, with impressive results. This exclusive trigger strategy, in which only the $B^0 \rightarrow K^{*0}\gamma$ and $B_s^0 \rightarrow \phi\gamma$ decay channels are included, has been used successfully for radiative decays studies during 2011. However, this strategy does not scale well with the number of channels and completely discards the possibility of data mining.

An inclusive trigger strategy has been developed in order to overcome this problem and to open the possibility of new analyses involving channels for which no exclusive trigger line existed. However, in order to broaden the scope of radiative decays trigger lines, which involve in all cases the reconstruction of the photon, it has been necessary to rethink and redesign how the calorimeter reconstruction works in the HLT2. Reducing the timing of the calorimeter reconstruction was mandatory before larger event samples could make use of photons in the HLT.

A new reconstruction procedure for the calorimeter in the HLT2 environment, based on L0 objects, has been devised, providing a three-fold reduction in executing time at the cost of a small efficiency loss.

A new set of HLT2 inclusive radiative lines, in which only certain common aspects among radiative decays are exploited when making a trigger decision, and a redesigned inclusive ϕ line, have been introduced. Their performance on simulated data has been remarkable, and in three out of the four analyzed radiative channels they have

6. Conclusions

outperformed the exclusive approach. A direct comparison with the exclusive approach has also been presented for $B^0 \rightarrow K^{*0}(K^\pm\pi^\mp)\gamma$ and $B_s^0 \rightarrow \phi(K^+K^-)\gamma$ data from 2011. In addition, the experience of the 2011 data taking has led to new ideas on how to improve the inclusive lines in order to access the lower part of the transverse energy spectrum of the photon.

LHCb has decided that inclusive radiative lines will form the base of the trigger strategy for radiative decays in 2012, opening the way for several new analyses of radiative B decays, such as the CP asymmetry studies in $B^+ \rightarrow \phi K^+\gamma$ and $B^0 \rightarrow \rho\gamma$. This decision has also caused a shift of the radiative stripping strategy towards inclusiveness, and will open the way for new studies on the optimization of the offline selection.

Data collected by the LHCb experiment during 2011 have been used to extract the ratio of branching fractions of the $B^0 \rightarrow K^{*0}\gamma$ and $B_s^0 \rightarrow \phi\gamma$ decays. The theoretical prediction for this ratio has an uncertainty of 20%, while the error of the current experimental value is $\sim 40\%$, mainly due to the poor knowledge of the $B_s^0 \rightarrow \phi\gamma$ branching fraction.

By extracting the ratio of branching fractions directly, applying common selection and trigger criteria for both decays, the cancellation of systematics has been maximized and the total uncertainty has been reduced. The yield of each decay has been extracted from a simultaneous fit to the $K^\pm\pi^\mp\gamma$ and $K^+K^-\gamma$ invariant mass distributions. Possible background sources have been studied in detail and they have been added to the invariant mass fit. Special care has also been taken to account for all discrepancies between data and its MC description.

The ratio of branching fractions has been measured to be

$$\frac{\mathcal{B}(B^0 \rightarrow K^{*0}\gamma)}{\mathcal{B}(B_s^0 \rightarrow \phi\gamma)} = 1.31 \pm 0.08 \text{ (stat)} \pm 0.04 \text{ (syst)} \pm 0.10 \text{ } (f_s/f_d), \quad (6.1)$$

and has been found to be compatible with the theory prediction of 1.0 ± 0.2 . This result has been combined with the well-measured value of the $B^0 \rightarrow K^{*0}\gamma$ branching fraction to extract the world-best measurement of the branching fraction of the radiative $B_s^0 \rightarrow \phi\gamma$ decay,

$$\mathcal{B}(B_s^0 \rightarrow \phi\gamma) = (3.3 \pm 0.3) \times 10^{-5}, \quad (6.2)$$

which is also in agreement with the theoretical prediction of $(4.6 \pm 1.4) \times 10^{-5}$. This result largely improves the previous knowledge of $\mathcal{B}(B_s^0 \rightarrow \phi\gamma)$, reducing its uncertainty from 35% down to 9%.

A

Helicity formalism and angular distributions

A.1. The helicity formalism

The helicity formalism is the preferred method for obtaining angular distributions in relativistic scattering and decay processes [195]. This formalism aims to solve the problem that in the spin-orbit formalism —developed in non-relativistic quantum mechanics [196]— the orbital and spin angular momentum operators are defined in reference frames that are not at rest with respect to one another. The helicity operator $h = \vec{S} \cdot \hat{p}$ allows to construct relativistic basis vectors that are either eigenstates of total angular momentum and helicity (or of linear momentum and helicity) thanks to the fact that h is invariant under both rotations and boosts along \hat{p} .

A.1.1. Rotation operators and Wigner D-Matrix

An arbitrary rotation $R(\alpha\beta\gamma)$ from one initial xyz coordinate system to a final XYZ coordinate system can be constructed from three successive rotations performed in a specific sequence [197]. The *Euler angles* (α, β, γ) are defined as the three successive angles of rotation:

1. The xyz axes are rotated counterclockwise about the z -axis by an angle α . The resulting coordinate system is labeled tuz .
2. The intermediate tuz axes are rotated counterclockwise about the u -axis by an angle β to produce a second intermediate set of axes, the $t'uZ$.
3. The $t'uZ$ axes are rotated counterclockwise by an angle γ about the Z -axis to produce the desired XYZ system of axes.

Since a rotation around a given axis \hat{n} is generated by the angular momentum operator $\vec{J} \cdot \hat{n}$, the complete rotation can be written as

$$R(\alpha\beta\gamma) = R_Z(\gamma)R_u(\beta)R_z(\alpha) = e^{-iJ_z\gamma}e^{-iJ_u\beta}e^{-iJ_z\alpha}. \quad (\text{A.1})$$

The previous expression is not very useful because it is not expressed in terms of the original axes xyz . Applying the invariance under rotation of observables of some physical system, and exploiting the unitarity of the rotation operators, an arbitrary rotation specified by the Euler angles (α, β, γ) can be expressed in terms of rotations of the fixed axes xyz :

$$R(\alpha\beta\gamma) = R_z(\gamma)R_y(\beta)R_z(\alpha) = e^{-iJ_z\gamma}e^{-iJ_y\beta}e^{-iJ_z\alpha}. \quad (\text{A.2})$$

Angular momentum eigenstates $|jm\rangle$ transform irreducibly under rotations because $[R, J^2] = 0$. The action of $R(\alpha\beta\gamma)$ on the basis state $|jm\rangle$ can be written as

$$R(\alpha\beta\gamma)|jm\rangle = \sum_{m'=-j}^j D_{m'm}^j(\alpha\beta\gamma)|jm'\rangle. \quad (\text{A.3})$$

The *Wigner D-matrix* [198] is defined as a $2j + 1$ -dimensional square matrix with elements

$$D_{m'm}^j(\alpha\beta\gamma) \equiv \langle jm'|R(\alpha\beta\gamma)|jm\rangle. \quad (\text{A.4})$$

Making use of Eq. A.2, the D-matrix can be expressed as

$$D_{m'm}^j(\alpha\beta\gamma) = \langle jm'|e^{-iJ_z\gamma}e^{-iJ_y\beta}e^{-iJ_z\alpha}|jm\rangle = e^{-im'\alpha}d_{m'm}^j(\beta)e^{-im\gamma}, \quad (\text{A.5})$$

in which the elements

$$d_{m'm}^j = \langle jm'|e^{-iJ_y\beta}|jm\rangle \quad (\text{A.6})$$

define *Wigner's d-matrix*. These matrix elements are given by the complex Wigner formula, which can be found elsewhere [199]. They have, however, many simple properties, the most useful of which are:

$$\begin{aligned} d_{m'm}^j(-\beta) &= (-1)^{m'-m}d_{m'm}^j(\beta) \\ d_{m'm}^j(-\beta) &= d_{mm'}^j(\beta) \\ D_{m'm}^j(\alpha, \beta, \gamma) &= D_{mm'}^j(\gamma, -\beta, \alpha) \\ d_{m'm}^j(\pi) &= (-1)^{j-m}\delta_{m'm}(\beta) \\ d_{m'm}^j(2\pi) &= (-1)^{2j}\delta_{m'm}(\beta). \end{aligned} \quad (\text{A.7})$$

A.1.2. Plane-Wave helicity states

The states of a free particle of arbitrary spin s , momentum p , and mass m correspond to plane-wave solutions of the relativistic wave equation. For each p there are $2s + 1$ linearly independent states of definite helicity ($\lambda = -s, s+1, \dots, s$) if the particle is massive, and only two if the particle is massless ($\lambda = \pm 1$). If a rotation $R(\alpha\beta\gamma)$ of the system of axes is applied to one of these states, the direction of p changes, but λ remains constant. Similarly, when a Lorentz boost ($L(\vec{p})$) along \hat{p} is applied to the system, p changes magnitude and λ remains unchanged as long as the direction of p is not reversed.

Therefore, to obtain a state $|\vec{p}, s, \lambda\rangle$ $|0, s, \lambda\rangle$ is rotated so that its quantization axis points along \hat{p} and afterwards apply a Lorentz boost along \hat{p} (the reversed operation is completely equivalent):

$$|\vec{p}, s, \lambda\rangle = L(\vec{p})R(\alpha = \varphi, \beta = \theta, \gamma = -\varphi)|0, s, \lambda\rangle. \quad (\text{A.8})$$

The choice of $\gamma = -\varphi$ is conventional and has no physical meaning [199].

The next step is construct states of two free particles with masses m_1 and m_2 , and spins s_1 and s_2 . These states are constructed as direct products of the previously studied one-particle plane-wave states,

$$|\vec{p}_1, \lambda_1; \vec{p}_2, \lambda_2\rangle \equiv |\vec{p}_1, s_1, \lambda_1\rangle \otimes |\vec{p}_2, s_2, \lambda_2\rangle. \quad (\text{A.9})$$

The spins s_1 and s_2 are fixed and therefore suppressed from the notation.

Moving to the CM frame, in which the particles are back to back ($\vec{p}_1 = -\vec{p}_2 = \vec{p}$), the same two-particle state can be fully specified in terms of the magnitude of \vec{p} and its direction. Defining $p = |\vec{p}_1| = |\vec{p}_2|$ and (θ, φ) as the angles of \hat{p}_1 , the state can be written as $|p, \theta, \varphi, \lambda_1, \lambda_2\rangle$. Furthermore, since the two-particle CM plane-wave states are eigenstates of the total four-momentum \mathbf{P}^α , the eigenstate $|\mathbf{P}^\alpha\rangle$ can be factored out and, with suitable normalization,

$$|p, \theta, \varphi, \lambda_1, \lambda_2\rangle = (2\pi)^3 \sqrt{\frac{4\sqrt{s}}{p}} |\theta, \varphi, \lambda_1, \lambda_2\rangle |\mathbf{P}^\alpha\rangle. \quad (\text{A.10})$$

However, in order to apply conservation of angular momentum to the transition matrix element one needs to use eigenstates of total angular momentum as the basis for the two-particle CM states, *i.e.*, one needs to move from a basis of states of definite direction (*plane-wave states*) to a basis of states of definite angular momentum (*spherical-wave states*). For that purpose one can use p , J , the total angular momentum, M , the eigenvalue of J_z , and λ_1 and λ_2 to identify states in a new basis, $|p, J, M, \lambda_1, \lambda_2\rangle$. With that, the transformation between the two bases can be written as

$$|p, \theta, \varphi, \lambda_1, \lambda_2\rangle = \sum_{J,M} c_{JM}(p, \theta, \varphi, \lambda_1, \lambda_2) |p, J, M, \lambda_1, \lambda_2\rangle. \quad (\text{A.11})$$

The $c_{JM}(p, \theta, \varphi, \lambda_1, \lambda_2)$ coefficients can easily be evaluated for $\theta = \varphi = 0$. After applying the rotation operator and normalization conditions, one obtains the final expression of the transformation between the bases:

$$|p, \theta, \varphi, \lambda_1, \lambda_2\rangle = \sum_{J,M} \sqrt{\frac{2J+1}{4\pi}} D_{M\lambda}^J(\Omega) |p, J, M, \lambda_1, \lambda_2\rangle, \quad (\text{A.12})$$

with the definitions $\lambda \equiv \lambda_1 - \lambda_2$ and $\Omega \equiv (\varphi, \theta, -\varphi)$.

Again, the states $|p, J, M, \lambda_1, \lambda_2\rangle$ have total momentum $\vec{P} = 0$ and, since they are expressed in the CM frame, they are eigenstates of the total 4-momentum \mathbf{P}^α . That allows to factor out the $|\mathbf{P}^\alpha\rangle$ part of the state, similarly to Eq. A.10,

$$|p, J, M, \lambda_1, \lambda_2\rangle = (2\pi)^3 \sqrt{\frac{4\sqrt{s}}{p}} |J, M, \lambda_1, \lambda_2\rangle |\mathbf{P}^\alpha\rangle, \quad (\text{A.13})$$

and thus, taking into account that $|\mathbf{P}^\alpha\rangle$ is invariant under rotations, Eq. A.12 becomes

$$|\theta, \varphi, \lambda_1, \lambda_2\rangle = \sum_{J,M} \sqrt{\frac{2J+1}{4\pi}} D_{M\lambda}^J(\Omega) |J, M, \lambda_1, \lambda_2\rangle. \quad (\text{A.14})$$

A.2. Angular distributions in two-body decays

Now the process $1 \rightarrow 2 3$, in which the decaying particle 1 has spin s_1 and spin projection m_1 along an arbitrarily chosen z -axis, is considered. The final state particles 2,3 have helicities λ_2, λ_3 and momenta $\vec{p}_2 = \vec{p}_f, \vec{p}_3 = -\vec{p}_f$ in the CM frame (rest frame of particle 1). The final state can be expressed by making use of Eqs. A.13-A.14:

$$|f\rangle = (2\pi)^3 \sqrt{\frac{4\sqrt{s}}{p_f}} |\theta_f, \varphi_f, \lambda_1, \lambda_2\rangle |\mathbf{P}_f^\alpha\rangle, \quad (\text{A.15})$$

where θ_f, φ_f are the angles of \vec{p}_f . Therefore, the amplitude for 1 to decay into the final state $|f\rangle$ is

$$A(1 \rightarrow 2 3) = (2\pi)^3 \sqrt{\frac{4\sqrt{s}}{p_f}} \delta(\mathbf{P}_f^\alpha - \mathbf{P}_i^\alpha) \langle \theta_f, \varphi_f, \lambda_1, \lambda_2 | U | s_1, m_1 \rangle, \quad (\text{A.16})$$

where conservation of momentum has been applied. The constants in Eq. A.16 don't have any effect in the angular distributions, so they can be absorbed into U for easier notation

$$A(1 \rightarrow 2 3) \equiv \langle \theta_f, \varphi_f, \lambda_2, \lambda_3 | U | s_1, m_1 \rangle. \quad (\text{A.17})$$

Inserting the two-particle helicity basis states $|s_f, m_f, \lambda_2, \lambda_3\rangle$ and making use of Eq. A.14, the amplitude can be expressed as

$$\begin{aligned} A(1 \rightarrow 2 3) &= \langle \theta_f, \varphi_f, \lambda_2, \lambda_3 | U | s_1, m_1 \rangle \\ &= \sum_{s_f, m_f} \langle \theta_f, \varphi_f, \lambda_2, \lambda_3 | s_f, m_f, \lambda_2, \lambda_3 \rangle \langle s_f, m_f, \lambda_2, \lambda_3 | U | s_1, m_1 \rangle \\ &= \sum_{s_f, m_f} \sqrt{\frac{2s_1 + 1}{4\pi}} D_{m_1 \lambda}^{s_1 *}(\Omega) \lambda_{s_f, s_1} \lambda_{m_f, m_1} \langle \lambda_2, \lambda_3 | U | m_1 \rangle, \end{aligned} \quad (\text{A.18})$$

and since $\langle \lambda_2, \lambda_3 | U | m_1 \rangle$ must be rotationally invariant, the m_1 dependence can be removed and the braket can be rewritten as $A_{\lambda_2 \lambda_3}$:

$$A(1 \rightarrow 2 3) = \sqrt{\frac{2s_1 + 1}{4\pi}} D_{m_1 \lambda}^{s_1 *}(\Omega) A_{\lambda_2 \lambda_3}. \quad (\text{A.19})$$

From this equation, one would expect $(2s_2 + 1)(2s_3 + 1)$ helicity amplitudes. However, conservation of angular momentum requires

$$|\lambda_2 - \lambda_3| \leq s_1, \quad (\text{A.20})$$

and also it can be shown that, if parity is conserved in the decay,

$$A_{-\lambda_2 - \lambda_3} = \eta_1 \eta_2 \eta_3 (-1)^{s_2 + s_3 - s_1} A_{\lambda_2 \lambda_3}. \quad (\text{A.21})$$

The angular distribution is found by squaring the amplitude in Eq. A.19,

$$\frac{d\Gamma}{d\Omega_{m_1 \lambda_2 \lambda_3}}(\theta_f, \varphi_f) = \frac{2s_1 + 1}{4\pi} |D_{M\lambda}^{J*}(\Omega) A_{\lambda_2 \lambda_3}|^2 = \frac{2s_1 + 1}{4\pi} |d_M^J(\theta)|^2 |A_{\lambda_2 \lambda_3}|^2. \quad (\text{A.22})$$

If the experiment does not measure the final state helicities λ_2, λ_3 they must be summed over.

The total decay rate is obtained by applying the sum and integrating over Ω . It does not depend on m_1 because the decay rate of a free particle should not depend on which way its spin vector is pointing. With that in mind, the notation can be simplified by denoting the angular distribution as

$$I(\Omega, m_1) = \frac{1}{\Gamma} \frac{d\Gamma}{d\Omega_{m_1}}. \quad (\text{A.23})$$

A.2.1. Spin density matrix

Until this point the considered initial state has always been prepared with a definite value of m_1 and no distinction has been made between m_1 and λ_1 . Under experimental conditions, it is usually not possible to obtain a measurement for λ_1 on an event-by-event basis. Therefore, the amplitude in these cases must contain a coherent sum over λ_1 , and also, in the general case, a dependence in the lab direction of particle 1, as well as other variables related to the process which generates particle 1.

Considering the parity-conserving process $a b \rightarrow 1 (\rightarrow 2 3) X$, and recalling [196] that a mixture of states $|\psi_i\rangle$ with fractional populations ω_i can be characterized by the density operator

$$\rho = \sum \omega_i |\psi_i\rangle \langle \psi_i|, \quad (\text{A.24})$$

and denoting T as the transition operator corresponding to the interaction, the final state density operator can be expressed as

$$\rho \propto \sum_{\lambda_a, \lambda_b} T |\vec{p}_1, \lambda_a, \lambda_b\rangle \langle \vec{p}_1, \lambda_a, \lambda_b| T^\dagger, \quad (\text{A.25})$$

and be used to construct the density matrix $\rho_{\lambda_1, \lambda'_1}$ corresponding to particle 1 by taking the trace over all final state variables. Thus, the angular distribution becomes

$$\begin{aligned} I(\Omega) &= \frac{1}{\Gamma} \sum_{\lambda_1, \lambda'_1, \lambda_2, \lambda_3} A^*(\Omega; \lambda_1, \lambda_2, \lambda_3) \rho_{\lambda_1 \lambda'_1} A(\Omega; \lambda'_1, \lambda_2, \lambda_3) \\ &= \frac{1}{\Gamma} \frac{2s_1 + 1}{4\pi} \sum_{\lambda_1, \lambda'_1, \lambda_2, \lambda_3} D_{\lambda_1, \lambda}^{s_1}(\Omega) A_{\lambda_2 \lambda_3}^* \rho_{\lambda_1 \lambda'_1} D_{\lambda'_1, \lambda}^{s_1*}(\Omega) A_{\lambda_2 \lambda_3}. \end{aligned} \quad (\text{A.26})$$

A.2.2. Sequential two-body decays

When considering the decay $1 \rightarrow 2 (\rightarrow 4 5) 3$, the first thing that must be done is construct a new coordinate system $(x'y'z')$ in the rest frame of particle 2. First the original axes by are rotated $R(\varphi, \theta, -\varphi)$, which effectively aligns the z' -axis onto the flight direction of particle 2 in the rest frame of particle 1. With that choice of axes, if particle 2 has helicity λ_2 in the rest frame of 1, it will have a spin component in its own rest frame of $m_2 = \lambda_2$ along the z' -axis.

The angles $\Omega \equiv (\varphi', \theta', -\varphi')$ are defined in the direction of particle 4 in the $x'y'z'$ coordinate system, so θ' is defined with respect to the spin quantization axis of particle 2. The amplitude for the sequential decay is given by

$$A(1 \rightarrow 2 (\rightarrow 4 5) 3) = \sum_{\lambda_2} \langle \Omega' \lambda_4 \lambda_5 | U(2) | s_2, \lambda_2 \rangle \langle \Omega | U(1) | s_1 \lambda_1 \rangle. \quad (\text{A.27})$$

Following a similar derivation as Eq. A.19, the helicity formalism can be used to obtain the final expression for the amplitude

$$A(\Omega, \Omega'; \lambda_1, \lambda_3, \lambda_4, \lambda_5) = \sqrt{\frac{2s_1 + 1}{4\pi}} \sqrt{\frac{2s_2 + 1}{4\pi}} \sum_{\lambda_2} D_{\lambda_1, \lambda_2 - \lambda_3}^{s_1*}(\Omega) A_{\lambda_2 \lambda_3} D_{\lambda_2, \lambda_4 - \lambda_5}^{s_2*}(\Omega') B_{\lambda_4 \lambda_5}, \quad (\text{A.28})$$

where $B_{\lambda_4 \lambda_5}$ are the helciity amplitudes for the $2 \rightarrow 4$ 5 decay. Note the coherent sum over λ_2 . From this expression, the angular distribution is again obtained squaring the amplitude and summing over spins taking into account the spin density matrix:

$$I(\Omega, \Omega') = \frac{1}{\Gamma_1} \frac{1}{\Gamma_2} \frac{2s_1 + 1}{4\pi} \frac{2s_2 + 1}{4\pi} \sum_{\lambda_1 \lambda'_1 \lambda_2 \lambda'_2 \lambda_3 \lambda_4 \lambda_5} \rho_{\lambda_1 \lambda'_1} \times \\ \times \left\{ D_{\lambda'_1, \lambda'_2 - \lambda_3}^{s_1*}(\Omega) D_{\lambda_1, \lambda_2 - \lambda_3}^{s_1}(\Omega) A_{\lambda'_2 \lambda_3}^* A_{\lambda_2 \lambda_3} D_{\lambda_2, \lambda_4 - \lambda_5}^{s_2*}(\Omega') D_{\lambda'_2, \lambda_4 - \lambda_5}^{s_2}(\Omega') B_{\lambda_4 \lambda_5}^* A_{\lambda_4 \lambda_5} \right\}. \quad (\text{A.29})$$

Expanding the term in braces in Eq. A.29 using Eq. A.5 the angular dependence is

$$e^{i(\lambda_1 - \lambda'_1)\varphi} e^{i(\lambda_2 - \lambda'_2)(\varphi' - \varphi)} \quad (\text{A.30})$$

times a product of d -functions that depend on θ and θ' .

Since usually the interest lies in the angular distributions of particles 4 and 5, the number of observables in Eq. A.29 can be reduced by performing a change of variables $\chi \equiv (\varphi' - \varphi)$ —so the amplitude depends on $(\theta, \theta', \varphi, \chi)$ — and

- Integrating over φ , yielding $\delta_{\lambda_1 \lambda'_1}$.
- Integrating over χ , yielding $\delta_{\lambda_2 \lambda'_2}$.
- Using the ortogonality relation of the D -matrix.

$$\int D_{mn}^{j*}(\alpha \beta \gamma) D_{m'n'}^{j'} d\alpha d\cos\beta d\gamma = \frac{8\pi^2}{2j+1} \delta_{jj'} \delta_{mm'} \delta_{nn'}. \quad (\text{A.31})$$

Making use of the fact that the trace of the spin density matrix is 1, the angular distribution in Ω' can be expressed as

$$I(\Omega') = \frac{1}{\Gamma_1 \Gamma_2} \frac{2s_2 + 1}{4\pi} \sum_{\lambda_1 \lambda_2 \lambda_3 \lambda_4 \lambda_5} \rho_{\lambda_1 \lambda_1} |D_{\lambda_2, \lambda_4 - \lambda_5}^{s_2}(\Omega')|^2 |A_{\lambda_2 \lambda_3}|^2 |B_{\lambda_4 \lambda_5}|^2 \\ = \frac{1}{\Gamma_1 \Gamma_2} \frac{2s_2 + 1}{4\pi} \underbrace{\left[\sum_{\lambda_1} \rho_{\lambda_1 \lambda_1} \right]}_{\text{Tr}(\rho)=1} \sum_{\lambda_2 \lambda_3 \lambda_4 \lambda_5} |d_{\lambda_2, \lambda_4 - \lambda_5}^{s_2}(\theta')|^2 |A_{\lambda_2 \lambda_3}|^2 |B_{\lambda_4 \lambda_5}|^2 \\ = \frac{1}{\Gamma_1 \Gamma_2} \frac{2s_2 + 1}{4\pi} \sum_{\lambda_2 \lambda_3 \lambda_4 \lambda_5} |d_{\lambda_2, \lambda_4 - \lambda_5}^{s_2}(\theta')|^2 |A_{\lambda_2 \lambda_3}|^2 |B_{\lambda_4 \lambda_5}|^2, \quad (\text{A.32})$$

Thus the angular distribution does not depend on φ' .

B decay	K^{*0} decay	B decay	K^{*0} decay
$\lambda_{K^{*0}} = 0, \pm 1$	$\lambda_K = 0$	$\lambda_{K^{*0}} = 0, \pm 1$	$\lambda_K = 0$
$\lambda_\gamma = \pm 1$	$\lambda_\pi = 0$	$\lambda_\pi^0 = 0$	$\lambda_\pi = 0$
(a) $B \rightarrow K^{*0}(K\pi)\gamma$		(b) $B \rightarrow K^{*0}(K\pi)\pi^0$	

Table A.1. Possible helicities for the different particles involved in $B \rightarrow K^{*0}(K\pi)\gamma/\pi^0$. The table is analogous in the case of the $B_s^0 \rightarrow \phi(K^+K^-)\gamma/\pi^0$ decays, replacing $\pi \rightarrow K$.

A.2.3. Angular distribution of $B \rightarrow K^{*0}(K\pi)\gamma$

Using Eq. A.32 and the selection rule Eq. A.20 it is easy to determine the angular distribution of the $B \rightarrow K^{*0}(K\pi)\gamma$ decay and the analogous $B_s^0 \rightarrow \phi(K^+K^-)\gamma$. Table A.1a shows all possible helicity values given the spins of the particles involved in the decay.

However, the selection rule Eq. A.20 only allows $\lambda_{K^{*0}} = \lambda_\gamma$, so only the A_{-1-1} and A_{11} amplitudes are allowed. Therefore, the angular distribution is

$$I(\theta') \propto \{|d_{-10}^1(\theta')|^2|A_{-1-1}|^2 + |d_{10}^1(\theta')|^2|A_{11}|^2\}. \quad (\text{A.33})$$

Making use of the d -function properties, it can be seen that

$$d_{1,0}^1(\theta) = d_{0,-1}^1(\theta) = (-1)d_{-1,0}^1(\theta), \quad (\text{A.34})$$

and since the -1 is irrelevant when squared,

$$I(\theta') \propto |d_{1,0}^1(\theta)|^2. \quad (\text{A.35})$$

The value of $d_{1,0}^1(\theta)$ can be extracted from [21],

$$d_{1,0}^1(\theta) = -\frac{\sin \theta}{\sqrt{2}}, \quad (\text{A.36})$$

which, when squared, gives the angular dependence for the daughters of the vector meson in $B \rightarrow K^{*0}(K\pi)\gamma$ and $B_s^0 \rightarrow \phi(K^+K^-)\gamma$:

$$I(\theta') \propto \sin^2 \theta'. \quad (\text{A.37})$$

A.2.4. Angular distribution of $B \rightarrow K^{*0}(K\pi)\pi^0$

Analogously to §A.2.3, Table A.1b shows all possibilities for the helicity values of the particles involved in the $B \rightarrow K^{*0}(K\pi)\pi^0$ and $B_s^0 \rightarrow \phi(K^+K^-)\pi^0$ decays.

In this case, the selection rule Eq. A.20 only allows $\lambda_{K^{*0}} = \lambda_{\pi^0} = 0$, so only the A_{00} amplitude is allowed. This makes matters simpler, and the angular distribution for the daughter particles of the vector mesons in the $B \rightarrow K^{*0}(K\pi)\pi^0$ and $B_s^0 \rightarrow \phi(K^+K^-)\pi^0$ decays is found to be

$$I(\theta') \propto |d_{00}^1|^2 \propto \cos^2 \theta'. \quad (\text{A.38})$$

B

Isospin-conserving decay of the K^{*0} vector meson

The K^{*0} decay is almost a 100% isospin-conserving strong decay. If the particles involved in the K^{*0} decay are characterized, taking into account the fact that K^{*0} and K have the same quark content, all the states involved in the K^{*0} decay can be built:

$$\begin{aligned} |K^0\rangle &= |K^{*0}\rangle = d\bar{s} = |\frac{1}{2} - \frac{1}{2}\rangle & |\bar{K}^0\rangle &= |\bar{K}^{*0}\rangle = \bar{d}s = |\frac{1}{2} \frac{1}{2}\rangle \\ |K^+\rangle &= |K^{*+}\rangle = u\bar{s} = |\frac{1}{2} \frac{1}{2}\rangle & |K^-\rangle &= |K^{*-}\rangle = \bar{u}s = |\frac{1}{2} - \frac{1}{2}\rangle \\ |\pi^0\rangle &= \frac{u\bar{u} + d\bar{d}}{\sqrt{2}} = |1 0\rangle \\ |\pi^+\rangle &= u\bar{d} = |1 1\rangle & |\pi^-\rangle &= \bar{u}s = |1 - 1\rangle \end{aligned}$$

The Clebsch-Gordan coefficients [21] can then be used to construct the possible final states for the strong decay:

$$\begin{aligned} |K^0\pi^0\rangle &= \sqrt{\frac{2}{3}} |\frac{3}{2} - \frac{1}{2}\rangle + \sqrt{\frac{1}{3}} |\frac{1}{2} - \frac{1}{2}\rangle & |\bar{K}^0\pi^0\rangle &= \sqrt{\frac{2}{3}} |\frac{3}{2} - \frac{1}{2}\rangle - \sqrt{\frac{1}{3}} |\frac{1}{2} - \frac{1}{2}\rangle \\ |K^-\pi^+\rangle &= \sqrt{\frac{1}{3}} |\frac{3}{2} \frac{1}{2}\rangle + \sqrt{\frac{2}{3}} |\frac{1}{2} \frac{1}{2}\rangle & |K^+\pi^-\rangle &= \sqrt{\frac{1}{3}} |\frac{3}{2} - \frac{1}{2}\rangle - \sqrt{\frac{2}{3}} |\frac{1}{2} - \frac{1}{2}\rangle \\ |K^+\pi^0\rangle &= \sqrt{\frac{2}{3}} |\frac{3}{2} \frac{1}{2}\rangle - \sqrt{\frac{1}{3}} |\frac{1}{2} \frac{1}{2}\rangle & |K^-\pi^0\rangle &= \sqrt{\frac{2}{3}} |\frac{3}{2} - \frac{1}{2}\rangle + \sqrt{\frac{1}{3}} |\frac{1}{2} - \frac{1}{2}\rangle \\ |K^0\pi^+\rangle &= \sqrt{\frac{1}{3}} |\frac{3}{2} \frac{1}{2}\rangle + \sqrt{\frac{2}{3}} |\frac{1}{2} \frac{1}{2}\rangle & |K^0\pi^-\rangle &= |\frac{3}{2} - \frac{3}{2}\rangle \\ |\bar{K}^0\pi^+\rangle &= |\frac{3}{2} \frac{3}{2}\rangle & |\bar{K}^0\pi^-\rangle &= \sqrt{\frac{1}{3}} |\frac{3}{2} - \frac{1}{2}\rangle - \sqrt{\frac{2}{3}} |\frac{1}{2} - \frac{1}{2}\rangle \end{aligned}$$

Finally, the fractions of each decay mode can be calculated:

$$\begin{aligned} |\langle K^0\pi^0|K^{*0}\rangle|^2 &= \frac{1}{3} & |\langle K^+\pi^-|K^{*0}\rangle|^2 &= \frac{2}{3} \\ |\langle K^0\pi^0|\bar{K}^{*0}\rangle|^2 &= \frac{1}{3} & |\langle K^-\pi^+|\bar{K}^{*0}\rangle|^2 &= \frac{2}{3} \\ |\langle K^+\pi^0|K^{*+}\rangle|^2 &= \frac{1}{3} & |\langle K^0\pi^+|K^{*+}\rangle|^2 &= \frac{2}{3} \\ |\langle K^-\pi^0|K^{*-}\rangle|^2 &= \frac{1}{3} & |\langle \bar{K}^0\pi^-|K^{*-}\rangle|^2 &= \frac{2}{3} \end{aligned}$$

Bibliography

- [1] B. Pontecorvo, *Neutrino experiments and the question of leptonic-charge conservation*, Sov. Phys. JETP **26** (1968) 984.
- [2] Super-Kamiokande Collaboration, Y. Ashie *et al.*, *Evidence for an oscillatory signature in atmospheric neutrino oscillation*, Phys. Rev. Lett. **93** (2004) 101801, arXiv:hep-ex/0404034.
- [3] SNO Collaboration, B. Aharmim *et al.*, *Electron energy spectra, fluxes, and day-night asymmetries of 8B solar neutrinos from measurements with NaCl dissolved in the heavy-water detector at the Sudbury Neutrino Observatory*, Phys. Rev. C**72** (2005) 055502.
- [4] MINOS Collaboration, P. Adamson *et al.*, *Measurement of Neutrino Oscillations with the MINOS Detectors in the NuMI Beam*, Phys. Rev. Lett. **101** (2008) 131802, arXiv:0806.2237.
- [5] LEP Working Group for Higgs boson searches, R. Barate *et al.*, *Search for the standard model Higgs boson at LEP*, Phys. Lett. B**565** (2003) 61, arXiv:hep-ex/0306033.
- [6] ATLAS Collaboration, A. Nisati, *Standard Model Higgs boson searches with the ATLAS detector at the Large Hadron Collider*, arXiv:1111.7132.
- [7] CMS Collaboration, K. Sung, *A Search for Higgs Boson in $H \rightarrow W^+W^-$* , arXiv:1109.2457.
- [8] A. Einstein, *Zur Elektrodynamik bewegt Körper*, Annalen der Physik **17** (1905) 891.
- [9] V. Fock, *Über die invariante Form der Wellen- und der Bewegungsgleichungen für einen geladenen Massenpunkt*, Zeitschrift für Physik A Hadrons and Nuclei **39** (1926) 226.
- [10] H. Weyl, *Elektron und Gravitation. I*, Zeitschrift für Physik A Hadrons and Nuclei **56** (1929) 330.
- [11] C.-N. Yang and R. L. Mills, *Conservation of isotopic spin and isotopic gauge invariance*, Phys. Rev. **96** (1954) 191.
- [12] S. L. Glashow, *Partial Symmetries of Weak Interactions*, Nucl. Phys. **22** (1961) 579.

- [13] S. Weinberg, *A Model of Leptons*, *Phys. Rev. Lett.* **19** (1967) 1264.
- [14] A. Salam, *Weak and Electromagnetic Interactions*, in *Svartholm: Elementary Particle Theory, Proceedings Of The Nobel Symposium Held 1968 At Lerum, Sweden*, pp. 367–377, 1968.
- [15] M. Y. Han and Y. Nambu, *Three-triplet model with double SU(3) symmetry*, *Phys. Rev.* **139** (1965) B1006.
- [16] Y. Nambu, *Axial vector current conservation in weak interactions*, *Phys. Rev. Lett.* **4** (1960) 380.
- [17] J. Goldstone, *Field Theories with Superconductor Solutions*, *Nuovo Cim.* **19** (1961) 154.
- [18] J. Goldstone, A. Salam, and S. Weinberg, *Broken Symmetries*, *Phys. Rev.* **127** (1962) 965.
- [19] P. W. Higgs, *Broken symmetries, massless particles and gauge fields*, *Phys. Lett.* **12** (1964) 132.
- [20] P. W. Higgs, *Spontaneous Symmetry Breakdown without Massless Bosons*, *Phys. Rev.* **145** (1966) 1156.
- [21] Particle Data Group, K. Nakamura *et al.*, *Review of particle physics*, *J. Phys. G* **37** (2010) 075021.
- [22] S. Tomonaga, *On a Relativistically Invariant Formulation of the Quantum Theory of Wave Fields*, *Progress of Theoretical Physics* **1** (1946), no. 2 27.
- [23] J. Schwinger, *On Quantum-Electrodynamics and the Magnetic Moment of the Electron*, *Phys. Rev.* **73** (1948) 416.
- [24] J. Schwinger, *Quantum Electrodynamics. I. A Covariant Formulation*, *Phys. Rev.* **74** (1948) 1439.
- [25] F. J. Dyson, *The S Matrix in Quantum Electrodynamics*, *Phys. Rev.* **75** (1949) 1736.
- [26] R. P. Feynman, *The Theory of Positrons*, *Phys. Rev.* **76** (1949) 749.
- [27] F. J. Dyson, *The Radiation Theories of Tomonaga, Schwinger, and Feynman*, *Phys. Rev.* **75** (1949) 486.
- [28] R. P. Feynman, *Space-Time Approach to Quantum Electrodynamics*, *Phys. Rev.* **76** (1949) 769.
- [29] R. P. Feynman, *Mathematical Formulation of the Quantum Theory of Electromagnetic Interaction*, *Phys. Rev.* **80** (1950) 440.
- [30] D. J. Gross and F. Wilczek, *Ultraviolet Behavior of Non-Abelian Gauge Theories*, *Phys. Rev. Lett.* **30** (1973) 1343.
- [31] H. D. Politzer, *Reliable Perturbative Results for Strong Interactions?*, *Phys. Rev. Lett.* **30** (1973) 1346.

- [32] E. Noether, *Invariante Variationsprobleme*, Nachr. d. König. Gesellsch. d. Wiss. zu Göttingen, Math.-phys. Klasse (1918) 235. Translation by M.A.Tavel in *Transport Theory and Statistical Physics*, **1** (3), 183–207 (1971).
- [33] C. S. Wu, E. Ambler, R. W. Hayward, D. D. Hoppes, and R. P. Hudson, *Experimental Test of Parity Conservation in Beta Decay*, *Phys. Rev.* **105** (1957) 1413.
- [34] R. L. Garwin, L. M. Lederman, and M. Weinrich, *Observations of the Failure of Conservation of Parity and Charge Conjugation in Meson Decays: the Magnetic Moment of the Free Muon*, *Phys. Rev.* **105** (1957) 1415.
- [35] J. Christenson, J. Cronin, V. Fitch, and R. Turlay, *Evidence for the 2π Decay of the K_2^0 Meson*, *Phys. Rev. Lett.* **13** (1964) 138.
- [36] Belle Collaboration, K. Abe *et al.*, *Observation of large CP violation and evidence for direct CP violation in $B^0 \rightarrow \pi^+ \pi^-$ decays*, *Phys. Rev. Lett.* **93** (2004) 021601, [arXiv:hep-ex/0401029](https://arxiv.org/abs/hep-ex/0401029).
- [37] BaBar Collaboration, B. Aubert *et al.*, *Observation of direct CP violation in $B^0 \rightarrow K^+ \pi^-$ decays*, *Phys. Rev. Lett.* **93** (2004) 131801, [arXiv:hep-ex/0407057](https://arxiv.org/abs/hep-ex/0407057).
- [38] LHCb Collaboration, R. Aaij *et al.*, *Evidence for CP violation in time-integrated $D^0 \rightarrow h^- h^+$ decay rates*, [arXiv:1112.0938](https://arxiv.org/abs/1112.0938).
- [39] G. Lüders, *Proof of the TCP theorem*, *Ann. Phys.* **2** (1957), no. 1 1 .
- [40] H. Georgi, *Lie Algebras in Particle Physics. From Isospin to Unified Theories*, *Front. Phys.* **54** (1982) 1.
- [41] P. W. Higgs, *Broken Symmetries and the Masses of Gauge Bosons*, *Phys. Rev. Lett.* **13** (1964) 508.
- [42] F. Englert and R. Brout, *Broken Symmetry and the Mass of Gauge Vector Mesons*, *Phys. Rev. Lett.* **13** (1964) 321.
- [43] G. Guralnik, C. Hagen, and T. Kibble, *Global Conservation Laws and Massless Particles*, *Phys. Rev. Lett.* **13** (1964) 585.
- [44] N. Cabibbo, *Unitary Symmetry and Leptonic Decays*, *Phys. Rev. Lett.* **10** (1963) 531.
- [45] M. Kobayashi and T. Maskawa, *CP-Violation in the Renormalizable Theory of Weak Interaction*, *Progress of Theoretical Physics* **49** (1973), no. 2 652.
- [46] L. Wolfenstein, *Parametrization of the Kobayashi-Maskawa Matrix*, *Phys. Rev. Lett.* **51** (1983) 1945.
- [47] CKMfitter Group, J. Charles *et al.*, *CP violation and the CKM matrix: Assessing the impact of the asymmetric B factories*, *Eur. Phys. J.* **C41** (2005) 1, [arXiv:hep-ph/0406184](https://arxiv.org/abs/hep-ph/0406184). Updated results and plots available at: <http://ckmfitter.in2p3.fr>.

- [48] S. L. Glashow, J. Iliopoulos, and L. Maiani, *Weak Interactions with Lepton-Hadron Symmetry*, Phys. Rev. **D2** (1970) 1285.
- [49] J. R. Ellis, M. Gaillard, D. V. Nanopoulos, and S. Rudaz, *The Phenomenology of the Next Left-Handed Quarks*, Nucl. Phys. **B131** (1977) 285.
- [50] M. Antonelli *et al.*, *Flavor Physics in the Quark Sector*, Phys. Rept. **494** (2010) 197, arXiv:0907.5386.
- [51] M. Misiak *et al.*, *Estimate of $\mathcal{B}(\bar{B} \rightarrow X_s \gamma)$ at $\mathcal{O}(\alpha_s^2)$* , Phys. Rev. Lett. **98** (2007) 022002, arXiv:hep-ph/0609232.
- [52] M. Beneke, T. Feldmann, and D. Seidel, *Systematic approach to exclusive $B \rightarrow V l^+ l^-$, $V \gamma$ decays*, Nucl. Phys. **B612** (2001) 25, arXiv:hep-ph/0106067.
- [53] A. L. Kagan and M. Neubert, *Isospin breaking in $B \rightarrow K^* \gamma$ decays*, Phys. Lett. **B539** (2002) 227, arXiv:hep-ph/0110078.
- [54] S. W. Bosch and G. Buchalla, *The Radiative decays $B \rightarrow V \gamma$ at next-to-leading order in QCD*, Nucl. Phys. **B621** (2002) 459, arXiv:hep-ph/0106081.
- [55] C. W. Bauer, S. Fleming, and M. E. Luke, *Summing Sudakov logarithms in $B \rightarrow X_s \gamma$ in effective field theory*, Phys. Rev. **D63** (2000) 014006, arXiv:hep-ph/0005275.
- [56] C. W. Bauer, S. Fleming, D. Pirjol, and I. W. Stewart, *An effective field theory for collinear and soft gluons: Heavy to light decays*, Phys. Rev. **D63** (2001) 114020, arXiv:hep-ph/0011336.
- [57] C. W. Bauer and I. W. Stewart, *Invariant operators in collinear effective theory*, Phys. Lett. **B516** (2001) 134, arXiv:hep-ph/0107001.
- [58] C. W. Bauer, D. Pirjol, and I. W. Stewart, *Soft-Collinear Factorization in Effective Field Theory*, Phys. Rev. **D65** (2002) 054022, arXiv:hep-ph/0109045.
- [59] S. Weinberg, *The quantum theory of fields. Vol. 2: Modern applications*. Cambridge University Press, 1996.
- [60] A. Pich, *Effective field theory: Course*, arXiv:hep-ph/9806303.
- [61] S. Bertolini, F. Borzumati, and A. Masiero, *QCD Enhancement of Radiative b Decays*, Phys. Rev. Lett. **59** (1987) 180.
- [62] N. G. Deshpande, P. Lo, J. Trampetic, G. Eilam, and P. Singer, *Prediction of $B \rightarrow K^* \gamma$ as a Test of the Standard Model*, Phys. Rev. Lett. **59** (1987) 183.
- [63] T. Becher, R. J. Hill, and M. Neubert, *Factorization in $B \rightarrow V \gamma$ decays*, Phys. Rev. **D72** (2005) 094017, arXiv:hep-ph/0503263.
- [64] T. Hurth and M. Nakao, *Radiative and Electroweak Penguin Decays of B Mesons*, Ann. Rev. Nucl. Part. Sci. **60** (2010) 645, arXiv:1005.1224.
- [65] E. Eichten and B. R. Hill, *An Effective Field Theory for the Calculation of Matrix Elements Involving Heavy Quarks*, Phys. Lett. **B234** (1990) 511.

- [66] H. Georgi, *An Effective Field Theory For Heavy Quarks At Low-Energies*, *Phys. Lett.* **B240** (1990) 447.
- [67] A. Ali, B. D. Pecjak, and C. Greub, *$B \rightarrow V\gamma$ Decays at NNLO in SCET*, *Eur. Phys. J.* **C55** (2008) 577, [arXiv:0709.4422](#).
- [68] I. Balitsky, V. M. Braun, and A. Kolesnichenko, *Power corrections $1/Q^2$ to parton sum rules for deep inelastic scattering from polarized targets*, *Phys. Lett.* **B242** (1990) 245, [arXiv:hep-ph/9310316](#).
- [69] V. Chernyak and I. Zhitnitsky, *B meson exclusive decays into baryons*, *Nucl. Phys.* **B345** (1990) 137.
- [70] M. A. Shifman, A. Vainshtein, and V. I. Zakharov, *QCD and Resonance Physics: Sum Rules*, *Nucl. Phys.* **B147** (1979) 385.
- [71] M. A. Shifman, A. Vainshtein, and V. I. Zakharov, *QCD and Resonance Physics: Applications*, *Nucl. Phys.* **B147** (1979) 448.
- [72] M. A. Shifman, *Snapshots of hadrons or the story of how the vacuum medium determines the properties of the classical mesons which are produced, live and die in the QCD vacuum*, *Prog. Theor. Phys. Suppl.* **131** (1998) 1, [arXiv:hep-ph/9802214](#). Review.
- [73] K. G. Wilson, *Nonlagrangian models of current algebra*, *Phys. Rev.* **179** (1969) 1499.
- [74] P. Ball, G. W. Jones, and R. Zwicky, *$B \rightarrow V\gamma$ beyond QCD factorisation*, *Phys. Rev.* **D75** (2007) 054004, [arXiv:hep-ph/0612081](#).
- [75] CLEO Collaboration, T. E. Coan *et al.*, *Study of Exclusive Radiative B Meson Decays*, *Phys. Rev. Lett.* **84** (2000), no. 23 5283.
- [76] BaBar Collaboration, B. Aubert *et al.*, *Measurement of Branching Fractions and CP and Isospin Asymmetries in $B \rightarrow K^*(892)\gamma$ Decays*, *Phys. Rev. Lett.* **103** (2009) 211802, [arXiv:0906.2177](#).
- [77] Belle Collaboration, M. Nakao *et al.*, *Measurement of the $B \rightarrow K^*\gamma$ branching fractions and asymmetries*, *Phys. Rev.* **D69** (2004), no. 11 112001.
- [78] Belle Collaboration, J. Wicht *et al.*, *Observation of $B_s^0 \rightarrow \phi\gamma$ and Search for $B_s^0 \rightarrow \gamma\gamma$ Decays at Belle*, *Phys. Rev. Lett.* **100** (2008) 121801, [arXiv:0712.2659](#).
- [79] Heavy Flavor Averaging Group, D. Asner *et al.*, *Averages of b -hadron, c -hadron, and τ -lepton Properties*, [arXiv:1010.1589](#).
- [80] S. Descotes-Genon, D. Ghosh, J. Matias, and M. Ramon, *Exploring New Physics in the $C\gamma$ - $C\gamma'$ plane*, *JHEP* **1106** (2011) 099, [arXiv:1104.3342](#).
- [81] F. Mahmoudi and M. R. Ahmady, *Constraints on mSUGRA from isospin asymmetry in $B \rightarrow K^*\gamma$* , *AIP Conf. Proc.* **903** (2007) 283, [arXiv:hep-ph/0610144](#).

- [82] M. Beneke, T. Feldmann, and D. Seidel, *Exclusive radiative and electroweak $b \rightarrow d$ and $b \rightarrow s$ penguin decays at NLO*, *Eur. Phys. J.* **C41** (2005) 173, [arXiv:hep-ph/0412400](#).
- [83] Y. Y. Keum, M. Matsumori, and A. I. Sanda, *CP asymmetry, branching ratios and isospin breaking effects of $B \rightarrow K^*\gamma$ with perturbative QCD approach*, *Phys. Rev.* **D72** (2005) 014013, [arXiv:hep-ph/0406055](#).
- [84] LHCb Collaboration, *Roadmap for selected key measurements of LHCb*, [arXiv:0912.4179](#).
- [85] L. Evans and P. Bryant, *LHC Machine*, *JINST* **3** (2008) S08001.
- [86] R. Fernow, *Introduction to experimental particle physics*. Cambridge University Press, 1989. doi: [10.2277/0521379407](#).
- [87] W. Herr and B. Muratori, *Concept of luminosity*, in *CAS (CERN Accelerator School): Intermediate Course on Accelerator Physics*, pp. 361–378, Sep, 2006.
- [88] ALICE Collaboration, K. Aamodt *et al.*, *The ALICE experiment at the CERN LHC*, *JINST* **3** (2008) S08002.
- [89] ATLAS Collaboration, G. Aad *et al.*, *The ATLAS Experiment at the CERN Large Hadron Collider*, *JINST* **3** (2008) S08003.
- [90] CMS Collaboration, R. Adolphi *et al.*, *The CMS experiment at the CERN LHC*, *JINST* **3** (2008) S08004.
- [91] LHCb Collaboration, A. Augusto Alves Jr *et al.*, *The LHCb Detector at the LHC*, *JINST* **3** (2008) S08005.
- [92] LHCf Collaboration, O. Adriani *et al.*, *The LHCf detector at the CERN Large Hadron Collider*, *JINST* **3** (2008) S08006.
- [93] TOTEM Collaboration, G. Anelli *et al.*, *The TOTEM experiment at the CERN Large Hadron Collider*, *JINST* **3** (2008) S08007.
- [94] LCG, C. Eck *et al.*, *LHC computing Grid: Technical Design Report*, [CERN-LHCC-2005-024](#).
- [95] LHCb Collaboration, R. Antunes-Nobrega *et al.*, *LHCb reoptimized detector design and performance: Technical Design Report*, [CERN-LHCC-2003-030](#).
- [96] LHCb Collaboration, S. Amato *et al.*, *LHCb: Technical Proposal*, [CERN-LHCC-98-004](#).
- [97] LHCb Collaboration, R. Aaij *et al.*, *Measurement of $\sigma(pp \rightarrow b\bar{b}X)$ at $\sqrt{s}=7$ TeV in the forward region*, *Phys. Lett.* **B694** (2010) 209, [arXiv:1009.2731](#).
- [98] LHCb collaboration, R. Aaij *et al.*, *Measurement of b hadron production fractions in 7 TeV pp collisions*, *Phys. Rev.* **D85** (2012) , [arXiv:1111.2357](#).
- [99] G. Lopez, *Notes About the Beta Function*, SSC-N-783, SSCL, 1991.

- [100] LHCb Collaboration, P. R. Barbosa-Marinho *et al.*, *LHCb VELO (VErtex LOcator): Technical Design Report*, [CERN-LHCC-2001-0011](#).
- [101] LHCb Collaboration, P. R. Barbosa-Marinho *et al.*, *LHCb inner tracker: Technical Design Report*, [CERN-LHCC-2002-029](#).
- [102] LHCb Collaboration, P. R. Barbosa-Marinho *et al.*, *LHCb outer tracker: Technical Design Report*, [CERN-LHCC-2001-024](#).
- [103] LHCb Collaboration, S. Amato *et al.*, *LHCb magnet: Technical Design Report*, [CERN-LHCC-2000-007](#).
- [104] LHCb Collaboration, S. Amato *et al.*, *LHCb RICH: Technical Design Report*, [CERN-LHCC-2000-037](#).
- [105] LHCb Collaboration, S. Amato *et al.*, *LHCb Calorimeters*, [CERN-LHCC-2000-0036](#).
- [106] LHCb Collaboration, P. R. Barbosa-Marinho *et al.*, *LHCb muon system: Technical Design Report*, [CERN-LHCC-2001-010](#).
- [107] LHCb Collaboration, P. R. Barbosa-Marinho *et al.*, *LHCb online system, data acquisition and experiment control: Technical Design Report*, [CERN-LHCC-2001-040](#).
- [108] J. Andre *et al.*, *Status of the LHCb magnet system*, *IEEE Transactions on Applied Superconductivity* **12** (2002) 366 .
- [109] J. Andre, W. Flegel, P. Giudici, O. Jamet, and M. Losasso, *Status of the LHCb dipole magnet*, *IEEE Transactions on Applied Superconductivity* **14** (2004) 509 .
- [110] LHCb Collaboration, R. Aaij *et al.*, *Prompt production in pp collisions at $\sqrt{s} = 0.9 \text{ TeV}$* , *Phys. Lett.* **B693** (2010) 69, [arXiv:1008.3105](#).
- [111] P. A. Cherenkov, *Visible emission of clean liquids by action of γ radiation*, Doklady Akademii Nauk SSSR **2** (1934) 451.
- [112] N. Brook *et al.*, *LHCb RICH1 Engineering Design Review Report*, [LHCb-2004-121](#).
- [113] M. Adinolfi *et al.*, *LHCb RICH 2 engineering design review report*, [LHCb-2002-009](#).
- [114] A. Arefev *et al.*, *Beam Test Results of the LHCb Electromagnetic Calorimeter*, [LHCb-2007-149](#).
- [115] J. Lefrançois, F. Machefert, and A. Martens, *Calibration of the LHCb calorimeters with energy flow*, [LHCb-INT-2010-021](#).
- [116] I. Belyaev, V. Egorychev, and D. Savrina, *ECAL calibration within Kali framework: Mass distribution fit method calibration with the real data*, [LHCb-INT-2011-049](#).

- [117] R. W. Forty and O. Schneider, *RICH pattern recognition*, **LHCb-98-040**.
- [118] LHCb RICH Collaboration, A. Powell, *Reconstruction and PID performance of the LHCb RICH detectors*, **Nucl. Instrum. Meth.** **A639** (2011) 260.
- [119] *RICH Performance Plots*, <https://lbtwiki.cern.ch/bin/view/RICH/RichPIDPerformancePlots>.
- [120] M. Gandelman and E. Polycarpo, *The Performance of the LHCb Muon Identification Procedure*, **LHCb-2007-145**.
- [121] J. R. T. De Mello-Neto and M. Gandelman, *Muon ID performance with the reoptimized LHCb detector*, **LHCb-2003-089**.
- [122] R. Aaij *et al.*, *Measurement of J/ψ production in pp collisions at $\sqrt{s} = 7 \text{ TeV}$* , **Eur. Phys. J.** **C71** (2011) 1645, [arXiv:1103.0423](https://arxiv.org/abs/1103.0423).
- [123] H. Terrier and I. Belyaev, *Particle identification with LHCb Calorimeters*, **LHCb-2003-092**.
- [124] O. Deschamps, F. Machefert, M.-H. Schune, G. Pakhlova, and I. Belyaev, *Photon and Neutral Pion reconstruction*, **LHCb-2003-091**.
- [125] LHCb Collaboration, R. Antunes-Nobrega *et al.*, *LHCb Trigger System Technical Design Report*, **CERN-LHCC-2003-031**.
- [126] V. V. Gligorov, *A single track HLT1 trigger*, **LHCb-PUB-2011-003**.
- [127] R. Aaij and J. Albrecht, *Muon triggers in the High Level Trigger of LHCb*, **CERN-LHCb-PUB-2011-017**.
- [128] E. V. Herwijnen, *HLT2 Rates*, <https://twiki.cern.ch/twiki/bin/view/LHCb/Hlt2Rates>.
- [129] M. Williams *et al.*, *The HLT2 Topological Lines*, **LHCb-PUB-2011-002**.
- [130] F. Soomro and I. Belyaev, *HLT2 exclusive selections for $B_s \rightarrow \phi\gamma$ and $B_d \rightarrow K^*\gamma$* , **LHCb-PUB-2010-007**.
- [131] M. Lieng, *An Inclusive ϕ Stream for the LHCb High Level Trigger*, *DC06 Analysis*, **CERN-LHCb-2009-010**.
- [132] LHCb Collaboration, N. Tatsuya, E. Aslanides, A. Smith, and W. Witzeling, *Addendum to the LHCb Online System Technical Design Report*, **CERN-LHCC-2001-040-ADD-1**, **CERN-LHCC-2005-039**.
- [133] G. Haefeli *et al.*, *The LHCb DAQ interface board TELL1*, **Nucl. Instrum. Meth.** **A560** (2006) 494.
- [134] W. Salter, *The LHC experiments' joint controls project (JCOP)*, **Conf. Proc. C0109031** (2001) 2.
- [135] *CERN PVSS Service*, <http://j2eeps.cern.ch/wikis/display/EN/PVSS+Service>.

- [136] B. Franek and C. Gaspar, *SMI++ object oriented framework used for automation and error recovery in the LHC experiments*, *J. Phys. Conf. Ser.* **219** (2010) 022031.
- [137] *SMI++ - State Management Interface*, <http://smi.web.cern.ch/smi/>.
- [138] P. Mato, *GAUDI — Architecture design document*, [LHCb-98-064](#).
- [139] G. Barrand *et al.*, *GAUDI — A software architecture and framework for building HEP data processing applications*, *Comput. Phys. Commun.* **140** (2001) 45. See also: <http://proj-gaudi.web.cern.ch/proj-gaudi/>.
- [140] LHCb Collaboration, R. Antunes-Nobrega *et al.*, *LHCb computing: Technical Design Report*, [CERN-LHCC-2005-019](#).
- [141] R. Brun and F. Rademakers, *ROOT: An object oriented data analysis framework*, *Nucl. Instrum. Meth.* **A389** (1997) 81.
- [142] *The ROOT Project*, <http://root.cern.ch/>.
- [143] I. Belyaev *et al.*, *Simulation application for the LHCb experiment*, [arXiv:physics/0306035](https://arxiv.org/abs/physics/0306035). See also: <http://lhcb-release-area.web.cern.ch/LHCb-release-area/DOC/gauss/>.
- [144] I. Belyaev *et al.*, *Handling of the generation of primary events in Gauss, the LHCb simulation framework*, [LHCb-PROC-2010-056](#). To appear in the proceedings of NSS 2010, the 2010 Nuclear Science Symposium, October 30-November 6, 2010, Knoxville, USA.
- [145] T. Sjostrand, S. Mrenna, and P. Z. Skands, *PYTHIA 6.4 Physics and Manual*, *JHEP* **0605** (2006) 026, [arXiv:hep-ph/0603175](https://arxiv.org/abs/hep-ph/0603175).
- [146] D. J. Lange, *The EvtGen particle decay simulation package*, *Nucl. Instrum. Meth.* **A462** (2001), no. 1-2 123.
- [147] E. Barberio, B. van Eijk, and Z. Was, *PHOTOS: A Universal Monte Carlo for QED radiative corrections in decays*, *Comput. Phys. Commun.* **66** (1991) 115.
- [148] E. Barberio and Z. Was, *PHOTOS: A Universal Monte Carlo for QED radiative corrections. Version 2.0*, *Comput. Phys. Commun.* **79** (1994) 291.
- [149] S. Agostinelli *et al.*, *GEANT4—a simulation toolkit*, *Nucl. Instrum. Meth.* **A506** (2003), no. 3 250.
- [150] LHCb Collaboration, *The BOOLE Project*, <http://lhcb-release-area.web.cern.ch/LHCb-release-area/DOC/BOOLE/>.
- [151] LHCb Collaboration, *The MOORE Project*, <http://lhcb-release-area.web.cern.ch/LHCb-release-area/DOC/moore/>.
- [152] LHCb Collaboration, *The BRUNEL Project*, <http://lhcb-release-area.web.cern.ch/LHCb-release-area/DOC/brunel/>.

- [153] LHCb Collaboration, *The DA VINCI Project*, <http://lhcb-release-area.web.cern.ch/LHCb-release-area/DOC/davinci/>.
- [154] R. Graciani, *LHCb Computing Resources: 2011 re-assessment, 2012 request and 2013 forecast*, [LHCb-PUB-2011-009](#).
- [155] B. Souza de Paula, *Studies on Systematic Effects of the Trigger on Flavour Tagging at the Generator Level*, [LHCb-PUB-2009-014](#).
- [156] J. A. Hernando Morata, E. Lopez Asamar, D. Martinez Santos, H. Ruiz-Pérez, and F. Teubert, *Measurement of trigger efficiencies and biases*, [LHCb-2008-073](#).
- [157] M. Calvo and H. Ruiz, *Photon/Electron trigger at high luminosity*, [LHCb Calorimeter Upgrade Meeting](#), 5th Oct, 2010.
- [158] K. Senderowska, M. Witek, and A. Zuranski, *HLT1 Electromagnetic Alley*, [LHCb-PUB-2009-001](#).
- [159] V. Breton, N. Brun, and P. Perret, *A clustering algorithm for the LHCb electromagnetic calorimeter using a cellular automaton*, [LHCb-2001-123](#).
- [160] M. Williams, *HLT2 Topological Lines for 2011*, LHCb Software & Analysis Week, CERN, Geneva, Feb, 2011.
- [161] I. Narski, *StatPatternRecognition: A C++ Package for Statistical Analysis of High Energy Physics Data*, [arXiv:physics/0507143](#).
- [162] V. Gligorov, C. Thomas, and M. Williams, *The HLT inclusive B triggers*, [LHCb-PUB-2011-016](#).
- [163] A. Puig, *Inclusive ϕ trigger*, Talk at the PPMTS Meeting on May 30th, 2011.
- [164] M. Pivk and F. R. Le Diberder, *sPlot: A statistical tool to unfold data distributions*, [Nucl. Instrum. Meth. A555](#) (2005) 356, [arXiv:physics/0402083](#).
- [165] Y. Amhis *et al.*, *Absolute Luminosity Measurements at $\sqrt{s} = 7$ TeV*, [LHCb-INT-2011-018](#).
- [166] LHCb Collaboration, *LHCb Luminosity Project*, <https://twiki.cern.ch/twiki/bin/viewauth/LHCbPhysics/LuminosityMeasurements>, Jan, 2012.
- [167] L. Shchutska, A. Golutvin, and I. Belyaev, *Study of radiative penguin decays $B \rightarrow K^{*0}\gamma$ and $B_s \rightarrow \phi\gamma$ at LHCb*, [LHCb-2007-030](#).
- [168] O. Callot and M. Schiller, *PatSeeding: A Standalone Track Reconstruction Algorithm*, [LHCb-2008-042](#).
- [169] M. Calvo, *π^0/γ separation tool*, Talk at the Radiative Decays Meeting on Nov 17th, 2011.
- [170] M. Calvo, *π^0/γ separation status*, Talk at the Calorimeter Objects Meeting on Feb 10th, 2011.
- [171] J. Jackson, *Remarks on the Phenomenological Analysis of Resonances*, [Il Nuovo Cimento 34 \(1964\) 1644](#).

- [172] HERA-B Collaboration, I. Abt *et al.*, *K^{*0} and ϕ meson production in proton-nucleus interactions at $\sqrt{s} = 41.6$ GeV*, *Eur. Phys. J. C* **50** (2007) 315, [arXiv:hep-ex/0606049](#).
- [173] S. Baker and R. D. Cousins, *Clarification of the use of chi-square and likelihood functions in fits to histograms*, *Nucl. Instrum. Meth.* **221** (1984) 437.
- [174] T. Skwarnicki, *A study of the radiative cascade transitions between the Upsilon-prime and Upsilonon resonances*. PhD thesis. Cracow Institute of Nuclear Physics, 1986. DESY-F31-86-02.
- [175] P. David *et al.*, *Measurement of the relative yields of the decay modes $B^0 \rightarrow D^\pm \pi^\mp$, $B^0 \rightarrow D^\pm K^\mp$, $B_s^0 \rightarrow D_s^\pm \pi^\mp$ and determination of f_s/f_d for 7 TeV pp collisions*, [LHCb-ANA-2010-010](#).
- [176] K. D. Bruyn and P. Koppenburg, *Understanding the High Mass Tail of the Reconstructed B Mass distribution*, Talk at the PPMTS Meeting on Sep 12th, 2011.
- [177] BaBar Collaboration, B. Aubert *et al.*, *Dalitz Plot Analysis of the Decay $B^0(\bar{B}^0) \rightarrow K^\pm \pi^\mp \pi^0$* , *Phys. Rev. D* **78** (2008) 052005, [arXiv:0711.4417](#).
- [178] Belle Collaboration, S. Nishida *et al.*, *Radiative B meson decays into K pi gamma and K pi pi gamma final states*, *Phys. Rev. Lett.* **89** (2002) 231801, [arXiv:hep-ex/0205025](#).
- [179] Y. Grossman and D. Pirjol, *Extracting and using photon polarization information in radiative B decays*, *JHEP* **0006** (2000) 029, [arXiv:hep-ph/0005069](#).
- [180] A. Carbone *et al.*, *Measurement of direct CP violation in charmless charged two-body B decays at LHCb using 2010 data*, [LHCb-CONF-2011-011](#).
- [181] ARGUS Collaboration, H. Albrecht *et al.*, *Search for Hadronic $b \rightarrow u$ Decays*, *Phys. Lett. B* **241** (1990) 278.
- [182] W. Verkerke and D. P. Kirkby, *The RooFit toolkit for data modeling*, [arXiv:physics/0306116](#).
- [183] F. James and M. Roos, *Minuit: A System for Function Minimization and Analysis of the Parameter Errors and Correlations*, *Comput. Phys. Commun.* **10** (1975) 343.
- [184] M. Williams, *How good are your fits? Unbinned multivariate goodness-of-fit tests in high energy physics*, *JINST* **5** (2010) P09004, [arXiv:1006.3019](#).
- [185] Belle Collaboration, K. Kinoshita, *Evaluating quality of fit in unbinned maximum likelihood fitting*, in *Proceedings of the Conference on Advanced Techniques in Particle Physics* (M. Whaley and L. Lyons, eds.), pp. 176–181, 2002. www.ippp.dur.ac.uk/Workshops/02/statistics/proceedings/kinoshita.ps.
- [186] J. Heinrich, *Pitfalls of Goodness-of-Fit from Likelihood*, eConf **C030908** (2003) MOCT001, [arXiv:physics/0310167](#).

Bibliography

- [187] G. Cowan, *Statistical data analysis*. Clarendon Press (Oxford), 1998.
- [188] LHCb Collaboration, R. Aaij *et al.*, *Measurement of b-hadron production fractions in 7 TeV centre-of-mass energy pp collisions*, [LHCb-CONF-2011-028](#).
- [189] LHCb Collaboration, R. Aaij *et al.*, *Determination of f_s/f_d for 7 TeV pp collisions and a measurement of the branching fraction of the decay $B_d \rightarrow D^- K^+$* , [arXiv:1106.4435](#).
- [190] *LHCb MC11 generator and simulation statistics*, <http://lhcb-release-area.web.cern.ch/LHCb-release-area/DOC/STATISTICS/MC11STAT/index.shtml>.
- [191] J. V. Tilburg, *LHCb Tracking Efficiencies status/results*, <https://twiki.cern.ch/twiki/bin/view/LHCb/TrackingEffStatusUpdated>.
- [192] S. Miglioranzi and G. Corti, *Material interaction cross section studies*, [LHCb-INT-2011-002](#).
- [193] A. Powell, *PID Performance Package*, Internal talk at University of Oxford, Mar, 2011.
- [194] A. Powell, *Latest News on PIDCalib Package and PID Performance*, RICH Meeting, CERN, Aug, 2011.
- [195] J. D. Richman, *An Experimenter's Guide to the Helicity Formalism*, DOE Research and Development Report CALT-68-1148, California Institute of Technology, June, 1984.
- [196] J. J. Sakurai, *Modern Quantum Mechanics*. Addison-Wesley Publishing Company, Reading, MA, Revised ed., 1994.
- [197] H. Goldstein, *Classical Mechanics*. Addison-Wesley, 2nd ed., 1980.
- [198] E. P. Wigner, *Group Theory and Its Application to the Quantum Mechanics of Atomic Spectra*. Academic Press, 1959.
- [199] M. Jacob and G. C. Wick, *On the General Theory of Collisions for Particles with Spin*, *Ann. Phys.* **7** (1959) 404.